Chem. Rev. 2006, 106, 976−1031

Calorimetric Investigation of Phase Transitions Occurring in Molecule-Based Magnets[†]

Michio Sorai,*,[‡] Motohiro Nakano,[§] and Yuji Miyazaki[‡]

Research Center for Molecular Thermodynamics, Graduate School of Science, Osaka University, Toyonaka, Osaka 560-0043, and Department of Applied Chemistry, Graduate School of Engineering, Osaka University, Suita, Osaka 565-0871, Japan

Received June 20, 2005

Contents

1. Introduction

1.1. Scope

Magnetism is one of the important functionalities of materials and has been a basic research subject to understand materials. Magnetism has been explored mainly in the field of solid-state physics for inorganic substances consisting of atoms or ions of transition elements, in which electron spins on atomic orbitals mainly contribute to the magnetism. In this sense, traditional magnetism may be called "atom-based magnetism".[1] However, the situation in this field of science changed dramatically after the discovery of bulk ferromagnetism in molecular complexes such as decamethylferrocenium tetracyanoethenide $[Fe^{III}\{C_5(CH_3)_5\}_2][TCNE]$ (the Curié temperature $T_C = 4.8$ K) reported in 1987, $Mn^{II}Cu^{II}(obbz)\cdot H_2O$ [obbz = N,N'-oxamidobis(benzoato)] ($T_C = 14$ K) reported in 1989, and even in the pure organic compound p-NPNN (p-nitrophenylnitronyl-nitroxide) ($T_C = 0.60$ K) reported in 1991. Because spins of unpaired electrons on delocalized molecular orbitals are responsible for the magnetism, this new magnetism has been called "molecule-based magnetism".[1−7]

Magnetic functionality has widely been used for various practical applications, and this need will be further increased in the future. One of the great advantages of the use of

---

[†] We dedicate the present review article to Professor Emeritus Syûzô Seki of Osaka University (a member of the Japan Academy) in honor of his 90th Birthday. Contribution No. 100 from the Research Center for Molecular Thermodynamics.

* To whom correspondence should be addressed. Tel/Fax: +81-72-753-0922. E-mail: sorai@chem.sci.osaka-u.ac.jp.

[‡] Graduate School of Science.

[§] Graduate School of Engineering.

10.1021/cr960049g CCC: $59.00

Michio Sorai was born in 1939 and educated at Osaka University, where he started research in the field of chemical thermodynamics under the supervision of Professor Syûzô Seki. He received the B.Sc. degree in 1962 and the Ph.D. degree in 1968. He obtained a position of research at Osaka University in 1964 and was promoted to Associate Professor in 1981 and then to a full Professor of Physical Chemistry in 1987. He retired from Osaka University in 2003. As a postdoctoral fellow, he joined the research group of Professor Philipp Gütlich of Technische Hochschule Darmstadt (and then the University of Mainz) in the period of 1974–1976 to study the mechanism of spin crossover phenomena by use of Mössbauer spectroscopy. His research has focused on molecular thermodynamic studies of the phase transitions occurring in functional materials such as molecule-based magnets and liquid crystals, in particular phase transitions that directly involve electrons, such as spin crossover phenomena, intramolecular electron transfer in mixed-valence compounds, thermochromic phenomena, and charge-transfer phenomena. He served as an Associate Member of the IUPAC I.2 Commission on Thermodynamics from 1998 to 2001 and as the President of the Japan Society of Calorimetry and Thermal Analysis from 1999 to 2001. He was the Secretary General of the IUPAC International Conference on Chemical Thermodynamics, ICCT-1996 (Osaka), a member of the International Advisory Board of ICCT-2000 (Halifax), ICCT-2002 (Rostock), ICCT-2004 (Beijing), and that of the Russian International Conference on Chemical Thermodynamics, RCCT-2002 (St. Petersburg) and RCCT-2005 (Moscow). As the Editor-in-Chief, he contributed to the publication of a book entitled “Comprehensive Handbook of Calorimetry and Thermal Analysis” (John Wiley & Sons, 2004). He received the Hugh M. Huffman Memorial Award from the 56th Calorimetry Conference held in Colorado Springs in August 2001.

molecule-based magnets lies in the various possibilities of chemical modification onto a molecule; thereby, the magnetic property is finely adjusted by the chemical tuning. In the last two decades, various kinds of molecule-based magnets have been synthesized, and their chemical and physical properties have been elucidated from microscopic and macroscopic standpoints by use of various experimental methods. Among them, thermodynamic methods are unique in the sense that the energetic and entropic aspects inherent in materials can be directly observed. However, the number of scientific papers concerning thermodynamic research is not so many in comparison to other spectroscopic and structural studies. This is partly based on the misunderstanding that thermodynamics is a classical and old-fashioned science.

The aim of this paper is to survey calorimetric studies on molecule-based magnets published in the last two decades and to reveal the important roles played by calorimetric studies. It should be remarked here that in many papers referred to in this review article, the use of physical quantities “magnetic field strength” (symbol, H; unit, A m^{-1}) and “magnetic flux density” (symbol, B; unit, T) has often been confused. However, in view of a review article, we shall follow descriptions adopted in the original papers without correction.

Motohiro Nakano was born in 1963 in Matsumoto, Japan. He received his B.Sc. in Chemistry from Osaka University in 1985 and a Ph.D. degree in Inorganic and Physical Chemistry from Osaka University in 1990, working on heat-capacity calorimetry of paramagnetic compounds at very low temperatures, under the supervision by Professor Michio Sorai. Then, he moved to Professor Gen-etsu Matsubayashi’s group at Osaka University, where chemical and physical properties of sulfur-rich molecular conductors and transition metal complexes were investigated. In 1998–1999, he worked with Professor David N. Hendrickson at UCSD on the magnetism of single-molecule magnets. His research interests are mainly in energy level structures and dynamics of the transition metal complexes showing molecular bistability, including magnetization reversal processes of single-molecule magnets, dielectric responses of mixed-valence complexes, and field-induced spin crossover phenomena.

Yuji Miyazaki was born in Nagasaki in Japan in 1964. After graduating from Osaka University in 1987, he received his M.Sc. degree and his Ph.D. degree in Inorganic and Physical Chemistry from Osaka University in 1989 and 1993, respectively. Under the supervision of Professors Hiroshi Suga and Takasuke Matsuo, his thesis work dealt with the development of an adiabatic heat-capacity microcalorimeter and the LT thermal behavior of some crystalline proteins. He then joined the group of Professor Michio Sorai at Microcalorimetry Research Center (now the Research Center for Molecular Thermodynamics) at the same university as a Research Associate. His current research interests are mainly dynamics of biomolecules and synthetic macromolecules, magnetic properties of molecule-based magnets, and thermal properties of organic charge-transfer complexes.

1.2. Characteristic Aspects of Molecular Thermodynamics

Physical quantities obtained from thermodynamic measurements reflect macroscopic aspects of materials in the sense that they are derived as the ensemble averages in a given system. However, because those quantities are closely related to the microscopic energy schemes of all kinds of molecular degrees of freedom in a statistical manner, one can gain detailed knowledge on the microscopic level on the basis of precise calorimetry. This field of study has been recognized as "molecular thermodynamics". Among various thermodynamic measurements, heat-capacity calorimetry is an extremely useful tool to investigate thermal properties of materials at low temperatures. In most thermodynamic textbooks and monographs, interpretation of the thermodynamic laws and derivation of thermodynamic equations occupy many parts of the pages. However, descriptions about how to interpret experimental results are scarce or limited to very classical examples, if any. Therefore, a brief description will be made, at first, about what kinds of microscopic and macroscopic information are derived from actual calorimetry.[8−14]

Heat capacity is usually measured under constant pressure and designated as C_p. From the definition $C_p \equiv (\partial H/\partial T)_p$, enthalpy is determined by integration of C_p with respect to temperature T: $H = \int C_p\, dT$. Because C_p is alternatively defined as $C_p \equiv T(\partial S/\partial T)_p$, entropy S is also obtainable by integration of C_p with respect to ln T: $S = \int C_p\, d \ln T$.

Condensed states of matter are basically controlled by the interplay among molecular structures, intermolecular interactions, and molecular motions. Functionalities of materials manifest themselves as the result of a concerted effect among these three factors. When a delicate balance of these three factors is broken, the condensed state faces a catastrophe and is transformed into another phase. This is the so-called phase transition. Therefore, phase transition is a good probe for elucidation of the interplay among these three factors. Most phase transitions observed in molecule-based magnets are not first-order but second-order or higher-order phase transitions. Although the first-order phase transition takes place isothermally with a latent heat, the higher-order phase transition exhibits a sharp peak at a critical temperature T_c with long heat-capacity tails below and above T_c. The extent of order lost in the higher-order phase transition is described in terms of "order parameter". The heat-capacity tail above T_c reflects the short-range order still remaining in the system. In the vicinity of the critical temperature T_c, the heat capacity C is often reproduced by the following equations: $C \propto \epsilon^{-\alpha}$ $(T > T_c)$ and $C \propto |-\epsilon|^{-\alpha'}$ $(T < T_c)$, where $\epsilon \equiv (T - T_c)/T_c$ and α and α' are critical exponents, from which one can get information such as the lattice structure and the interaction involved in the system.

The entropy gain at the phase transition plays a diagnostic role for interpretation of the mechanisms governing the phase transitions. A clue to correlate the entropy with the microscopic aspect is the Boltzmann principle given by $S = kN_A \ln W = R \ln W$, where k and N_A are the Boltzmann and the Avogadro constants, R is the gas constant, and W stands for the number of energetically equivalent microscopic states. If one applies this principle to the transition entropy, the following relationship is easily derived because ΔS is the entropy difference between the high- (HT) and low-temperature (LT) phases: $\Delta S = R \ln(W_H/W_L)$, where W_H and W_L mean the number of microscopic states in the HT and LT phases, respectively. In many cases, the LT phase corresponds to an ordered state and hence $W_L = 1$. Therefore, on the basis of experimental ΔS value, one can determine the value of W_H.

Because the molecule-based magnets consist of molecular parts as the building blocks, their structures are anisotropic; thus, physical properties inevitably become structurally anisotropic. In many cases, this leads to low-dimensional magnets in which one- (1D) or two-dimensional (2D) interaction is dominant.[15−17] Short-range and long-range orders formed by spins crucially depend on the magnetic lattice structure. These features are very sensitively reflected in heat capacity.

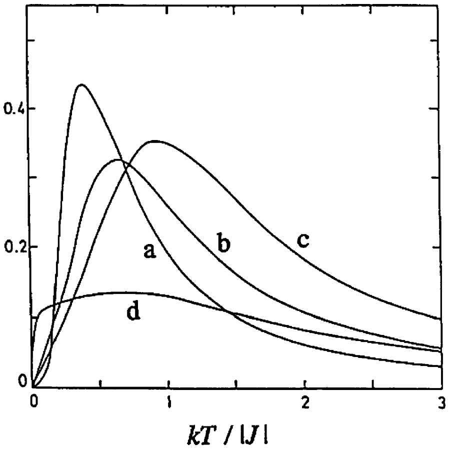

Figure 1. Theoretical heat capacities of magnetic chains with spin $S = 1/2$: (a) ferro- or antiferromagnetic Ising model, (b) ferro- or antiferromagnetic XY model, (c) antiferromagnetic Heisenberg model, and (d) ferromagnetic Heisenberg model. Reprinted with permission from ref 15. Copyright 1974 Taylor & Francis Group.

When paramagnetic species form clusters magnetically isolated from one another, the magnetic clusters can be regarded as being of zero-dimension (0D), whose spin-energy scheme consists of a bundle of energy levels. In such a case, there exists no phase transition and the magnetic heat capacity exhibits a broad anomaly characteristic of the cluster geometry. For a linear-chain structure (1D lattice), no phase transition is theoretically expected because fluctuation of the spin orientation is extremely large. As shown in Figure 1 for the 1D $S = 1/2$ case,[15] only a broad heat-capacity anomaly characteristic of 1D structure is observed. Heat capacities of the 1D magnetic systems characterized by Ising and XY type interactions are identical for ferromagnetic and antiferromagnetic interactions (curves a and b). Contrary to this, the system characterized by Heisenberg type interaction provides quite different heat-capacity curves between antiferromagnetic (curve c) and ferromagnetic chains (curve d). By comparing experimental heat capacity with these theoretical curves, one can easily estimate the type of spin−spin interaction operating in the material.

In the case of a 2D lattice, a phase transition showing a remarkable short-range order effect takes place when the interaction is of the Ising type, while there is no phase transition for the Heisenberg type. Contrary to this, a three-dimensional structure (3D) gives rise to a phase transition with a minor short-range order effect, independent of the type of spin−spin interaction.

In actual magnetic materials, interaction paths, through which exchange spin−spin interaction takes place, are often much more complicated than being classified into a homogeneous single dimension. As a result, it happens that apparent dimensionality seems to change with temperature. This feature is called "dimensional crossover". Figure 2 shows the dimensional crossover between 1D and 2D lattices for the spin $S = 1/2$ ferromagnetic Ising model with the intrachain interaction parameter J and the interchain interaction parameter J'.[18] The dashed curve corresponds to 1D ($J' = 0$) and the dot−dashed curve is the heat capacity of a

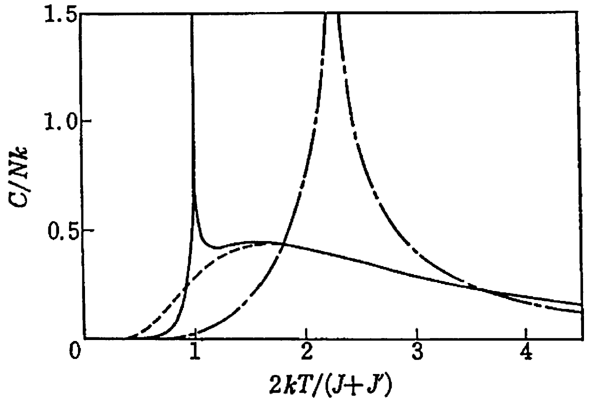

Figure 2. Dimensional crossover between 1D and 2D lattices for the spin $S = 1/2$ ferromagnetic Ising model with the intrachain interaction parameter J and the interchain interaction parameter J'. Dashed and dot−dashed curves correspond to 1D ($J' = 0$) and 2D ($J = J'$) models, respectively. A solid curve indicates the heat capacity of a rectangular lattice ($J' = 0.01J$), showing the dimensional crossover between 1D and 2D lattices. Reprinted with permission from ref 18. Copyright 1960 Taylor & Francis Group.

square planar 2D lattice ($J = J'$) corresponding to the exact solution by Onsager.[19] The solid curve indicates the heat capacity of a rectangular lattice ($J' = 0.01J$), which shows the dimensional crossover between 1D and 2D lattices. At high temperatures, the heat-capacity curve asymptotically approaches the 1D curve, while at low temperatures the existent 2D interchain interaction, although weak, diminishes the fluctuation of the system and leads to a phase transition.

When a system consists of a finite number of energy levels, its heat capacity exhibits a broad anomaly, which asymptotically approaches zero at high temperatures. This type of anomaly is designated as the Schottky anomaly and is encountered in paramagnetic clusters and in systems involving Zeeman splitting, tunnel splitting, zero-field splitting, and so on.

Spin-wave (magnon) theory has been proven to be a good approximation to describe the LT properties of magnetic substances. The limiting LT behavior of heat capacity due to spin-wave excitation C_{SW} is conveniently given by the formula,[15] $C_{\mathrm{SW}} \propto T^{d/n}$, where d is the dimensionality and n is defined as the exponent in the dispersion relation. For antiferromagnetic magnons, n is equal to 1, while for ferromagnetic magnons $n = 2$. Thus, for example, the spin-wave heat capacity of a 3D ferromagnet is proportional to $T^{3/2}$ and that of a 2D antiferromagnet is proportional to T^2. However, because actual low-dimensional magnets contain, more or less, weak 3D interactions, the dimensionality sensed by spin at extremely low temperatures is $d = 3$.

One of the most characteristic aspects inherent in thermodynamics is that there exists no selection rule. In other words, any degrees of freedom originating in atoms, molecules, electrons, and spins can contribute to thermodynamic quantities. For example, the heat capacity of a solid measured at constant pressure, C_p, consists of contributions from lattice vibrations, C_{lat}, and magnetic freedom, C_{mag}. Therefore, if one discusses the magnetic event, one should separate the magnetic part from the observed value. Except for scarce materials with simple crystal structures, it is usually very difficult to estimate C_{lat} on the basis of the first principle of lattice dynamics. To avoid this difficulty, various approximate methods for separation have been proposed. Usually, the lattice heat capacity (or normal heat capacity) has been approximated by a polynomial function of temperature in a narrow interval or a combination of Debye and/or Einstein heat-capacity functions. In particular, the polynomial function of odd power of temperature, $C_{\mathrm{lat}} = aT^3 + bT^5 + cT^7 + \cdots$, is often a good approximation at low temperatures. At moderate and high temperatures, the effective frequency-distribution method proposed by Sorai and Seki[20] is a useful method. In this method, an effective frequency-distribution spectrum of lattice vibrations is first determined in the temperature region(s), where a relevant event has no contribution, and then, the hypothetical lattice heat capacity in the event temperature region is estimated on the basis of the obtained spectrum.

1.3. Heat-Capacity Calorimetry

Roughly classifying the methods of determination of heat capacity, there are four experimental methods: (i) adiabatic calorimetry, (ii) a.c. calorimetry, (iii) relaxation calorimetry, and (iv) differential scanning calorimetry (DSC).[21]

(i) Adiabatic calorimetry is a static method to determine precisely absolute values of heat capacity in thermal equilibrium. Because this calorimetry has mainly been used for the purposes of basic research, commercially available apparatuses are scarce. Consequently, researchers construct their own calorimeters suitable for the specific purposes. The adiabatic principle can be employed for heat-capacity measurements from cryogenic temperatures to ∼1000 K. A shortcoming of this method is that it requires a large amount of specimen, usually several grams to ∼100 mg.

(ii) The other three calorimetries belong to dynamic methods. In a.c. calorimetry, the sample is heated periodically by chopped light or sinusoidal Joule heating. The amplitude of the temperature response at the same frequency is inversely proportional to the heat capacity. Because the absolute values of heat capacity of a sample cannot directly be obtained by this method, it is necessary to adjust the scale of the experimental values by use of known heat-capacity data determined by another method. The amount of sample needed for the a.c. method is as small as several micrograms. Therefore, this method enables us to measure the heat capacity of a tiny single crystal.

(iii) In the relaxation method, the sample is heated with a short pulse of energy and the resulting temperature rise and fall (due to the environment) is measured. The time constant of the exponential decay of temperature gives the heat capacity, provided the thermal resistance is known by a calibration measurement. In addition to home-built apparatuses, one can use commercially available calorimeters. The amount of specimen used for this method is ∼10 to ∼100 mg.

(iv) DSC is one of the methods belonging to thermal analysis, in which the physical property of a sample is monitored under a programmed temperature control and the results are recorded together with the temperature. Many kinds of DSC are commercially available. The amount of sample used for this method is a few milligrams to ∼10 mg. The great merit is a simple operation supported by an equipped computer.

2. Organic Free Radicals

The study of genuine organic ferromagnets is one of the research subjects attracting many organic and physical chemists, because the carrier of the spin is neither *d*- nor *f*-electron but *p*-electron and also because one can easily design a variety of molecular and crystal structures in comparison to traditional magnets such as metals and metal oxides. Furthermore, because most organic molecules are magnetically isotropic, they can be regarded as ideal Heisenberg spin systems, which lead to interesting quantum spin systems. Despite tiny magnetic anisotropy of the spins, however, most organic free radical crystals exhibit low-dimensional magnetic properties owing to structural anisotropy and relative arrangement of their constituent molecules.

In 1991, Kinoshita and his collaborators[22] discovered that the β-phase crystal of *p*-nitrophenyl nitronyl nitroxide (*p*-NPNN) becomes a bulk ferromagnet. Since then, several bulk ferromagnetic organic radical crystals have successfully been synthesized as follows: nitronyl nitroxide derivatives,[23−26] 2,2,6,6-tetramethylpiperidin-1-oxyl (TEMPO) derivatives,[27−32] verdazyl derivatives,[33] the α-phase crystal of *N*,*N*′-dioxy-1,3,5,7-tetramethyl-2,6-diazaadamantane,[34] and a complex consisting of tetrakis(dimethylamino)ethylene (TDAE) and C_{60}.[35]

2.1. Nitronyl Nitroxide Radicals

Crystalline *p*-NPNN (Figure 3) forms four crystalline polymorphs, a monoclinic α-phase,[36] orthorhombic β-phase,[37,38] monoclinic β_h-phase,[36,39] and triclinic γ-phases,[40] which all have ferromagnetic intermolecular coupling. In 1991, Kinoshita et al.[41,42] discovered on the basis of magnetic and heat-capacity measurements that the γ-phase of *p*-NPNN exhibits a ferromagnetic phase transition at $T_C = 0.65$ K (see Figure 4) and the heat-capacity hump above T_C is well-approximated by the $S = 1/2$ 1D ferromagnetic Heisenberg model with $J/k = 4.3$ K. In the same year, they also discovered that the β-phase of *p*-NPNN shows a ferromagnetic phase transition at $T_C = 0.60$ K (Figure 4).[22] Nakazawa et al.[39] reported that the magnetic phase transition of the γ-phase of *p*-NPNN at $T_C = 0.65$ K is not ferromagnetic but antiferromagnetic from the magnetic field variable a.c. magnetic susceptibility and heat-capacity data. It was found by DTA measurement that the β-phase is more stable than the γ-phase, and the γ-phase sample reported previously[41,42] was contaminated by a small amount of the β-phase. Spin-wave analyses for the magnetic heat capacities of both the β- and the γ-phases below their magnetic phase transition temperatures revealed that the magnetic heat-capacity data of the β-phase are proportional to $T^{3/2}$, corresponding to a 3D ferromagnet, while those of the γ-phase are proportional to T^3, suggesting a 3D antiferromagnet. The magnetic entropy of the β-phase rose very steeply at T_C as encountered in ordinary 3D ferromagnets and reached the value $R \ln 2$ expected for $S = 1/2$ spin systems, while that of the γ-phase increased gradually above T_N due to the short-range order effect characteristic of 1D magnetic systems and approached $R \ln 2$. The magnetic field dependence of the heat capacity of the γ-phase was analyzed in the framework of a mean field approximation to provide the interchain interactions $J'/k = 0.224$ K and $J''/k = -0.176$ K.[43] On the other hand, the 3D magnetic interaction of the β-phase was estimated to be $J/k = 0.6$ K. The critical temperature and the magnetic properties of all of the radical crystals described in this chapter are summarized in Table 1.

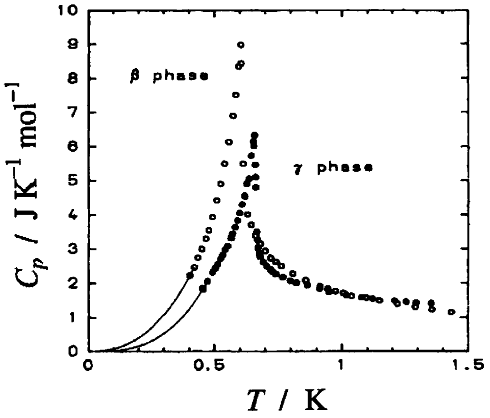

Figure 4. Molar heat capacities of β- and γ-phases of *p*-NPNN. The solid curves for these phases at the LT side represent the spin-wave approximation for 3D ferromagnetic and 3D antiferromagnetic systems, respectively. Reprinted Figure 3 with permission from Nakazawa, Y.; Tamura, M.; Shirakawa, N.; Shiomi, D.; Takahashi, M.; Kinoshita, M.; Ishikawa, M. *Phys. Rev. B 46*, 8906, 1992 (http://link.aps.org/abstract/PRB/v46/p8906). Copyright 1992 by the American Physical Society.

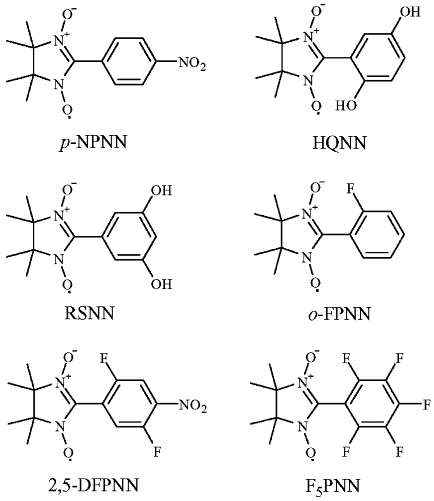

Figure 3. Molecular structures of nitronyl nitroxide radicals.

Takeda et al.[44−46] investigated the mechanism of the intermolecular magnetic interactions of the β-phase of *p*-NPNN by experiments under pressure and magnetic field. From the pressure variable heat-capacity and a.c. magnetic susceptibility measurements, a drastic depression of the Curie temperature and a pressure-induced ferromagnetic-to-antiferromagnetic transition at $P_c = (0.65 \pm 0.05)$ GPa were observed. This transition was also detected by the pressure dependence of the lattice parameters. At ambient pressure, the effective intermolecular magnetic interaction was estimated to be $zJ/k = 2.3$ K by the magnetic heat capacity under magnetic field. Furthermore, the magnetic heat capacity turned out to be 2D ferromagnetic under a high pressure such as $P = 0.72$ GPa.

Sugawara et al.[24,47] designed a new nitronyl nitroxide derivative carrying a hydroquinone moiety, 2-(2′,5′-dihydroxyphenyl)-4,4,5,5-tetramethyl-4,5-dihydro-1*H*-imidazolyl-1-oxy-3-oxide (HQNN; Figure 3), to control the molecular assembly and thus the magnetic property by the intra- and intermolecular hydrogen bonding. HQNN crystallizes into either of two polymorphs: monoclinic α- and β-phases. The temperature dependence of the magnetic susceptibility of α-HQNN was reproduced well by the singlet−triplet model with the ferromagnetic intradimer exchange interaction of $J/k = 0.93$ K with a positive Weiss constant of $\theta = +0.46$

Table 1. Critical Temperature and Magnetic Properties of Organic Radical Crystals

compound	T_c (K)	dimensionality below T_c	dimensionality above T_c	Weiss constant θ (K)	interaction parameter $J \cdot k^{-1}$ (K)	refs
p-NPNN (β-phase)	0.60	3D-F	3D-F	1.2	0.6 (3D)	22, 39
p-NPNN (γ-phase)	0.65	3D-AF	1D-F	2	4.3 (1D); 0.224, −0.176 (inter-1D)	39, 41, 42
HQNN (α-phase)	0.42	3D-F	F-dimer	0.46	0.93 (intradimer)	47
HQNN (β-phase)			F-dimer	−0.32	5.0 (intradimer)	47
RSNN			F-dimer	−4.0	10 (intradimer)	47
o-FPNN	0.3	3D-F	1D-F	0.48	0.6 (1D)	23
2,5-DFPNN	0.45		1D-F	0.66	0.70 (1D)	26, 48
F_5PNN			1D-AF		−3.1, −1.24 (alternate-1D)	53
MOTMP	0.14	3D-AF	1D-F	0.16	0.45 (1D); 0.03, −0.02 (inter-1D)	59, 61, 62
MATMP	0.15	3D-AF	1D-F		0.70 (1D); −0.045 (inter-1D)	63, 65
CATMP	0.28	3D-F	2D-F	0.69	0.42 (2D); 0.024 (inter-2D)	30, 66
BATMP	0.19	3D-F	1D-F	0.7	0.95 (1D); 0.026 (inter-1D)	27, 67
p-CDTV	0.68	3D-AF	1D-F	3.0	6.0 (1D)	74, 78, 81
p-BDTV			1D-AF	−25	−20.6 (1D)	74, 78
p-CDpOV	0.21	3D-F	1D-F	3.35	5.5 (1D); 3×10^{-2} (inter-1D)	33
DPTOV	5.45	3D-AF	1D-AF	−7.5	7.25 (1D)	71
p-NTpV	1.16	3D-AF	1D-F	3.1	3.5 (1D); −1.5 (inter-1D)	72
NDpV			1D-AF	−7.3	−5.8 (1D)	72
NDpMV				−18		72
p-NDpMV			1D-AF		−56.5, −22.5 (alternate-1D)	72
TOV	4.8	3D-AF	2D-AF	−9.9	−4.5 (2D)	80
p-CyDOV	0.135	3D-AF	SP		−42.1 (1D)	82, 84−86
p-NCC_6F_4CNSSN (α-phase)	8	3D-AF		−25		90, 93
p-NCC_6F_4CNSSN (β-phase)	35.5	3D-AF		−102	−83 (1D)	90, 93, 94
BDTA	11	3D-AF		−93		96
DMTzNC-TCNQ	1.49	3D-AF	1D-AF		−32.5 (1D)	97
m-MPYNN$\cdot BF_4$			2D-AF		−1.6 (2D)	98
DCPTTCPPA	0.40	3D-AF	1D-F		14.0 (1D); 0.02, −0.01 (inter-1D)	101
PNNNO (biradical)	1.1	3D-AF	1D-AF		319 (intraradical); −7.3 (1D)	102
F_2PNNNO (biradical)			2D-AF		204 (intraradical); −34, −3.7 (2D)	102
PIMNO (biradical)	2.5	3D-AF	1D-AF		108 (intraradical); −6 (1D)	102
PNNBNO (triradical)	0.28	3D-F	SL		430, −108 (intraradical); −0.3 (1D)	103
BImtBN	1.7	3D-AF	BL		−1.2 (2D); −1.9 (inter-2D)	104, 106
BImPhtBN			2D-AF		−1.6 (2D)	105
ClBImtBN			AF-dimer		−22 (intradimer)	105
Me2BImtBN			AF-dimer		−24 (intradimer)	105

Table 2. Ratio of T_C/θ and Entropy of Spin System in Lower Temperature Region than T_C (S_C) and That in Higher Temperature Region than T_C ($S_\infty - S_C$)[a,b]

model or crystal	T_C/θ	S_C (%)	($S_\infty - S_C$) (%)
mean field	1	100	0
Ising sc	0.75	81	19
Ising diamond	0.67	74	26
Heisenberg fcc	0.67	67	33
Heisenberg bcc	0.63	65	35
Heisenberg sc	0.56	62	38
α-HQNN[47]	0.56	60	40

[a] Reprinted with permission from ref 47. Copyright 1997 American Chemical Society. [b] S_C, entropy change between 0 K and T_C; S_∞, entropy change of magnetic phase transition.

K. The a.c. magnetic susceptibility increased rapidly around 0.5 K, suggesting a ferromagnetic phase transition around this temperature. The temperature dependence of the heat capacity of α-HQNN exhibited a λ-shaped anomaly with a peak due to the ferromagnetic phase transition at $T_C = 0.42$ K. The associated entropy change was evaluated to be 5.4 J K^{-1} mol^{-1}, which is in accord with the theoretical value R ln 2. As seen in Table 2,[47] the ratio of T_C and θ and the relative ratio of the entropy gained below T_C (designated as S_C) and that above T_C [designated as ($S_\infty - S_C$)] are close to the 3D Heisenberg model for a simple cubic lattice. These facts suggest that α-HQNN is a 3D ferromagnet. On the other hand, the temperature dependence of the magnetic susceptibility of β-HQNN was fitted well by the singlet−triplet model with the ferromagnetic intradimer exchange interaction of $J/k = 5.0$ K assuming the interdimer interaction as a negative Weiss constant of $\theta = -0.32$ K. They also synthesized an analogous organic radical 2-(3′,5′-dihydroxyphenyl)-4,4,5,5-tetramethyl-4,5-dihydro-1H-imidazolyl-1-oxy-3-oxide

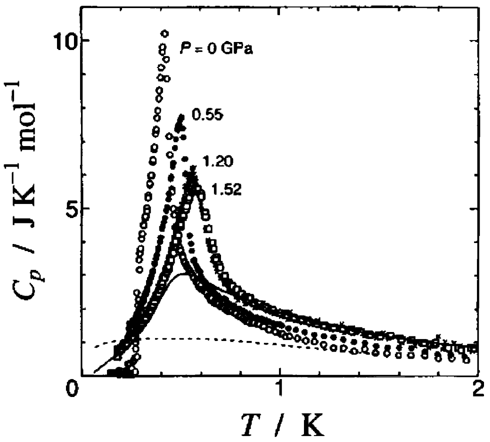

Figure 5. Pressure dependence of the magnetic heat capacity of 2,5-DFPNN in the hydrostatic pressure region up to 1.52 GPa. The dotted and solid curves express the theoretical curves of $S = 1/2$ 1D Heisenberg ferromagnetic system with intrachain interaction $J_{1D}/k = 0.70$ K and $S = 1/2$ 2D Heisenberg ferromagnetic system with intraplane interaction $J_{2D}/k = 0.70$ K, respectively. Reprinted Figure 3 with permission from Mito, M.; Deguchi, H.; Tanimoto, T.; Kawae, T.; Nakatsuji, S.; Morimoto, H.; Anzai, H.; Nakao, H.; Murakami, Y.; Takeda, K. *Phys. Rev. B 67*, 024427, 2003 (http://link.aps.org/abstract/PRB/v67/p24427). Copyright 2003 by the American Physical Society.

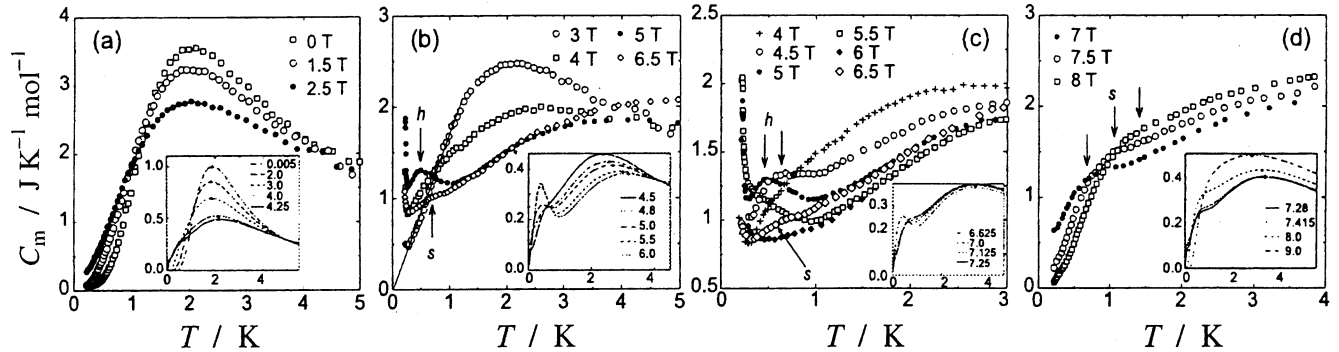

Figure 6. Temperature dependence of the magnetic heat capacity C_m in magnetic fields. (a) $0 \leq H/T \leq 2.5$ (spin-gapped phase), (b and c) $3 \leq H/T \leq 6.5$ (gapless phase), and (d) $7 \leq H/T \leq 8$ (spin-polarized phase). A solid line in panel b shows linear *T* dependence of C_m. Down arrows in panels b and c indicate a hump in C_m. Up arrows in panels b and c and down arrows in panel d indicate a shoulder C_m. Inserts show theoretical calculations of the strongly coupled two-leg ladder system. Reprinted Figure 3 with permission from Yoshida, Y.; Tateiwa, N.; Mito, M.; Kawae, T.; Takeda, K.; Hosokoshi, Y.; Inoue, K. *Phys. Rev. Lett. 94*, 037203, 2005 (http://link.aps.org/abstract/PRL/v94/p37203). Copyright 2005 by the American Physical Society.

(RSNN; Figure 3) whose crystal structure resembles that of β-HQNN. The temperature dependence of the magnetic susceptibility was also reproduced well by the singlet−triplet model with the ferromagnetic intradimer exchange interaction of $J/k = 10$ K with a negative Weiss constant of $\theta = -4.0$ K. Although the analysis using the Bleaney−Bowers equation modified with an enhancement factor $T/(T - \theta)$ is widely applied to weakly coupled spin-dimer systems, it is not obvious for these compounds possessing no remarkable short-range order to be modeled by such a singlet−triplet system.

Nakatsuji et al. prepared some halogen-substituted nitronyl nitroxide derivatives, 2-(2′-halophenyl)-α-nitronyl nitroxides[23] and difluorophenyl-α-nitronyl nitroxides[26] (Figure 3). Among four kinds of 2-(2′-halophenyl)-α-nitronyl nitroxides, only 2-(2′-fluorophenyl)-α-nitronyl nitroxide (*o*-FPNN) indicated a positive Weiss constant $\theta = +0.48$ K.[23] A.c. magnetic susceptibility and heat-capacity measurements revealed a magnetic phase transition around 0.3 K. A broad heat-capacity hump observed at the HT side of the phase transition peak was well-reproduced by the $S = 1/2$ 1D ferromagnetic Heisenberg model with $J/k = (0.6 \pm 0.1)$ K. The temperature dependence of the a.c. magnetic susceptibility below 0.25 K also suggested that this magnetic transition is ferromagnetic. On the other hand, among four difluorophenyl-α-nitronyl nitroxides, only the 2,5-derivative (2,5-DFPNN) had ferromagnetic interactions.[26] A.c. magnetic susceptibility and heat-capacity measurements revealed that 2,5-DFPNN exhibits a ferromagnetic phase transition at $T_C = 0.45$ K at ambient pressure.[26,48] As shown in Figure 5, when pressure was applied, the heat-capacity anomaly was linearly shifted toward HT side up to 0.57 K at 1.52 GPa.[48,49] Furthermore, application of pressure made the shape of the heat-capacity anomaly above T_C change to that characteristic of the $S = 1/2$ 2D Heisenberg ferromagnet of a square lattice with $J_{2D}/k = 0.70$ K. The enhancement of T_C was considered to originate mainly from the development of the 2D ferromagnetic interaction on the *ac* plane. The ferromagnetic signal of the a.c. magnetic susceptibility, however, was decreased by applying pressure and almost disappeared at $P \geq 5.0$ GPa, which would arise from the decrease of the ferromagnetic interaction along the *b*-axis.

One of the halogen-substituted nitronyl nitroxide derivatives, pentafluorophenyl nitronyl nitroxide (F_5PNN; Figure 3), was synthesized by Hosokoshi et al.[50−52] This is an $S = 1/2$ 1D Heisenberg antiferromagnet with the alternating magnetic interaction ratio $\alpha = |J_2/J_1| = 0.4$ ($J_1/k = -3.1$ K) giving rise to a spin-gap system. Mito et al.[53] performed heat-capacity measurements of a F_5PNN crystal under pressures up to 0.78 GPa to confirm the pressure-induced crossover from the alternating bond system to the uniform one. The exponential temperature dependence of the heat capacity at low temperature and at ambient pressure was changed gradually and continuously to a linear one with increasing pressure, and eventually the alternating magnetic interaction was transformed into the uniform one ($\alpha = 1$, $J_1/k = -4.5$ K) at 0.65 GPa. On the other hand, Yoshida et al.[54−56] investigated the magnetic field dependence of the heat capacity of a F_5PNN crystal. Two critical magnetic fields were found at H_{C1} (= 3 T) and H_{C2} (= 6.5 T). In the $H \leq H_{C1}$ magnetic field region (spin-gapped phase; Figure 6a), a heat-capacity hump around 2 K due to the short-range ordering in 1D magnets was suppressed and broadened with an increasing magnetic field. Moreover, the exponential behavior changed gradually to an almost linear *T* dependence, indicating the suppression of the energy gap, which was estimated to be $\Delta/k = 4.0$ K in the zero magnetic field.[55] However, the magnetic heat capacity at 2.5 T was not monotonically decreased to zero when the temperature approached 0 K. In the $H_{C1} \leq H \leq H_{C2}$ magnetic field region (gapless Tomonaga−Luttinger liquid phase; Figure 6b,c), an upturn or a cusplike anomaly[54] due to the field-induced magnetic ordering (FIMO) was observed for $T \leq 0.2$ K, which was enhanced with increasing magnetic field up to 5 T and suppressed in the higher magnetic field. Furthermore, another hump emerged around 0.6 K at 4.5 T. With increasing magnetic field, this hump was shifted to the lower temperature and then merged with the sharp anomaly due to the FIMO at 5.5 T. This hump was not finally observed at 6 T, while a shoulder appeared around 0.7 K at 6.5 T. In the $H \geq H_{C2}$ magnetic field region (spin-polarized phase; Figure 6d), the exponential decay was seen again at low temperatures as in the case for $H \leq 2.5$ T. However, the magnetic heat capacity at 7 T did not approach zero monotonically down to 0 K as is the case of 2.5 T. The shoulder found at 6.5 K was also seen and developed with increasing magnetic field. These features were qualitatively in good agreement with the theoretical calculations on the $S = 1/2$ two-leg spin-ladder model with the intra- and interchain interactions, $J_{\|}/k = 1$ and $J_{\perp}/k = 5.28$, respectively[57] (see the insets in Figure 6).

2.2. TEMPO Radicals

Most TEMPO radical crystals possess antiferromagnetic interactions.[32,58−60] Kamachi et al.[59−65] prepared some TEMPO derivatives (Figure 7) and investigated their magnetic properties. They found ferromagnetic interactions in 4-methacryloyloxy-TEMPO (MOTMP) and 4-acryloyloxy-TEMPO (MATMP) crystals.[59−61] Ohmae et al. carried out heat-capacity measurements of MOTMP[59,61] and MATMP.[63] As shown in Figure 8, MOTMP exhibited a magnetic phase transition at $T_c = 0.14$ K together with a broad hump arising from a short-range ordering characteristic of low-dimensional magnets. This broad anomaly was well-reproduced by the ferromagnetic 1D Heisenberg model with the exchange interaction parameter of $J/k = 0.45$ K (curve 2). As far as the crystal structure of this compound is concerned, there seems to be no indication of any 1D structure concerning the packing of molecules. This finding of 1D character was afterward confirmed by magnetic susceptibility measurements done below 1 K.[62] Because the lattice heat capacity (curve 1) was extremely small in this temperature region, the separation of the magnetic contribution from the observed value was accurately done. The entropy gain due to the phase transition and the hump amounted to 5.8 J K^{-1} mol^{-1}, which is substantially the same as the expected spin entropy of $R \ln 2$ (= 5.76 J K^{-1} mol^{-1}). A similar result has been obtained for MATMP. Although the spin-wave analysis (line 3) suggested a ferromagnetic 3D long-range order, magnetic measurements below T_c revealed that the magnetic state is not ferromagnetic but antiferromagnetic.[62,64,65]

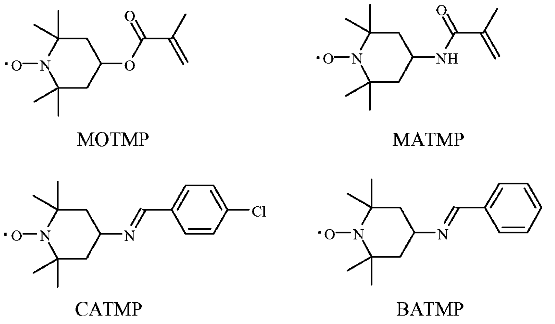

Figure 7. Molecular structures of TEMPO radicals.

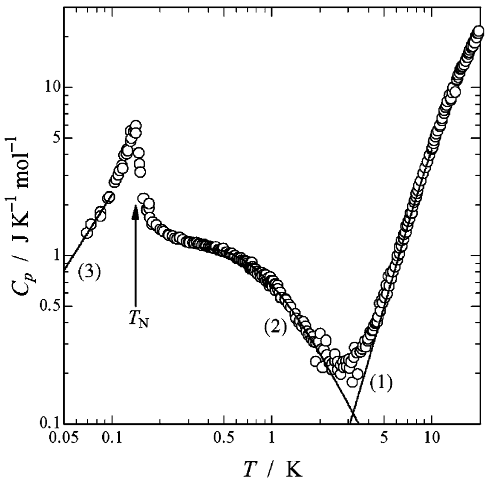

Figure 8. Molar heat capacity of MOTMP. Curve 1, lattice heat capacity; curve 2, ferromagnetic 1D Heisenberg model ($J/k = 0.45$ K); and line 3, spin-wave contribution. Reprinted with permission from ref 61. Copyright 1993 Taylor & Francis Group.

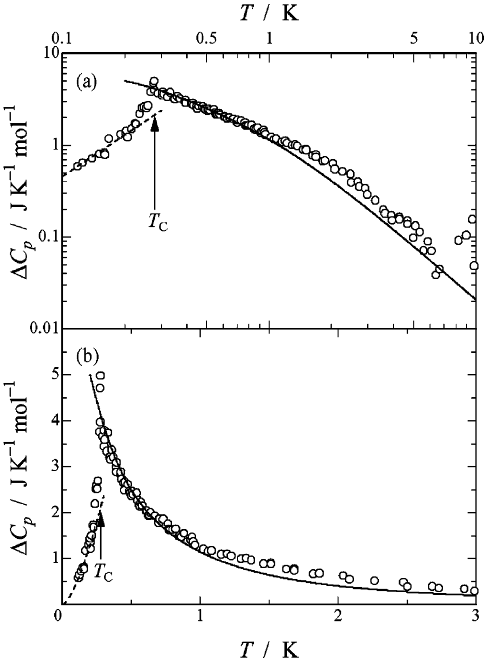

Figure 9. Magnetic heat capacities of CATMP free radical crystal on (a) logarithmic and (b) normal scales. Solid curves indicate the heat capacities calculated from the HT series expansion for the $S = 1/2$ 2D ferromagnetic Heisenberg model of square lattice with $J/k = 0.42$ K. Broken curves show the heat capacities derived from the spin-wave theory for 3D ferromagnets. Reprinted with permission from ref 66. Copyright 2000 The Chemical Society of Japan.

Nogami et al.[27−32] synthesized many TEMPO radicals and discovered bulk ferromagnetic behaviors in some TEMPO crystals (Figure 7). Among them, Miyazaki et al. measured heat capacities of CATMP[66] and 4-benzylideneamino-TEMPO (BATMP)[67] crystals and found ferromagnetic phase transitions at $T_C = 0.28$ and 0.19 K, respectively. Figure 9 illustrates the excess heat capacity of CATMP plotted on logarithmic and normal scales. As shown by the solid curves, the heat-capacity anomaly appearing above T_C is well-reproduced by the 2D ferromagnetic Heisenberg model with the intralayer magnetic interaction of $J/k = 0.42$ K. The spin-wave analysis (broken curves in Figure 9) suggested a 3D ferromagnetic state in the long-range ordered phase with an interlayer magnetic interaction of $J'/k = 0.024$ K. X-ray structural analyses[27,30] revealed that both crystals have 2D sheet structures. This result is consistent with the observation of the heat-capacity anomaly above T_C.

Mito et al.[68] performed magnetic and heat-capacity measurements under pressure to investigate the pressure dependence of the ferromagnetic phase transition of CATMP crystal. They found three pressure-induced phenomena: (i) a down−up variation with a period of about 0.4 GPa for $P < 0.9$ GPa and monotonic and slight increases for $P \geq 0.9$ GPa of the magnetic transition temperature, (ii) a ferromagnetic-to-antiferromagnetic transition around 0.5 GPa, and (iii) a reduction of the magnetic lattice dimensionality from 2D Heisenberg ferromagnet to a 1D one, which can be understood by the pressure-induced rotation of the methyl moiety relevant to the interaction mechanism through C−H···O−N contacts.

2.3. Verdazyl Radicals

Verdazyls provide a family of stable organic radicals (Figure 10). Ferromagnetic interactions were first demonstrated in 3-(4-nitrophenyl)-1,5,6-triphenylverdazyl (*p*-NTpV), which indicated a positive Weiss constant of $\theta =$

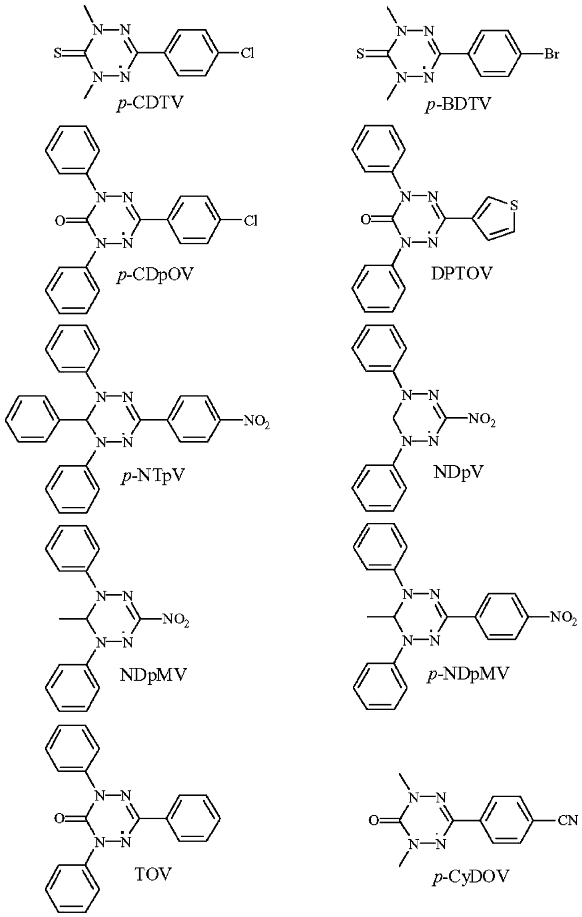

Figure 10. Molecular structures of verdazyl radicals.

1.6 K.[69] Several verdazyl derivatives have so far been reported to exhibit magnetic phase transitions.[33,70−73]

Mukai et al. measured magnetic susceptibility[74] and heat-capacity[70,75−78] measurements of 3-(4-chlorophenyl)-1,5-dimethyl-6-thioxoverdazyl (*p*-CDTV) and 3-(4-bromophenyl)-1,5-dimethyl-6-thioxoverdazyl (*p*-BDTV) crystals. Takeda and his collaborators[33,79] investigated magnetic field dependence of the heat capacity of a 3-(4-chlorophenyl)-1,5-diphenyl-6-oxoverdazyl (*p*-CDpOV) crystal. They observed a sharp peak due to a ferromagnetic phase transition at $T_C = 0.21$ K and a wide plateau around 1−4 K, characteristic of 1D quantum ferromagnets (Figure 11). This sharp peak was easily affected by the small magnetic field, and another round hump appeared, increased in height, and shifted toward the HT region as the magnetic field was increased. They also investigated the magnetic and thermal properties of four 1D antiferromagnets,[72] *p*-NTpV, 3-nitro-1,5-diphenylverdazyl (NDpV), 6-methyl-3-nitro-1,5-diphenylverdazyl (NDpMV), and 6-methyl-3-(4-nitrophenyl)-1,5-diphenylverdazyl (*p*-NDpMV), and a 2D antiferromagnet 1,3,5-triphenyl-6-oxoverdazyl (TOV) crystal.[80,81]

Recently, this research group studied the doping effect of 3-(4-cyanophenyl)-1,5-dimethyl-6-thioxoverdazyl (*p*-CyDTV) on 3-(4-cyanophenyl)-1,5-dimethyl-6-oxoverdazyl (*p*-CyDOV), which shows a spin-Peierls transition at $T_{SP} = 15.0$ K,[82,83] by heat-capacity measurements of $(p\text{-CyDOV})_{1-x}(p\text{-CyDTV})_x$ crystals.[84−86] Figure 12 represents the T vs x phase diagram for the $(p\text{-CyDOV})_{1-x}(\text{p-CyDTV})_x$ systems. Antiferromagnetic phase transitions were observed at $T_N = (0.135 \pm 0.02)$, (0.290 ± 0.02), and (0.164 ± 0.02) K for the crystals with $x = 0$, 0.01, and 0.07, respectively. The coexistence of antiferromagnetic long-range order and the spin-Peierls state was confirmed in the systems with $x = 0$ and 0.01, while in the system with $x = 0.07$ only a single antiferromagnetic phase appeared below $T_N = 0.164$ K.

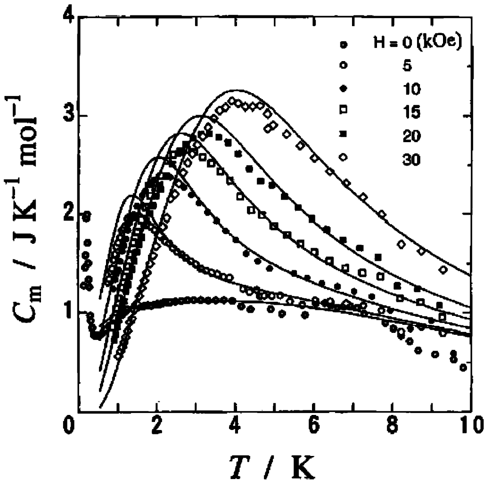

Figure 11. Field dependence of the magnetic heat capacity of *p*-CDpOV crystal. Solid curves are the theoretical results for the $S = 1/2$ 1D ferromagnetic system. Reprinted with permission from ref 33. Copyright 1995 The Physical Society of Japan.

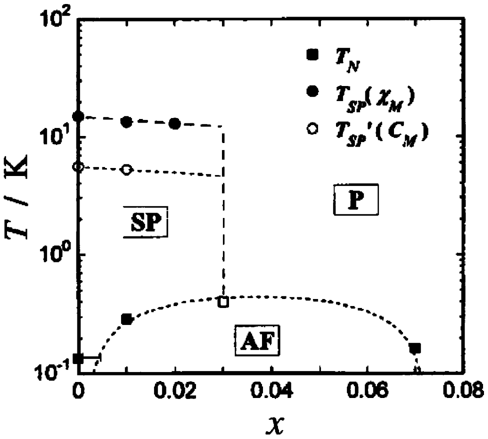

Figure 12. $T-x$ phase diagram of the doped *p*-CyDOV crystals, $(p\text{-CyDOV})_{1-x}(p\text{-CyDTV})_x$, obtained from the magnetic susceptibility (T_{SP}) and heat-capacity (T_{SP} and T_N) measurements. Closed and open circles and closed squares indicate T_{SP}, T_{SP}', and T_N, respectively. SP, AF, and P mean spin-Peierls, antiferromagnetic, and paramagnetic states, respectively. Reprinted with permission from ref 85. Copyright 2003 The Physical Society of Japan.

2.4. Thiazyl Radicals

Thiazyl radicals (Figure 13) are candidates of HT bulk magnets because they are characterized by strong antiferromagnetic exchange interactions between radical centers.[87] Their unique intermolecular interactions have resulted in unusual solid-state properties.[88−92]

The dithiadiazolyl radical *p*-NCC_6F_4CNSSN (Figure 13) has two crystal polymorphs: triclinic α-phase[93] and ortho-

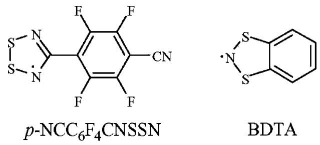

Figure 13. Molecular structures of thiazyl radicals.

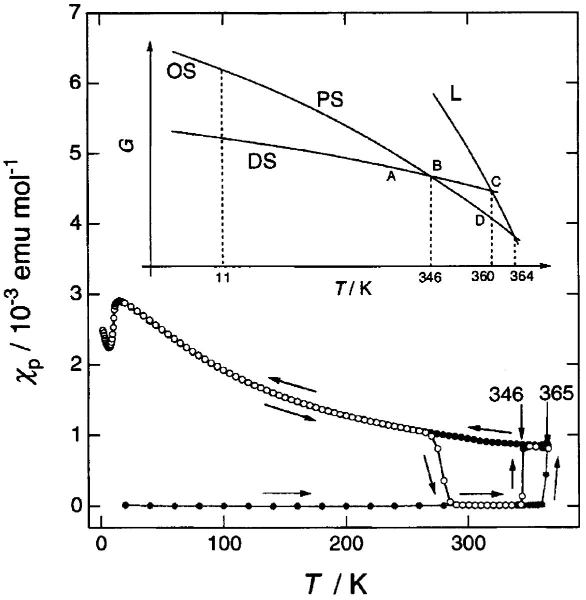

Figure 14. Temperature dependence of the paramagnetic susceptibility χ_p for the virginal sample of BDTA radical crystal upon heating (gray circles) and upon cooling (closed circles). Open circles show the dependence for the sample after the thermal cycles upon heating. The inset shows the expected Gibbs energy phase diagram. Reprinted with permission from ref 96. Copyright 2002 Elsevier Ltd.

rhombic β-phase.[94] The α-phase becomes antiferromagnetic below $T_N = 8$ K.[93] Although the β-phase is also an antiferromagnet, it gives rise to a spontaneous magnetization below $T_N = 36$ K. This implies noncollinear antiferromagnetism.[94] Palacio et al.[95,96] performed heat-capacity measurements of the β-phase and observed a peak due to the noncollinear antiferromagnetic phase transition at $T_N = 35.5$ K, above which a broad shoulder characteristic of low-dimensional magnets was found.

Fujita et al.[96] studied the magnetic and thermal properties of 1,3,2-benzodithiazolyl (BDTA; Figure 13). The temperature dependence of the magnetic susceptibility of BDTA is shown in Figure 14. The as-prepared sample is in a diamagnetic state (DS) in the range from 4.4 to 360 K, at which it is suddenly transformed into a paramagnetic state (PS). On cooling to 4.2 K, the sample remains in PS. However, when the temperature is increased, the PS state is irreversibly transformed to the DS around 270 K. On the basis of this result, together with the result of the calorimetric study, one can get a Gibbs energy phase diagram shown in Figure 14. Namely, DS is the stable phase and PS is a metastable phase below 346 K, above which the stabilities of both phases are reversed. The heat-capacity measurement of the supercooled PS phase indicated an antiferromagnetic phase transition at $T_N = 11$ K.

2.5. Other Radicals

Takagi et al.[97] reported magnetic susceptibility and heat capacity of an organic radical salt, [3,3′-dimethyl-2,2′-thiazolinocyanine]-TCNQ (DMTzNC-TCNQ) (Figure 15). The heat capacity showed a sharp peak due to an antiferromagnetic phase transition at $T_N = 1.49$ K, below which it gave rise to T^n dependence expected for a gapless spin-wave excitation.

Wada et al.[98] studied the magnetic property of an organic radical salt, *m*-*N*-methylpyridinium α-nitronyl nitroxide (*m*-MPYNN)-BF$_4$ (Figure 15), which is known to be an $S = 1$ 2D Kagomé Heisenberg antiferromagnet.[99] The heat-capacity maximum due to a magnetic short-range order was observed at 1.4 K, which was about half of the antiferromagnetic interaction $2|J|/k = 3.1$ K in the Kagomé lattice. However, Uekusa and Oguchi[100] suggested that *m*-MPYNN·BF$_4$ is not the $S = 1$ Kagomé antiferromagnet but a magnetic hexagonal-network system with $2J_1/k = 20.1$ K, $2J_2/k = -3.1$ K, and $2J_3/k = -2.0$ K.

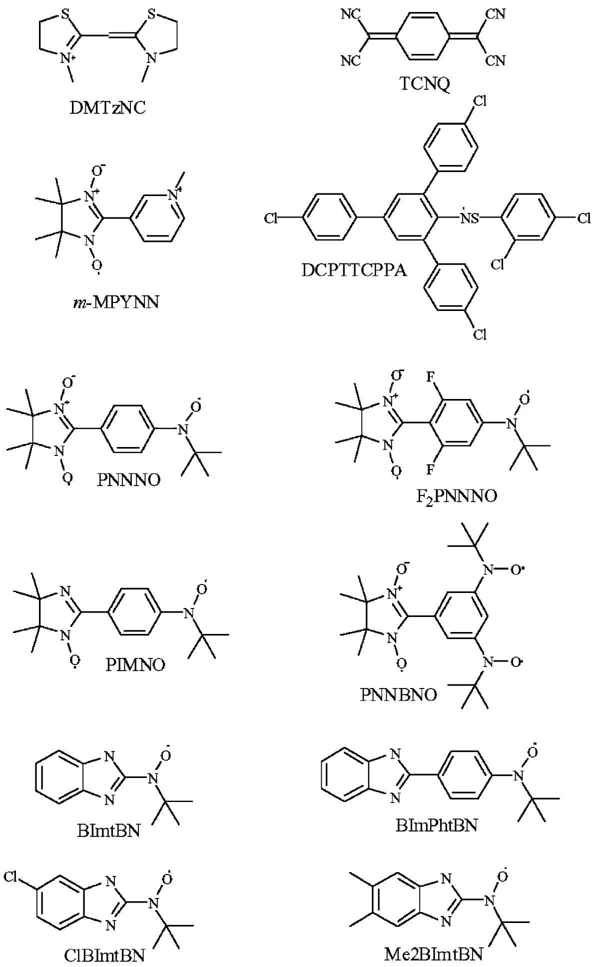

Figure 15. Molecular structures of other radicals.

Teki et al.[101] investigated the magnetic and thermal properties of *N*-[(2,4-dichlorophenyl)thio]-2,4,6-tris(4-chlorophenyl)phenylaminyl (DCPTTCPPA) (Figure 15). The heat capacity indicated a λ-type anomaly due to an antiferromagnetic phase transition at $T_N = 0.40$ K. The interchain exchange interactions were estimated to be $J'/k = 0.02$ K and $J''/k = -0.01$ K.

Hosokoshi et al. synthesized stable biradicals 2-[4′-(*N*-*tert*-butyl-*N*-oxyamino)phenyl]-4,4,5,5-tetramethyl-4,5-dihydro-1*H*-imidazol-1-oxyl3-oxide (PNNNO), 2-[2′,6′-difluoro-4′-(*N*-*tert*-butyl-*N*-oxyamino)phenyl]-4,4,5,5-tetramethyl-4,5-dihydro-1*H*-imidazol-1-oxyl 3-oxide (F$_2$PNNNO), and 2-[4′-(*N*-*tert*-butyl-*N*-oxyamino)phenyl]-4,4,5,5-tetramethyl-4,5-dihydro-1*H*-imidazol-1-oxyl (PIMNO) (Figure 15).[102] From the magnetic measurements of PNNNO and PIMNO, both biradicals were well-understood by 1D antiferromagnetic chain models of ferromagnetic spin pairs with $2J_F/k = 638$ K and $2J_{AF}/k = -14.5$ K for PNNNO and with $2J_F/k = 216$ K and $2J_{AF}/k = -12$ K for PIMNO. The heat capacities of PNNNO and PIMNO showed λ-shaped peaks due to anti-

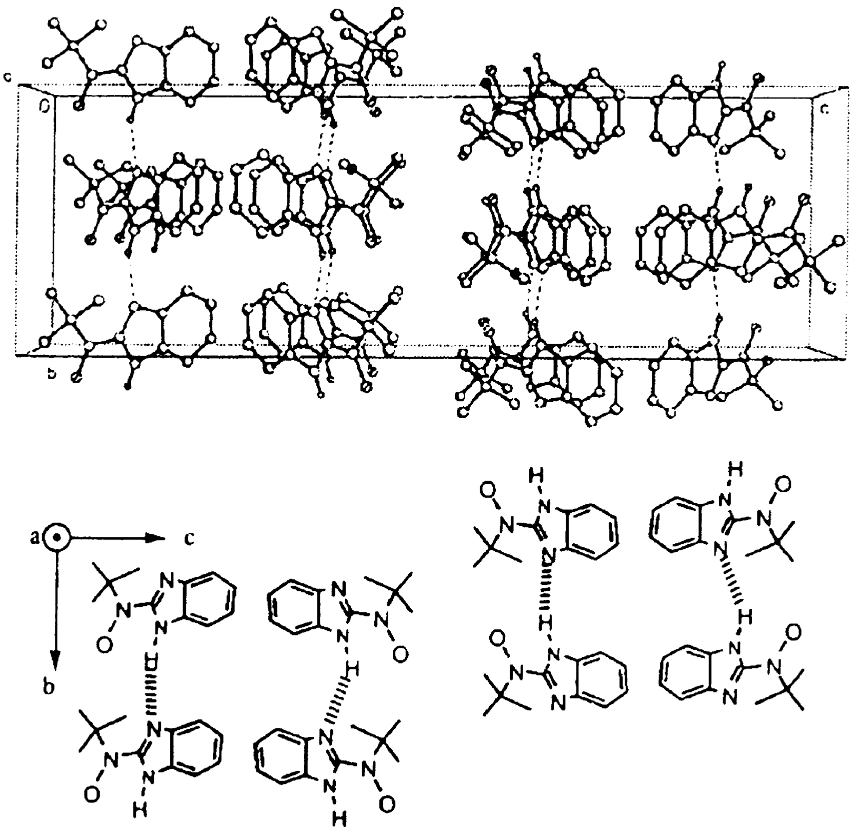

Figure 16. Schematic drawing of the bilayer structure for the BImtBN crystal. Reprinted with permission from ref 104. Copyright 1999 American Chemical Society.

ferromagnetic phase transitions at $T_N = 1.1$ and 2.5 K, respectively. On the other hand, F_2PNNNO was thought to be a 2D Heisenberg system, in which the spin pairs were connected by two types of antiferromagnetic interactions with $2J'_{AF}/k = -67$ K and $2J_{AF}/k = -7.4$ K and a ferromagnetic interaction with $2J_F/k = 407$ K. They also designed a novel triradical, 2-[3′,5′-bis(*N*-*tert*-butylaminoxyl)phenyl]-4,4,5,5-tetramethyl-4,5-dihydro-1*H*-imidazol-1-oxyl 3-oxide (PNNBNO) (Figure 15) to obtain an organic ferrimagnet.[103] The magnetic susceptibility of PNNBNO was well-reproduced by the calculation with $2J_F/k = 860$ K, $2J_{AF}/k = -216$ K, and $2J'_{AF}/k = -0.6$ K. In the heat capacity of PNNBNO, a λ-shaped peak due to a ferromagnetic phase transition was observed at $T_C = 0.28$ K. The total magnetic entropy gain reached 91% of R ln 2 at 3.3 K, which suggested that the effective $S = 1/2$ species underwent a magnetic phase transition at $T_C = 0.28$ K.

One of the promising strategies for controlling packing of organic free radicals in the solid state is to use hydrogen bonding. Recently, Lahti et al.[104,105] synthesized new organic radicals hydrogen-bonded benzimidazole-based *tert*-butylnitroxides, benzimidazole-2-*tert*-butylnitroxide (BImtBN), 4-(1*H*-benzimidazol-2-yl-phenyl)-*tert*-butylnitroxide (BImPhtBN), 5(6)-chloro-BImtBN (ClBImtBN), and 5,6-dimethyl-BImtBN (Me2BImtBN) (Figure 15). The single-crystal X-ray crystallography[104] of BImtBN showed that bilayers made up of two sheets parallel to the *ab* plane are formed (see Figure 16),[104] whereas the magnetic susceptibility[104] measurement revealed that its magnetism can be well-expressed by the $S = 1/2$ square planar 2D antiferromagnetic Heisenberg model with the intralayer exchange interaction of $J/k = -1.6$ K. The magnetic structure of BImPhtBN resembled that of BImtBN, while ClBImtBN and Me2BImtBN obeyed the singlet−triplet models with the intradimer exchange interactions $J/k = -22$ and -24 K, respectively.

Miyazaki et al.[106] performed heat-capacity measurements of BImtBN. An antiferromagnetic phase transition was observed at $T_N = 1.7$ K. As compared in Figure 17, the heat-capacity hump observed above T_N was well-reproduced by the $S = 1/2$ antiferromagnetic bilayer Heisenberg model with the intralayer interaction $J_1/k = -1.2$ K and the interlayer interaction $J_2/k = -1.9$ K.

3. One-Dimensional Magnets

Because superexchange interactions are principally confined within nearest neighbors, the lattice dimensionality of molecule-based magnets is basically influenced by the anisotropy of the constituent molecule carrying spins and by the relative arrangement of the molecules. This situation leads to low-dimensional magnets in which 1D or 2D interactions are dominant.

3.1. Metallocenium Salts of Radical Anions

As a strategy to realize molecule-based bulk ferromagnets, Miller et al.[107,108] proposed charge-transfer complexes, for example, decamethylferrocenium tetracyanoethenide [DMFc][TCNE]. As shown in Figure 18,[109] the solid-state structure of [DMFc][TCNE] consists of parallel stacks of alternating $[DMFc]^+$ and $[TCNE]^-$ radical ions, although disorder in the anion positions[108] has prevented refinement of the orthorhombic structure. The crystal structure includes neighboring stacks that are in and out of registry. Magnetic ordering in this complex was intensively studied by magnetization and magnetic susceptibility measurements, ^{57}Fe

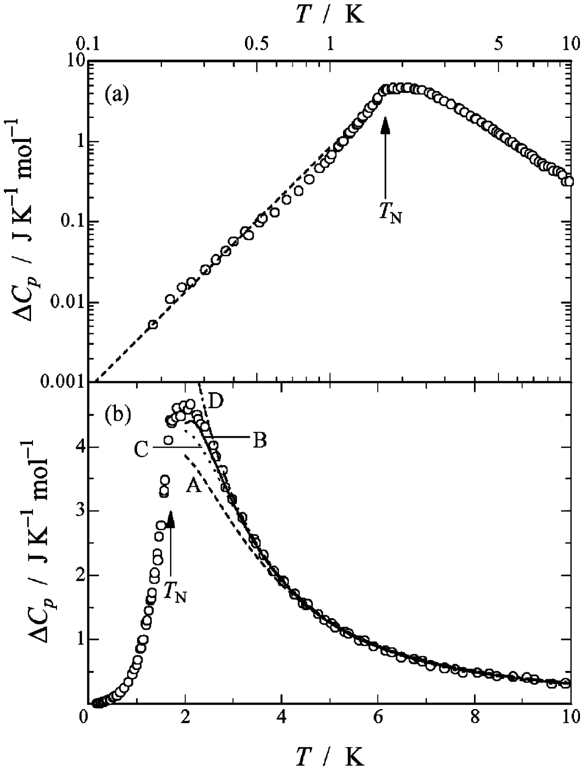

Figure 17. Magnetic heat capacity of BImtBN crystal on (a) logarithmic and (b) normal scales. The broken curve drawn in plot a shows the heat capacity obtained from the spin-wave theory for 3D antiferromagnets. In plot b, curves A and B indicate the heat capacities calculated on the basis of the HT series expansion for the $S = 1/2$ square planar 2D Heisenberg model with $J/k = -1.6$ K and for the bilayer model with the intralayer interaction $J_1/k = -1.2$ K and the interlayer interaction $J_2/k = -1.9$ K, respectively. Curve C shows the heat capacity calculated by the dimer model with $J_d/k = -2.8$ K. Curve D represents the heat capacity calculated by the bilayer model with $J_1/k = -1.4$ K and $J_2/k = -1.3$ K derived from the magnetic data. Reprinted with permission from ref 106. Copyright 2002 American Chemical Society.

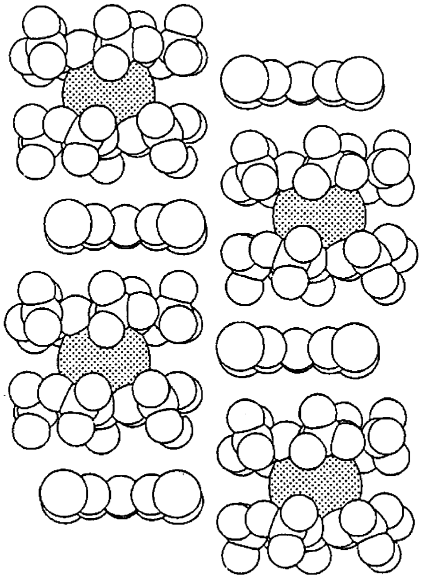

Figure 18. Example of one type of stacking arrangement of donor and acceptor molecules for out of registry chains of the compound [DMFc][TCNE].

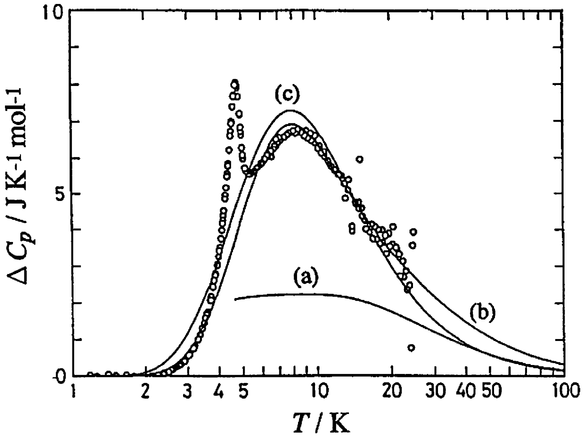

Figure 19. Magnetic heat capacity of [DMFc][TCNE]. (a) 1D $S = 1/2$ ferromagnetic Heisenberg model ($J_{\perp}/k = J_{\parallel}/k = 13$ K), (b) 1D anisotropic Heisenberg model ($J_{\parallel}/k = 25$ K; $J_{\perp}/J_{\parallel} = 0.5$), and (c) Ising model ($J_{\parallel}/k = 19$ K; $J_{\perp}/k = 0$ K). Reprinted with permission from ref 111. Copyright 1990 Elsevier Ltd.

Mössbauer spectroscopy, and neutron diffraction. Below 4.8 K, the charge-transfer complex displays the onset of spontaneous magnetization in zero-applied magnetic field, consistent with a 3D ferromagnetic ground state. However, ^{57}Fe Mössbauer spectroscopy exhibited zero-field Zeeman split spectra even up to 20 K. This was a great mystery, and at that time, there had been reported no conclusion about the question, whether the Mössbauer line-width broadening is due to single ion relaxation or to a cooperative effect involving solitons in a 1D magnet.

Heat capacities of [DMFc][TCNE] were reported by Chakraborty et al.[110] and by Nakano and Sorai.[111] Figure 19 represents the magnetic heat capacity of [DMFc][TCNE].[111] The phase transition expected for the ferromagnetic ordering was actually observed at 4.74 K. Another feature is a remarkable hump centered around 8.5 K. This hump corresponds to the strong short-range order characteristic of the 1D stacking structure in this crystal. The temperature region of this hump coincides with the anomalous region of the ^{57}Fe Mössbauer spectra. The total entropy gain due to the phase transition at 4.74 K and the noncooperative anomaly around 8.5 K amounted to $\Delta S = (12 \pm 1)$ J K^{-1} mol^{-1} and is well-approximated by $2R \ln 2 = 11.53$ J K^{-1} mol^{-1}. This fact confirms that the charge transfer from the donor to the acceptor is complete and that the present complex consists of a spin 1/2 cation and a spin 1/2 anion.

As can be seen in Figure 19, the hump cannot be reproduced by a usual 1D $S = 1/2$ isotropic Heisenberg model (curve a: $J_{\perp}/k = J_{\parallel}/k = 13$ K). This anomaly is favorably accounted for in terms of anisotropic Ising character (curve c: $J_{\parallel}/k = 19$ K; $J_{\perp}/k = 0$ K). The fit was obtained for an anisotropic Heisenberg model (curve b: $J_{\parallel}/k = 25$ K; $J_{\perp}/J_{\parallel} = 0.5$). The origin of this Ising anisotropy can be attributed to the anisotropic g-tensor of the [DMFc]$^{+}$ cation radical. For the superexchange interaction between two magnetic ions A and B, the anisotropy of magnetic interaction is known to be proportional to the product of the g-values, $J_{\perp}/J_{\parallel} \approx (g_{\perp}^{A}g_{\perp}^{B})/(g_{\parallel}^{A}g_{\parallel}^{A})$. The present cation [DMFc]$^{+}$ has anisotropic g-values ($g_{\parallel} = 4.0$ and $g_{\perp} = 1.3$), whereas the anion [TCNE]$^{-}$ is isotropic ($g_{\perp} = g_{\parallel} = 2.0$). Consequently, the magnitude of the interaction anisotropy is expected to be $J_{\perp}/J_{\parallel} = 0.33$. This value agrees well with $J_{\perp}/J_{\parallel} = 0.30$ derived from the magnetic susceptibility for single crystals.[112] The calorimetric result suggesting a very strong Ising character of the magnetic interaction, $J_{\perp}/J_{\parallel} < 0.5$, supports the conclusion obtained from the single-crystal susceptibility.

Close examination of the magnetic elementary excitations in the ordered phase provides more evidence for the strong Ising character. The excess heat capacity obviously exhibits the exponential temperature dependence characteristic of excitation over an energy gap rather than the power-law dependence of spin-wave excitation. The energy gap was estimated to be $\Delta E/k = 28$ K from the data in the range of 1−3 K. The dominant thermal excitation in [DMFc][TCNE] is inferred to be the bound-state type inherent in the Ising magnet.

Decamethylferrocenium 7,7,8,8-tetracyano-*p*-quinodimethanikde [DMFc][TCNQ] is isomorphous with [DMFc]-[TCNE]. Miller et al.[113] have reported the metamagnetic behavior of [DMFc][TCNQ], in which a dominant interaction is intracolumnar ferromagnetism with a weak intercolumnar antiferromagetism. Heat-capacity measurements of [DMFc]-[TCNQ][114] exhibited an antiferromagnetic phase transition at $T_N = 2.54$ K with the entropy gain of $\Delta S = 11.2$ J K^{-1} mol^{-1}. The magnetic lattice anisotropy of the [TCNQ] complex was smaller than that of the [TCNE] complex, as exemplified by a smaller energy gap of $\Delta E/k = 6.5$ K.

3.2. Bimetallic Chain Complexes

Kahn and his collaborators[115] proposed a strategy to design molecule-based compounds exhibiting a spontaneous magnetization by assembling ordered bimetallic chains within the crystal lattice in a ferromagnetic fashion. The novel ferromagnet that they prepared was $Mn^{II}Cu^{II}(obbz)\cdot H_2O$ [obbz = *N*,*N*′-oxamidobis(benzoato)] with a high Curié temperature, which is obtained by partial dehydration of the molecule-based antiferromagnet $Mn^{II}Cu^{II}(obbz)\cdot 5H_2O$. On the basis of powder X-ray diffraction (XRD) patterns and XANES and EXAFS spectra at both Mn and Cu edges for $MnCu(obbz)\cdot 5H_2O$ and $MnCu(obbz)\cdot H_2O$, it has been shown that these complexes have very similar structures and that Mn^{2+} and Cu^{2+} ions are in octahedral and elongated tetragonal surroundings, respectively. These structural results imply that Mn^{2+} and Cu^{2+} ions are bridged alternately by oxamido and carboxylato groups to form 1D chain structures, which are two- or three-dimensionally connected through Mn^{2+}−O(oxamido) bonds. In $MnCu(obbz)\cdot 5H_2O$, only one water molecule is coordinated to the Mn^{2+} ion and the remaining four water molecules are noncoordinated, consistent with the easy dehydration. Magnetic measurements[115] indicate that $MnCu(obbz)\cdot H_2O$ exhibits a 3D ferromagnetic order below $T_c = 14$ K while $MnCu(obbz)\cdot 5H_2O$ shows a 3D antiferromagnetic order below $T_c = 2.3$ K.

Heat capacities of $MnCu(obbz)\cdot 5H_2O$ and $MnCu(obbz)\cdot H_2O$ were measured by Sorai and his collaborators[116] at temperatures from 0.1 to 300 K by means of adiabatic calorimetry. Figure 20 shows the excess heat capacities ΔC_p below 20 K.[116a] A phase transition peak due to 3D antiferromagnetic ordering was observed at $T_N = 2.18$ K. A heat-capacity hump centered around 4 K is due to the short-range order effect characteristic of a low-dimensional magnet. The entropy arising from these two anomalies was 12.1 J K^{-1} mol^{-1}.

$MnCu(obbz)\cdot 5H_2O$ has a 2D or 3D network structure formed by assembly of 1D chains, in which Mn^{2+} and Cu^{2+} ions are alternately bridged by two different kinds of groups: oxamido and carboxylato. The magnetic susceptibility measurement[115] indicated that this complex can be regarded as a 1D ferrimagnet composed of two different spins $S = 5/2$ of Mn^{2+} and $S = 1/2$ of Cu^{2+} above T_N. The magnetic structure of this 1D ferrimagnetic chain is schematically drawn in Figure 21. The exchange interaction parameters for the oxamido and carboxylato bridges between Mn^{2+} and Cu^{2+} have been determined to be $J_1/k = -21$ K and $J_2 = -3.6$ K, respectively. This strong alternation shows that the 1D ferrimagnetic chain can be regarded as a 1D pseudo-ferromagnetic chain made up of $S = 2$ resultant spins arising from pairing between the spins of Mn^{2+} and Cu^{2+}. This approximation is reasonable from the fact that the exchange interaction for the oxamido bridge is much stronger than that for the carboxylato bridge.

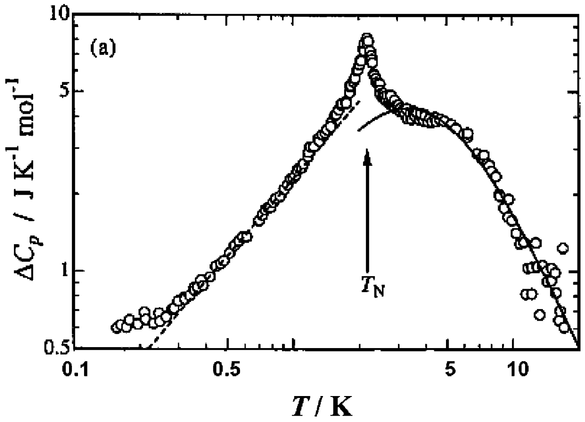

Figure 20. Excess heat capacities of $MnCu(obbz)\cdot 5H_2O$ around the antiferromagnetic phase transition temperature T_N. The solid line indicates the theoretical heat-capacity curve estimated by the HT series expansion for $S = 2$ 1D ferromagnetic Heisenberg model with $J/k = 0.75$ K. The broken straight line shows the heat capacity due to the spin-wave excitation. Reprinted with permission from ref 116a. Copyright 1999 The Chemical Society of Japan.

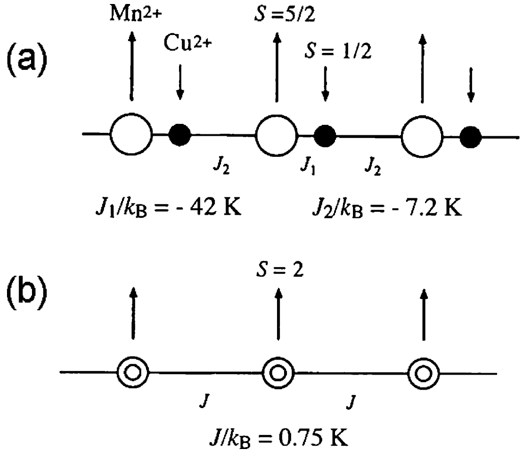

Figure 21. (a) Schematic magnetic structure of the 1D ferrimagnetic chain in $MnCu(obbz)\cdot 5H_2O$. Open and filled circles stand for Mn^{2+} and Cu^{2+} ions, respectively. Long and short arrows indicate spins 5/2 and 1/2, respectively. Antiferromagnetic interaction J_1 is much stronger than J_2. (b) One-dimensional ferromagnetic chain consisting of the resultant $S = 2$ spins expected for the antiferromagnetically strongly coupled Mn^{2+} and Cu^{2+} spin pair. Double circle stands for the Mn^{2+}−Cu^{2+} pair.[116a]

The total entropy gain theoretically expected for the spin multiplicity of Mn^{2+} and Cu^{2+} amounts to $R \ln(6 \times 2)$ (= 20.7 J K^{-1} mol^{-1}). However, because this ferrimagnetic chain can be regarded as an $S = 2$ pseudo-ferromagnetic chain for the reason described above, only $R \ln 5$ (= 13.4 J K^{-1} mol^{-1}) contributes to the entropy at low temperatures. Because the experimental entropy gain 12.1 J K^{-1} mol^{-1} agrees rather well with this value, one may conclude that the pseudo-ferromagnetic chain model is a good approximation. The remaining entropy of $R \ln(12/5)$ ($= 7.3$ J K^{-1} mol^{-1}) would be acquired at higher temperatures by thermal excitation to the $S = 3$ excited spin level. As seen in Figure 20, the validity of the present pseudo-ferromagnetic chain approximation is given by the fact that the heat-capacity tail above T_N is well-reproduced by this model with $J/k = 0.75$ K. The effective value for the exchange parameter J between the adjacent resultant spins with $S = 2$ is derived as $J/k = 0.70$ K from the experimental values ($J_1/k = -21$ K and $J_2 = -3.6$ K) on the basis of the spin-vector projection method.[117]

In the case of MnCu(obbz)$\cdot$H$_2$O, a broad phase transition due to 3D ferromagnetic ordering was observed around 17 K.[116b] Above the transition temperature, a heat-capacity tail arising from the short-range order characteristic of a low-dimensional magnet was found. As in the case of MnCu(obbz)$\cdot$5H$_2$O, the entropy gained by the phase transition (12.7 J K^{-1} mol^{-1}) was close to $R \ln 5$ ($= 13.4$ J K^{-1} mol^{-1}) expected for the resultant spin model with the $S = 2$ ground state.

Magnetization measurements[116b] for MnCu(obbz)$\cdot$H$_2$O revealed a bend of the hysteresis loop above the transition temperature and a magnetic relaxation below the transition temperature. These results lead to the conclusion that the broadness of the phase transition may be attributed to superparamagnetism caused by the fact that the present complex is prepared only in a fine powder.

Coronado et al.[118] reported magnetic and thermal properties of bimetallic chain complexes Mn^{II}M^{II}(EDTA)$\cdot$6H$_2$O (M = Co, Ni, Cu; EDTA = hexadentate ligand ethylenediamine-*N*,*N*,*N*′,*N*′-tetraacetate) in the 1.4−30 K temperature region. Their structure consists of infinite zigzag chains, built up from two alternating [Mn,M] sites. The degree of *J*-alternation of these compounds varies in the order [Mn,Ni] < [Mn,Cu] ≪ [Mn,Co]. A qualitative explanation of this trend is given on the basis of the structural features and the electronic ground state of the interacting ions. The magnetic behavior exhibits the characteristic features of 1D ferrimagnets, but interchain interactions lead at very low temperature to a long-range antiferromagnetic ordering as outlined by the λ-type heat-capacity peak.

Drillon and his collaborators[119] reported a theoretical model for ferrimagnetic Heisenberg bimetallic chains $[1/2 - S]$ ($S = 1$ to $5/2$) and provided heat-capacity curves as a function of temperature. It was shown that the main features for the infinite chain are conveniently given by extrapolating the results obtained for spin rings consisting of several pairs of spins. Because the model chains have been characterized by uniform interaction parameter J, application of this model to the systems with strongly alternating interaction should be careful.

Evangelisti et al. reported heat capacities of bimetallic compounds containing 4f-3d electrons. They involve (i) Gd$_2$(ox)[Cu(pba)]$_3$[Cu(H$_2$O)$_5$]$\cdot$20H$_2$O and Gd$_2$[Cu(opba)]$_3$$\cdot$6DMSO$\cdot$4H$_2$O [opba = *o*-phenylenebis(oxamato)],[120] (ii) Ln$_2$[Cu(opba)]$_3$$\cdot$S (S = solvated molecules; Ln = Tb, Dy, Ho);[121a] and (iii) L$_2$[M(opba)]$_3$$\cdot$$x$DMSO$\cdot$$yH_2$O (L = La, Gd, Tb, Dy, Ho; M = Cu, Zn; DMSO = dimethyl sulfoxide; hereafter abbreviated by L$_2$M$_3$).[121b] As to (i), both compounds undergo 3D ferromagnetic ordering with $T_C = 1.05$ K and $T_C = 1.78$ K, respectively. For the compounds of (ii), three compounds undergo 3D magnetic ordering, with $T_c = 0.81$ K and $T_c = 0.74$ K for the Tb- and Dy-containing compounds, respectively. For the Ho-containing compound, only the HT tail of the λ-type anomaly was detected by the heat-capacity measurement. These results are compared with the magnetic properties of the isostructural compound Gd$_2$[Cu(opba)]$_3$$\cdot$S, which is a ferromagnet. The results for L$_2$[M(opba)]$_3$$\cdot$$x$DMSO$\cdot$$yH_2$O showed that the Cu-containing complexes (with the exception of La$_2$Cu$_3$) undergo long-range magnetic order at temperatures below 2 K and that the magnetic ordering is ferromagnetic for Gd$_2$Cu$_3$, whereas for Tb$_2$Cu$_3$ and Dy$_2$Cu$_3$, it is probably antiferromagnetic.

The authors[120,121] have claimed that these compounds belong to the spin-ladder system owing to their ladder-shaped molecular packing in the crystal lattice. However, their heat capacities do not show the quantum effects at low temperatures characteristic of the spin-ladder system, which is one of the spin-gapped systems. Therefore, as far as the magnetic heat capacities are concerned, these complexes are a family of low-dimensional magnets showing long-range order.

3.3. Helical Chain with Competing Interactions

One-dimensional localized magnets have served as suitable systems by which theoretical predictions are tested. Harada[122] proposed that the competition between nearest-neighbor (nn) and next-nearest-neighbor (nnn) exchange can give rise to a helical phase, whose 2-fold chiral degeneracy (clockwise and counterclockwise turns of spins along a chain) leads to the excitation of topologically stable chiral domain walls, separating two domains of opposite chirality.

Quasi-1D molecular magnets Gd^{III}(hfac)$_3$NITR (hfac = hexafluoro-acetylacetonate, NITR = 2-R-4,4,5,5-tetramethyl-4,5-dihydro-1H-imidazolyl-1-oxyl 3-oxide and R = alkyl or phenyl groups)[123] were regarded as good candidates to test Harada's prediction. Their magnetic properties are determined by Gd^{3+} rare-earth ions with spin $S = 7/2$ and the NITR organic radicals with spin $s = 1/2$, alternating along the chain and interacting via competing nn and nnn exchange. It should be noted here that a capital S and a lower case s are used for the spin quantum number to discriminate the two kinds of spins in a chain. The chains are well-separated one from the other by the presence of the bulky ligands, and only weak dipolar interactions are supposed between chains. The spin Hamiltonian describing the exchange interaction in a single chain is written as follows:

$$H = -J_1 \sum_{n=1}^{N/2} (S_{2n-1} \cdot s_{2n} + s_{2n} \cdot S_{2n+1}) - J_2 \sum_{n=1}^{N/2} S_{2n-1} \cdot S_{2n+1} - J_2{}' \sum_{n=1}^{N/2} s_{2n} \cdot s_{2n+2} \quad (1)$$

where the index n refers to the spin position along the chain, N is the number of spins along the chain, $J_1 > 0$ is the ferromagnetic nn exchange consant, and $J_2 < 0$ and $J_2{}' < 0$ are the antiferromagnetic nnn exchange constants. Under an appropriate condition, the ground state of this isolated chain is characterized by 2-fold degeneracy: clockwise turn of the spins and counterclockwise turn shown in Figure 22a,b, respectively.[123]

Gatteschi and his collaborators studied thermal properties of Gd(hfac)$_3$NITR, where R = isopropyl (= i-Pr), ethyl (= Et), methyl (= Me), and phenyl (= Ph), at low temperature.[123−126] As a result, it was found that the thermal behavior is classified into two groups: One is that shown by the compounds with R = Me and Ph, and the other is

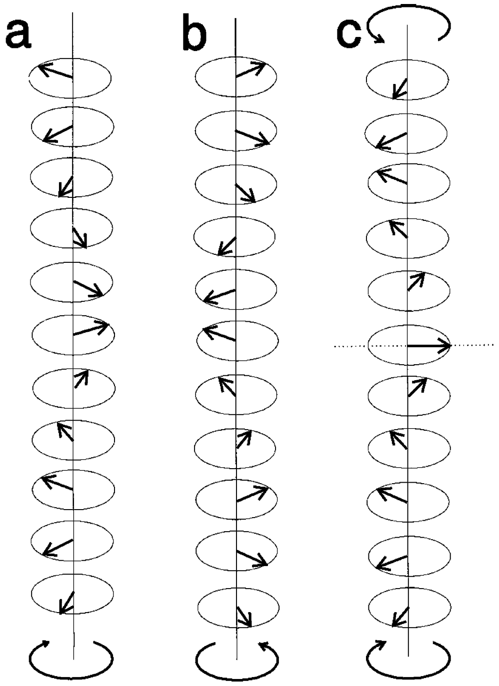

Figure 22. Helical configurations of a spin chain with easy-plane anisotropy. (a) Helical ground state with clockwise turn of the spins (+chirality); (b) helical ground state with counterclockwise turn of the spin (−chirality); and (c) dotted line, domain wall separating two regions with opposite chirality. The simplest case of $S = s$ and of a localized domain wall was represented in the figures. Reprinted Figure 1 with permission from Affronte, M.; Caneschi, A.; Cucci, C.; Gatteschi, D.; Lasjaunias, J. C.; Paulsen, C.; Pini, M. G.; Rettori, A.; Sessoli, R. *Phys. Rev. B 59*, 6282, 1999 (http://link.aps.org/abstract/PRB/v59/p6282). Copyright 1999 by the American Physical Society.

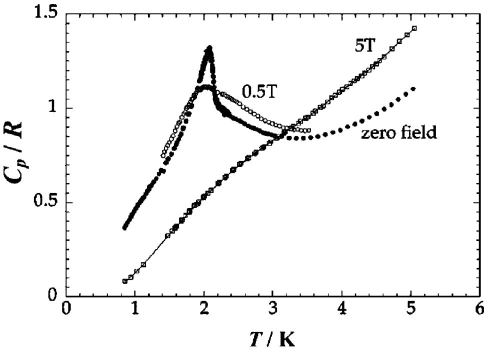

Figure 23. Molar heat capacities (normalized to the gas constant R) against temperature of Gd(hfac)$_3$NITiPr, measured in zero field (solid circles), in a field of 0.5 T (open circles) and 5 T (open squares). The solid line is a guide for the eye. Reprinted Figure 1 with permission from Lascialfari, A.; Ullu, R.; Affronte, M.; Cinti, F.; Caneschi, A.; Gatteschi, D.; Rovai, D.; Pini, M. G.; Rettori, A. *Phys. Rev. B 67*, 224408, 2003 (http://link.aps.org/abstract/PRB/v67/p224408). Copyright 2003 by the American Physical Society.

that given by the compounds with $R = i$-Pr and Et. In the case of Gd(hfac)$_3$NITMe and Gd(hfac)$_3$NITPh, they exhibited a neat λ-type heat-capacity peak at $T_c = 0.68$ and 0.6 K, respectively.[125] The total entropy gain due to the phase transition was 22.9 and 22.0 J K^{-1} mol^{-1}, respectively. Because these values are close to the expected spin entropy due to Gd^{3+} and the radical spin, $\Delta S = R \ln(8 \times 2) = 23.0$ J K^{-1} mol^{-1}, the phase transitions observed in these compounds arise from the magnetic origin. On the LT side of the peak, both compounds showed a tendency to a $T^{3/2}$ temperature dependence, suggesting a 3D ferromagnetic spin-wave contribution. Therefore, the λ-type peak corresponds to the onset of 3D long-range order and a dimensional crossover takes place from 1D at high temperature to 3D at low temperature.

In contrast, Gd(hfac)$_3$NITEt and Gd(hfac)$_3$NIT*i*-Pr are strongly frustrated compounds. Although these two compounds gave rise to very small heat-capacity peaks at $T_{peak} \approx 2$ K, the experimental heat-capacity curves are drastically different from the previous cases. In the case of Gd(hfac)$_3$NITEt, because the total entropy was $\Delta S = 22.7$ J K^{-1} mol^{-1}, all of the magnetic contributions have been observed. The initial slope of the heat capacity near 0 K was almost linear with respect to T, suggesting a 1D antiferromagnetic state even below the peak temperature. On the basis of these results, Bartolomé et al.[125] assumed that the peaks observed for Gd(hfac)$_3$NITEt and Gd(hfac)$_3$NIT*i*-Pr are not due to 3D ordering but to a different mechanism, and they hypothesized that the peaks at $T_{peak} \approx 2$ K could be due to the excitation of topologically stable chiral domain walls, separating two domains of opposite chirality, first predicted by Harada.[122] To confirm this interpretation, Bartolomé et al. performed numerical transfer matrix calculations of the magnetic heat capacity for the classical planar model and obtained a justification in a qualitative way. For the compounds with lower frustration (R = Me, Ph), this model provided a broad heat-capacity peak with no indication for the excitation of chiral domain walls. For the compounds with a higher degree of frustration (R = Et, *i*-Pr), a peak showing the signature of the excitation of chiral domain walls appeared.

Affronte et al.[123] further studied the LT heat capacity $C(T)$ of Gd(hfac)$_3$NIT*i*-Pr. The anomaly observed in $C(T)$ was reproducibly found at $T_0 = 2.09$ K, although the $C(T)$ curves measured on different samples showed clear evidence for aging effects. An interpretation, capable of explaining the $C(T)$ data both in the LT and in the critical region, calls for the onset, below T_0, of nonconventional chiral long-range order due to interchain interactions. The chiral phase can be described as a collection of parallel corkscrews, all turning clockwise (or all counterclockwise), whereas their phases are random. An estimation of T_0 according to this model and using the exchange constants evaluated from the linear C-vs-T slope supports this interpretation. The chiral order is compatible with the breaking of the chain into finite segments, due to aging effects, while the phase coherence necessary for the onset of 3D helical long-range order is destroyed.

Lascialfari et al.[126] measured the heat capacity of Gd(hfac)$_3$NIT*i*-Pr under magnetic field and zero-field muon spin resonance (μ^+SR). The heat capacity measured in zero magnetic field exhibited a λ-type peak at $T_0 = (2.08 \pm 0.01)$ K that disappeared upon the application of a 5 T magnetic field (Figure 23). Conversely, the μ^+SR data do not present any anomaly at $T \approx 2$ K, proving the lack of divergence of the two-spin correlation function as required for usual 3D long-range helical order. Moreover, no muon spin precession can be evinced from the μ^+SR asymmetry curves, thus excluding the presence of a long-range-ordered magnetic lattice. These results provide indications for a LT phase where chiral order is established in the absence of long-range helical order.

3.4. Lithium Phthalocyanine

The 1D molecular semiconductor lithium phthalocyanine (LiPc) has a half-filled conduction band and is expected to be an organic metal.[127] However, because of the strong Coulomb repulsion, the system is a 1D Mott−Hubbard insulator with a Hubbard gap of 72 kJ mol^{-1} as inferred from optical measurements. LiPc has one unpaired electron on the inner ring of the macrocycle. These electrons are localized along the molecular stack and behave like an $S = 1/2$ antiferromagnetic spin chain.

The heat capacity of LiPc has been measured by Dumm et al.[127,128] in the temperature range of $1.5 \leq T \leq 300$ K. The magnetic heat capacity shows a broad maximum at $T_{max} \approx 18$ K. This anomaly originates in the short-range order effect in the spin chains and is well-described by a model of an $S = 1/2$ antiferromagnetic Heisenberg chain. The intrachain exchange constant is given by $J/k \approx 40$ K.

3.5. Quasi-1D Inorganic Complex

To understand the intrinsic properties of quantum criticality, it is important to explore its phenomenology in simple and well-controlled model systems. One of the simplest quantum critical many-body systems is a linear chain of antiferromagnetically coupled spin 1/2 objects. Quantum criticality in this system is particularly interesting because it is possible to continuously tune the critical exponents by the application of a magnetic field. Hammar et al.[129] explored the magnetic properties of a copper complex $[Cu^{II}(NO_3)_2(pyr)]$ (pyz = pyrazine; $C_4H_4N_2$) on the basis of high-field magnetization, field-dependent heat-capacity measurements, and zero-field inelastic magnetic neutron scattering.

Heat capacities of $[Cu^{II}(NO_3)_2(pyr)]$ were measured by use of a relaxation method in the range of 0.1−10 K up to an applied magnetic field of 9 T.[129] Figure 24 shows the temperature dependence of the total heat capacity of $[Cu(NO_3)_2(pyr)]$ for a number of magnetic fields H parallel to b-axis. As H is increased, the broad feature observed in zero-field is suppressed, and the maximum gradually shifts to lower T. The solid curves are the results of a fit to a model based on exact diagonalization of short chains. The dashed line is the estimated phonon contribution determined from the fit. Because the results are in excellent agreement with numerical calculations based on the Bethe ansatz with no adjustable parameters, this material is an ideal 1D $S = 1/2$ Heisenberg antiferromagnet with nearest-neighbor exchange constant of $J/k = 5.2$ K (in the $-2JS_i \cdot S_j$ scheme). This makes the material an excellent model system for exploring the $T = 0$ critical line that is expected in the $H-T$ phase diagram of the 1D $S = 1/2$ Heisenberg antiferromagnet.

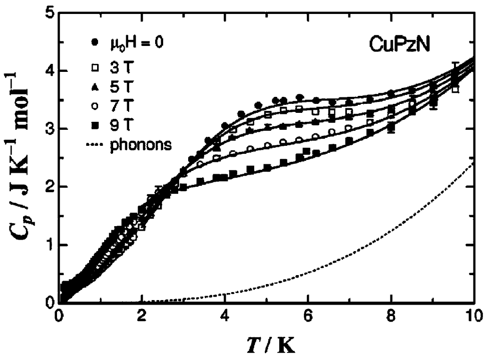

Figure 24. Molar heat capacity of $[Cu^{II}(NO_3)_2(pyr)]$ vs temperature at constant magnetic field parallel to b. Solid curves are a fit to an exact diagonalization model. The dashed line is the phonon contribution determined from the fit. Reprinted Figure 4 with permission from Hammar, P. R.; Stone, M. B.; Reich, D. H.; Broholm, C.; Gibson, P. J.; Turnbull, M. M.; Landee, C. P.; Oshikawa, M. *Phys. Rev. B 59*, 1008, 1999 (http://link.aps.org/abstract/PRB/v59/p1008). Copyright 1999 by the American Physical Society.

3.6. Mixed-Valence MMX Type Complexes

Halogen-bridged mixed-valence binuclear metal complexes, the so-called MMX chain compounds, have drawn attention as quasi-1D electronic systems characterized by strong electron−phonon, electron−electron, and magnetic interactions. There are following four extreme valence-ordering states:

(a) averaged valence (AV) state:

$$\cdots -X^{-}-M^{2.5+}-M^{2.5+}-X^{-}-M^{2.5+}-M^{2.5+}- \cdots$$

(b) charge density wave (CDW) state:

$$\cdots -X^{-}-M^{2+}-M^{2+}-X^{-}-M^{3+}-M^{3+}- \cdots$$

(c) charge polarization (CP) state:

$$\cdots -X^{-}-M^{2+}-M^{3+}-X^{-}-M^{2+}-M^{3+}- \cdots$$

(d) alternate charge polarization (ACP) state:

$$\cdots -X^{-}-M^{2+}-M^{3+}-X^{-}-M^{3+}-M^{2+}- \cdots$$

Mode (a) is an AV state and has the possibility of either a Mott−Hubbard insulator ($U > W \approx 4t$) or a 1D metal ($U < W$), where U, W, and t are the on-site Coulomb repulsion, bandwidth, and transfer integral, respectively. Mode (b) is a CDW insulating state, where doubling of the unit cell occurs. Modes (c) and (d) are a CP state and an ACP state, respectively. As an unpaired electron exists in the $(-M^{2+}-M^{3+}-)$ unit, modes (c) and (d) are anticipated to be paramagnetic. Because no cell doubling occurs in the case of mode (c), either a Mott−Hubbard insulator or a 1D metal is expected. On the other hand, mode (d) is expected to be an insulator analogous to a spin-Peierls state. Platinum complexes $[Pt^{II}Pt^{III}(RCS_2)_4I]$ are typical examples of this category, where R is n-alkyl-group. Two platinum atoms are bridged by four bidentate RCS_2^{-} ligands, and such binuclear complex units are linearly bridged by iodide ions to one another.

Kitagawa et al.[130−133] reported the first observation of a metallic property in $[Pt_2(dta)_4I]$ (dta: dithioacetato, R = CH_3-). The electrical conductivity and thermoelectric power measurements for a single crystal of $[Pt_2(dta)_4I]$ parallel to the chain axis b revealed that this complex exhibits a metallic temperature dependence above a metal−semiconductor transition temperature $T_{M-S} = 300$ K. This metal−semiconductor transition was also confirmed by magnetic susceptibility measurement for a polycrystalline sample.[132,133] Furthermore, temperature dependence of the electrical conductivity and thermoelectric power measurements showed a first-order phase transition around 360 K. From single-crystal X-ray structure analyses,[134] it was revealed that a first-order phase transition occurs at $T_{trs} = 365$ K from the LT phase with space group $C2/c$ to the HT phase with $A2/m$, in which the cell volume is a half of that of the LT phase. Moreover, the magnetic susceptibility shows a convexity at 80 K, which suggests the existence of a phase transition. From variable-

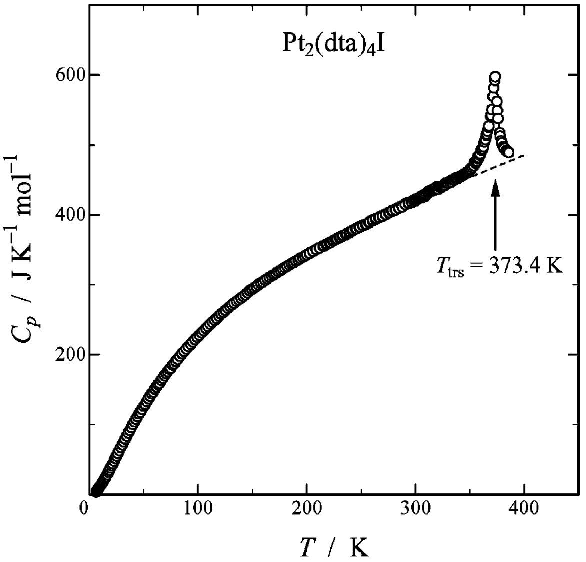

Figure 25. Molar heat capacity of [$Pt_2(dta)_4I$] crystal. The broken curve implies normal heat capacity. Reprinted with permission from ref 135. Copyright 2002 American Chemical Society.

temperature infrared and polarized Raman spectroscopies at room temperature and ^{129}I Mössbauer spectroscopy[132,133] at 16 and 80 K, together with the experimental results mentioned above, it is expected that the [$Pt_2(dta)_4I$] complex is in a 1D metallic phase of the AV state above $T_{M-S} = 300$ K, in a semiconducting phase of the CP state between 90 and 300 K, and in an insulating phase of the ACP state below 80 K.

To elucidate the relationship between various phases, heat-capacity measurements based on adiabatic calorimetry were made by Miyazaki et al.[135] for a powder sample of this complex. Molar heat capacities of [$Pt_2(dta)_4I$] crystal are plotted in Figure 25. As described above, various experiments so far reported have suggested the metal−semiconductor transition at $T_{M-S} = 300$ K, corresponding to a Mott transition from a quasi-1D metallic phase of the AV state to a semiconducting phase of the CP state and a spin-Peierls-like phase transition at 80 K to the ACP state. However, the calorimetric results did not give rise to any thermal anomalies at 80 and 300 K. Very sensitive heat-capacity measurements based on a.c. calorimetry were performed for a single crystal of [$Pt_2(dta)_4I$] in the 15−317 K range at a frequency of 2 Hz. However, no thermal anomaly was detected around 80 and 300 K. In general, the change of a crystal lattice involved in a Mott transition is extremely small. Therefore, the thermal anomaly due to the Mott transition at 300 K, if any, is too small to be detected by these calorimetric methods. On the other hand, because a Peierls or spin-Peierls transition gives rise to a change of crystal lattice due to dimerization, a thermal anomaly would be observed at 80 K if the transition actually occurs. In the case of [$Pt_2(dta)_4I$] crystal, however, as the spin in the crystal is still alive below 80 K, the change in the lattice would be very small. This might be the reason for no detection of a thermal anomaly around 80 K by these two calorimetries.

In contrast, a heat-capacity peak due to a structural phase transition was observed at $T_{trs} = 373.4$ K. An XRD study[134] revealed that the plane formed by SCS atoms of a ligand is statically tilted at room temperature, while above about 370 K the ligand plane can randomly convert between two tilted directions available for right and left sides with equal probability. Therefore, this phase transition is of the order−disorder type concerning conformational change of the dta ligands (see Figure 26). The total entropy gain due to the phase transition was only $\Delta S = (5.25 \pm 0.07)$ J K^{-1} mol^{-1}. If the four dithioacetato ligands reorient independently between two positions, the total entropy gain expected for the order−disorder phase transition would be $4 \times R \ln 2 = 23.05$ J K^{-1} mol^{-1}. However, this is quite far from the observed value. The observed entropy is just 1/4 of the independent motion model. This fact clearly indicates that order−disorder motions of the four dithioacetato ligands might be synchronized. In that case, the theoretical entropy is only $R \ln 2 = 5.75$ J K^{-1} mol^{-1}. This value agrees well with the observed value. Therefore, one can safely conclude that the ligand motions in this complex are not independent but synchronized.

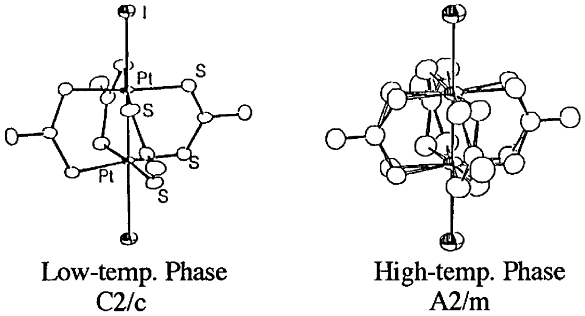

Low-temp. Phase
C2/c

High-temp. Phase
A2/m

Figure 26. Part of a 1D arrangement of the halogen-bridged mixed-valence complex [$Pt_2(dta)_4I$]. In the HT phase, two conformational disorders of each dta-ligand are drawn with equal probability.[134]

Similar structural phase transitions have been found by adiabatic calorimetry for the homologous series of complexes with longer alkyl chains: [$Pt_2(n\text{-}C_3H_7CS_2)_4I$],[136] [$Pt_2(n\text{-}C_4H_9CS_2)_4I$],[137] and [$Pt_2(n\text{-}C_5H_{11}CS_2)_4I$].[138] Table 3 lists the transition temperatures and the entropy gains at the phase transitions calorimetrically determined for the [$Pt_2(n\text{-}C_mH_{2m+1}CS_2)_4I$] ($1 \le m \le 5$) complexes. The phase transitions with a large entropy gain always involve a order−disorder mechanism of the conformational changes of the ligands.

In the case of [$Pt_2(n\text{-}C_4H_9CS_2)_4I$], for example, the heat-capacity measurement by Ikeuchi et al.[137] revealed two large phase transitions at 213.5 and 323.5 K (see Figure 27). These transition temperatures agree well with those found by the transport, magnetic, and a single-crystal XRD studies by Mitsumi et al.[142] These structural phase transitions were afterward confirmed by ESR[143] and resistance measurements under uniaxial compression.[143] The X-ray structural study[142] revealed that the space group changes from tetragonal *P*4/*n* in the LT phase (below 213.5 K) to tetragonal *I*4/*m* in the room-temperature (RT) phase persisting between 213.5 and 323.5 K. In both phases, the crystal consists of a neutral 1D chain with a Pt−Pt−I− repeating unit lying on the crystallographic 4-fold axis parallel to the *c*-axis. The periodicity of the crystal lattice in the 1D chain direction, however, changes from 2-fold with a Pt−Pt−I− period in the LT phase to 3-fold in the RT phase. As judged by Pt−Pt and Pt−I bond distances, the valence-ordering structure in the LT phase can be regarded as an ACP state, while that in the RT phase is close to the AV state. The HT phase appearing above 323.5 K has uniform structure along the 1D chain (the *c*-axis of tetragonal system) with an inversion center, implying tetragonal *I*4/*m* and the AV electronic state.

ORTEP diagrams of the LT, RT, and HT phases of [$Pt_2(n\text{-}C_4H_9CS_2)_4I$] are shown in Figure 28.[142] In the LT phase, no

Table 3. Transition Temperature and the Entropy Gain at the Phase Transitions in Halogen-Bridged Mixed-Valence Quasi-1D Complexes $[Pt_2(n\text{-}C_mH_{2m+1}CS_2)_4I]$

	LT phase → RT phase		RT phase → HT phase		
complexes	T_{trs} (K)	$\Delta_{trs}S$ (J K^{-1} mol^{-1})	T_{trs} (K)	$\Delta_{trs}S$ (J K^{-1} mol^{-1})	refs
$[Pt_2(CH_3CS_2)_4I]$[a]			373.4	5.25 ± 0.07	135
$[Pt_2(C_2H_5CS_2)_4I]$[b]	~180 and ~230	0.21 and 0.13			148
$[Pt_2(n\text{-}C_3H_7CS_2)_4I]$[c]	209	14.6	358.8	10	136
$[Pt_2(n\text{-}C_4H_9CS_2)_4I]$[d]	213.5	20.09	323.5	7.46	137
$[Pt_2(n\text{-}C_5H_{11}CS_2)_4I]$[e]	207.4	49.1	324	~0	138
$[Pt_2(n\text{-}C_5H_{11}CS_2)_4I]$[f]	220.5	52.4			138
model of disorder[g]		15.36		7.68	

[a] No thermal anomalies at T_{M-S} = 300 K and T(spin Peierls-like transition) = 80 K.[132,134] [b] Electrical properties show a metal-semiconductor transition at T_{M-S} = 205 K.[139,142] [c] Structural phase transition was reported at T_{trs} = 359 K.[140] [d] Phase transitions were reported at 210 and 324 K.[141−143] The calorimetric study[137] additionally detected a small phase transition at 114 K. [e] Data for as-grown sample. The phase transition was reported at 210 K.[143] [f] Data for the sample once heated above the transition at 324 K and then supercooled. A very broad higher-order phase transition was detected around 170 K. [g] See the text.

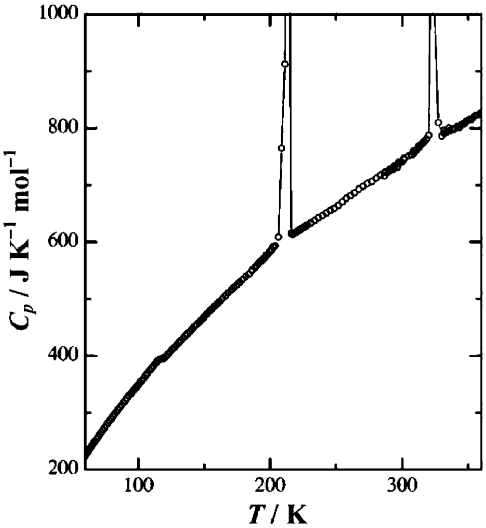

Figure 27. Molar heat capacity of $[Pt_2(n\text{-}C_4H_9CS_2)_4I]$ as a function of temperature. A small heat-capacity anomaly was also detected at 114 K. Reprinted with permission from Ikeuchi, S.; Saito, K.; Nakazawa, Y.; Sato, A.; Mitsumi, M.; Toriumi, K.; Sorai, M. *Phys. Rev. B 66*, 115110, 2002 (http://link.aps.org/abstract/PRB/v66/p115110). Copyright 2002 by the American Physical Society.

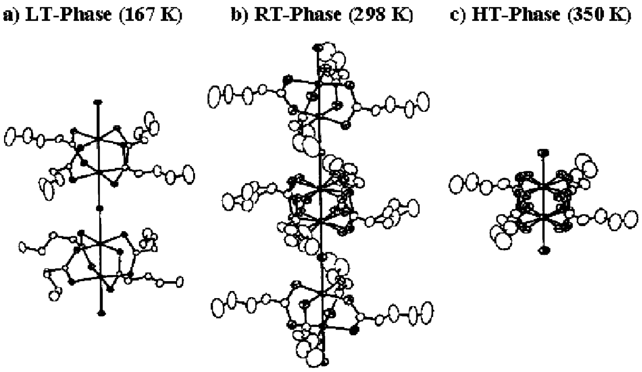
a) LT-Phase (167 K) b) RT-Phase (298 K) c) HT-Phase (350 K)

Figure 28. ORTEP diagram (thermal ellipsoids set at the 50% probability level) of $[Pt_2(n\text{-}C_4H_9CS_2)_4I]$: (a) LT phase at 167 K, (b) RT phase at 298 K, and (c) HT phase at 350 K. Reprinted with permission from ref 142. Copyright 2002 Wiley-VCH.

structural disorder has been detected. In contrast, the RT phase has a lattice periodicity of three in the Pt−Pt−I− repeating unit. There are two crystallographically independent Pt−Pt−I− units with the population ratio of 1:2. Whereas structural disorder does not exist in two units, in the remaining third unit, the dithiocarboxylato (CS_2^-) groups undergo a structural disordering between two tilted positions realized by clockwise and counterclockwise twist motions with a population ratio of 1:1; moreover, each butyl group has two conformations with a ratio of 1:1. On the other hand, the HT phase has a lattice periodicity of one, showing that all of the Pt−Pt−I− units are equivalent. Interestingly, although the CS_2^- groups show 2-fold disorder with respect to the twist motion in the HT phase, the butyl chains are seemingly ordered.

Because the twist motions of the four CS_2^- groups in $[Pt_2(CH_3CS_2)_4I]$ were synchronized,[135] Ikeuchi et al.[137] estimated possible structural entropies of each phase on the basis of various combinations of synchronized and independent motions of the CS_2^- and butyl groups and compared them with the experimental values. As a result, good agreement was obtained for the independent motion model. When the entropy due to structural disorder is assumed to be zero in the LT phase, the configurational entropy of the RT phase is estimated as $R/3 \cdot \ln(2^4 \times 2^4)$ (= 15.36 J K^{-1} mol^{-1}), in which the factor 1/3 originates in the portion of the disorder unit in the 3-fold periodicity of Pt−Pt−I− units and the double 2^4 terms correspond to the number of conformations attained by four CS_2^- and four butyl groups in a Pt−Pt−I− unit. The entropy of the HT phase is simply $R \cdot \ln 2^4$ (= 23.04 J K^{-1} mol^{-1}), because only the four CS_2^- groups contribute to the entropy. Therefore, the entropy changes at the phase transitions amount to ΔS(LT → RT phase) = 15.36 J K^{-1} mol^{-1} and ΔS(RT → HT phase) = 7.68 J K^{-1} mol^{-1}. As shown in Table 3, agreement between the experimental value and the disorder model is excellent for the RT−HT phase transition, whereas the experimental entropy gain at the LT−RT phase transition (20.09 J K^{-1} mol^{-1}) is fairly large. The excess entropy beyond the present disorder model has been attributed to the contribution from the spin-Peierls behavior inherent in this phase transition. This disorder model is also applicable to the phase transitions in $[Pt_2(n\text{-}C_3H_7CS_2)_4I]$.[136]

In the case of $[Pt_2(n\text{-}C_5H_{11}CS_2)_4I]$,[138] the LT−RT phase transition with a large entropy gain (49.1 J K^{-1} mol^{-1}) occurs at 207.4 K. Although the RT−HT phase transition also takes place at 324 K, the entropy change is substantially zero and this phase transition is always supercooled. Therefore, the interpretation of the phase transitions is not so easy as compared with other homologous complexes. Saito et al.[138] proposed a more general interpretation of the RT−HT phase transitions occurring in $[Pt_2(n\text{-}C_3H_7CS_2)_4I]$, $[Pt_2(n\text{-}C_4H_9CS_2)_4I]$,

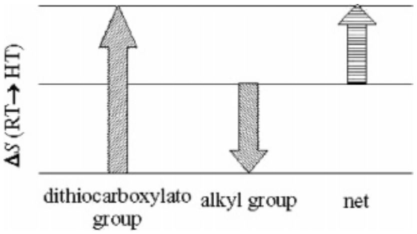

Figure 29. Schematic relationship of the entropies possessed by dithiocarboxylato ligands and alkyl chains for the RT−HT phase transitions in [$Pt_2(n\text{-}C_3H_7CS_2)_4I$], [$Pt_2(n\text{-}C_4H_9CS_2)_4I$], and [$Pt_2(n\text{-}C_5H_{11}CS_2)_4I$].[138]

and [$Pt_2(n\text{-}C_5H_{11}CS_2)_4I$] in terms of "alkyl group acting as entropy reservoir" and "entropy transfer between dithiocarboxylato and alkyl groups". Because alkyl chains are very flexible and capable of doing labile motions in condensed states,[144] they have a potential capacity of entropy amounting to about 10 J K^{-1} (mol of CH_2)$^{-1}$.[145] Therefore, the alkyl chain attached to the ligand can serve as "entropy reservoir". This concept and the "entropy transfer mechanism" have recently been proposed for the interpretation of phase transitions occurring in liquid crystalline systems by Saito et al.[146,147] The "entropy transfer mechanism" can be seen in the fact that the entropy reserved in alkyl groups in the RT phase is transferred to the dithiocarboxylato groups when the RT−HT phase transition occurs (see Figure 29).

It is of interest to remark here that the complex [$Pt_2(C_2H_5CS_2)_4I$] does not give rise to any structural phase transition[148] and that the synchronized twist motion of he four CS_2^- groups is observed only in [$Pt_2(CH_3CS_2)_4I$].

3.7. Mn^{III}-Porphyrin-TCNE and M(TCNQ)$_2$

An interesting family of molecule-based magnets is the charge-transfer complexes between manganese(III)-tetraphenylporphyrin and TCNE, [MnTPP][TCNE]·(solv), where solv implies the crystalline solvent molecule. They form a quasi-1D-ferrimagnetic chain structure with the spin quantum numbers of 2 of [MnTPP]$^+$ and 1/2 of [TCNE]$^-$. The first example was reported by Miller et al.[149] for [MnTPP][TCNE]·2PhMe, where PhMe is toluene. The real part of the a.c. magnetic susceptibility of this complex exhibits a maximum at the critical temperature $T_c = 12.5$ K.[150] Because the magnetic properties of this complex are sensitive to the stoichiometry of the solvent molecule and thus the lattice defects and disorder, the magnetic properties are rather complicated. The imaginary part of the a.c. magnetic susceptibility shows a second, lower temperature peak, which is similar to those seen in "reentrant" spin glass or superparamagnetism.[150]

The compounds introduced here are analogous complexes [MnT(R)PP][TCNE]·(solv). Molecular structures of [MnT(R)PP] and TCNE are shown in Figure 30. The complexes with (**1**, R = $n\text{-}C_{12}H_{25}$ and solv = 2PhMe), (**2**, R = $n\text{-}C_{14}H_{29}$ and solv = MeOH), and (**3**, R = F and solv = 0.5MeOH). The complexes **1**, **2**, and **3** exhibit the phase transition evidenced by the spontaneous magnetization at the critical temperature T_c = 22,[151] 20.5,[152] and 27 K,[151] respectively. The a.c. magnetic susceptibility exhibits a very large peak at the critical temperatures. For the complex **1**, the transition peak is especially sharp. In the sense that although the spontaneous magnetization appears below T_c, the real and imaginary parts of the a.c. magnetic susceptibility depend on the frequency of measurements, and there exists simultaneously both the ferrimagnetic order and the spin-glass property; the latter is caused by random anisotropy due to the crystalline solvent molecules.[151]

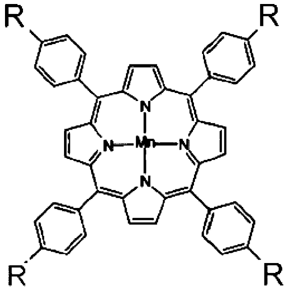

[MnT(R)PP]

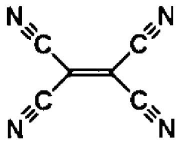

TCNE

Figure 30. Molecular structures of [MnT(R)PP] and TCNE.

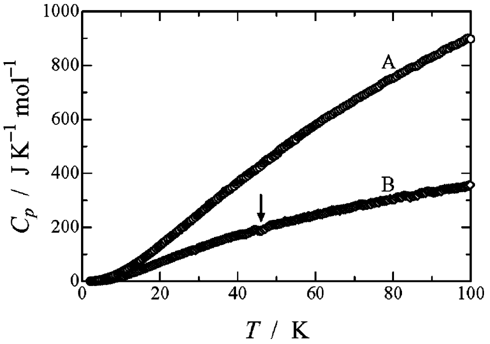

Figure 31. Molar heat capacity of [MnT(R)PP][TCNE]·(solv). Curve A: R = $n\text{-}C_{14}H_{29}$ and solv = MeOH. Curve B: R = F and solv = 0.5 MeOH. Reprinted with permission from ref 153. Copyright 2005 Elsevier Ltd.

One may naturally expect some heat-capacity anomalies around the critical temperatures. Figure 31 illustrates the molar heat capacities of **2** and **3**.[153] Quite mysteriously, any heat-capacity anomalies due to the magnetic ordering have not been detected around 20.5 and 27 K. A clue to solve this mystery is hidden in the characteristic magnetic structure of these complexes. They consist of a quasi-1D-ferrimagnetic chain with a very strong antiferromagnetic interaction between the spin quantum number 2 of the manganese ion and the spin 1/2 of the TCNE radical. The intrachain spin−spin interaction parameters for **2** and **3** are as large as $J_{\text{intra}}/k = -148$[152] and −236 K,[151] respectively. This type of magnetic chain brings about a very broad heat capacity extending over a wide temperature region. A very large fraction of the magnetic entropy above T_c cannot contribute to the magnetic phase transition, because this entropy corresponds to the strong short-range order still remaining above T_c. The entropy available for the phase transition is an extremely small fraction below T_c. This is the reason for substantially no effect in the heat capacity. The heat-capacity measurement supporting this situation was recently reported by Nakazawa et al.[154] for [MnT(X)PP][TCNE]·2PhMe, where X = Cl, Br, and 2PhMe = toluene.

However, there still remains a big mystery. Why is an enhanced effect possible for the magnetic susceptibility, while substantially no effect in the heat capacity? To solve this mystery, Sorai and his collaborators[153] anticipated formation of magnetic domains in the actual crystal. They assumed the following model: (i) An antiferromagnetically coupled pair of spins ($S = 2$ and 1/2) forms a resultant spin ($S = 3/2$). (ii) The resultant spins have a tendency to form ferromagnetic short-range order. A region of the short-range order is assumed to form a magnetic domain of uniform size. (iii) The number of spins in a domain is n. (iv) Under zero magnetic field, the net magnetic moments of domains fluctuate paramagnetically. The number of domains with up-spin and down-spin are designated as $N_D(\uparrow)$ and $N_D(\downarrow)$, respectively. These numbers are related to the Avogadro constant N_A through the following equation,

$$[N_D(\uparrow) + N_D(\downarrow)] \cdot n = N_A \tag{2}$$

As the magnetization M is proportional to the effective number of spins orienting to an easy axis, it is expressed by the equation,

$$M \propto [N_D(\uparrow) - N_D(\downarrow)] \cdot n = N_A \cdot [N_D(\uparrow) - N_D(\downarrow)]/[N_D(\uparrow) + N_D(\downarrow)] \tag{3}$$

Because the parameter n does not appear in the final form of the magnetization equation, the formation of domain does not influence the magnetization at all. On the other hand, when the magnetic domains are formed, the magnetic susceptibility χ is given by the following equation,

$$\chi = (N_A/n) \cdot [(n \cdot \mu_{eff})^2/3kT] = n \cdot [N_A \cdot \mu_{eff}^2/3kT] \tag{4}$$

where μ_{eff} is the effective magnetic moment of a single spin. From this equation, one can know that the magnetic susceptibility is enhanced in proportion to n. Consequently, the enhanced effect observed in the magnetic susceptibility is surely based on the formation of magnetic domains in the crystal.

Dunbar and her collaborators[155,156] prepared the homologous series M(TCNQ)$_2$ [M = Mn(II), Fe(II), Co(II), and Ni(II)] and characterized magnetic properties by the tools of d.c. and a.c. magnetometry. The d.c. magnetic measurements reveal a spontaneous magnetization for the four materials at low temperatures with a weak field coercivity of 20, 750, 190, and 270 G at 2 K for Mn(TCNQ)$_2$, Fe(TCNQ)$_2$, Co(TCNQ)$_2$, and Ni(TCNQ)$_2$, respectively. At low temperatures, a.c. susceptibility measurements confirm the presence of a magnetically ordered phase at 44, 28, 7, and 24 K for Mn(TCNQ)$_2$, Fe(TCNQ)$_2$, Co(TCNQ)$_2$, and Ni(TCNQ)$_2$, respectively, but do not support the description of this system as a typical magnet. In the absence of the a.c. magnetic data, the behavior is indicative of ferri- or ferromagnetic ordering (depending on the metal), but in fact, a complete investigation of their physical properties revealed their true nature to be a glassy magnet. The glassiness, which is a high magnetic viscosity known to originate from randomness and frustration, is revealed by a frequency dependence of the a.c. susceptibility data and is further supported by a lack of a λ-type peak in the heat-capacity data. These results clearly demonstrate that molecule-based materials with a presumed magnetic ordering may not always be exhibiting truly cooperative behavior.

3.8. Spin-Gapped Systems

Haldane's conjecture[157] that 1D antiferromagnetic chains consisting of integer spins should have "spin gaps" in their excitation spectra, making a sharp contrast to gapless half-odd spin chains, has launched a lot of research both theoretically and experimentally on spin-gapped systems where the Néel-order ground states are suppressed by strong quantum fluctuations.[158] The spin-gapped systems include Haldane systems,[159,160] spin-ladder systems with even-numbered legs,[161] bond alternation systems, and so on. Because their common feature is the existence of an energy gap above the singlet ground state (Figure 32), the magnetic heat capacity at low temperatures shows an exponential growth with temperature and allows quantitative estimation of spin gaps.

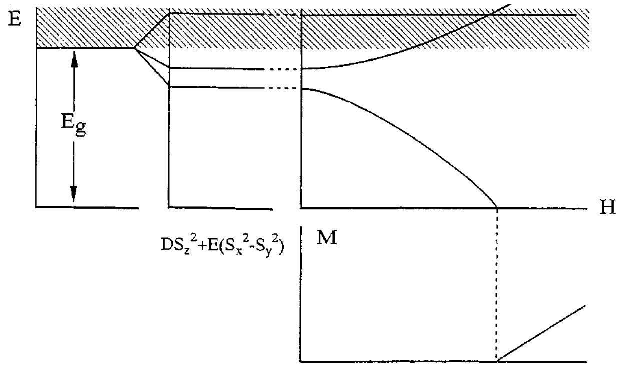

Figure 32. Schematic diagram of excitation energy and magnetization for Ni-based Haldane systems under magnetic field. E_g stands for the Haldane gap above the singlet ground state, and the shaded area means spin-wave continuum. Reprinted with permission from ref 160. Copyright 2000 Elsevier Ltd.

Among molecule-based Haldane systems, calorimetric studies were reported on a series of antiferromagnetic $S = 1$ Heisenberg chain systems, [Ni(en)$_2$(NO$_2$)]ClO$_4$ (NENP),[162] NMe$_4$[Ni(NO$_2$)$_3$] (TMNIN),[163,164] [Ni(dmpn)$_2$N$_3$]ClO$_4$ (NDMAZ),[165] and [Ni(dmpn)$_2$N$_3$]PF$_6$ (NDMAP).[166-169] Magnetic heat capacities deduced from temperature dependence of optical linear birefringence were also reported on NENP and [Ni(en)$_2$(NO$_2$)]PF$_6$ (NENF).[170] These studies clearly showed that the magnetic long-range order is absent under zero magnetic field and that the spin gaps are dominated by the exchange interaction J along the chains rather than the single-ion anisotropy D of spin bearer Ni(II). The effect of external magnetic field was thoroughly examined to bring about quantum phase transitions. As shown in Figure 33, the field-induced magnetic phase transitions were clearly detected for NDMAP as sharp λ-type heat-capacity anomalies. The field temperature phase diagram was presented in Figure 34. It revealed that the critical fields are varied with the angle between the external field and the crystallographic axis, since the Ni(II) ions have magnetic anisotropy of easy-plane type.

As a candidate of two-leg spin-ladder systems, the heat capacity of [Cu$_2$(C$_5$H$_{12}$N$_2$)Cl$_4$] was reported.[171-174] Round heat-capacity peaks characteristic of spin-gapped systems were observed. Field-induced magnetic order similar to the Haldane systems was also found under external fields from 7 to 13 T, where spin-gap behaviors were suppressed and alternatively λ-type peaks appeared. However, it should be mentioned that a recent neutron diffraction study suggested another interpretation of the spin gap in this compound on the basis of a frustrated 3D spin-liquid model rather than a spin-ladder model.[175] It has already been pointed out that the magnetism of weakly coupled spin dimers is not sensitive to the lattice dimensionality and special care should be taken at the choice of theoretical models.[176]

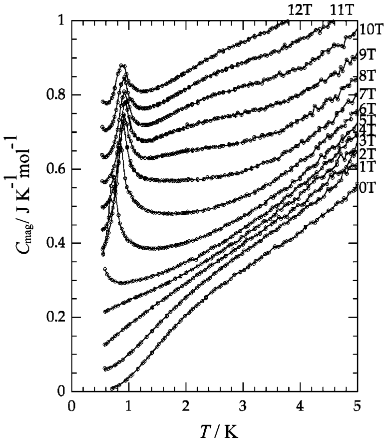

Figure 33. Temperature dependence of magnetic heat capacity of NDMAP under magnetic field parallel to c-axis. Reprinted Figure 3c with permission from Honda, Z.; Katsumata, K.; Nishiyama, Y.; Harada, I. *Phys. Rev. B 63*, 064420, 2001 (http://link.aps.org/abstract/PRB/v63/p64420). Copyright 2001 by the American Physical Society.

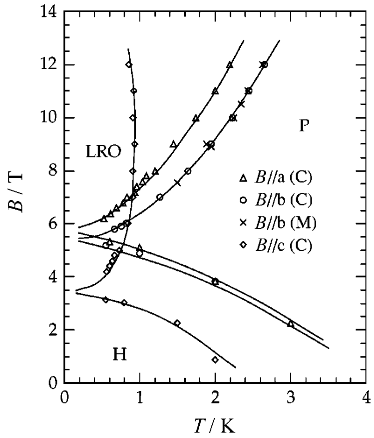

Figure 34. $B-T$ phase diagram of NDMAP determined from the heat capacity (C) and magnetization (M) measurements. H, quantum-disordered Haldane phase; P, thermally disordered paramagnetic phase; and LRO, field-induced long-range ordered phase. Reprinted Figure 5 with permission from Honda, Z.; Katsumata, K.; Nishiyama, Y.; Harada, I. *Phys. Rev. B 63*, 064420, 2001 (http://link.aps.org/abstract/PRB/v63/p64420). Copyright 2001 by the American Physical Society.

Ferromagnetic−antiferromagnetic alternating Heisenberg chains are also interesting spin-gapped systems, whose strong ferromagnetic-coupling limit coincides with an $S = 1$ Haldane system. On the basis of the calorimetric results, a spin gap $\Delta/k = 20.9$ K was reported in $(Me_2CHNH_3)CuCl_3$, exhibiting good agreement with the estimate from the magnetic susceptibilities.[177] This compound showed λ-type heat-capacity anomalies indicating the occurrence of a field-induced long-range order above 9.0 T.

4. Two-Dimensional Magnets

To obtain spontaneous magnetization in metal-assembled complexes, 3D ferromagnetic or ferrimagnetic ordering over a whole crystal is required. One of the useful synthetic strategies was to bundle 1D ferro- or ferrimagnetic chains three-dimensionally and to afford a net magnetization. This idea was applied first by Kahn and his collaborators[178−180] to synthesize the ferromagnetic compound $[Mn^{II}Cu^{II}(pbaOH)(H_2O)_3]$ [pbaOH = 2-hydroxy-1,3-propylene-bis(oxamato)]. They proposed an idea to bring about ferromagnetic interactions among ferrimagnetic chains. However, it owes much to accidental matching of overlap phase in neighboring chains. Avoiding the difficulty of crystal packing regulation of 1D element, Ōkawa and his collaborators adopted another strategy to build a higher-dimensional structure of coordination polymer by a single reaction process.

4.1. Assembled-Metal Complexes

Ōkawa et al. prepared the ferromagnetic assembled-metal complexes $NBu_4[M^{II}Cr^{III}(ox)_3]$ (Bu = n-C_4H_9, M = Mn, Fe, Co, Ni, Cu, Zn; H_2ox = oxalic acid)[181,182] and $NBu_4[M^{II}Fe^{III}(ox)_3]$ (M = Fe, Ni).[183] These complexes except for the Zn compound exhibit ferromagnetic phase transitions around 6−14 K. The network structure of $\{[M^{II}Cr^{III}(ox)_3]^-\}_\infty$ is depicted schematically in Figure 35. The hub unit with D_3 point symmetry, $[Cr^{III}(ox)_3]^{3-}$, combines three M^{2+} ions through its ox groups. This network structure can be embedded in two possible crystal structures, i.e., 2D honeycomb or 3D helical structures. A tris(chelate) complex can take left-handed or right-handed helicity around a D_3 axis, which are called Δ- or Λ-isomers, respectively. When the neighboring M^{2+} and Cr^{3+} coordination octahedra take a combination of (Δ + Λ), a 2D honeycomb lattice with alternating hetero spins is formed (Figure 36a), while the combination of either (Δ + Δ) or (Λ + Λ) provides a 3D structure, i.e., a complicated helix with 10-membered rings (Figure 36b).

Unfortunately, however, becuase these complexes were prepared as fine powders, a single-crystal XRD study was unsuccessful. As heat capacity is sensitive to lattice dimensionality, the present authors and co-workers tried to determine the actual dimensionality on the basis of heat-capacity measurements for the complexes $NBu_4[Cu^{II}Cr^{III}(ox)_3]$,[184,185] $NBu_4[Fe^{II}Cr^{III}(ox)_3]$,[186] and $PPh_4[Mn^{II}Cr^{III}(ox)_3]$ (Ph = C_6H_5).[184,185] For example, as shown in Figure 37, the mixed-metal $NBu_4[Cu^{II}Cr^{III}(ox)_3]$ complex gave rise to a phase transition at 6.98 K.[184,185] This phase transition is attributable to the ferromagnetic spin ordering because the entropy gain $\Delta S = 16.2$ J K^{-1} mol^{-1} agrees well with the theoretical value $R \ln(2 \times 4) = 17.28$ J K^{-1} mol^{-1} expected for the spin system consisting of Cu^{2+} (spin 1/2) and Cr^{3+} (spin 3/2) and also because the transition temperature agrees well with the onset temperature of the spontaneous magnetization.[182] Figure 38 represents the excess heat capacity

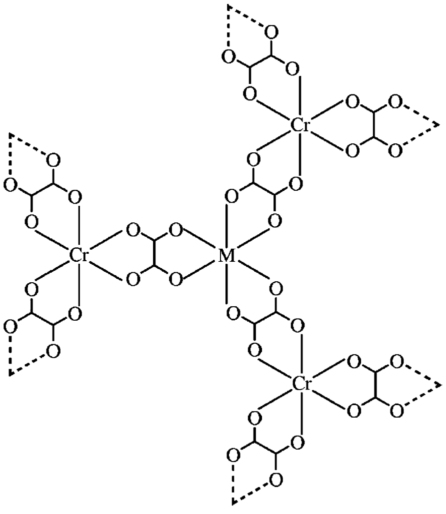

Figure 35. $[M^{II}Cr^{III}(ox)_3]^-$ network structure (M = Mn, Fe, Co, Ni, Cu, Zn; H_2ox = oxalic acid).

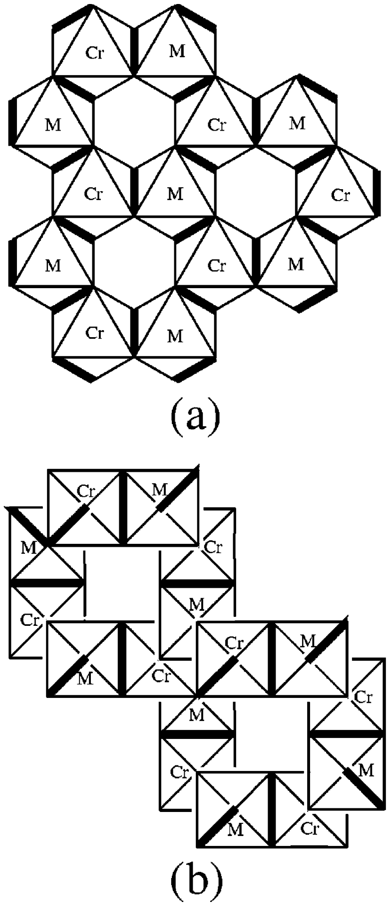

Figure 36. Possible schematic network structure of $[M^{II}Cr^{III}(ox)_3]^-$. (a) Two-dimensional honeycomb and (b) 3D helical structures.

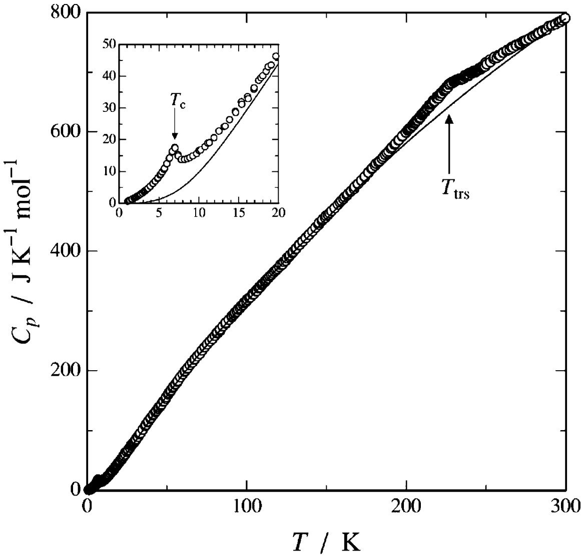

Figure 37. Molar heat capacities of $NBu_4[Cu^{II}Cr^{III}(ox)_3]$. Solid curves indicate the normal heat capacities. Reprinted with permission from ref 185. Copyright 2003 American Institute of Physics.

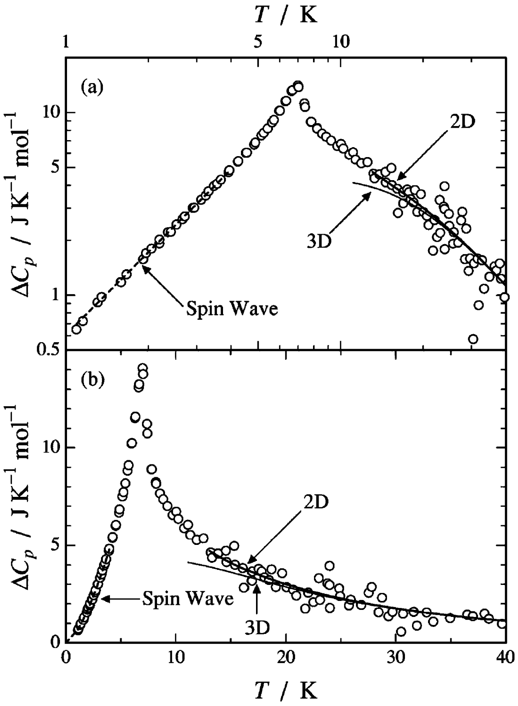

Figure 38. Excess heat capacities due to the magnetic phase transition of $NBu_4[Cu^{II}Cr^{III}(ox)_3]$ on (a) logarithmic and (b) normal scales. Thick curves represent the 2D structure, while thin curves correspond to the 3D structure. Dashed curves at the lowest temperature region indicate the spin-wave contribution. Reprinted with permission from ref 185. Copyright 2003 American Institute of Physics.

due to the magnetic phase transition of this complex. A remarkable feature is the existence of a dominant short-range order manifested by the large tail of the magnetic heat capacity. This type of heat-capacity anomaly is characteristic of low-dimensional magnets. Because 1D magnetic interaction paths cannot be found in this complex, one may conclude that this series of mixed-metal complexes has 2D magnetic structures. Because the spin−spin interaction in this complex is of Heisenberg type, no phase transition is theoretically expected for 2D systems. However, the occurrence of the magnetic phase transition does not conflict with the existence of dominant 2D interactions. When a 3D interaction, even though weak, exists at low temperatures, dimensional crossover between 2D and 3D may happen and bring about a phase transition. In fact, the heat capacities of $NBu_4[Cu^{II}Cr^{III}(ox)_3]$ in the spin-wave excitation region are well-reproduced by $T^{1.51}$, whose exponent is approximated by $d/n = 3/2$, implying that the ordered state at low temperatures is actually a 3D ferromagnet.[15]

On the basis of this fact, the authors concluded that the dominant magnetic interaction may be 2D. However, one should be very careful to draw a conclusion about the dimensionality when the number of the nearest neighbor paramagnetic ions z is extremely small. The value $z = 3$ for the present complexes is extremely small in comparison with $z = 6$ (sc), $z = 8$ (bcc), and $z = 12$ (fcc) of 3D lattices or $z = 4$ (square and Kagomé) and $z = 6$ (triangular) of 2D lattices. In many cases, the short-range order effect is regarded as a direct manifestation of low-dimensionality of spin lattices. Exceptional cases rarely arise where a 3D magnet shows a large short-range order effect comparable to low-dimensional magnets. In this point, the present series of compounds are very unique, because they have extremely small numbers of the nearest neighbor spins, $z = 3$, in either 2D honeycomb or 3D helical lattices. A small z may bring about a remarkable short-range order effect, and the discrimination between 2D and 3D structures becomes a delicate problem.

To examine quantitatively the dimensionality of the magnetic structure of the present complex, Hashiguchi et al.[185] formulated the magnetic heat capacities for possible

Table 4. Transition Temperature and Entropy of Transition in Assembled-Metal Complexes Bridged by Oxalato Ligands

complexes	T_c (K)	Δ_cS (J K^{-1} mol^{-1})	Δ_cS(spin) (J K^{-1} mol^{-1})	T_{trs} (K)	$\Delta_{trs}S$ (J K^{-1} mol^{-1})	refs
$N(n\text{-}C_4H_9)_4[Fe^{II}Fe^{III}(ox)_3]$	16.3 and 43.3	4.89 + 22.65 (= 27.54)	28.27 [= R ln(5 × 6)]	217	11.47	189−191
$N(n\text{-}C_4H_9)_4[Zn^{II}Fe^{III}(ox)_3]$	paramagnetic till at least 5 K		14.90 [= R ln(1 × 6)]	227	13.32	189, 190
$N(n\text{-}C_3H_7)_4[Fe^{II}Fe^{III}(ox)_3]$	10 and 38	31.98	28.27 [= R ln(5 × 6)]	none		192
$N(n\text{-}C_4H_9)_4[Co^{II}Fe^{III}(ox)_3]$	12 and 29.7	25.5	26.42 [= R ln(4 × 6)]	210	28.5	193
$N(n\text{-}C_5H_{11})_4[Mn^{II}Fe^{III}(ox)_3]$	23 and 27.1	33.22	29.80 [= R ln(6 × 6)]	226	13.07	194
$P(C_6H_5)_4[Fe^{II}Cr^{III}(ox)_3]$	10.4	5.4	24.90 [= R ln(5 × 4)]			195
$N(n\text{-}C_4H_9)_4[Fe^{II}Cr^{III}(ox)_3]$	12.0	23.3	24.90 [= R ln(5 × 4)]	235.5	23.5	186
$N(n\text{-}C_4H_9)_4[Cu^{II}Cr^{III}(ox)_3]$	6.98	16.2	17.28 [= R ln(2 × 4)]	226.9	11.0	184, 185
$P(C_6H_5)_4[Mn^{II}Cr^{III}(ox)_3]$	5.59	25.1	26.42 [= R ln(6 × 4)]	71.3	1.48	184, 185
	5.85	23.2	26.42 [= R ln(6 × 4)]			195

2D and 3D structures by the HT series expansion up to the seventh cumulant with the Padé approximation and fitted the excess heat capacities above the transition temperature. Because the number of the nearest neighbors is extremely small, two formulas for 2D and 3D structures closely resemble each other. As a result, the short-range order effect was extremely large for both 2D and 3D structures. However, as can be seen in Figure 38, good agreement is obtained for the 2D structure, where the superexchange interaction parameter is $J/k = 5.0$ K. Therefore, from a thermodynamic viewpoint, it is concluded that the magnetic lattice structure might be 2D. It is of great interest, however, that the short-range order effect estimated for 3D structure is also unusually large as compared with those for sc, bcc, or fcc lattices. This fact clearly implies that in addition to the dimensionality the important factor governing the short-range order effect due to magnetic fluctuation is the number of the nearest neighbors. It should be remarked here that X-ray structural study has been made for $PPh_4[Mn^{II}Cr^{III}(ox)_3]$ by Decurtins et al.[187] and for $NBu_4[Mn^{II}Cr^{III}(ox)_3]$ and $NBu_4[Fe^{II}Cr^{III}(ox)_3]$ by Ovanesyan et al.[188] These complexes are crystallized in 2D honeycomb structures. The coincidence of the dimensionality derived from the HT series expansion method with the results of X-ray structural analysis would guarantee the usefulness of the calorimetry.

Recently, Bhattacharjee et al. measured heat capacities of analogous assembled-metal complexes $NBu_4[Fe^{II}Fe^{III}(ox)_3]$,[189−191] $NBu_4[Zn^{II}Fe^{III}(ox)_3]$,[189,190] $NPr_4[Fe^{II}Fe^{III}(ox)_3]$ (Pr = $n\text{-}C_3H_7$),[192] $NBu_4[Co^{II}Fe^{III}(ox)_3]$,[193] and $NPe_4[Mn^{II}Fe^{III}(ox)_3]$ (Pe = $n\text{-}C_5H_{11}$)[194] and showed that these compounds exhibit similar behavioral characteristics of 2D structures. Antorrena et al.[195] also reported that the magnetic heat capacities of $PPh_4[MnCr(ox)_3]$ and $PPh_4[Fe^{II}Cr^{III}(ox)_3]$ indicate 2D characters. Except for $NBu_4[Zn^{II}Fe^{III}(ox)_3]$, all of the complexes exhibited the magnetic phase transitions at low temperatures. The critical temperatures due to the magnetic ordering T_c and the entropy gains at T_c are listed in Table 4. Many of the complexes showed a small subpeak below T_c, which would be characterized by a spin-glasslike behavior. In addition to the magnetic phase transition, these complexes exhibited, respectively, a heat-capacity peak above 200 K. These phase transitions seem to be attributable to an order−disorder mechanism of tetra-alkylammonium cations. The structural transition temperatures T_{trs} and the entropy gains are listed in Table 4.

Day and his collaborators[196] found that the mixed-valence assembled-metal complexes $N(n\text{-}C_nH_{2n+1})_4[Fe^{II}Fe^{III}(ox)_3]$ (n = 3−5) behave as ferrimagnets with T_c between 33 and 48 K and that they exhibit a crossover from positive to negative magnetization near 30 K when cooled in a field of 10 mT. To get more insights into this rarely occurring negative magnetization phenomenon, Bhattacharjee et al. measured heat capacities of $NBu_4[Fe^{II}Fe^{III}(ox)_3]$[189−191] and $NPr_4[Fe^{II}Fe^{III}(ox)_3]$[192] under a nonmagnetic field. Figure 39 shows the excess heat capacity observed under nonmagnetic field for $NBu_4[Fe^{II}Fe^{III}(ox)_3]$. Two heat-capacity anomalies were detected at T_2 (= T_c) = 43.3 K and at T_3 = 16.3 K. Because the entropy gain due to these two anomalies, 27.54 J K^{-1} mol^{-1}, is well-approximated by the theoretical value 28.27 J K^{-1} mol^{-1} [= R ln(5 × 6)] expected for the spin multiplicity of high-spin (HS) Fe^{2+} (spin 2) and HS Fe^{3+} (spin 5/2), these two anomalies can be attributed to the magnetic origin. The anomaly at 16.3 K was attributed, without definite evidence, to the formation of a spin-glasslike state at low temperatures. This state was assumed to be caused by the existence of a small fraction of metal vacancies, which would be produced to compensate electrically a partial oxidation $Fe^{II} \rightarrow Fe^{III}$ occurring during sample preparation.

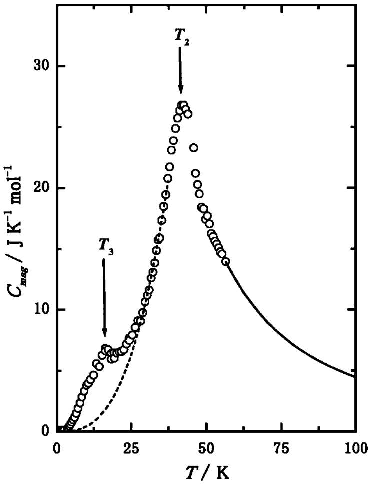

Figure 39. Magnetic heat capacities of $NBu_4[Fe^{II}Fe^{III}(ox)_3]$. The solid and broken curves represent the values estimated by assuming T^{-2} and T^3 temperature dependences, respectively. Reprinted with permission from ref 189. Copyright 2000 The Physical Society of Japan.

No heat-capacity anomaly has been detected around 30 K in $NBu_4[Fe^{II}Fe^{III}(ox)_3]$, as expected from the magnetic measurements.[196] However, it should be noted here that the magnetic measurements were made with precooled samples under certain magnetic fields. Thus, Bhattacharjee et al.[191] measured its heat capacities under various applied magnetic fields. The magnetic heat capacity was tentatively fitted with the relation $C_{mag} = \alpha H^{\beta}$. The temperature variation of the parameter β exhibited two sharp minima below and above 30 K. This observation seems to be in good correlation with the negative magnetization phenomenon.

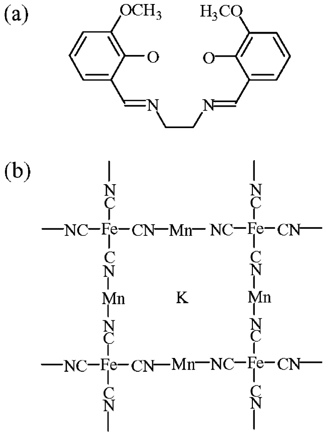

Figure 40. (a) Molecular structure of 3-MeOsalen. (b) Schematic drawing of 2D assembly of K[Mn^{III}(3-MeOsalen)]$_2$[$Fe^{III}(CN^-)_6$], where [Mn^{III}(3-MeOsalen)]$^+$ is simply expressed by Mn.

Another family of 2D assembled-metal complex is the cyanide-bridged molecule-based magnets given by the formula $X_k[A(L)]_l[B(CN)_6]_m{\cdot}n$S (X, monovalent nonmagnetic ion; A, B, di- or trivalent transition metal ions; L, organic ligand; S, solvent molecule; *k*, *l*, *m*, *n*, numbers of stoichiometry). Various network structures can be realized depending on the choice of A, B, and L. On the basis of this strategy, many complexes have so far been synthesized and investigated.[197−200] Miyazaki et al. measured heat capacities of an antiferromagnet K[Mn^{III}(3-MeOsalen)]$_2$[$Fe^{III}(CN^-)_6$] (3-MeOsalen = *N*,*N*′-ethylenebis-(3-methoxysalicylideneaminato)[201] and a ferrimagnet [NEt_4][Mn^{III}(salen)]$_2$[$Fe^{III}(CN)_6$] (salen = *N*,*N*′-ethylenebis(salicylideneaminato).[202] Their molecular assembly is schematically drawn in Figure 40. When these crystals were mechanically perturbed by grinding or pressing, their heat capacities around the magnetic phase transition temperatures were decreased. A plausible explanation for this type of mechanochemical effect is that enhanced lattice defects and imperfections in the crystal lattice produced by mechanical perturbation would lead to an incomplete magnetic phase transition and consequently a part of the paramagnetic species characteristic of the HT phase would remain as the so-called residual paramagnetism even below the magnetic transition temperature. The mechanochemical effect has often been encountered in other soft matter. A dramatic mechanochemical effect was observed in the spin crossover complex [Fe^{III}(3MeO-salenEt)$_2$]PF_6.[11,203−206]

Bhattacharjee et al.[207] reported the heat capacity of a weak ferromagnet [Mn^{III}(cyclam)][$Fe^{III}(CN)_6$]·$3H_2O$ (cyclam = 1,4,8,11-tetraazacyclotetradecane) under zero magnetic field in the 0.1−300 K range by adiabatic calorimetry. A heat-capacity anomaly corresponding to the magnetic phase transition was detected at 6.2 K. The observed entropy gain (ΔS = 19.29 J K^{-1} mol^{-1}) is in good agreement with the theoretical magnetic entropy ($R \ln 5 \times 2 = 19.14$ J K^{-1} mol^{-1}) considering the spin multiplicity of HS Mn^{3+} and low-spin (LS) Fe^{3+} ions. Heat-capacity studies under applied magnetic fields indicated an antiferromagnetic to ferromagnetic transition. A field dependence study of magnetization at different temperatures revealed a field-induced metamagnetic transition.

The most intensively studied cyanide-bridged magnets have been Prussian blue analogues with 3D network structures. Recently, new cyanide-bridged molecule-based magnets having 2D structures were synthesized as follows: $K^I_2Mn^{II}_3(H_2O)_6[Mo^{III}(CN)_7]_2{\cdot}6H_2O$ by Kahn et al.,[208] $(tetrenH_5)_{0.8}Cu^{II}_4[M^V(CN)_8]_4{\cdot}7.2H_2O$ (M = W, Mo; tetren = tetraethylenepentamine) by Podgajny et al.,[209] and $(dienH_3)\{Cu^{II}_3[M^V(CN)_8]_3\}{\cdot}4H_2O$ (M = W, Mo; dien = diethylenetriamine) by Korzeniak et al.[210] Heat-capacity measurements have been made on a single-crystal sample of the double-layered coordination polymer $\{(tetrenH_5)_{0.8}Cu^{II}_4[W^V(CN)_8]_4 7.2H_2O\}_n$ in the presence of the external magnetic field (up to 5 T) directed perpendicular to the plane of the layers.[211,212] The heat capacities determined at zero magnetic field exhibited a rather broad peak centered at T_C = 32.7 K arising from the ferromagnetic to paramagnetic phase transition. Ferromagnetism can be attributed to the interaction through the CN bridges of the unpaired electrons of Cu^{II} (spin $S = 1/2$) and W^V ($S = 1/2$). The layered structure brings about the quasi-2D character of the magnetic coupling. In relation to the 2D character, the heat-capacity curve has a large tail above T_C. As the external magnetic field was increased, the peak temperature of the heat-capacity curve was lowered and the peak was suppressed. The entropy gain due to the magnetic anomaly was much less than the maximum value $S_{max} = 8R \ln 2$ (= 46.1 J K^{-1} mol^{-1}) expected for eight unpaired electrons. The entropy change at zero magnetic field was only 15% of S_{max}, indicating that there is a great deal of magnetic ordering at temperatures above T_C.

4.2. Mixed-Valence Assembled-Metal Complexes

By replacing the symmetric oxalate ligand ox^{2-} (= $C_2O_4^{2-}$) in the assembled-metal complex with an asymmetric dithiooxalato ligand dto^{2-} (= $C_2O_2S_2^{2-}$), Kojima et al.[213,214] reported a novel mixed-valence assembled-metal complex $N(n\text{-}C_3H_7)_4[Fe^{II}Fe^{III}(dto)_3]$. This complex consists of Fe(II) and Fe(III) ions, which are quasi-octahedrally coordinated either by six oxygen atoms, the [FeO_6] site, or by six sulfur atoms, the [FeS_6] site (see Figure 41) and is crystallized at room temperature in the tetragonal crystal system with the space group $P6_3$.[215] Because the ligand field at the [FeS_6] site is much stronger than that at the [FeO_6] site, the iron ion surrounded by sulfur atoms is characterized by a LS state, while that surrounded by oxygen atoms shows a HS state. As shown in Figure 42,[213,214] at RT iron ions sitting in the [FeS_6] site are LS Fe(III) with spin quantum numbers $S = 1/2$, while those of the [FeO_6] site are HS Fe(II) with $S = 2$. When the temperature is decreased, electron transfer occurs from the [FeO_6] site to the [FeS_6] site around 110 K and their oxidation states are interchanged. As the result, iron ion at the [FeO_6] site becomes HS Fe(III) with $S = 5/2$ and that at the [FeS_6] site is LS Fe(II) with $S = 0$. On the other hand, when the temperature of the crystal is

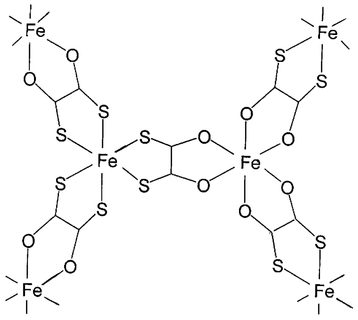

Figure 41. Schematic drawing of the dto-bridged network structure in $N(n\text{-}C_3H_7)_4[Fe^{II}Fe^{III}(dto)_3]$.

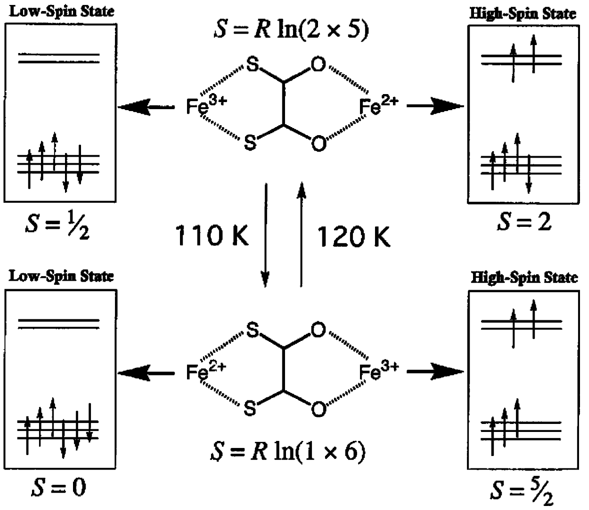

Figure 42. Schematic representation of the electron-transfer phenomenon in $N(n\text{-}C_3H_7)_4[Fe^{II}Fe^{III}(dto)_3]$. It should be remarked that symbol *S* has been used both for the spin quantum number and for the entropy due to the spin multiplicity. Reprinted with permission from ref 214. Copyright 2001 Elsevier Ltd.

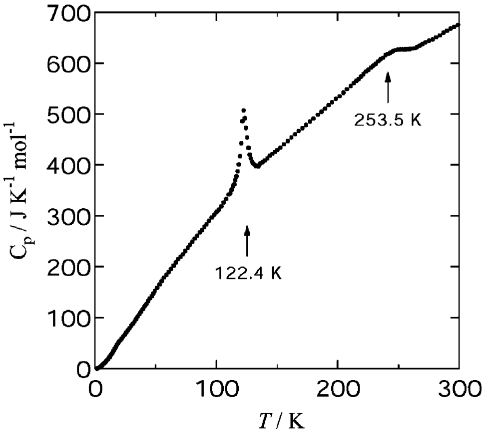

Figure 43. Molar heat capacity of $N(n\text{-}C_3H_7)_4[Fe^{II}Fe^{III}(dto)_3]$ crystal as a function of temperature. Reprinted with permission from ref 216. Copyright 2001 Wiley-VCH.

increased, the electron is reversely transferred around 120 K. The spin multiplicity at the HT phase is 2 × 5 = 10, while that at the LT phase is 1 × 6 = 6. Because the spin-state conversion takes place in the whole $[FeO_6][FeS_6]$ system by the electron transfer, this phenomenon seems to be, at first glance, spin crossover. However, this is not the case, because the spin state at a given site always remains either HS or LS state when the electron transfer occurs.

Nakamoto et al.[216] measured the heat capacities of this complex under constant pressure (see Figure 43) and observed a sharp peak at 122.4 K, a broad heat-capacity anomaly centered at 253.5 K, and a very small anomaly due to the magnetic ordering around 7 K. The origin of the heat-capacity anomaly at 253.5 K can be attributed to an order−disorder type of phase transition of the $N(n\text{-}C_3H_7)_4^+$ cation, judging from the fact that similar heat-capacity anomalies have been observed in the analogous molecule-based oxalate complexes (see Table 4). The anomaly at 122.4 K obviously arises from the phase transition due to the charge transfer, because the transition temperature agrees well with the temperature at which the anomaly was observed in the magnetic susceptibilities.[214] Although the phase transition at 122.4 K does not take place isothermally, this can be regarded as a first-order phase transition, because a super-cooling phenomenon has been observed. As shown in Figure 44a, no anomaly was detected in the measurement done for the specimen cooled to 110 K. The sample cooled to 100 K exhibited a small anomaly. This anomaly became larger as the cool-down temperature was lowered. The heat capacities shown by the open circles in Figure 44a correspond to the values obtained for the specimen well-annealed around 90 K. The excess heat capacity due to the phase transition is shown in Figure 44b.

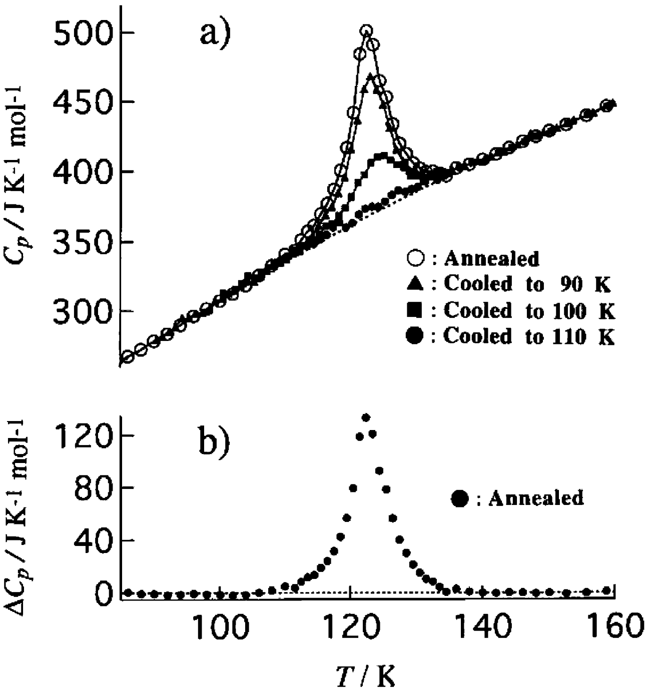

Figure 44. (a) Molar heat capacities of $N(n\text{-}C_3H_7)_4[Fe^{II}Fe^{III}(dto)_3]$ crystal in the vicinity of the phase transition at 122.4 K. Open circles are the same data as shown in Figure 43, corresponding to the heat capacities of the specimen well-annealed. Filled marks indicate the data obtained after cooling to the temperatures as follows: 110 (●), 100 (■), and 90 K (▲). The solid curves are for an eye guide. The dotted curve stands for the normal heat capacity. (b) Excess molar heat capacities due to the phase transition. Reprinted with permission from ref 216. Copyright 2001 Wiley-VCH.

The entropy arising from the charge-transfer phenomenon was $\Delta_{trs}S = 9.20$ J K^{-1} mol^{-1}, which is by 4.95 J K^{-1} mol^{-1} larger than the value expected for the change in the spin multiplicity $R \ln(10/6) = 4.25$ J K^{-1} mol^{-1}. To interpret the origin responsible for this excess entropy, two possibilities have been discussed as follows:[216] One is the orbital angular momentum, and the other is the lattice vibrations. The orbital angular momentum depends on the ligand-field symmetry. In the case of O_h symmetry, the ground terms of Fe^{II}(HS) and Fe^{III}(LS) ions in the HT phase are $^5T_{2g}$ and $^2T_{2g}$, respectively. Because the ground terms of Fe^{III}(HS) and Fe^{II}(LS) ions in the LT phase are $^6A_{1g}$ and $^1A_{1g}$, respectively, the contribution of entropy from the orbital degeneracy is $R \ln [(3 \times 3)/(1 \times 1)] = 18.27$ J K^{-1} mol^{-1}. This value is far beyond the experimental entropy. However, the orbital degeneracy is lifted by the low-symmetry ligand field to give a nondegenerate or lower-degenerate ground state. When a trigonal distortion is encountered in the $[FeO_6]$ and $[FeS_6]$ sites, the ground terms $^5T_{2g}$ of Fe^{II}(HS) and $^2T_{2g}$ of Fe^{III}(LS) in O_h ligand-field symmetry are altered to ^5E and ^2A, respectively. In that case, the orbital entropy is reduced to *R*

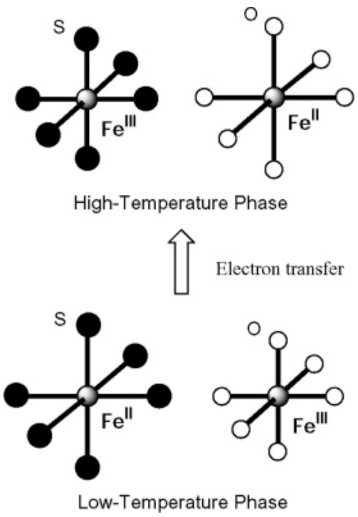

Figure 45. Schematic representation of the relationship between the electron transfer and the metal−ligand bond lengths.

$\ln [(2 \times 1)/(1 \times 1)] = 5.76$ J K^{-1} mol^{-1}. This value is fairly close to the excess entropy of 4.95 J K^{-1} mol^{-1}.

When the ligand-field symmetry is lower than trigonal symmetry, the orbital contribution to the entropy is further reduced and eventually the contribution to entropy becomes the so-called “spin only” value. In such a case, one should look for another cause for the excess entropy. The most plausible candidate is the change in the intramolecular vibrations, in particular the metal−ligand skeletal vibrations. The magnitude of vibrational entropy crucially depends on the bond lengths between the metal ion and the ligands. The bond length is basically affected either by the spin state or by the oxidation state of the metal ion. In the case of the present complex, the bond lengths are determined by the oxidation state of the metal ion. According to Shannon,[217] typical ionic radii of LS iron ion with coordination number 6 are 75 and 69 pm for Fe^{II}(LS) and Fe^{III}(LS), respectively. Namely, the bond length between the metal ion and the ligand is shorter when the oxidation state of the metal ion is high. As schematically shown in Figure 45, the metal−ligand bond lengths are elongated by 13.5 pm at the [FeO_6] site at the phase transition while those at the [FeS_6] site are contracted by 6 pm. As a result, when the phase transition due to the electron transfer occurs, the [FeO_6] site remarkably contributes positively to the vibrational entropy, whereas the [FeS_6] site has a negative contribution. If the oxidation and reduction sites consisted of identical ligands, these two conflicting contributions to entropy would cancel out each other and thus no vibrational entropy would be expected. In the present case, however, because the ligands are not identical and the relative atomic masses are different (O, 15.9994; S, 32.065), the imbalance part of the cancellation seems to be the origin of the small excess entropy beyond the contribution from the change in the spin multiplicity.

The present mixed-valence complex surely provides an interesting system, in which the spin state of the whole system dramatically changes by virtue of the electron transfer. From a viewpoint of functionality, the present material is expected to have a great potentiality.

4.3. Inorganic Layered Complex

It is well-known that 2D Ising spin systems give rise to a magnetic phase transition,[19] while ideal 2D Heisenberg spin systems do not bring about any magnetic phase transitions.[218] However, actual 2D magnetic substances exhibit a magnetic phase transition at low temperatures and lead to a 3D magnetically ordered state due to the presence of weak Ising anisotropy, the existence of weak interlayer magnetic interaction between the 2D magnetic layers, or both.

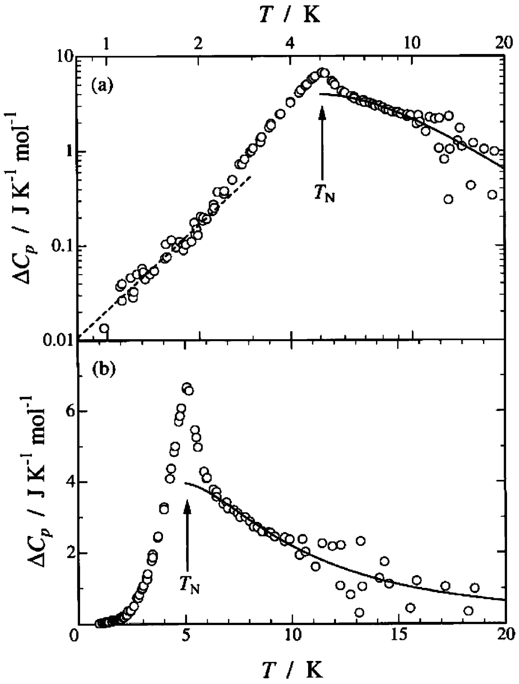

Figure 46. Magnetic heat capacities of [$(5CAP)_2CuBr_4$] crystal as a function of temperature on (a) logarithmic and (b) normal scales. Solid curves indicate theoretical heat capacities for the $S = 1/2$ square planar antiferromagnetic Heisenberg model with $J/k = -4.3$ K. The broken line shows the heat capacity in accordance with the spin-wave theory for 3D antiferromagnets. Reprinted with permission from ref 220. Copyright 2000 American Chemical Society.

Landee and his collaborators are endeavoring to expand the available examples of 2D quantum antiferromagnets through the application of the principles of molecule-based magnetism. They are focusing on layered $S = 1/2$ Heisenberg antiferromagnets with a formula [A_2CuX_4], where A = 5CAP (2-amino-5-chloropyridinium) or 5MAP (2-amino-5-methylpyridinium) and X = Cl or Br. The compound [$(5CAP)_2CuBr_4$] contains $S = 1/2$, Cu^{2+} ions related by *C* centering, yielding four equivalent nearest neighbors. The crystal structure[219] of [$(5CAP)_2CuBr_4$] shows the existence of layers of distorted copper-bromide tetrahedra parallel to the *ab* plane, separated by the organic cations along the *c*-axis. Magnetic pathways are available through the bromide−bromide contacts within the layers and provide for moderate antiferromagnetic exchange. Magnetic susceptibility measurements[219] of polycrystalline [$(5CAP)_2CuBr_4$] reveal a broad maximum around 7 K. This maximum is well-reproduced above 5.5 K by a curve based on a HT series expansion for the $S = 1/2$ square planar Heisenberg antiferromagnet with the exchange parameter of $J/k = -4.3$ K. The experimental and the theoretical values sharply diverge near 5.1 K, indicating the existence of a long-range magnetic ordering.

Figure 46 shows the magnetic heat capacity of this compound below 20 K.[220] A heat-capacity peak with a large tail was observed at 5.08 K. As the entropy gain due to this phase transition $\Delta S = 5.65$ J K^{-1} mol^{-1} agrees well with the $R \ln 2$ (= 5.76 J K^{-1} mol^{-1}) expected for the $S = 1/2$

spin system, this phase transition is surely based on the magnetic origin. The large heat-capacity tail at the HT side of the peak due to a short-range order effect is well-accounted for in terms of the $S = 1/2$ square planar antiferromagnetic Heisenberg model with the intralayer exchange interaction of $J/k = -4.3$ K. This value is in excellent agreement with the value $J/k = -4.3$ K, obtained from the magnetic susceptibility analysis.[219] The magnetic state in the ordered phase is estimated from the low-temperature heat capacity by applying the spin-wave analysis. As described in section 1.2, the spin-wave heat capacity C_{SW} is proportional to $T^{d/n}$. By fitting this relation to the experimental values in the 0.9–2.3 K range, the parameter has been determined as $d/n = 2.98$, which is approximated as 3/1. This fact suggests a 3D antiferromagnetic state.

4.4. Multilayer Systems

According to the concept "magnetic lattice engineering" introduced by de Jongh,[221] Coronado and his collaborators[222] have succeeded in preparing hybrid functional materials formed by two molecular networks: (i) Hybrid magnets constructed from combinations of an extended ferromagnetic or ferrimagnetic inorganic network with a molecular paramagnetic metal complex acting as a template. (ii) Hybrid organic–inorganic compounds combining an organic π-electron donor network that furnishes the pathway for electronic conductivity, with inorganic metal complexes that act as structural and/or magnetic components.

The first is a family of organometallic–inorganic magnetic compounds of formula [metallocenium]$[M^{II}M^{III}(ox)_3]$,[222–224] formed by 2D bimetallic oxalato-bridged honeycomb net $[Mn^{II}M^{III}(ox)_3]^-$ (M^{II} = Mn, Fe, Co, Cr, Ni, Cu; M^{III} = Cr, Fe) and a metallocenium cation (decamethylferrocenium $[DMFe]^+$, decamethylcobaltocenium $[DMCo]^+$, and decamethylmanganocenium $[DMMn]^+$) (see Figure 47),[223] where $[DMFe]^+$ is paramagnetic while $[DMCo]^+$ is nonmagnetic. Heat-capacity measurements[224] revealed the ferromagnetic phase transitions for the complexes $[DMFe][Mn^{II}Cr^{III}(ox)_3]$ (M^{II} = Mn, Fe, Co, Cu). Interestingly, as far as the magnetic ordering is concerned, the paramagnetic $[DMFe]^+$ cations are not directly involved in the long-range magnetic ordering. As summarized in Table 5,[222,225] the Curié temperatures T_C for all of the hybrid compounds are roughly the same as those observed in the NBu_4^+ derivatives.[182]

The second family is characterized by the coexistence of ferromagnetism and conductivity in molecule-based layered compounds. The presence of two cooperative properties in the same crystal lattice might result in new physical phenomena and novel applications. Coronado et al.[222,225] synthesized a hybrid organic–inorganic compound $(BEDT\text{-}TTF)_3[Mn^{II}Cr^{III}(ox)_3]$ consisting of organic π-electron donor cation bis(ethylenedithio)tetrathiafulvalene (BEDT-TTF) and the bimetallic oxalato complex anion $[Mn^{II}Cr^{III}(ox)_3]^-$. This layered compound displays both ferromagnetism and metallic conductivity. As shown in Figure 48,[225] the structure consists of organic layers of BEDT-TTF cations alternating with honeycomb layers of the bimetallic oxalate complex $[Mn^{II}Cr^{III}(ox)_3]^-$. The BEDT-TTF cations are tilted with respect to the inorganic layer by an angle of 45°. The magnetic properties of this compound show that it is a ferromagnet below a Curié temperature of $T_C = 5.5$ K. The magnetic features are identical to those already reported for [metallocenium]$[M^{II}M^{III}(ox)_3]$[223,224] and $NBu_4[M^{II}M^{III}(ox)_3]$.[182] This fact implies that the magnetic ordering in these 2D phases occurs within the bimetallic layers. This compound exhibits a metallic behavior over the whole temperature region of 2–300 K studied. Although the thermal properties seem to be of interest, there are no reports on heat-capacity measurements.

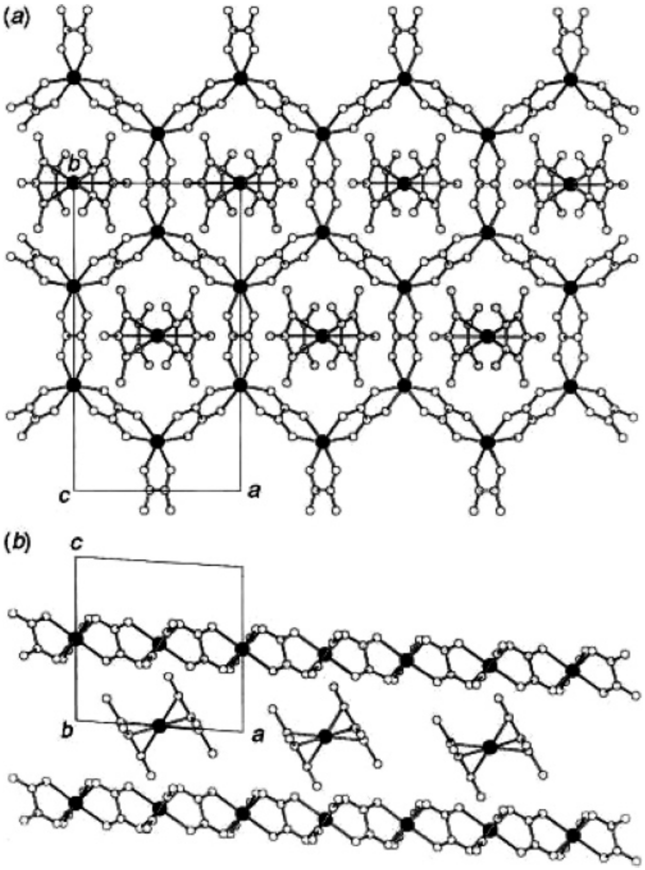

Figure 47. View of the structure of [decamethylmetallocenium]-$[M^{II}M^{III}(ox)_3]$ in the *ab* plane showing the honeycomb magnetic layers (a) and in the *ac* plane (b). Reprinted with permission from ref 223. Copyright 1997 The Royal Society of Chemistry.

Table 5. Curié Temperatures of the $A^+[M^{II}M^{III}(ox)_3]^-$ Complexes[222,225]

	T_C (K)				
M^{II}, M^{III}	$A^+ =$ $[DMFe]^+$	$A^+ =$ $[DMCo]^+$	$A^+ =$ $[DMMn]^+$	$A^+ =$ NBu_4^+	$A^+ =$ $(BEDT\text{-}TTF)_3^+$
Mn, Cr	5.3	5.1	5.3	6	5.5
Fe, Cr	13.0	12.7	13.0	12	
Co, Cr	9.0	8.2	9.3	10	
Cu, Cr	7.0	6.7	7.0	7	
Mn, Fe	28.4	25.4	27.8	28	
Fe, Fe	43.3	44.0	45.0	45	

5. Three-Dimensional Magnets

5.1. Cyanide-Bridged Bimetallic Complexes: Prussian Blue Analogues

Bimetallic transition metal hexacyanides form 3D network structures similar to the Prussian blue.[226,227] A very high T_c = 315 K was found for $V[Cr(CN)_6]_{0.86}\cdot 2.8H_2O$.[228]

Ohkoshi et al.[229,230] found an interesting temperature-induced phase transition due to the metal-to-metal charge-transfer mechanism in rubidium manganese hexacyanoferrate, $RbMn[Fe(CN)_6]$, with a large thermal hysteresis. The product of magnetic susceptibility and temperature ($\chi_m \cdot T$)

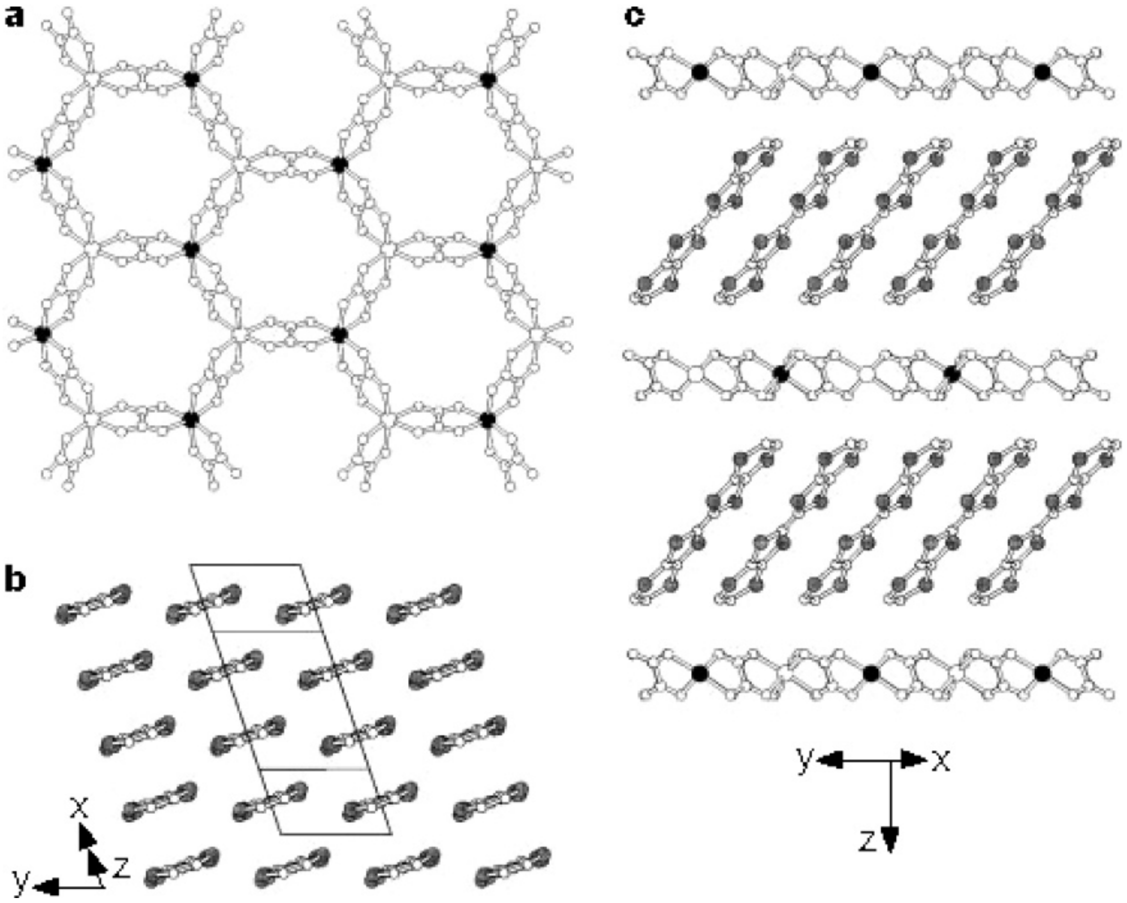

Figure 48. Structures of the hybrid material (BEDT-TTF)$_3$[Mn^{II}Cr^{III}(ox)$_3$]. (a) View of the [Mn^{II}Cr^{III}(ox)$_3$]$^-$ bimetallic layers. Filled and open circles in the vertices of the hexagons represent the two types of metals. (b) Structure of the organic layer. (c) Representation of the hybrid structures along the *c*-axis, showing the alternating organic/inorganic layers. Reprinted with permission from Nature (http://www.nature.com), ref 225. Copyright 2000 Nature Publishing Group.

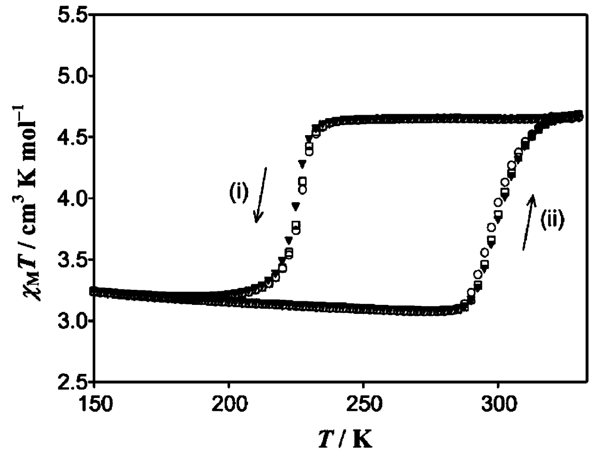

Figure 49. Observed $\chi_m \cdot T$ against T plot for RbMn^{II}[Fe^{III}(CN)$_6$] on cooling (i) and on heating (ii). First (○), second (□), and third (▼) measurements. Reprinted with permission from ref 230. Copyright 2004 American Chemical Society.

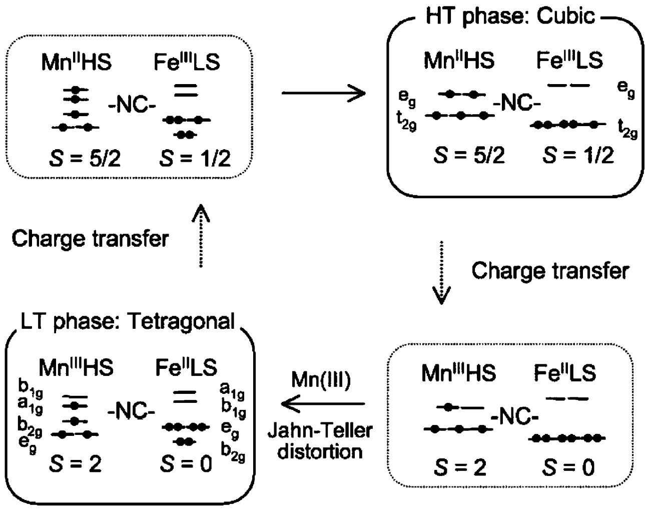

Figure 50. Relationship between the electronic states of Mn and Fe in the HT and LT phases and the charge transfer. Reprinted with permission from ref 230. Copyright 2004 American Chemical Society.

is decreased around 225 K on cooling and increased around 300 K on heating, a large thermal hysteresis of 75 K (see Figure 49). XRD revealed that the structure of the HT phase is a fcc system with a space group $F\bar{4}3m$ and that of the LT phase is a tetragonal system with $I\bar{4}m2$. X-ray photoelectron spectroscopy and IR spectroscopy indicated that the electronic and spin states in the HT and LT phases are assigned as Mn^{II}($t_{2g}^3e_g^2$, $^6A_{1g}$; $S = 5/2$)-NC-Fe^{III}(t_{2g}^5, $^2T_{2g}$; $S = 1/2$) and Mn^{III}($e_g^2b_{2g}^1a_{1g}^1$, $^5B_{1g}$; $S = 2$)-NC-Fe^{II}($b_{2g}^2e_g^4$, $^1A_{1g}$; $S = 0$), respectively. This phenomenon is caused by a metal-to-metal charge transfer between Mn and Fe ions and a Jahn−Teller distortion of Mn^{III} ion in the LT phase (see Figure 50). Molar heat capacity determined by use of a relaxation method[230] (Figure 51) showed a phase transition peak in the range of 290−300 K. The entropy gain at this phase transition was $\Delta S = \sim 6$ J K^{-1} mol^{-1}. Because the LT and

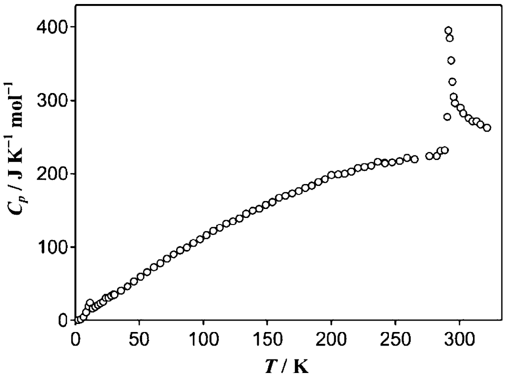

Figure 51. Molar heat capacity of $RbMn^{II}[Fe^{III}(CN)_6]$ and the phase transition due to charge-transfer mechanism. Reprinted with permission from ref 230. Copyright 2004 American Chemical Society.

HS phases consist of $[Mn^{III}(^5B_{1g})$ and $Fe^{II}(^1A_{1g})]$ and $[Mn^{II}(^6A_{1g})$ and $Fe^{III}(^2T_{2g})]$, respectively, the multiplicity arising from the spin-manifold and the electron orbital degeneracy is 5 ($= 5 \times 1 \times 1 \times 1$) and 36 ($= 6 \times 1 \times 2 \times 3$), respectively. Consequently, the expected entropy change would be $\Delta S = R \ln(36/5) = 16.4$ J K^{-1} mol^{-1}. This value is much larger than the experimental one. The extended X-ray absorption fine structure data of the HT phase shows a small distortion in the octahedral coordinates of the metal ions. Because $^2T_{2g}$ of Fe^{III} is reduced to $^2B_{2g}$ under this situation, the entropy gain is reduced to $\Delta S = R \ln(12/5) = 7.3$ J K^{-1} mol^{-1}. If the ambiguity involved in the estimate of the normal heat capacity is taken into account, this theoretical value is close to the experimental value of ~6 J K^{-1} mol^{-1}. The saturated value of $\chi_m \cdot T$ at the HT phase supports the absence of the orbital degeneracy and thus no contribution of the orbital to the entropy.

Tokoro et al.[230] suggested a possible mechanism of the phase transition as follows: Prussian blue analogues belong to the class II mixed-valence compounds,[231] which have the potential to exhibit a charge-transfer phase transition and are represented by two parabolic adiabatic potential-energy surfaces due to valence isomers in the nuclear coordinate of the vibronic coupling model.[232] When these two vibronic states interact, the ground-state surface has two minima. In the present crystal, the $Mn^{III}-NC-Fe^{II}$ vibronic state becomes a ground state in the LT phase and Mn^{III} ions show an elongation type Jahn−Teller distortion. When the temperature is increased, the Jahn−Teller distortion is diminished and the $Mn^{II}-NC-Fe^{III}$ vibronic state becomes a ground state in the HT phase via a phase transition.

Because the electronic state in the LT phase is $[Mn^{III}(^5B_{1g})$ and $Fe^{II}(^1A_{1g})]$, there still remains a spin multiplicity of five. Tokoro et al.[233] measured its heat capacity at low temperatures and found a phase transition at $T_{trs} = 11.0$ K arising from the spin ordering (Figure 52). The entropy of phase transition was estimated as (11.8 ± 0.9) J K^{-1} mol^{-1}. This value is close to $R \ln(2S + 1) = 13.4$ J K^{-1} mol^{-1}, the value expected for the ordering of magnetic spins on the Mn^{III} ($S = 2$) sites for $Rb^IMn^{III}[Fe^{II}(CN)_6]$. On the basis of the spin-wave analysis and the comparison of the entropies gained below and above T_{trs},[16] the ordered magnetic state was determined to be a 3D Heisenberg type ferromagnetic lattice of Mn^{III} sites. Because the diamagnetic LS Fe^{II} sites are connected with the paramagnetic Mn^{III} sites, simple application of the superexchange mechanism to the present ferromagnetic ordering is difficult. As a plausible mechanism, the authors[233] assumed the valence delocalization mechanism, in which ferromagnetic coupling arises from the charge-transfer configuration.[234] With respect to the conclusion of isotropic 3D long-range order, the authors noted that the absence of anisotropic behavior in the magnetic heat capacity was unexpected for tetragonally distorted Mn(III) ions.

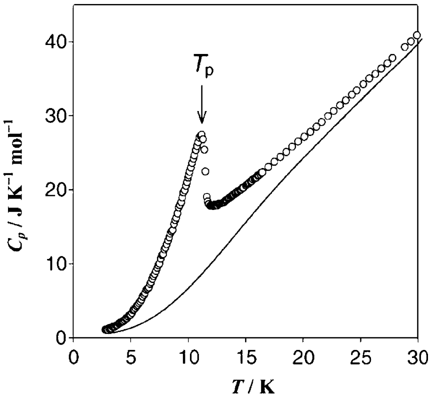

Figure 52. Molar heat capacity of $RbMn^{II}[Fe^{III}(CN)_6]$ below 30 K and the magnetic phase transition. The solid curve corresponds to the lattice heat capacity. Reprinted with permission from ref 233. Copyright 2004 Elsevier Ltd.

Materials showing a large thermal hysteresis loop are useful for applications such as memory device. Ohkoshi et al.[235] succeeded in expanding the thermal hysteresis of 75 K for $RbMn^{II}[Fe^{III}(CN)_6]$ by tuning the chemical composition. They found unusually large thermal hysteresis for the phase transitions in a series of compounds $Rb_xMn^{II}[Fe^{III}(CN)_6]_{(x+2)/3} \cdot zH_2O$, where $x = 0.94$ and $z = 0.3$ for (**1**); $x = 0.85$ and $z = 0.8$ for (**2**); and $x = 0.73$ and $z = 1.4$ for (**3**). As x is decreased, the transition temperatures detected both on heating and on cooling are lowered and the hysteresis loop width is increased as $\Delta T = 86$, 94, and 116 K for **1**, **2**, and **3**, respectively.

The heat-capacity measurement has also been reported for $[Mn_2(H_2O)_5Mo(CN)_7] \cdot 4H_2O$ by Larionova et al.[236] This is a 3D cyanide-bridged bimetallic complex consisting of ladders made of edge-sharing lozenge motifs ($Mo-C\equiv N-Mn-N\equiv C)_2$ running along the a-direction. These ladders are linked further along the b- and c-directions. Thus, the structure of this complex is totally different from that of the Prussian blue analogues characterized by fcc. A λ-type heat-capacity peak was observed at $T_C = 50.5$ K, corresponding to the transition between the ferromagnetic and the PSs. Magnetic susceptibility measurements revealed the presence of two ferromagnetically ordered states, and a transition between these two states occurred at 43 K. However, as the entropy change is very weak, no heat-capacity anomaly is detected around this temperature.

5.2. Dicyanamide-Bridged Bimetallic Complexes

Miller and his collaborators[237] have investigated the coordination chemistry of dicyanamide, $N(CN)_2^-$. As shown in Figure 53, this bifurcated molecule has the potential of being polydentate. $N(CN)_2^-$ can act as a terminal ligand (**1a**) or as a μ_2-ligand (**1b**,**c**), μ_3-ligand (**1d**), or μ_4-ligand (**1e**). The reaction of $[M^{II}(H_2O)_6](NO_3)_2$ (M = Mn, Fe, Co, Ni, Cu) and $N(CN)_2^-$ leads to formation of isostructural $[M\{N(CN)_2\}_2]$. Crystal structures are orthorhombic with a space group *Pnnm*.[237−240] The $N(CN)_2^-$ anion is triply coordinated through its three nitrogen atoms (**1d**). It bridges the metal ions to form infinite 3D metal-organic frameworks

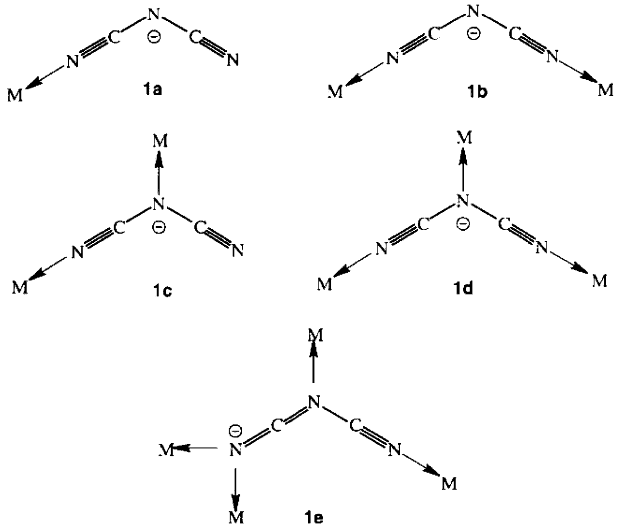

Figure 53. Bifurcated ligand molecule dicyanamide $N(CN)_2^-$. (**1a**) Terminal ligand, (**1b**) μ_2-ligand, (**1c**) μ_2-ligand, (**1d**) μ_3-ligand, and (**1e**) μ_4-ligand. Reprinted with permission from ref 237. Copyright 1998 American Chemical Society.

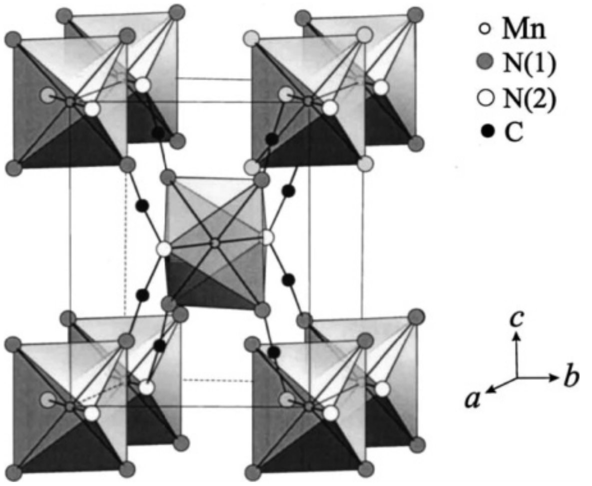

Figure 54. Crystallographic unit cell in the paramagnetic regime as well as in the ordered state for $[Mn\{N(CN)_2\}_2]$. The structure consists of discrete MnN_6 octahedra, which are axially elongated and successively tilted in the *ab* plane. Reprinted Figure 2 with permission from Kmety, C. R.; Huang, Q. Z.; Lynn, J. W.; Erwin, R. W.; Manson, J. L.; McCall, S.; Crow, J. E.; Stevenson, K. L.; Miller, J. S.; Epstein, A. J. *Phys. Rev. B 62*, 5576, 2000 (http://link.aps.org/abstract/PRB/v62/p5576). Copyright 2000 by the American Physical Society.

with a rutile type structure. The framework contains doubly bridged $\cdots M-(N{\equiv}C-N-C{\equiv}N)_2-M\cdots$ ribbons that link approximately orthogonally through the amide nitrogen atoms. As a representative one, the crystallographic unit cell in the paramagnetic state as well as in the ordered state for $[Mn\{N(CN)_2\}_2]$ is given in Figure 54.[240] The structure consists of discrete MnN_6 octahedra, which are axially elongated and successively tilted in the *ab* plane.

Two crystal polymorphs are known for $[Co^{II}\{N(CN)_2\}_2]$:[237] One is a pink crystal designated as α-$[Co\{N(CN)_2\}_2]$ in which Co^{2+} ion is octahedrally coordinated by six N atoms while the other is blue β-$[Co\{N(CN)_2\}_2]$ in which Co^{2+} ion is tetrahedrally coordinated by four N atoms.

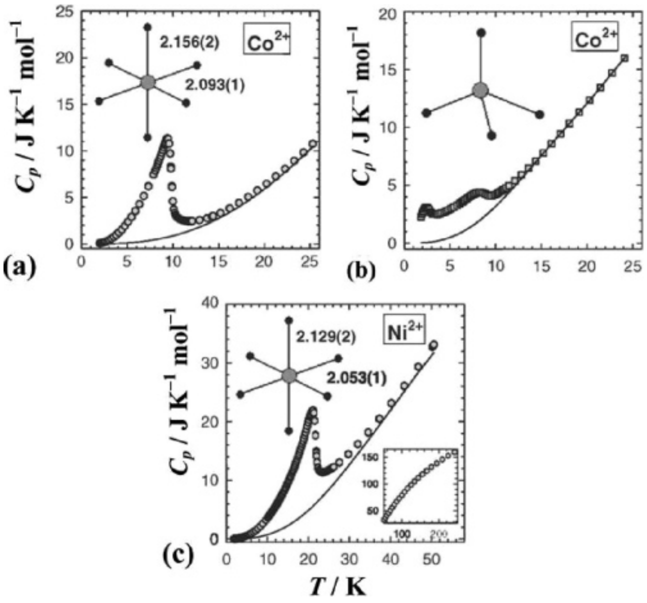

Figure 55. Molar heat capacities of (a) α-$[Co\{N(CN)_2\}_2]$, (b) β-$[Co\{N(CN)_2\}_2]$, and (c) $[Ni\{N(CN)_2\}_2]$. The solid curves represent the estimated lattice heat capacities. Reprinted with permission from ref 241. Copyright 2002 Elsevier Ltd.

Heat capacities of $[M\{N(CN)_2\}_2]$ have been measured for the complexes with M = Fe, α-Co, and Ni by Kurmoo and Kepert[238] and for those with M = α-Co, β-Co, Ni, Cu, and Zn by Kmety et al.[241] Figure 55 represents the molar heat capacities of α-$[Co\{N(CN)_2\}_2]$, β-$[Co\{N(CN)_2\}_2]$, and $[Ni\{N(CN)_2\}_2]$.[241] The essential features of the data are peaks followed by rather large heat-capacity tails at the HT side of the peak. The α-$[Co\{N(CN)_2\}_2]$ and $[Ni\{N(CN)_2\}_2]$ give rise to λ-type peaks at $T_C = 9.37$ and 21.1 K, respectively. These anomalies are associated with the onset of long-range ferromagnetic order. The entropy gains due to these phase transitions were $0.91R \ln 2$ and $R \ln 3$, respectively. This fact implies that the magnetic ordering originates from a ground-state doublet ($J = 1/2$) in the form of $R \ln(2J + 1)$ for the Co^{2+} ion in α-$[Co\{N(CN)_2\}_2]$ and a ground-state triplet ($J = 1$) for the Ni^{2+} system. On the other hand, β-$[Co\{N(CN)_2\}_2]$ showed a small peak at 2.45 K and a broader one at 8.35 K. These anomalies are assigned to a canted antiferromagnetic ordering at 8.35 K and then spin reorientation to a different canted antiferromagnetic state. Because the entropy gain ($0.89R \ln 2$) is close to $R \ln 2$, the ground state of the tetrahedral cobalt complex is also doublet. Because the Co^{2+} ion has a $3d^7$ electronic configuration, it gives rise to a ^4F ground state. In an octahedral crystal field, the orbital ground state is $^4T_{1g}$ followed by $^4T_{2g}$ (first excited state) and $^4A_{1g}$ (second excited state). On the basis of the crystal structure at 1.6 K, the Co^{2+} ion resides at the core of an axially distorted octahedron. In the presence of the axial crystal field, the $^4T_{1g}$ level is split further into $^4A_{2g}$ followed by ^4E_g. Through the combined effect of the axially distorted crystal field and spin−orbit coupling, the spin quartet of the $^4A_{2g}$ level is split into two Kramers doublets ($|\pm 1/2\rangle$ and $|\pm 3/2\rangle$). The value of $\Delta S = R \ln 2$ indicates that the separation between the two doublets is large as compared with T_C. As a result, at low temperature, only the lowest doublet is thermally populated and the system behaves as an effective $J = 1/2$ system. For a Co^{2+} ion in a tetrahedral crystal field encountered in β-$[Co\{N(CN)_2\}_2]$, the orbital ground state is $^4A_2$ followed by $^4T_2$ (first excited state) and $^4T_1$ (second excited state). As in the case of α-$[Co\{N(CN)_2\}_2]$, the spin quartet of $^4A_2$ is split into two Kramers

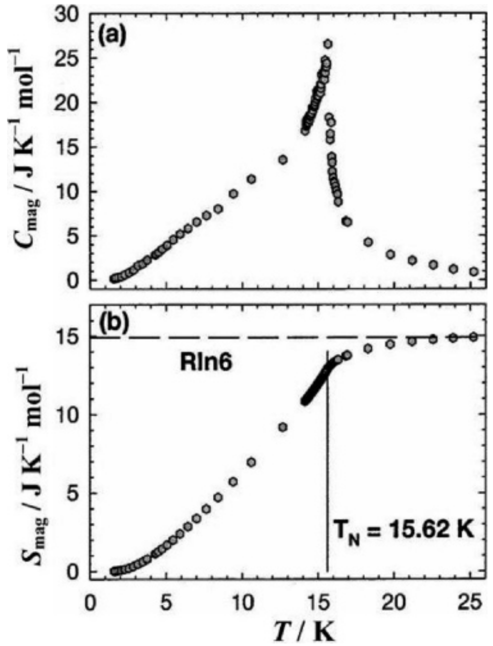

Figure 56. Magnetic heat capacity (a) and magnetic entropy gain (b) of [Mn$\{N(CN)_2\}_2$] as a function of temperature. Reprinted Figure 8 with permission from Kmety, C. R.; Huang, Q. Z.; Lynn, J. W.; Erwin, R. W.; Manson, J. L.; McCall, S.; Crow, J. E.; Stevenson, K. L.; Miller, J. S.; Epstein, A. J. *Phys. Rev. B 62*, 5576, 2000 (http://link.aps.org/abstract/PRB/v62/p5576). Copyright 2000 by the American Physical Society.

doublets and the system behaves as an effective $J = 1/2$ system.

[Cu$\{N(CN)_2\}_2$] is paramagnetic even at 1.7 K, the lowest temperature attainable by the calorimeter.[241] The LT upturn observed in the heat capacity against temperature plot suggests that [Cu$\{N(CN)_2\}_2$] ($J = 1/2$) undergoes a phase transition to an ordered state at a temperature below 1.7 K. The application of a large magnetic field of 8 T dramatically shifted the ordering heat-capacity peak from below 1.7 K to about 7.4 K. Judging from the direction of the peak shift, the ordered state has been concluded as being ferromagnetic state.

Heat-capacity measurements of [Mn$^{II}\{N(CN)_2\}_2$] have been reported by Batten et al.[239] and by Kmety et al.[240] Figure 56 shows the magnetic heat capacity and the entropy gain.[240] A λ-type anomaly is observed at $T_N = 15.62$ K, and the entropy gain due to this phase transition amounted to R ln 6, the value expected from the spin multiplicity of the HS manganese in an octahedral crystal field. Magnetization measurements[239] of [Mn$^{II}\{N(CN)_2\}_2$] confirmed that this phase transition originates in a magnetic long-range ordering into a spin-canted antiferromagnetic state (weak ferromagnet). In addition to the λ-type peak, a weak shoulder appeared around 7 K. This anomaly was connected to the observed anomalous behavior of the crystal structure below 10 K, at which a sign reversal of the thermal expansion occurs. The fractional changes in length between 10 and 300 K and those between 4.6 and 10 K are $\Delta a/a = +0.71$ and -0.05%, $\Delta b/b = +0.79$ and $+0.04\%$, and $\Delta c/c = -0.38$ and $+0.02\%$.[240]

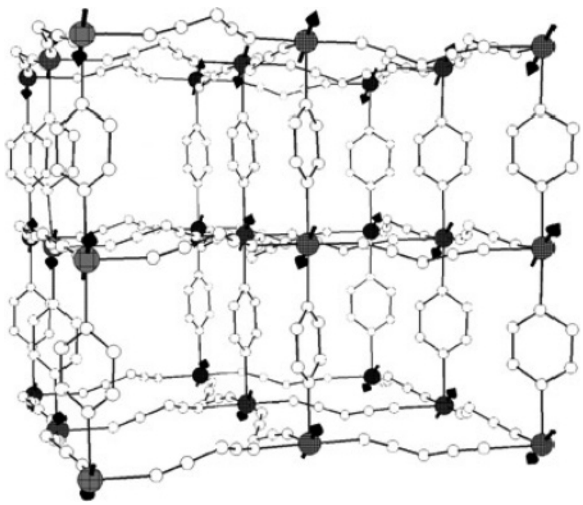

Figure 57. Zero-field magnetic structure of [Mn$\{N(CN)_2\}]_2$·(pyz) at 1.5 K. Arrows denote the spin configuration of the ordered Mn^{2+} moments aligned along the short *ac*-diagonal. Reprinted with permission from ref 242b. Copyright 2003 Elsevier Ltd.

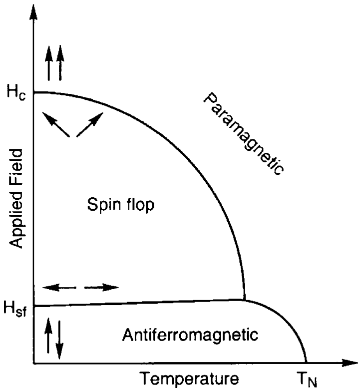

Figure 58. Schematic representation of the magnetic field vs temperature diagram for a weakly anisotropic antiferromagnet. Reprinted with permission from ref 242a. Copyright 2001 American Chemical Society.

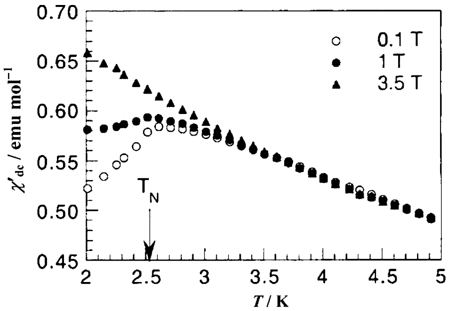

Figure 59. Variable-temperature magnetic susceptibility of [Mn$\{N(CN)_2\}]_2$·(pyz) at various external filed in the vicinity of T_N. Reprinted with permission from ref 242a. Copyright 2001 American Chemical Society.

Manson et al.[242] have studied the magnetic properties of [Mn$\{N(CN)_2\}]_2$·(pyz), where pyz = pyrazine, in detail by using d.c. magnetization, a.c. susceptibility, heat capacity, and neutron diffraction. The material crystallizes in the monoclinic space group $P2_1/n$ with $Z = 4$ at 1.5 K (Figure 57).[242a] The heat capacity of this complex exhibited a 3D antiferromagnetic ordering below $T_N = 2.53$ K. Figure 58 presents a schematic illustration of a magnetic phase diagram for a weakly anisotropic antiferromagnet. At a specific temperature just below T_N, H_{sf} and H_c intersect at the tricritical point, which indicates the coexistence of the antiferromagnetic, spin-flop, and paramagnetic phases. As shown in Figure 59, the spin-flop transition was detected by variable temperature d.c. magnetic susceptibility measurement under magnetic field. Figure 60 is the magnetic susceptibility measured at 2 K as a function of applied

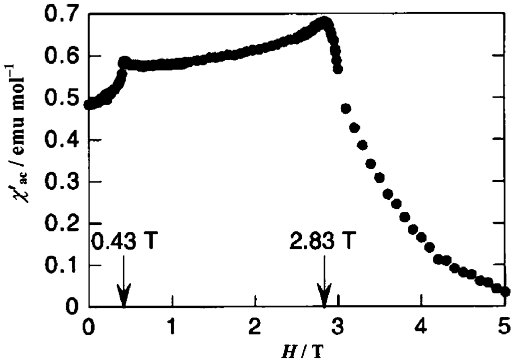

Figure 60. A.c. magnetic susceptibility of $[Mn\{N(CN)_2\}]_2{\cdot}(pyz)$ as a function of external magnetic field obtained at 2 K. Reprinted with permission from ref 242a. Copyright 2001 American Chemical Society.

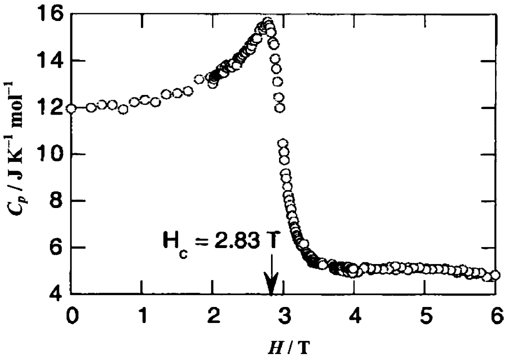

Figure 61. Field-dependent heat capacity of $[Mn\{N(CN)_2\}]_2{\cdot}(pyz)$ obtained at 2 K. Reprinted with permission from ref 242a. Copyright 2001 American Chemical Society.

magnetic field. The spin-flop and the critical fields were determined as $H_{sf} = 0.43$ T and $H_c = 2.83$ T, respectively. To confirm the type of field-induced magnetic phase transition found in the magnetic measurements, Manson et al.[242a] performed isothermal heat-capacity measurements at 2 K (Figure 61). The $C_p(H)$ data yielded a single anomaly at 2.83 T, which is attributed to the spin-flop to paramagnetic phase transition. Although the spin-flop transition is first-order, it was difficult to detect using this technique.

5.3. Dicyanoargentate-Bridged Complexes

Černák et al.[243] reported the crystal structure and magnetic properties of dicyanoargentate-bridged complex $[Cu(en)_2Ag_2(CN)_4]$ (en = ethylenediamine or 1,2-diaminoethane). This compound crystallizes in the orthorhombic space group *Pnnm*. The structure is formed of free linear $[Ag(CN)_2]^-$ anions and infinite cationic chains $[-Cu(en)_2-NC-Ag-CN-]^+$ containing paramagnetic copper atoms bridged by a second kind of linear dicyanoargentate species. The coordination geometry of the copper atoms corresponds to an elongated tetragonal bipyramid with two chelating (en) molecules in the equatorial positions and N-bonded bridging cyano groups in the axial positions.

The heat-capacity measurements in the 40 mK to 2 K temperature range detected only the HT part of a λ-like anomaly associated with the onset of a long-range order because the lowest available temperature of 40 mK is still too high for detailed study of magnetic correlations. However, the heat-capacity study revealed that despite the chain structure this compound may represent an $S = 1/2$ 3D magnetic system characterized by a low value of the exchange coupling constant, J/k much less than 60 mK.

Heat capacities of similar compounds $[Cu(bpy)_2Ag_2(CN)_4]{\cdot}H_2O$ (bpy = 2,2′-bipyridine)[244] and $[Cu(en)Ni(CN)_4]$[245,246] measured in the temperature range from 80 mK to 8 K revealed significant deviations from the assumed 1D magnetic behavior. The behavior of short-range correlations was described by an $S = 1/2$ quadratic Heisenberg antiferromagnetic model with the exchange constant $J/k = -60$ and -180 mK, respectively. Intrachain covalent bonds are completed by bifurcated hydrogen bonds of the N···H···N(C)···H···N type connecting adjacent chains and creating a 2D net of exchange paths. The origin of the λ-like anomaly in the heat capacity observed at (81 ± 2) mK for $[Cu(bpy)_2Ag_2(CN)_4]{\cdot}H_2O$ and at (128 ± 2) mK for $[Cu(en)Ni(CN)_4]$ were ascribed to a 2D−3D crossover in magnetic lattice dimensionality activated by the interlayer dipolar interaction.

6. Single-Molecule Magnets

Single-molecule magnets (SMMs) are a class of paramagnetic metal complex compounds, which show slow magnetization reversal at low temperatures as an isolated molecule property.[247,248] In this meaning, they belong to 0D spin systems, whose spin Hamiltonian should be exactly solved in principle even though it is too laborious of a task. Most of them are polynuclear complexes where paramagnetic transition metal ions are magnetically coupled through some bridging ligands to provide a large resultant spin on a molecule. There is a requirement for the SMM behavior that a large molecular magnetic anisotropy of easy-axis type should impose a restriction on the molecular spin so as to fix magnetic poles with respect to the molecular shape. Figure 62 depicts a set of energy levels for a giant spin, e.g., $S = 10$, affected by uniaxial zero-field splitting DS_z^2 ($D < 0$), which forms a parabolic profile of energy barrier prohibiting spin reversal. As a result, molecular magnetizations hardly overcome the anisotropy energy barrier at low temperatures and show a typical magnetic relaxation behavior with single relaxation time. This monodispersivity of relaxation is the unique point of SMMs distinguished from other nonequilibrium magnets such as spin glasses with temperature-dependent energy barriers or conventional superparamagnets with barrier-height distributions.

Another notable feature of SMMs is resonant tunneling of molecular magnetization characteristic of mesoscopic magnets. When a longitudinal or transverse magnetic field

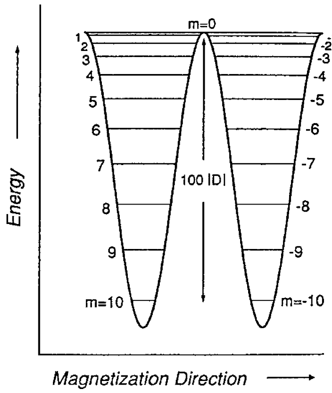

Figure 62. Plot of potential energy vs magnetization direction for a single Mn12 molecule in zero-applied magnetic field with a $S = 10$ ground state. There is an axial zero-field splitting, characterized by $H = DS_z^2$, where $D < 0$.

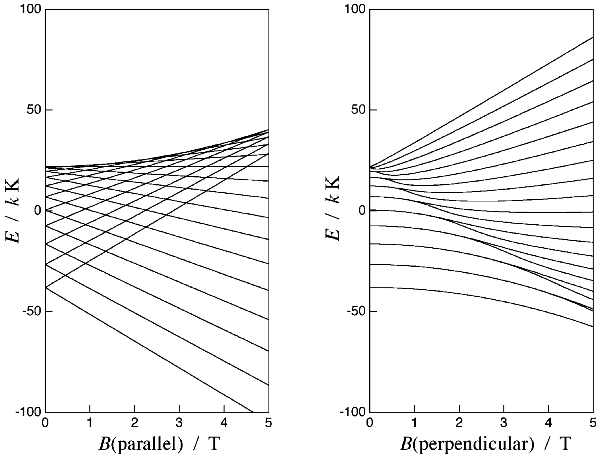

Figure 63. Longitudinal and transverse Zeeman splitting for spin-energy levels of molecular spin $S = 10$ affected by uniaxial zero-field splitting DS_z^2 ($D < 0$). B stands for magnetic flux density.

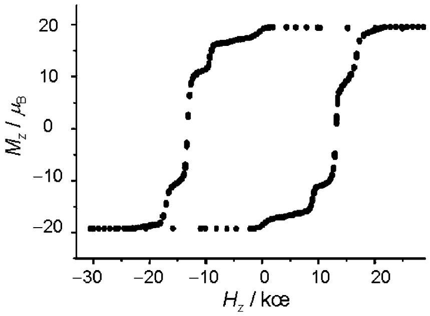

Figure 64. Magnetization hysteresis loop of $[Mn_{12}O_{12}(OAc)_{16}(H_2O)_4]$. Resonant tunneling extremely promotes the reversal of molecular magnetizations, resulting in the stepped loop structure. Reprinted with permission from ref 248. Copyright 2003 Wiley-VCH.

is applied on a uniaxial molecular spin whose level scheme is provided by Figure 62, the Zeeman effect lifts the 2-fold degeneracy of up-spin and down-spin states as shown in Figure 63. In the case of longitudinal field, the spin levels make crossings each other at even intervals of field. The level crossing greatly enhances magnetization reversal via quantum tunneling through the anisotropy barrier, satisfying energy conservation. This tunneling process is called resonance tunneling, and the crossing fields are thus referred to as resonance fields B_{reson}. As a result, a mesoscopic permanent magnet, SMM, has a strange-shaped hysteresis loop with multiple step structures at each B_{reson} (Figure 64).[248] It is essentially a single-molecule property and should be discriminated from well-known cross relaxations in a weakly coupled spin pair.

Calorimetry can provide important information characterizing SMMs, e.g., the blocking temperature (T_B), level-crossing fields (B_{reson}) where quantum tunneling of magnetization occurs, and the magnitude of hyperfine interactions between electron and nuclear spins, which are supposed to be a dominant factor of magnetic relaxation in SMMs. As stated in the chapter 1, heat-capacity calorimetry has an aspect of spectroscopy resolving energy level structures, due to the fact that the heat capacity is related with the canonical partition function, which is exactly a Laplace transform of the density of states. Heat capacity contributed from a finite number of discrete energy levels is known as a Schottky anomaly, rising as $\exp(-\Delta E/kT)/T^2$ and decaying as T^{-2}. In contrast, a continuous density of states, characteristic of elementary excitations such as phonons and magnons, contributes T^n terms according to the dispersion relation and the spatial (lattice) dimension.

Blocking temperature T_B is a kind of glass transition temperature, where the characteristic time for activated reversal of molecular magnetization overtakes the observation time scale (typically ~100 s) and the molecule behaves as a molecular-sized permanent magnet below this temperature. Because the spin-up and spin-down states of a molecule are energetically degenerate without any intermolecular interactions, calorimetric detections of T_B are usually conducted under a magnetic field giving a Zeeman splitting in the spin doublet. On lowering temperatures, an HT tail $\sim T^{-2}$ of the Schottky anomaly corresponding to the thermal excitation between the ground doublet $S_z = +S$ and $-S$ is observed, which is quenched below T_B where the spin states become nonergodic. Thus, a step indicating a glass transition occurs in the heat-capacity curve at T_B. It is noted that such a crossover from ergodic to nonergodic situation in calorimetry can be interpreted as a switching in the *selection rule* for thermal excitation from allowed to forbidden, similar to other spectroscopic methods using photoexcitation. Below T_B, nuclear spins contained in an SMM molecule feel a rather stationary hyperfine field and the nuclear spin-energy levels contribute another Schottky heat capacity.

When the intermolecular interactions are not negligible, SMMs start deviating from the isolated molecule behavior and heat-capacity anomalies accompanying the growth of short-range order are observed at low temperatures. In such cases, there is a competition between the kinetic freezing of magnetization reversal and the spin correlation leading to a magnetic long-range order. If the supposed phase transition temperature T_c is much lower than T_B, the SMM behavior should be sustained despite the intermolecular interactions. On the other hand, the long-range order is established at the lowest temperatures and the magnetic entropy of R ln 2, corresponding to an SMM-like Ising spin, should be detected by calorimetry, when the T_c is higher than the T_B estimated by extrapolation of the Arrhenius plot. There is an interesting discussion whether the long-range order is achieved below T_B via quantum tunneling processes, and this question will be revisited later.

6.1. Dodecanuclear Manganese Clusters (Mn12)

The dodecanuclear mixed-valence manganese cluster $[Mn_{12}O_{12}(OAc)_{16}(H_2O)_4]$ (hereafter, Mn12) consisting of four Mn(IV) and eight Mn(III) ions (see Figure 65)[249] has a large resultant spin of $S = 10$ and is known as the first discovered SMM with a high activation barrier of magnetization reversal $U_{eff}/k \sim 60$ K. Chemical modifications, e.g., substitution of acetate ligands with other carboxylates and one- or two-electron reduction of the $Mn_{12}O_{12}$ core, afforded many derivatives also behaving as SMMs. The large magnetic anisotropy of the molecule is attributed to the nearly parallel arrangement of easy axes of eight Jahn−Teller distorted Mn(III) ions. Because of a partial fluxionality of Mn12 molecules, there are some “Jahn−Teller isomers” with one of eight Jahn−Teller elongation axes tending to a wrong direction out of the molecular axis.[250] In some Mn12 derivatives, Jahn−Teller isomers are unable to be purified chemically and only a mixture sample is available.

The temperature dependence of heat capacity of several Mn12 compounds was reported for polycrystalline samples[251−255] and for single crystals.[256−260] In several works,

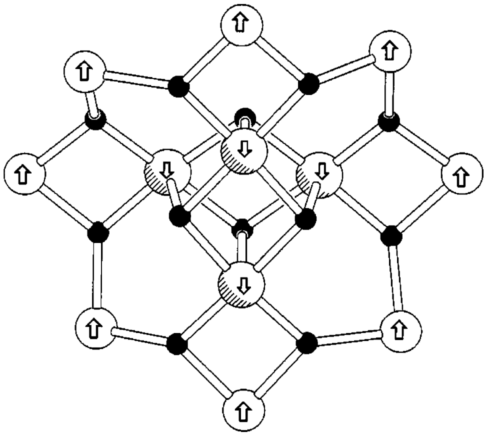

Figure 65. Skeletal structure of $Mn_{12}O_{12}$ core. Four ferromagnetically coupled Mn(IV) ions carrying $S = 3/2$ are surrounded by eight peripheral Mn(III) ions carrying $S = 2$. Reprinted Figure 1 with permission from Barra, A. L.; Gatteschi, D.; Sessoli, R. *Phys. Rev. B 56*, 8192, 1997 (http://link.aps.org/abstract/PRB/v56/p8192). Copyright 1997 by the American Physical Society.

clear heat-capacity drops at T_B were observed by application of magnetic field.[251,252,255] Because the dipolar fields exerted from neighboring molecules are also effective to remove the degeneracy of the ground doublet, the heat capacity under zero external field was closely examined to obtain the information on the freezing process.[254] The results showed lowering of the T_B and the blocking process over a certain temperature range. Those were not consistent with the other works performed under finite field, revealing sharp blockings. The effect of transverse magnetic field, which promotes tunneling processes in magnetization reversal, was also examined.[258−260] Obvious depression of T_B was observed owing to phonon-assisted incoherent quantum tunneling (Orbach process) at relatively lower magnetic fields, while at higher applied fields the spin−lattice relaxation is dominated by coherent tunneling and the blocking phenomena are completely lost.

Because the nuclide ^{55}Mn with nuclear spin $I = 5/2$ has the natural abundance of 100%, a Schottky anomaly arising from the hyperfine splitting of ^{55}Mn nuclear spin levels has a certain contribution below 0.5 K.[252,254,255,258−260] Although the hyperfine interaction constants from calorimetric studies were almost consistent with internal field provided by other methods including ^{55}Mn NMR and DFT (density functional theory) calculation,[254,255] it was pointed out that the magnetic field dependence of the nuclear heat capacity requires taking into account the slow nuclear spin−lattice relaxation.[260]

The total heat capacity of Mn12 is well-reproduced by accumulating the contributions stated above. For example, the total heat capacity of $[Mn_{12}O_{12}(O_2CEt)_{16}(H_2O)_3]$ was analyzed as a sum of four contributions, C_{lat}, $C_{spin}(D_1)$, $C_{spin}(D_2)$, and C_{hf}, shown in Figure 66.[255] C_{lat} is the heat capacity of the phonon system and is well-approximated by the Debye function with Debye temperature $\Theta_D = 30$ K. C_{spin} is a multilevel Schottky heat capacity due to electron spin under uniaxial zero-field splitting (D); however, it is required to adopt two components corresponding to Jahn−Teller isomers. The last term C_{hf} is the contribution from hyperfine interactions of ^{55}Mn nuclei and is well-approximated by the first term of HT expansion,

$$C_{hf} \approx \frac{nN_A k}{3} I(I+1)\left(\frac{h\nu_n}{kT}\right)^2 \qquad (5)$$

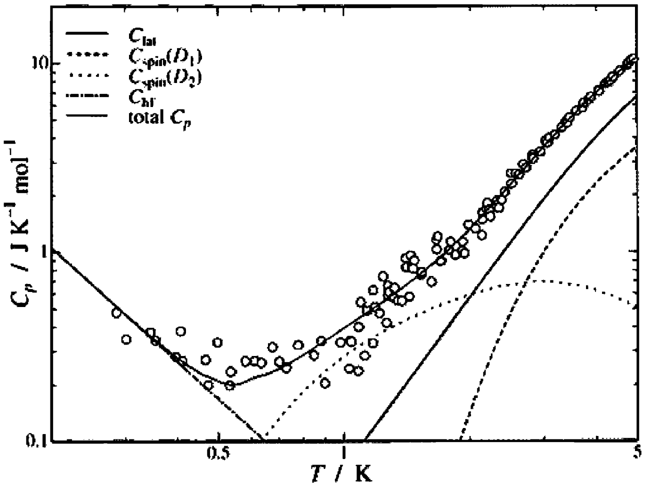

Figure 66. Temperature dependence of heat capacity of $[Mn_{12}O_{12}(O_2CEt)_{16}(H_2O)_3]$. C_{lat}, C_{spin}, C_{hf}, and total C_p indicate the Debye heat capacity, the multilevel Schottky heat capacities from two Jahn−Teller isomers, the contribution from the hyperfine interaction, and the net heat capacity, respectively. Reprinted with permission from ref 255. Copyright 2001 American Chemical Society.

where n is the total number of nuclei having the nuclear spin quantum number I, N_A is the Avogadro constant, h is the Planck constant, and ν_n is the resonance frequencies in ^{55}Mn NMR.

A.c. calorimetry utilizing heater power modulation with frequency ω is especially advantageous in research of time-dependent phenomena. Time-dependent heat capacities $C(\omega)$ of Mn12 were reported with respect to the effect of longitudinal magnetic field.[257,261−263] If the spin−lattice relaxation time τ is short enough to achieve thermal equilibrium ($\omega\tau \ll 1$), spin levels at both sides of the energy barrier can participate in population exchange and contribute to the Schottky heat capacity due to Zeeman splitting (*bilateral* heat capacity, C_{bil}, in Figure 67).[257] When the relaxation time exceeds the measurement time scale ($\omega\tau \gg 1$) by cooling, the population flow between the up-spin side and the down-spin side is kinetically forbidden and a smaller heat capacity (*unilateral* heat capacity, C_{uni}) is observed. The remarkable peaks observed at B_{reson} in Figure 67 arise from phonon-assisted incoherent tunneling processes, breaking the kinetic *selection rule* of calorimetry. However, these peaks are suppressed below T_B.

6.2. Octanuclear Iron Clusters (Fe8)

The octanuclear Fe(III) cluster $[(tacn)_6Fe_8O_2(OH)_{12}](Br)_8$ (hereafter, Fe8) is another SMM with a spin ground state of $S = 10$, thoroughly investigated next to the Mn12. A distinctive feature of the Fe8 is the rhombicity of its magnetic anisotropy, in clear contrast to the Mn12, which has complete tetragonal symmetry. Because of the deviation from axial symmetry, it is the first compound in which the quantum interference effect (Berry's phase) of magnetization tunneling was demonstrated.[248]

The temperature dependence of heat capacity of the Fe8 was also reported under zero external field[254] and under transverse magnetic fields.[258−260,264] The effect of longitudinal field was also investigated by a.c. calorimetry.[265] The results for Fe8 resemble ones for Mn12, except Fe8 has a lower anisotropy barrier and some rhombicity.

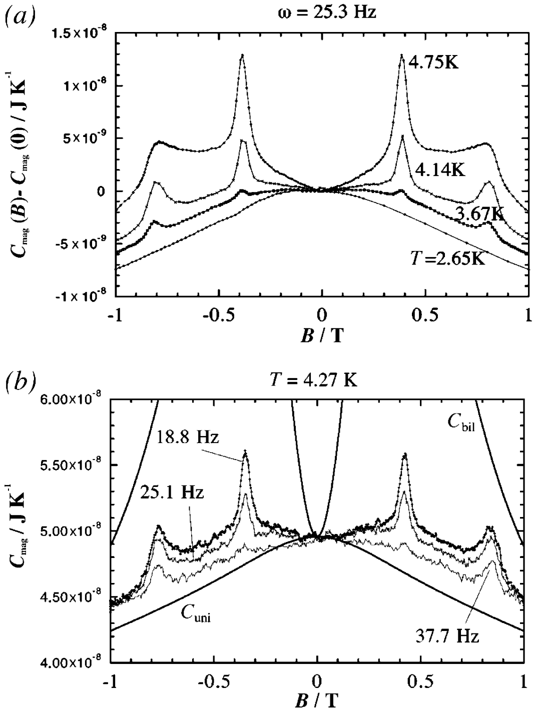

Figure 67. (a) Magnetic heat capacity of the Mn12 single crystal vs the applied magnetic field, measured at $\omega = 25$ Hz. The zero-field-calculated magnetic heat capacity $C_{mag}(0)$ is 56.0, 47.7, 40.2, and 21.3 nJ K^{-1} for, respectively, $T = 4.75$, 4.14, 3.67, and 2.65 K. (b) A.c. heat capacity $C(\omega)$ of an Mn12 single-crystal sample under magnetic field applied parallel to the molecular axis. Remarkable enhancement is recognized at the level-crossing fields B_{reson}, which disappears below the temperature where the relaxation time of spin reversal coincides with the time scale of measurement frequency ω. Reprinted Figures 3 and 6 with permission from Fominaya, F.; Villain, J.; Fournier, T.; Gandit, P.; Chaussy, J.; Fort, A.; Caneschi, A. *Phys. Rev. B 59*, 519, 1999 (http://link.aps.org/abstract/PRB/v59/p519). Copyright 1999 by the American Physical Society.

Quite peculiar heat-capacity anomalies were reported at around 2.6 K for an Fe8 single-crystal sample examined by a.c. calorimetry.[266] These anomalies were not affected by changing measurement frequency, and the peak temperature was found to be depressed under applied magnetic field up to 4.0 T, showing a close resemblance to a Néel temperature of antiferromagnetic long-range ordering. The origin is still not clear and waiting for further investigations.

6.3. Other Single-Molecule Magnets

Among other SMMs, some are known to have magnetic phase transitions yielding long-range order and calorimetric researches on them were carried out. λ-Shaped heat-capacity anomalies were reported at $T_c = 1.33$ K for $[Mn_4(hmp)_6Br_2(H_2O)_2]Br_2$,[267] $T_c = 1.19$ K for $[Fe_{19}(metheidi)_{10}(OH)_{14}(O)_6(H_2O)_{12}]NO_3{\cdot}24H_2O$,[268,269] and $T_c = 0.99$ K for $(enH_2)_2[Fe_6(\mu_3\text{-}O)_2(\mu_2\text{-}OH)_6(ida)_6]{\cdot}6H_2O{\cdot}2EtOH$.[269] The intermolecular interactions causing long-range orders in these compounds were supposed to be superexchange rather than magnetic dipolar interactions in origin, which are claimed to be dominant in the case of $[Mn_6O_4Br_4(Et_2dbm)_6]$ possessing $T_c = 0.161$ K.[264,270] Although the long-range order in $[Fe_4(OCH_3)_6(dpm)_6]$ was suggested,[271] no heat-capacity anomalies were found by calorimetry in the measurement temperature range ($T > 2$ K).[272]

Heat capacities of a series of manganese tetramers with $S = 9/2$, $[Mn_4O_3L(dbm)_3]$ (L = $Cl(OAc)_3$, $(OAc)_4$, and $(O_2CC_6H_4Me)_4$, abbreviated to Mn_4Cl, Mn_4Ac, and Mn_4Me, respectively), were investigated by thermal relaxation method.[264,273−275] The equilibration time (or instrumental relaxation time, in other words) dependence of heat capacities $C_p(\tau_e)$ revealed a remarkable difference among them. The Mn_4Cl having a relatively slow spin−lattice relaxation shows a large τ_e dependence below 1 K, i.e., a longer τ_e is required to achieve thermal equilibrium. On the other hand, the Mn_4Me having a fast electron spin−lattice relaxation shows equilibrium heat capacity with a λ-peak anomaly of magnetic long-range order at $T_c = 0.21$ K. Despite such a very low T_c, the dominant intermolecular interaction is not attributed to dipole−dipole but superexchange in origin, being $|J|/k \approx 0.14$ K.[275] It is inferred from these observations that in this temperature range thermal equilibration of the spin systems is promoted via incoherent magnetization tunneling in the lowest Kramers doublet. Thus, the answer to the question, whether the long-range order is achieved below T_B via quantum tunneling processes, is presumably yes, since the spin system under incoherent tunneling couples with phonon bath through nuclear spin-mediated (I^+S^- etc.) spin−lattice interaction.

6.4. Single-Chain Magnets (SCMs)

In 1963, Glauber[276] found a slowing-down of magnetic relaxation in the 1D Ising model at low temperatures by using Monte Carlo simulation. SCMs are 1D systems consisting of Ising spins, which exhibit blocking phenomena similar to SMMs, as predicted by Glauber, and lack any magnetic long-range orders. Typical examples are an alternating Co(II)-radical chain with highly anisotropic exchange interactions[277] and a concatenated-SMM chain possessing remarkable single molecule anisotropy.[278] Although no calorimetric results were published for those typical systems, heat capacities of another concatenated-SMM chain $[Mn_4(hmp)_6R_2](ClO_4)_2$ (R = OAc or Cl)[279] and a rare-earth transition-metal mixed chain $[Ln(bpy)(H_2O)_4M(CN)_4]$ (Ln = Gd^{III}, Y^{III}; M = Fe^{III}, Co^{III})[280] were reported. The former shows a characteristic monodispersive magnetic relaxation,[281] and the latter shows similar relaxations under external fields. Except $[Gd(bpy)(H_2O)_4Fe(CN)_4]$, no indications of magnetic long-range order were observed. For the $[Mn_4(hmp)_6R_2](ClO_4)_2$ systems, magnetic entropies were well-accounted for by considering the contribution from the lowest zero-field splitting spin levels, $R \ln(2S + 1) = R \ln 19$.

6.5. Antiferromagnetic Spin Rings

Antiferromagnetic rings, especially *ferric wheels*, were extensively investigated aiming to elucidate the quantum coherence found in the avoided crossing in Zeeman-splitting spin levels.[282] Although the antiferromagnetic ring with a spin ground state of $S = 0$ does not fall into the SMM category, it should be discussed here since it is one of exchange-coupled finite spin systems of great interest in the quantum effect involved. Calorimetric studies reported cover $[LiFe_6(OCH_3)_{12}(dbm)_6]PF_6$,[283,284] $[NaFe_6(OCH_3)_{12}(pmdbm)_6]PF_6$,[283−285] $[LiFe_6(OCH_3)_{12}(dbm)_6]BPh_4$,[286] $[Fe_{10}(OCH_3)_{20}(C_2H_2O_2Cl)_{10}]$,[285] $[Fe_{12}(OCH_3)_{12}(dbm)_{12}]$,[287] and $[Cr_8F_8piv_{16}]$.[288,289]

As shown in Figure 68,[286] the six-membered antiferromagnetic iron wheel shows avoided crossing of spin levels, arising from anisotropic energy terms responsible for S-mixing, when an external magnetic field is applied in 25°

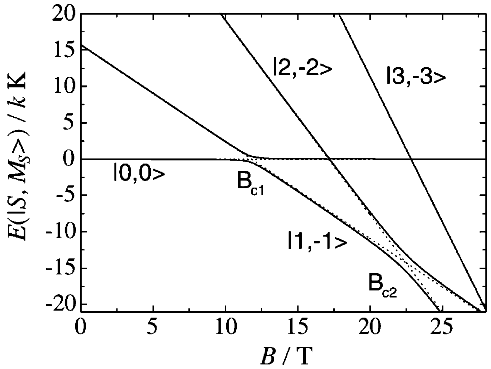

Figure 68. Zeeman splitting of lowest-lying spin levels of [LiFe$_6$(OCH$_3$)$_{12}$(dbm)$_6$]BPh$_4$. Reprinted Figure 1 with permission from Affronte, M.; Cornia, A.; Lascialfari, A.; Borsa, F.; Gatteschi, D.; Hinderer, J.; Horvatić, M.; Jansen, A. G. M.; Julien, M.-H. *Phys. Rev. Lett. 88*, 167201, 2002 (http://link.aps.org/abstract/PRL/v88/p167201). Copyright 2002 by the American Physical Society.

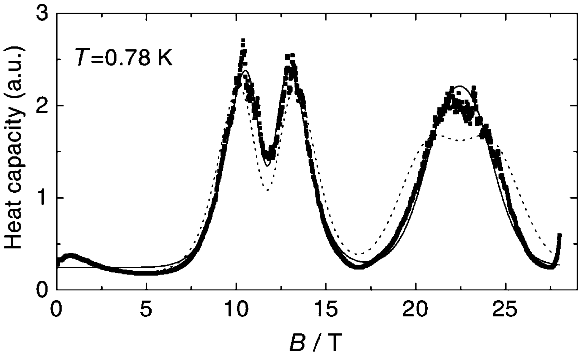

Figure 69. Field dependence of the isothermal heat capacity of [LiFe$_6$(OCH$_3$)$_{12}$(dbm)$_6$]BPh$_4$ measured at 0.78 K. The solid curve is a two-level Schottky anomaly calculated using the energy level scheme in Figure 68. The broken curve is the best fit assuming sample inhomogeneity and no avoided crossings. Reprinted Figure 3 with permission from Affronte, M.; Cornia, A.; Lascialfari, A.; Borsa, F.; Gatteschi, D.; Hinderer, J.; Horvatić, M.; Jansen, A. G. M.; Julien, M.-H. *Phys. Rev. Lett. 88*, 167201, 2002 (http://link.aps.org/abstract/PRL/v88/p167201). Copyright 2002 by the American Physical Society.

apart from the normal of the ring plane. Because the Schottky heat-capacity anomaly expected from thermal excitation between the lowest two levels has the maximum at the energy separation $\Delta(B) \approx 2.5\ kT$, an isothermal field sweep provides heat-capacity maxima at the fields satisfying this resonance condition and provides zero heat capacity at strict level crossings. Bearing it in mind, the heat-capacity curve in Figure 69 is consistent with the energy level scheme in Figure 68. The nonvanishing heat capacity at the level-crossing field B_{c1} and B_{c2} clearly demonstrates the presence of finite energy separation between the lowest two spin levels and this minimum gap corresponds to the off-diagonal matrix elements causing quantum coherence. Recently, similar avoided crossing was detected by calorimetry also in a nonring ferrimagnetic manganese cluster [Mn$_9$(2POAP-2H)$_6$](ClO$_4$)$_6$.[290]

7. Spin Crossover Phenomena

Complexes showing spin crossover phenomena are typical molecule-based magnets, because the magnetic properties dramatically change through the LS to HS transition.[291−293] However, the calorimetric studies have already been summarized by one of the authors (M.S.) in review articles,[11−13] and thus only a few topics will be picked up here.

7.1. Entropy-Driven Phenomena: Coupling with Phonon

Although the possibility of the spin-state transition was theoretically predicted in 1954 on the basis of the ligand field theory by Tanabe and Sugano,[294] it was in 1967 that the first experimental evidence was reported for iron(II) complexes [Fe(NCX)$_2$(phen)$_2$] (X = S or Se; phen = 1,10-phenanthroline) by König and Madeja,[295] in which the electronic state at room temperature is $^5T_{2g}$ with the spin quantum number of $S = 2$ while at low temperature it becomes $^1A_{1g}$ with $S = 0$. They gave a reasonable interpretation (as due to a spin crossover mechanism) for the unusual magnetic behaviors of these complexes reported first by Baker and Bobonich[296] in 1964. Because the spin crossover phenomenon is principally based on a change in the quantum state of the electron spin, many researchers believed that the dominant driving force leading to thermal spin crossover transition would be a change in the spin multiplicity. However, in 1972/1974, Sorai and Seki[297,298] reported calorimetric study on the spin crossover iron(II) complexes, [Fe(NCS)$_2$(phen)$_2$] and [Fe(NCSe)$_2$(phen)$_2$], for the first time, and their results showed that this interpretation was not correct.

As reproduced in Figure 70, a large phase transition was observed for [Fe(NCS)$_2$(phen)$_2$] at 176.29 K with an entropy change of $\Delta S = (48.8 \pm 0.7)$ J K^{-1} mol^{-1}. This entropy value is extremely large in comparison with the entropy gain $\Delta S = R \ln 5 = 13.38$ J K^{-1} mol^{-1} expected for a conversion from the $^1A_{1g}$ LS state to the $^5T_{2g}$ HS state. The entropy gain due to the change in the spin multiplicity is only 27% of the total entropy of transition. It should be remarked here that the change in the orbital degeneracies between the LS and the HS state does not generally contribute to the entropy gain at the spin crossover transition because the orbital degeneracy, if any, has been lifted by the low-symmetry ligand field to give a nondegenerate orbital.

As the spin crossover occurring, for example, in an octahedral symmetry involves a transfer of electrons between the bonding t_{2g} and antibonding e_g orbitals, the metal-to-ligand bond distances remarkably change, being about 20 pm shorter in the LS state than in the HS state. This brings about a drastic change in the density of vibrational states, mainly the metal−ligand skeletal vibrational modes.[299] Thus, the transition entropy involves a large contribution from the nonelectronic vibrations and the lattice heat capacity exhibits a discontinuity at the transition temperature. As seen in Figure 70 for the complex [Fe(NCS)$_2$(phen)$_2$], a jump of ΔC_p (normal) = 18.7 J K^{-1} mol^{-1} is observed. On the basis of variable-temperature IR absorption spectroscopy, they accounted for the excess entropy beyond the contribution from the spin multiplicity and the heat-capacity jump at the transition temperature in terms of the phonon contribution. Thermal spin crossover is possible only for the complexes whose ground electronic level is a LS state at low temperatures and the first excited HS level is located within a thermally accessible range. The energy difference is overwhelmed by the entropy term $T\Delta S$ mainly due to the drastic change in lattice vibrations, and consequently, the Gibbs energy of the HS state becomes lower than that of the LS state above a temperature at which the spin crossover takes place. Sorai and Seki[298] concluded that the thermal spin

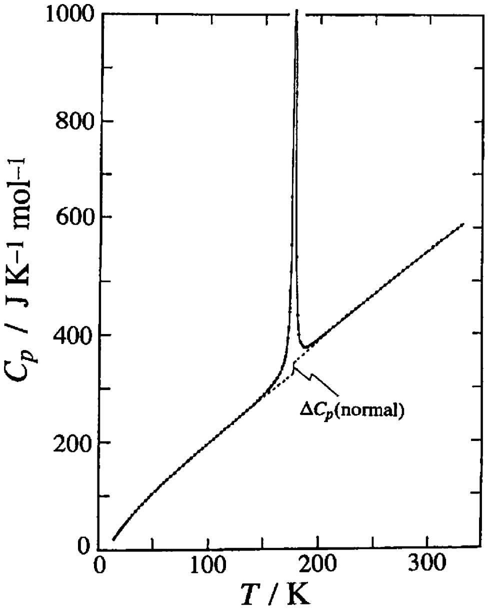

Figure 70. Molar heat capacity of $[Fe(NCS)_2(phen)_2]$. Broken curves indicate the normal heat capacities. Reprinted with permission from ref 298. Copyright 1974 Elsevier Ltd.

crossover is an entropy-driven phenomenon and coupling between the electronic states and the phonon system plays a fundamental role in the spin crossover phenomena occurring in the solid state. This concept has long since been accepted.

To verify this conclusion, Bousseksou et al.[300,301] performed Raman spectroscopy of this benchmark complex $[Fe(NCS)_2(phen)_2]$ at 300 and 100 K to obtain the frequency shifts associated with the HS-to-LS transition. Their overall result was consistent with the conclusion originally proposed by Sorai and Seki[298] that the vibrational entropy change is primarily attributable to the intramolecular vibrations. Recently, Brehm, Reiher, and Schneider[302] calculated the normal-mode frequencies of this complex in both the HS and the LS states on the basis of density functional theory (DFT/BP86) and compared the result with the IR and Raman spectra recorded at 298 and 100 K. The vibration-related entropy change due to the LS to HS transition estimated by their quantum chemical calculation was $\Delta S = 19.5$ J K^{-1} mol^{-1}. This value corresponds to 40% of the experimental value.[298] Because the share of the spin entropy is 27%, the remaining 33% of the entropy is attributed to the change in the lattice vibrations perturbed by intermolecular interactions. At any rate, a large part of the entropy gain due to the spin-state conversion beyond the spin contribution is caused by the change in the phonon. This situation is always encountered in any spin crossover complexes, irrespective of abrupt and gradual types of spin crossover phenomena.[302−319]

7.2. Phase Transition without Change in Crystal Symmetry

A very drastic change around the metal environment is involved when the spin-state conversion takes place, as easily recognized by the fact that the interatomic distances between the central metal atom and the ligands are drastically shortened on going from a HS to a LS state.[320−322] One may, therefore, anticipate a big change in the crystal symmetry for the spin crossover phenomena. Quite surprisingly, however, this is not the case. For example, Gallois et al.[323] reported that the most-studied spin crossover complex $[Fe(NCS)_2(phen)_2]$ is crystallized in the orthorhombic space group *Pbcn* with $Z = 4$ both at 293 K (HS phase) and at 130 K (LS phase). In disagreement with most of the predictions, the LS-to-HS transition is accompanied neither by a change in the crystal symmetry nor by an order−disorder transition involving NCS^- groups. Only a large reorganization of the iron(II) environment is detected. The main structural modifications, when passing from the HS to the LS form, consist of a remarkable shortening of the Fe−N distances (by about 20 to 10 pm) and a noticeable variation of the N−Fe−N angles, leading to a more regular shape of the $[Fe-N_6]$ octahedron.

The absence of a change in crystal symmetry at the spin-state conversion has been encountered in most spin crossover complexes. Table 6 lists space groups of mononuclear spin crossover complexes in both HS and LS states. The phase transition without change in the space group, which may be designated as “isomorphous” or “isostructural” phase transition, seems to be characteristic of spin crossover phenomena. In the case of usual order−disorder types of phase transitions, their mechanisms involve conversion of molecular orientations from ordered states at low temperature to disordered states at high temperature, which would give rise to a big change in the crystal symmetry. On the other hand, in the case of spin crossover transitions, molecular structures are retained as being approximately similar between LS and HS states, whereas big changes occur in the bond lengths.

The isomorphous character of the spin-state conversion has also been supported by spectroscopy. On the basis of ESR study of a precipitated sample of an iron complex doped with manganese(II), $[Fe_{0.99}Mn_{0.01}(NCS)_2(phen)_2]$, Rao et al.[344] found that the zero-field splitting parameters D and E appearing in the spin Hamiltonian for Mn^{2+} ion decrease steadily with increasing temperature and are not affected by the transition. Consequently, they described this as “It appears that any structural changes that occur during the spin transition are short-range ones inside the iron(II) complex and not long-range ones involving the total lattice.” Although a genuine phase transition is impossible unless a long-range order exists, this description is suggestive to understand the transition mechanisms of spin crossover in the solid state and the spin-state equilibrium in solution.

An interesting example of iron(III) spin crossover complex, which exhibits a single-step transition without change in the crystallographic symmetry, is a five-coordinate iron(III) complex, $[Fe^{III}(ISQ)_2Br]$, reported by Chun et al.,[340] where ISQ is *N*-phenyl-*o*-imino(4,6-di-*tert*-butyl)benzosemiquinonate π radical anion with spin $S = 1/2$. This complex contains a 1:1 mixture of the total spin $S_t = 3/2$ and 1/2 forms in the temperature range of 4.2−150 K. Above 150 K, the latter form undergoes a spin crossover from 1/2 to 3/2. The $S_t = 3/2$ ground state is attained via intramolecular antiferromagnetic coupling between a HS iron(II) ($S_{Fe} = 5/2$) and two ligand π radicals, whereas the $S_t = 1/2$ form is generated from exchange coupling between an intermediate spin iron(III) ($S_{Fe} = 3/2$) and two ligand π radicals.

A few exceptional complexes listed in Table 6 are $[Fe\{5\text{-}NO_2\text{-sal-N}(1,4,7,10)\}]$,[312] $[Fe(NCS)_2(PM\text{-}PEA)_2]$,[337] $[Fe\{HC(3,5\text{-}Me_2pz)_3\}_2]\cdot(BF_4)_2$,[338] and $[Fe^{III}(isoxazole)_6]\cdot(BF_4)_2$,[341] in which the space group changes between the LS LT phase, the mixed intermediate-temperature phase, and the HS HT phase. In the case of $[Fe\{HC(3,5\text{-}Me_2pz)_3\}_2]\cdot(BF_4)_2$, where pz = pyrazolyl ring, an abrupt single-step spin crossover at 204 K is exhibited. Above this temperature, the compound

Table 6. Crystallographic Data for Mononuclear Spin Crossover Complexes

compounds[a]	type of SCO[b]	T (K)[c]	crystal system	space group	Z	refs
$[Fe(2\text{-}pic)_3]Cl_2\cdot CH_3OH$	G, 1-step	115 (LS), 227 (HS)	orthorhombic	$Pbna$	8	324, 325
$[Fe(2\text{-}pic)_3]Cl_2\cdot C_2H_5OH$[d]	A, 2-step	90 (LS), 298 (HS)	monoclinic	$P\underline{2}_1/c$	4	325−329
$[Fe_3(Ettrz)_6(H_2O)_6](CF_3SO_3)_6$	A, 1-step	105 (LS), 300 (HS)	orthorhombic	$P\bar{3}1c$	2	330
$[Fe(2\text{-}pic)_3]Br_2\cdot CH_3OH$	A, 1-step	110 (LS), 298 (HS)	monoclinic	$P2_1/n$	4	331
$[Fe(NCS)_2(phen)_2]$	A, 1-step	130 (LS), 293 (HS)	orthorhombic	$Pbcn$	4	323
$[Fe(NCS)_2(py)_2(bpym)]\cdot 0.25py$	A, 1-step	298 (HS)	tetragonal	$I4_{\underline{1}}/a$	16	332
$[Fe^{III}(acpa)_2]BPh_4$	G, 1-step	120 (LS), 311 (HS)	triclinic	$P\bar{1}$	2	333
$[Fe^{III}(acpa)_2]PF_6$	G, 1-step	120 (LS), 290 (HS)	monoclinic	$P2/a$	2	333
$[Fe(NCS)_2(btz)_2]$	G, 1-step	130 (LS), 293 (HS)	orthorhombic	$P\bar{b}cn$	4	334
$[Fe(NCS)_2(tap)_2]\cdot CH_3CN$	G, 1-step	135 (LS), 290 (HS)	triclinic	$P\bar{1}$	2	335
$[Fe\{5\text{-}NO_2\text{-}sal\text{-}N(1,4,7,10)\}]$[e,f]	A, 2-step	292 (HS)	monoclinic	$P2/c$	2	312
		153 (IP)	monoclinic	$P2$	2	312
		103 (LS)	triclinic	$P1$	2	312
$[Fe(NCS)_2(PM\text{-}BiA)_2]$	A, 1-step	140 (LS), 298 (HS)	orthorhombic	$Pccn$	4	336
$[Fe(NCS)_2(PM\text{-}PEA)_2]$[e]	A, 1-step	298 (HS)	monoclinic	$P2_1/c$	4	337
		140 (LS)	orthorhombic	$Pccn$	4	337
$[Fe(NCS)_2(PM\text{-}TeA)_2]$	G, 1-step	11 (LS), 298 (HS)	orthorhombic	$Pccn$	4	337
$[Fe(NCS)_2(PM\text{-}AzA)_2]$	G, 1-step	110 (LS), 298 (HS)	monoclinic	$P\underline{2}_1/c$	4	337
$[Fe(btr)_3](ClO_4)_2$[f]	A, 2-step	150 (LS), 190 (IP), 260 (HS)	trigonal	$R\bar{3}$	6	313
$[Fe\{HC(3,5\text{-}Me_2pz)_3\}_2](BF_4)_2$[e,f]	A, 1-step	220 (HS)	monoclinic	$C\underline{2}/c$	4	338
		173 (IP)	triclinic	$P\bar{1}$	2	338
$[Fe(DPEA)(bim)](ClO_4)_2\cdot 0.5H_2O$[f]	G, 2-step	123 (LS), 293 (HS)	monoclinic	$P\underline{2}_1/c$	4	339
$[Fe^{III}(ISQ)_2Br]$[f,g]	G, 1-step	100 (LS), 295 (HS)	triclinic	$P\bar{1}$	4	340
$[Fe^{III}(ISQ)_2I]$[g]	G, 1-step	100 (LS), 295 (HS)	monoclinic	$P\underline{2}_1/c$	4	340
$[Fe^{III}(isoxazole)_6](ClO_4)_2$[f]	A, 1-step	150 (LS), 225 (HS), 295 (HS)	trigonal	$P\underline{\bar{3}}$	3	341
$[Fe^{III}(isoxazole)_6](BF_4)_2$[e,f]	G, 2-step	260 (HS)	trigonal	$P\underline{\bar{3}}$	3	341
		130 (IP)	triclinic	$P\bar{1}$	3	341
$[Fe(DAPP)(abpt)](ClO_4)_2$[h]	A, 1-step	123 (LS), 293 (HS)	monoclinic	$P2_1/n$	4	342
$[Fe(Hpy\text{-}DAPP)](BF_4)_2$[h]	A and G, 2-step	90 (LS), 130 (IP), 298 (HS)	monoclinic	$P2_1/c$	4	343

[a] 2-pic, 2-picolylamine (2-aminomethy-pyridine); Ettrz, 4-ethyl-1,2,4-triazole; phen, 1,10-phenanthroline; bpym, 2,2′-bipyrimidine; Hacpa, *N*-(1-acetyl-2-propylidene)-2-pyridylmethylamine; btz, 2,2′-bi-4,5-dihydrothiazine; tap, 1,4,5,8-tetraazaphenanthrene; 5-NO_2-sal-N(1,4,7,10), the Schiff base condensation of 5-nitrosalicylaldehyde with 1,4,7,10-tetraazadecane in a 2:1 ratio; PM-BiA, *N*-(2′-pyridylmethylene)-4-aminobiphenyl; PM-PEA, *N*-(2′-pyridylmethylene)-4-(phenylethynyl)aniline; PM-TeA, *N*-(2′-pyridylmethylene)-4-aminoterphenyl; PM-AzA, *N*-(2′-pyridylmethylene)-4-(phenylazo)aniline; btr, 4,4′-bis-1,2,4-triazole; pz, pyrazolyl ring; DPEA, 2-aminoethyl-bis(2-pyridylmethyl)amine; bim, 2,2-bisimidazole; ISQ, *N*-phenyl-*o*-imino(4,6-di-*tert*-butyl)benzosemiquinonate; DAPP, bis(3-aminopropyl)(2-pyridylmethyl)amine; abpt, 4-amino-3,5-bis(pyridin-2-yl)-1,2,4-triazole. [b] SCO, spin crossover; G, gradual type of SCO; A, abrupt type of SCO; 1-step, single-step SCO; 2-step, double-step SCO. [c] LS, low-spin state; IP, intermediate phase; HS, high-spin state. [d] Order−disorder of the solvate molecule. [e] The space group is different between the LT phase and the HT phase. [f] There exist two inequivalent iron sites or two sublattices. [g] The ligand "ISQ" is a free radical with spin $S = 1/2$. [h] Order−disorder of the ligand and the anions.

is completely HS with the structure in the monoclinic $C2/c$ space group with $Z = 4$ and there is one unique iron(II) site. Below 204 K, the compound converts to a 50:50 mixture of HS and LS. There is a radical change in the coordination sphere for half of the iron(II) sites, most notably a shortening of the Fe−N bond distances by ca. 20 pm. The crystal system changes to triclinic $P\bar{1}$ space group with $Z = 2$.

7.3. Cooperativeness of Spin Crossover Phenomena

As widely recognized, spin crossover transformations can phenomenologically assume two limiting cases: One is the so-called abrupt type in which the spin-state transformation takes place abruptly within a narrow temperature range of a few Kelvin, and the other is the gradual type in which the spin crossover occurs gradually over a wide temperature range, typically greater than 100 K. Calorimetric measurements of the gradual type have been made for the spin crossover complexes $[Fe^{III}(acpa)_2]PF_6$ [Hacpa = *N*-(1-acetyl-propylidene)-2-pyridylmethylamine],[304] $[Fe^{III}(3EtO\text{-}salAPA)_2]ClO_4\cdot C_6H_5Br$ (3EtO-salAPAH = the Schiff base condensed from 1 mol of 3-ethoxysalicylaldehyde with 1 mol of *N*-aminopropyl-aziridine),[11,308] and $[Fe^{II}(2\text{-}pic)_3]Cl_2\cdot CH_3OH$ (2-pic = 2-picolylamine or 2-aminomethylpyridine).[315] These complexes exhibit unusually broad heat-capacity peaks over a wide temperature region. As an example, the molar heat capacity of $[Fe(2\text{-}pic)_3]Cl_2\cdot CH_3OH$ is shown in Figure 71.

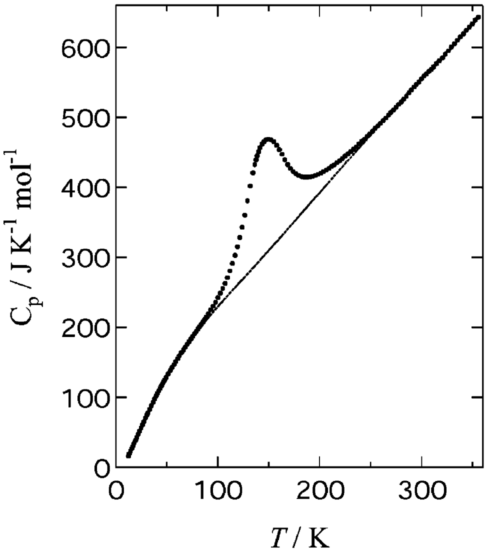

Figure 71. Molar heat capacity of the spin crossover complex $[Fe(2\text{-}pic)_3]Cl_2\cdot CH_3OH$. The dotted curve indicates the normal heat capacity. Reprinted with permission from ref 315. Copyright 2001 American Chemical Society.

To elucidate the reason for the gradual spin-state conversion and the degree of cooperativeness inherent in the spin-state conversion, Sorai and Seki[298] proposed in 1974 a simple

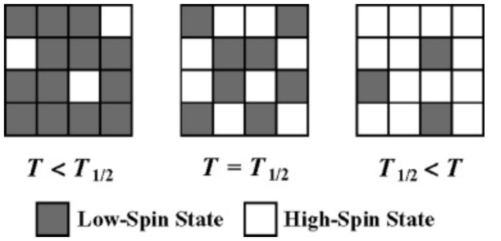

Figure 72. Schematic drawing of the domain model. The crystal lattice is considered to consist of domains of uniform size containing equal numbers of spin crossover complexes. $T_{1/2}$ is the transition temperature at which the number of LS domains becomes equal to that of HS domains.[298]

domain model based on the Frenkel theory[345] of heterophase fluctuations in liquids. As schematically shown in Figure 72, this model assumes that a crystal lattice consists of N noninteracting domains with uniform size containing n complexes and that the spin-state conversion in each domain takes place simultaneously, where $N \times n$ is equated to the Avogadro constant N_A. When a system consisting of the HS fraction f_{HS} and the LS fraction $(1 - f_{HS})$ is in a thermal equilibrium, the Gibbs energy of the system G at a temperature T is given by

$$G = f_{HS}G_H + (1 - f_{HS})G_L + NkT\{f_{HS} \ln f_{HS} + (1 - f_{HS}) \ln(1 - f_{HS})\} \quad (6)$$

where k is the Boltzmann constant and G_H and G_L are the Gibbs energies of the HT and LT phases at T, respectively. The HS fraction f_{HS} in thermal equilibrium is determined by the equilibrium condition $(\partial G/\partial f_{HS})_T = 0$ as follows:

$$f_{HS} = 1/\{1 + \exp(\Delta G/NkT)\} = 1/\{1 + \exp(n\Delta G/RT)\} \quad (7)$$

where ΔG is equal to $(G_H - G_L)$ and R implies the gas constant. The molar heat capacity at constant pressure C_p is obtained by the following relation:

$$C_p = \frac{\partial}{\partial T}\{f_{HS}H_H + (1 - f_{HS})H_L\} = \{f_{HS}C_{p,H} + (1 - f_{HS})C_{p,L}\} + \frac{n(H_H - H_L)^2 \exp(n\Delta G/RT)}{RT^2\{1 + \exp(n\Delta G/RT)\}^2} = C_p(\text{lattice}) + \Delta C_p \quad (8)$$

where H_H and H_L mean the molar enthalpy of the HT and LT phases, respectively. A convenient way to estimate the average number n of complexes per domain is to fit the ΔC_p term given by eq 8 with the observed heat-capacity anomaly ΔC_p(obsd) at the peak temperature $T_{1/2}$, at which the HS fraction becomes equal to the LS fraction and ΔG becomes zero:

$$\Delta C_p(\text{obsd}, T_{1/2}) = n\{H_H(T_{1/2}) - H_L(T_{1/2})\}^2/4RT_{1/2}^{\;2} \quad (9)$$

The excess heat capacity of $[Fe(2\text{-pic})_3]Cl_2{\cdot}CH_3OH$ beyond the normal heat capacity (see Figure 73)[315] is well-reproduced by the domain model (solid curve) when the number of complexes per domain is only $n = 1.5$. Small values of n have also been encountered in $[Fe(acpa)_2]PF_6$ ($n = 5$),[304] $[Fe(3EtO\text{-}salAPA)_2]ClO_4{\cdot}C_6H_5Br$ ($n = 1$),[11,308] and $[Fe(Hpt)_3](BF_4)_2{\cdot}2H_2O$ ($n = 1.5$),[318] where Hpt = 3-(pyrid-2-yl)-1,2,4-triazole. These small numbers of complex per domain make a sharp contrast to $n = 95$ for $[Fe(NCS)_2(phen)_2]$,[298] 77 for $[Fe(NCSe)_2(phen)_2]$,[298] and 2000 for $[CrI_2(depe)_2]$ [depe = *trans*-bis{1,2-bis-(diethylphosphino)ethane}],[307] which belong to the abrupt type complex.

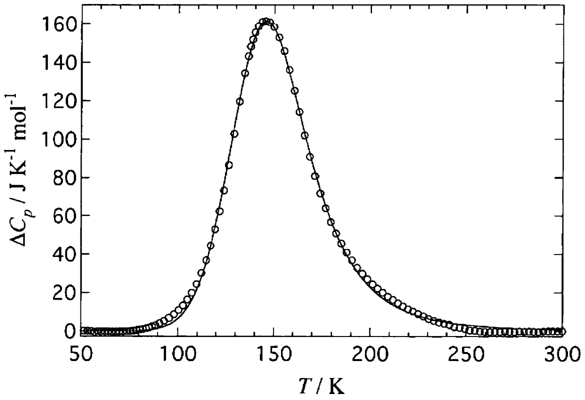

Figure 73. Excess heat capacity beyond the normal heat capacity arising from the spin-state conversion in $[Fe(2\text{-pic})_3]Cl_2{\cdot}CH_3OH$. Open circles are experimental values, and the solid curve corresponds to the domain model with $n = 1.5$. Reprinted with permission from ref 315. Copyright 2001 American Chemical Society.

As the value of n is decreased, the cooperativeness of the spin crossover becomes weaker and the heat-capacity peak due to the spin-state conversion becomes broader. The system characterized by $n = 1$ simply corresponds to a chemical equilibrium between two energy states described by the van't Hoff scheme, which is often encountered in denaturation of small globular proteins from a native state to a denatured one.[346,347] The fact that the spin crossover can proceed even without cooperativeness rationalizes the experimental facts that the iron(II) complex highly diluted with the zinc(II) analogue $[Fe_xZn_{1-x}(2\text{-pic})_3]Cl_2{\cdot}C_2H_5OH$ exhibits a spin-state conversion even for the specimen with $x = 0.0009$ as seen by Mössbauer spectroscopy reported by Gütlich et al.[348] and that the spin-state equilibrium is realized in solution.[349−353]

Among various models proposed for interpretation of cooperative interactions inherent in the spin crossover phenomena, Wajnflasz and Pick[354] introduced a statistical model in 1970 in which the microscopic interaction and the entropy effect are considered. Slichter and Drickamer[355] reported an essential model based on the concept of regular solution in 1972. Bolvin and Kahn[356] published in 1995 an Ising model within and beyond the mean-field approximation to establish a bridge between the regular solution model of Slichter and Drickamer[355] and the domain model proposed by Sorai and Seki[298] in 1974. Two main results emerged as follows: One is that the occurrence of a thermal hysteresis is less probable in the nonrandom distribution model and the other is that the like-spin molecules tend to assemble in like-spin clusters. The former is favorable to the regular solution model while the latter is favorable to the domain model. It should be remarked that evidence for the existence of domains has been obtained for $[Fe(2\text{-pic})_3]Cl_2{\cdot}C_2H_5OH$ based on EPR measurements in 1990 by Doan and McGarvey.[357] It should be remarked that Nishino et al.[358] derived in 2003 the relationship between the phenomenological macroscopic parameter n in the Sorai and Seki domain model[298] and the microscopic parameters in the Wajnflasz and Pick statistical model.[354]

7.4. Two-Step Spin-State Conversion

Next to [Fe(NCS)$_2$(phen)$_2$], extensively studied spin crossover complexes are [Fe(2-pic)$_3$]Cl$_2$•(solv).[359–361] Gütlich and his collaborators[362] reinvestigated the spin transition in [Fe(2-pic)$_3$]Cl$_2$•C$_2$H$_5$OH in 1982 by Mössbauer spectroscopy and magnetic susceptibility measurements. They found, for the first time, unusual “two-step” spin conversion in the crossover region with transition temperatures at 120.7 and 114.0 K. In the first step, the HS fraction decreases from 100% at room temperature to 50% near 120 K. In the second step below ~115 K, the HS fraction is further diminished from ~40% to the pure LS state at 4.2 K. Between ~115 and ~120 K, the spin transition is much more gradual than below and above this temperature range. Kaji and Sorai[303] reported a molar heat capacity of [Fe(2-pic)$_3$]Cl$_2$•C$_2$H$_5$OH and observed two peaks at 114.0 and 122.2 K corresponding to the two-step spin conversion (see Figure 74). The broken curves drawn in this figure represent the normal heat capacities estimated by an effective frequency distribution method.[20] Integration of the excess heat capacity beyond the normal heat-capacity curves with respect to ln T gives the entropy gain ΔS due to the phase transition. The observed entropy gain ($\Delta S = 50.6$ J K^{-1} mol^{-1}) is well accounted for in terms of the contributions from (i) the spin entropy due to the singlet-to-quintet conversion [$R \ln 5 = 13.4$ J K^{-1} mol^{-1}], (ii) orientational disordering of the ethanol solvate molecule over three sites with occupancies in the ratios 3:2:2 in the HS phase[327,328] [$-R$ (3/7) ln(3/7) $-$ 2R (2/7) ln(2/7) = 9.0 J K^{-1} mol^{-1}], and (iii) the phonon contribution (about 28 J K^{-1} mol^{-1}).

According to single-crystal X-ray studies at temperatures well above and well below the critical transition region by Mikami et al.,[327,328] the space group of [Fe(2-pic)$_3$]Cl$_2$•C$_2$H$_5$OH is monoclinic $P2_1/c$ for both the HS phase and the LS phase. Thus, the presence of a structural phase transition is not necessarily essential for both a single-step and a two-step spin-state conversion. On the basis of a single-crystal XRD study, Chernyshov et al.[329] showed quite recently that the structure of [Fe(2-pic)$_3$]Cl$_2$•C$_2$H$_5$OH undergoes two first-order phase transitions on cooling from a HS phase via an intermediate phase (IP) to a LS phase. Comparisons of structural data over large ranges of temperature clearly show that the structural changes from the HS to the LS phase, both with a single iron site, are discontinuous. The unit cell doubles in size in the IP phase. The relationship between the phases is isostructural. The IP reveals that, contrary to earlier assertions, the intermediate plateau in the two-step transition of this compound is the expression of a structure with two different iron sites showing long-range order, very much like that found for other compounds with two-step behavior. The absence of discernible diffuse scattering suggests that short-range correlations are very weak. The combination of the isostructural HS and LS phases with the ordered IP implies re-entrant phase transition behavior, a relatively rare phenomenon.

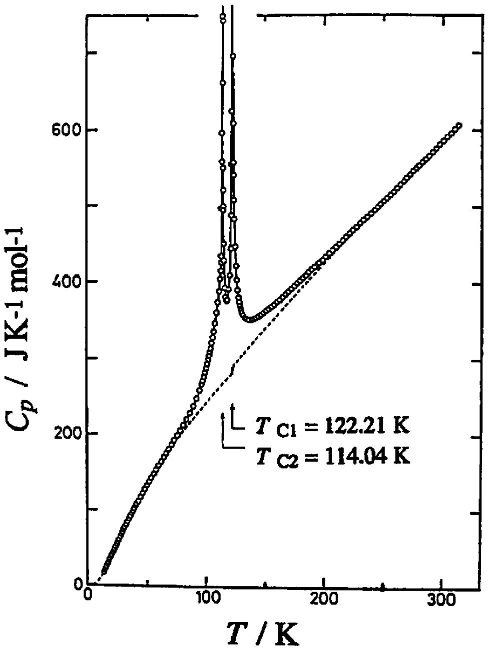

Figure 74. Molar heat capacity of [Fe(2-pic)$_3$]Cl$_2$•C$_2$H$_5$OH. Broken curves indicate the estimated normal heat capacities. Reprinted with permission from ref 303. Copyright 1985 Elsevier Ltd.

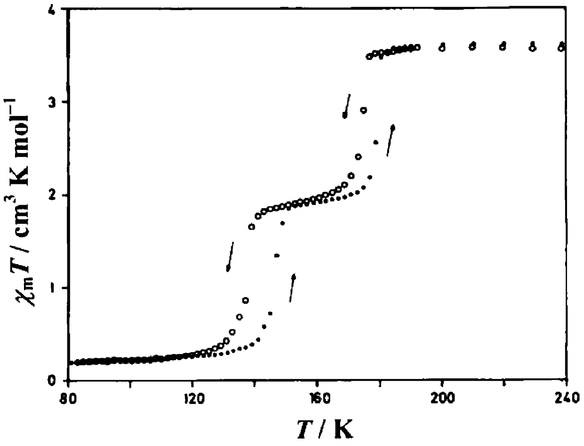

Figure 75. Temperature dependence of $\chi_m T$ for [Fe{5-NO$_2$-sal-N(1,4,7,10)}]. Both cooling (○) and heating (●) experimental data are shown. Reprinted with permission from ref 363. Copyright 1987 Elsevier Ltd.

In the case of [Fe(btr)$_3$](ClO$_4$)$_2$, where btr = 4,4′-bis-1,2,4-triazole, Garcia et al.[313] reported that the two-step spin conversion in this complex is associated with the presence of two slightly different iron(II) sites, whereas the space group (trigonal $R\bar{3}$) remains identical independently of the spin state. Matouzenko et al.[339] found a similar situation in the two-step spin-state conversion in [Fe(DPEA)(bim)]-(ClO$_4$)$_2$•0.5H$_2$O, where DPEA = 2-aminoethyl-bis(2-pyridyl-methyl)amine and bim = 2,2-bisimidazole, while the space group is monoclinic $P2_1/c$. Matouzenko et al.[343] reported that [Fe(Hpy-DAPP)](BF$_4$)$_2$, where DAPP = bis(3-aminopropyl)-(2-pyridylmethyl)amine, gives the first example of two-step spin transition in a mononuclear complex presenting a single iron(II) crystallographic site in the whole temperature range. The two-step spin transition behavior of the system is induced by two different geometries of the [FeN$_6$] coordination core generated in the lattice by the disorder in the ligand. The HS-to-LS transition is conjugated with the conformational change in the chelate cycle.

In contrast, the iron(II) spin crossover complex [Fe{5-NO$_2$-sal-N(1,4,7,10)}], where 5-NO$_2$-sal-N(1,4,7,10) = the Schiff base condensation of 5-nitrosalicylaldehyde with 1,4,7,10-tetraazadecane in a 2:1 ratio, changes its space group depending on the spin state. Petrouleas and Tuchagues[363] reported a well-separated two-step spin-state conversion in this complex on the basis of Mössbauer spectroscopy and magnetic susceptibility measurement. As shown in Figure 75, magnetic susceptibility (χ_m) times T against temperature plot for this complex clearly shows a two-step spin-state conversion at 173 and 136 K on cooling while it shows a two-step spin-state conversion at 146 and 180 K on heating. Boinnard et al.[312] studied in detail the two-step spin-state conversion in this complex with special emphasis on the structural changes by use of XRD analysis, IR, magnetic susceptibility, Mössbauer spectroscopy, DSC, and theoretical studies. The space group of [Fe{5-NO_2-sal-N(1,4,7,10)}] is altered from triclinic $P1$ in the LS phase to the monoclinic $P2/c$ in the HS phase via the monoclinic $P2$ in the intermediate phase (IP), in which a spin-state equilibrium at ∼50% of HS and LS molecules is realized over the ∼35 K temperature range. On the basis of these experimental and theoretical studies, they concluded that the origin of the two-step spin-state conversion is related to the structural phase transitions.

An interesting example of iron(III) spin crossover complex showing two-step spin-state transition is $[Fe^{III}(isoxazole)_6](BF_4)_2$ reported by Hibbs et al.[341] This complex undergoes two reversible spin crossover transitions at 91 and 192 K. As listed in Table 6, the crystal symmetry at 260 K is trigonal $P\bar{3}$, while it is triclinic $P\bar{1}$ at 130 K. There exist two different iron sites, Fe1 and Fe2, in a 1:2 ratio. The LS-to-HS transitions at Fe1 and Fe2 sites take place at 91 and 192 K, respectively.

Theoretical treatment for two-step spin transition was first made by Sasaki and Kambara[364] in 1989. Couplings of the spin states of the iron ion with a molecular distortion and a lattice strain have been taken into account in this cooperative molecular distortion model, in which two nonequivalent sites occupied by equivalent iron complexes are assumed in a unit cell of the lattice. Molecular distortions of a pair of the two complexes occupying the two nonequivalent sites couple with each other symmetrically and antisymmetrically. The merit of this model is that various patterns of the two-step spin conversion are obtained by changing the coupling strength of the iron ion with molecular distortion and with lattice strain and also the strength of interpair interactions. Afterward, other theoretical models were reported as follows: a model accounting for two-step spin transitions in binuclear compounds by Real et al.,[306] two-sublattice model by Bousseksou et al.,[365] Ising-like model taking into account the nonequivalence of the two sublattices by Boinnard et al.,[312] the Monte Carlo method treating both the nearest and the next nearest-neighbor interactions by Kohlhaas et al.,[366] the Bethe approximation to treat the nearest-neighbor interaction, which is present in addition to the long-range elastic interaction between the spin-changing molecules, by Romstedt et al.,[367,368] the modified Bragg-Williams approximation by Koudriavtsev,[369] an Ising-like model consisting of two equivalent sublattices with a “ferro” intrasublattice interaction, and an “antiferro” intersublattice interaction by Nishino et al.,[370] and so on. We may conclude now that the two-step spin-state conversion is accompanied either by structural phase transition involving two sublattices or by order−disorder phase transition of ligand and/or solvent molecules.

7.5. Thermal Hysteresis: Bistable States

The thermal hysteresis usually occurs when the phase transition is, at least to some extent, first-order and it involves a discontinuous change of volume.[371] Because the spin-state conversions always involve a remarkable change in the volume between the LS and the HS states, spin crossover complexes are favorable for thermal hysteresis, although the most spin-state conversions occurring in the solid state are characterized by the isomorphous phase transition without accompanying a change in the space group.

Table 7 chronologically lists the spin crossover complexes showing thermal hysteresis. König and Ritter[372] first remarked in 1976 the hysteresis occurring in $[Fe(NCS)_2(4,7\text{-}(CH_3)_2\text{-}phen)_2]$, where 4,7-$(CH_3)_2$-phen = 4,7-dimethyl-1,10-phenanthroline, and compared it with the Slichter and Drickamer model based on the theory of regular solution.[388] On the basis of ^{57}Fe Mössbauer spectroscopy, Sorai et al.[361] reported in 1977 unusually large thermal hysteresis as wide as $\Delta T_c = 91$ K in $[Fe(2\text{-pic})_3]Cl_2 \cdot H_2O$. Quite recently, however, it turned out[319] that this large hysteresis is not genuine but apparent in the sense that an extra metastable LS phase is involved in the mechanism of hysteresis. Details will be described later.

To cope with the demand for storing ever more information, Kahn and his collaborators[311,336,381−387,389] were turning their attentions to memory storage and display systems based on the bistability realized by thermal hysteresis in spin crossover complexes. Because the magnetic and optical properties are quite different between the HS and LS states, measurement of such a physical property may distinguish clearly the two states. The most appealing spin crossover complexes are those for which room temperature falls in the middle of a thermal hysteresis loop. They have succeeded in finding such candidates.

As seen in Table 7, many complexes have been found till now to exhibit thermal hysteresis. Among them, there are peculiar complexes showing extremely large hysteresis, such as $[Fe(NH_2trz)_3](tos)_2 \cdot 2H_2O$ ($\Delta T_c = 82$ K) [NH_2trz = 4-amino-1,2,4-triazole and tos = tosyl (= *p*-toluenesulfonyl)],[383] $[Fe(hyetrz)_3](nps)_2 \cdot 3H_2O$ ($\Delta T_c = 270$ K) [hyetrz = 4-(2′-hydroxyethyl)-1,2,4-triazole and Hnps = 3-nitrophenylsulfonic acid],[384,385] $[Fe(hyetrz)_3]Cl_2 \cdot 3H_2O$ ($\Delta T_c = 63$ K),[387] $[Fe(hyetrz)_3](NO_3)_2 \cdot 2H_2O$ ($\Delta T_c = 57$ K),[387] and $[Fe(hyetrz)_3](PF_6)_2 \cdot 2H_2O$ ($\Delta T_c = 127$ K).[387] However, as the large thermal hysteresis originates in the synergy between the spin-state conversion and the removal of noncoordinated solvate water molecules, such a hysteresis is realized only for the first thermal cycling. After dehydration, the hysteresis loop is remarkably reduced. For example (see Figure 76), the large hysteresis, $\Delta T_c = 270$ K, of $[Fe(hyetrz)_3](nps)_2 \cdot 3H_2O$ is diminished to $\Delta T_c = 15$ K for the dehydrated $[Fe(hyetrz)_3](nps)_2$.[384,385] Therefore, the large hysteresis observed in these complexes is not genuine but only apparent.

As mentioned above, ^{57}Fe Mössbauer spectroscopy for $[Fe(2\text{-pic})_3]Cl_2 \cdot H_2O$ gave a wide thermal hysteresis of $\Delta T_c = 91$ K [$T_c(\downarrow) = 204$ K and $T_c(\uparrow) = 295$ K].[361] To confirm this fact by other experimental methods, Nakamoto et al.[319] examined the thermal property of this complex by DTA (differential thermal analysis) and adiabatic calorimetry. As the result, it turned out that this thermal hysteresis is caused by the existence of a metastable phase. The cooling DTA run for the as-grown sample always gave rise to an exothermic peak at 199 K and the immediately succeeding heating run showed an endothermic peak at 211 K, while no anomaly was observed around 295 K. This thermal behavior is quite different from that previously derived from Mössbauer spectroscopy.[361] To solve this mystery, they measured the heat capacity of this complex with adiabatic calorimetry. The sample was first cooled from room tem-

Table 7. Genuine and Apparent Thermal Hysteresis Reported

compounds[a]	$T_c\downarrow$ (K)	$T_c\uparrow$ (K)	ΔT_c (K)[b]	experimental method	refs
[Fe(NCS)$_2$(4,7-(CH$_3$)$_2$-phen)$_2$]	118.6	121.7	3.1	Mössbauer	372
[Fe(2-pic)$_3$]Cl$_2$·H$_2$O	204	295	91[c]	Mössbauer	361
	220	280.8	60.8[c]	heat capacity	319
[Fe(NCS)$_2$(bt)$_2$]	172.3	181.9	9.6	Mössbauer	373, 374
	176.9	184.3	7.4	magnetic susceptibility	375
[Fe(phy)$_2$](ClO$_4$)$_2$	239.3	246.8	7.5	Mössbauer	376, 377
[Fe(bi)$_3$](ClO$_4$)$_2$	108.3	114.8	6.5	Mössbauer	378
[Fe(phy)$_2$](BF$_4$)$_2$	277	286	9	Mössbauer	379
[Fe(NCS)$_2${4,7-(CH$_3$)$_2$-phen}$_2$]·α-picoline	146	202	56	Mössbauer	380
[Fe(Htrz)$_{2.85}$(NH$_2$trz)$_{0.15}$](ClO$_4$)$_2$·nH$_2$O	288	304	16	magnetic susceptibility	381, 382
[Fe(Htrz)$_2$(trz)]BF$_4$	345	395	50	magnetic susceptibility	311, 382
[Fe(Htrz)$_3$](BF$_4$)$_2$·H$_2$O (α-form)	323	345	22	magnetic susceptibility	311, 382
[Fe(Htrz)$_3$](BF$_4$)$_2$·H$_2$O (β-form)	276	282	6	magnetic susceptibility	311, 382
[Fe(NH$_2$trz)$_3$](tos)$_2$·2H$_2$O[d]	279	361	82[c]	optical detection	383
[Fe(NH$_2$trz)$_3$](tos)$_2$	279	296	17	optical detection	383
[Fe(hyetrz)$_3$](nps)$_2$·3H$_2$O[d]	100	370	270[c]	optical detection	384, 385
[Fe(hyetrz)$_3$](nps)$_2$	100	115	15	optical detection	384, 385
[Fe(NCS)$_2$(PM-PEA)$_2$]	194	231	37	magnetic susceptibility	386
[Fe(NCS)$_2$(btr)$_2$]·H$_2$O	124	144	20	magnetic susceptibility	375
[Fe(NCS)$_2$(PM-BiA)$_2$]	168	173	5	magnetic susceptibility	336
[Fe(hyetrz)$_3$]Cl$_2$·3H$_2$O[d]	301	364	63[c]	optical detection	387
[Fe(hyetrz)$_3$]Cl$_2$	301	314	13	optical detection	387
[Fe(hyetrz)$_3$](NO$_3$)$_2$·2H$_2$O[d]	298	355	57[c]	optical detection	387
[Fe(hyetrz)$_3$](NO$_3$)$_2$	298	315	17	optical detection	387
[Fe(hyetrz)$_3$](PF$_6$)$_2$·2H$_2$O[d]	195	322	127[c]	optical detection	387
[Fe(hyetrz)$_3$](PF$_6$)$_2$	195	205	10	optical detection	387
[Fe(bzimpy)$_2$](ClO$_4$)$_2$·0.25H$_2$O	397	409	12	magnetic susceptibility	314, 316

[a] 4,7-(CH$_3$)$_2$-phen, 4,7-dimethyl-1,10-phenanthroline; 2-pic, 2-picolylamine or 2-aminomethylpyridine; bt, 2,2′-bi-2-thiazoline; phy, 1,10-phenanthroline-2-carbaldehyde phenylhydrazone; bi, 2,2′-bi-imidazoline; Htrz, 1,2,4−4*H*-triazole; trz, 1,2,4-triazolato; NH$_2$trz, 4-amino-1,2,4-triazole; tos, tosyl (= *p*-toluenesulfonyl); hyetrz, 4-(2′-hydroxyethyl)-1,2,4-triazole; Hnps, 3-nitrophenylsulfonic acid; PM-PEA, *N*-(2′-pyridylmethylene)-4-(phenylethynyl)aniline; btr, 4,4′-bis-1,2,4-triazole; PM-BiA, *N*-(2′-pyridylmethylene)-4-aminobiphenyl; bzimpy, 2,6-bis(benzimidazole-2-yl)pyridine. [b] ΔT_c (K) = $T_c\uparrow$ (K) − $T_c\downarrow$ (K). [c] Not genuine but apparent thermal hysteresis. [d] Synergy between the spin-state conversion and the removal of noncoordinated solvate water molecules.

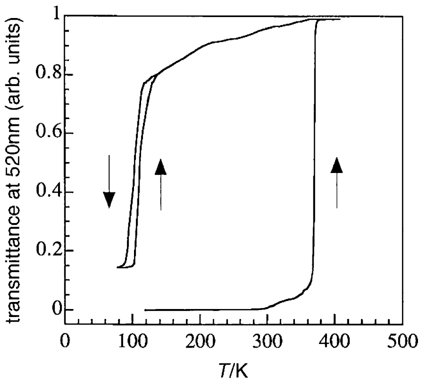

Figure 76. Thermal hysteresis observed by optical detection of the spin-state conversion for the complexes [Fe(hyetrz)$_3$](nps)$_2$·3H$_2$O and [Fe(hyetrz)$_3$](nps)$_2$. Reprinted with permission from ref 384. Copyright 1997 The Royal Society of Chemistry.

perature to 10 K. In the course of cooling, an exothermic peak due to a transition from the HT HS phase to the LS phase was detected at 200 K. The heat-capacity measurement was started for the specimen thus cooled. Although a heat-capacity peak originating in the phase transition from the LS phase to the HS phase was actually observed around 220 K, the magnitude of this peak depended on the heat treatment applied to the specimen. When the sample was annealed around 200 K, the more or less metastable LS phase was stabilized to the stable LS phase with evolution of heat and, as the result, the phase transition at 220 K disappeared. Instead, a large heat-capacity peak arising from the transition from the stable LS phase to the stable HS phase was observed at 280 K.

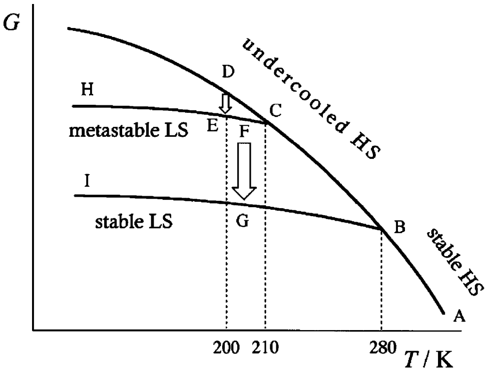

Figure 77. Gibbs energy relationship between various LS and HS phases realized in [Fe(2-pic)$_3$]Cl$_2$·H$_2$O. Reprinted with permission from ref 319. Copyright 2004 The Chemical Society of Japan.

The relationships between these phases are schematically shown in Figure 77 in terms of Gibbs energy. The phase transition at 280 K (temperature marked B in Figure 77) was always supercooled to about 200 K (path, A → B → C → D), and the supercooled HS phase was transformed to the metastable LS phase around 200 K (path, D → E). When the heating rate is high, this phase was transformed to the supercooled HS phase at 210 K (temperature marked C) through the path E → F → C → B → A. However, when the specimen was treated slowly around this temperature region, the metastable LS phase was stabilized to the stable LS phase around 200 K (path, F → G). The heat-capacity measurement for the specimen thus treated reflects the abrupt spin transition at 280 K (path, I → G → B → A). This new finding of the existence of the metastable LS phase clarifies the cause of the apparent thermal hysteresis loop spanning 204 and

295 K found in the earlier Mössbauer experiment.[361] As the time for recording a Mössbauer spectrum (usually several hours) is much longer than the annealing time, the sample relaxed near 200 K from the metastable to the stable LS phase (path, F → G). Thus, the cooling branch of the HS fraction derived from the Mössbauer spectra as a function of temperature followed the path A → B → C → D → E → F → G → I. When the sample was heated, the Mössbauer measurements recorded always the stable LS phase following the path I → G → B. At 280 K (B), the transition from the stable LS to the stable HS phase occurred. Thus, the path I → G → B → A in the heating mode is followed in both the Mössbauer and the heat-capacity experiments. A very similar phenomenon caused by the existence of a metastable LT phase is encountered in ferrocene crystal.[390,391]

8. Intramolecular Electron Transfer in Mixed-Valence Compounds

Mixed-valence chemistry is now a very attractive field of science.[231,392−395] In the mixed-valence MMX type and N(n-C_3H_7)$_4$[$Fe^{II}Fe^{III}(dto)_3$] complexes shown above, the charge transfer was involved in the relevant phase transitions and thereby the magnetic properties were altered. There is another category of mixed-valence complexes, in which the electronic state is strongly coupled with molecular vibrations and, as a result, labile molecular motions with large amplitude are excited. In these complexes, the magnetic properties remain unchanged between the valence-trapped state at LT and the valence-detrapped state at HT. Well-known examples of this category are the oxo-centered trinuclear basic metal acetate complexes with the formula [$M^{III}_2M^{II}O(O_2CCH_3)_6L_3$]·(solv) (L, monodentate ligand; solv, solvent molecule) and the 1′,1‴-disubstituted biferrocenium salts. Because the phase transitions arising from the intramolecular electron transfer in these mixed-valence complexes have already been reviewed by Sorai and Hendrickson,[11,12,396,397] a brief summary will be given here.

8.1. Trinuclear Mixed-Valence Compounds

Figure 78 shows the iron complex [$Fe_3O(O_2CCH_3)_6(py)_3$] (py, pyridine) at the valence-detrapped state at room temperature.[398] Each of three transition-metal ions is octahedrally coordinated by the central oxygen ion, a neutral pyridine, and four acetate ligands. Many of these complexes have been shown to convert from being valence-trapped at low temperatures to valence-detrapped at high temperatures.[396,397,399,400] One of the remarkable discoveries at the initial stage of the investigations was that the solvate molecules that are not explicitly coordinated to the central metal ions have a dramatic effect on the electron-transfer rate, while the nonsolvated analogue [$Fe_3O(O_2CCH_3)_6(py)_3$] remains in a valence-trapped state even at 315 K.[399,400]

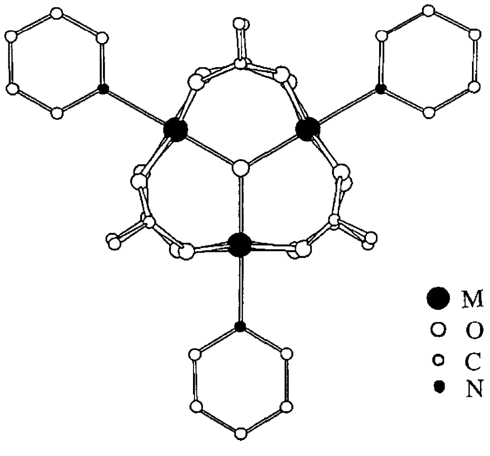

Figure 78. Molecular structure of the mixed-valence oxo-centered trinuclear basic metal acetate having a formula [$M^{III}_2M^{II}O(O_2CCH_3)_6(py)_3$] with D_{3h} symmetry in the valence-detrapped state.[398]

Formal states of oxidation in the trinuclear mixed-valence M_3O complex are two M(III) and one M(II). The M(II) ion is characterized by having an "extra" d-electron in comparison to the M(III). The electronic state of a free-molecule would be triply degenerated in the sense that the extra d-electron can reside on any one of three metal centers. Intramolecular electron-transfer between the metal centers in a trinuclear mixed-valence complex $M^{III}_2M^{II}O$ is usually treated by a theory incorporating vibronic interactions.[401−403] The extra d-electron residing on the low-oxidation metal center is coupled with the e_g symmetry M_3O stretching vibration via the vibronic interactions. In effect, the vibronic interaction includes a pseudo-Jahn−Teller distortion of the molecule and the 3-fold degeneracy may be lifted.[404] The adiabatic potential energy surface for the ground state of the mixed-valence M_3O complex provides three or four potential minima depending on the value of the electron-transfer integral between two metal ions, the force constant for the e_g stretching vibration, and the vibronic coupling constant of the d-electron to the e_g vibrational mode. The three potential minima correspond to three different isosceles triangles of a complex formed by the pseudo-Jahn−Teller distortion. In each of these states, the extra d-electron is located mainly on one of the three metal ions. The fourth potential minimum corresponds to a M_3O complex that has an equilateral triangular form, and the extra d-electron is coherently delocalized over all three metal ions.

Entropy gain due to the valence-detrapping phenomenon is straightforwardly related to a change in the number of microscopic states that are thermally accessible for a given mixed-valence complex. At low temperatures, the mixed-valence complex is valence-trapped and has statically one of the isosceles triangular configurations. However, depending on the magnitude of various parameters mentioned above, the dynamically interconverting mixed-valence complexes in the HT phase will gain either three or four microscopic states. In the former case, the valence-detrapping gives an entropy gain of $R \ln 3$, whereas in the latter case the entropy gain is $R \ln 4$.

The rate of intramolecular electron transfer is seriously affected by environmental effects in the solid state. In particular, solvate molecules that are not explicitly coordinated to the central metal ions but are stoichiometrically amalgamated in the crystal lattice play an important role for the intramolecular electron-transfer event.

The mixed-valence trinuclear complexes discussed here are [$M^{III}_2M^{II}O(L2)_6(L1)_3$]·(solv) (L1, monodentate ligand; L2, bidentate ligand; solv, solvate molecule). Sorai and his collaborators measured heat capacities of [$Fe_3O(O_2CCH_3)_6(py)_3$]·(py) (**1**),[405,406] [$Mn_3O(O_2CCH_3)_6(py)_3$]·(py) (**2**),[407,408] [$Fe_3O(O_2CCH_3)_6(py)_3$]·($CHCl_3$) (**3**),[409,410] [$Fe_3O(O_2CCH_3)_6$(4-Me-py)$_3$]·($CHCl_3$) (**4**),[411] [$Fe_3O(O_2CCH_3)_6$(3-Me-py)$_3$]·(3-Me-Py) (**5**),[412] and [$Fe_3O(O_2CCH_3)_6$(3-Me-py)$_3$]·(toluene) (**6**),[413] together with a solid solution [$Fe^{III}_2Fe^{II}_{0.5}Co^{II}_{0.5}O(O_2CCH_3)_6(py)_3$]·(py) (**7**)[414] and a nonmixed-valence ana-

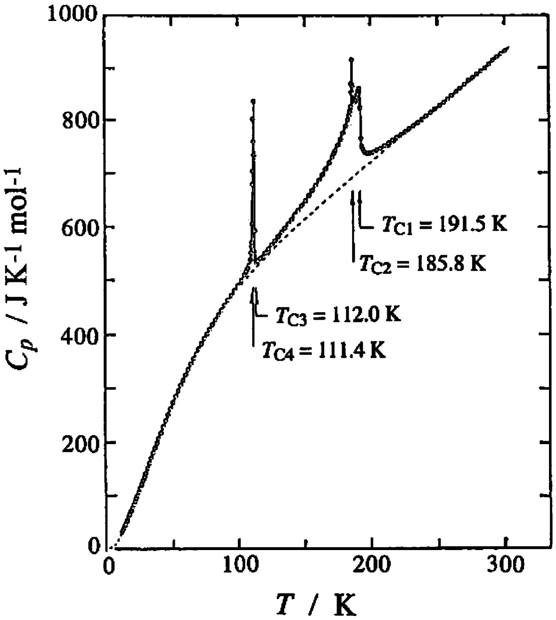

Figure 79. Molar heat capacity of the mixed-valence complex $[Fe_3O(O_2CCH_3)_6(py)_3]\cdot(py)$. The broken curve indicates the normal heat capacity. Reprinted with permission from ref 406. Copyright 1986 American Chemical Society.

logue $[Fe^{III}_2Co^{II}O(O_2CCH_3)_6(py)_3]\cdot(py)$ (**8**).[414] The complexes **1**−**4** commonly crystallize into an identical rhombohedral crystal system with the space group *R*32 in the valence-detrapped HT phases.

The variable-temperature ^{57}Fe Mössbauer spectra of the complex **1** reported by Hendrickson and his collaborators[399,400] showed dramatic changes with temperature. At temperatures below about 100 K, two quadrupole-split doublets are seen as follows: one characteristic of HS iron(II) and the other of HS iron(III). As the temperature is increased, an extra doublet appears abruptly around 110 K at the expense of the initial two doublets. This means that the new doublet arises from the electron-delocalized state. The spectrum eventually becomes a single doublet above about 190 K. This fact indicates that the rate of intramolecular electron-transfer exceeds the rate of 10^7 s^{-1}, which the Mössbauer technique can sense. Figure 79 shows the molar heat capacity of this complex.[405,406] This complex exhibits essentially two kinds of phase transitions: One is a first-order phase transition at about 112 K and the other is a higher-order phase transition around 190 K. Interestingly, the LT phase transition takes place at the temperature at which the first change in the Mössbauer spectrum occurs and the peak temperature of the HT phase transition is identical with the temperature where the Mössbauer spectrum becomes a single average doublet. Moreover, the large temperature range involved in the HT phase transition fully overlaps with the temperature region where the drastic change in the Mössbauer spectrum is occurring. Therefore, the observed phase transitions are concluded to arise from the intramolecular electron-transfer event in the mixed-valence complex. The entropy gain associated with the phase transitions is (30.6 ± 0.8) J K^{-1} mol^{-1}. The phase transition behavior is drastically altered only by substitution of the central metal ions. Figure 80 represents molar heat capacity of $[Mn_3O(O_2CCH_3)_6(py)_3]\cdot(py)$.[407,408] This complex brings about a sharp first-order phase transition at 184.7 K, and the transition entropy amounts to $\Delta S = 35.8$ J K^{-1} mol^{-1}, which is much greater than that of the homologous iron complex.

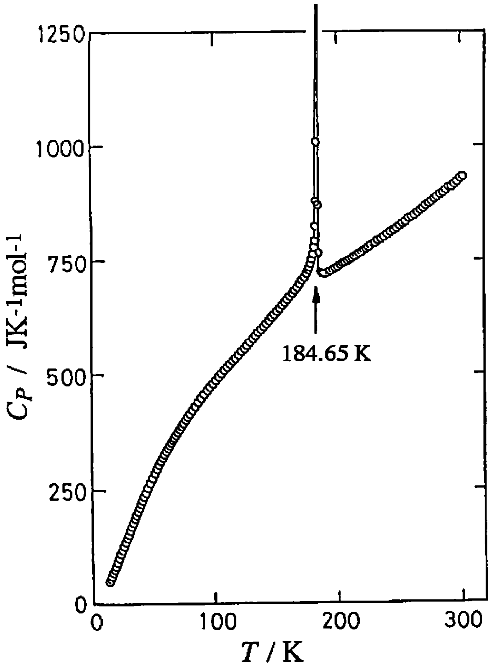

Figure 80. Molar heat capacity of the mixed-valence complex $[Mn_3O(O_2CCH_3)_6(py)_3]\cdot(py)$. Reprinted with permission from ref 407. Copyright 1989 American Chemical Society.

Thermodynamic data concerning the phase transition are summarized in Table 8. Because the entropy due to the valence-detrapping is either *R* ln 3 (= 9.1 J K^{-1} mol^{-1}) or *R* ln 4 (= 11.5 J K^{-1} mol^{-1}) at most, the observed transition entropies obviously contain extra contributions other than the intramolecular electron transfer. A clue for the extra candidates lies behind its crystal structure. A schematic drawing of the molecular packing in the valence-detrapped HT phase of $[Fe_3O(O_2CCH_3)_6(py)_3]\cdot(py)$ is shown in Figure 81.[398] For simplicity, the acetato ligands are not drawn. As described above, the space group of this crystal is *R*32. Along the crystallographic C_3 axis, the metal complexes and pyridine solvate molecules occupy alternating sites of the 32 symmetry. That is, each pyridine solvate molecule is sandwiched between two metal complexes. The plane of the pyridine solvate molecule is perpendicular to the metal-complex plane. As required by the presence of the C_3 axes along which the metal complexes are stacked, the pyridine solvate molecules are disordered, with at least three orientational positions. On the other hand, solid-state ^{2}H NMR for the iron complex with deuterated pyridine solvate molecule studied by Hendrickson and his collaborators[398] revealed detailed molecular dynamics. As illustrated in Figure 82, the molecular plane of the pyridine jumps among three positions about the crystallographic C_3 axis. In each planar position, the pyridine solvate molecule librates among four positions, where in each of these positions two carbon atoms are on the C_3 axis. As the result, the pyridine solvate molecule converts from being static to dynamically interconverting among 12 different orientations.

Now, the transition entropy can be interpreted as follows. If each metal complex converts from being statically distorted in one state to interconverting dynamically between three vibronic states when the complex is heated from low temperatures, this contributes *R* ln 3 to the entropy gain. The sum of *R* ln 3 for the metal complex and *R* ln 12 for the

Table 8. Entropy Gain at the Phase Transitions Observed in the Mixed-Valence Complexes with the Formula $[M^{III}_2M^{II}O(O_2CCH_3)_6L_3]\cdot$(solv) (in the Unit of J K^{-1} mol^{-1})[a]

	complex					entropy gain				
	M(III)	M(II)	L	solv	T_{trs} (K)	Δ*S*(metal)	Δ*S*(solv)	Δ*S*(calcd)	Δ*S*(obsd)	refs
1	Fe	Fe	py	py	112, 191	*R* ln 3	*R* ln 12	29.8	30.6 ± 0.8	405, 406
8	Fe	Co	py	py	150		*R* ln 3	9.1	10.3	414
2	Mn	Mn	py	py	185	*R* ln 4	*R* ln 18	35.6	35.8	407, 408
3	Fe	Fe	py	$CHCl_3$	208	*R* ln 4	*R* ln 8	28.8	28.1 ± 0.4	409, 410
4	Fe	Fe	4-Me-py	$CHCl_3$	94	*R* ln 4	*R* ln 2	17.3	17.2 ± 1.4	411
5	Fe	Fe	3-Me-py	3-Me-py	282	*R* ln 3	*R* ln 2	14.9	13.7 ± 0.7	412
6	Fe	Fe	3-Me-py	toluene	293	*R* ln 3	*R* ln 2	14.9	15.1	413

[a] Δ*S*(metal), entropy gain due to conformational change of the M_3O complex; Δ*S*(solv), entropy gain due to orientational disordering of the solvate molecule; and Δ*S*(calcd), Δ*S*(metal) + Δ*S*(solv).

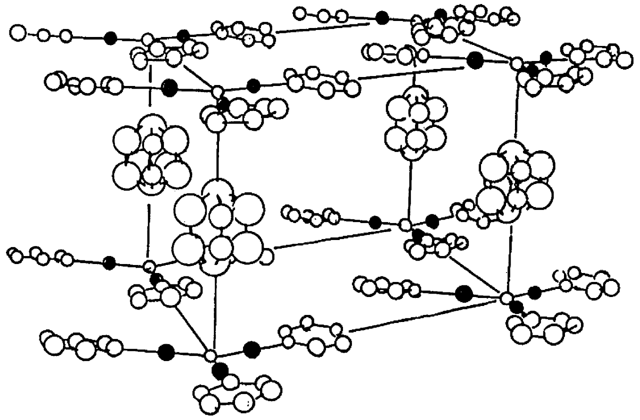

Figure 81. Schematic drawing of the crystal structure of $[Fe_3O(O_2CCH_3)_6(py)_3]\cdot$(py). The acetato ligands are not shown for clarity. Crystallographic C_3 axis runs through the central oxygen atoms of the Fe_3O complexes. Reprinted with permission from ref 398. Copyright 1987 American Chemical Society.

pyridine solvate molecules is *R* ln 36 (= 29.8 J K^{-1} mol^{-1}). This value agrees well with the observed entropy gain (30.6 ± 0.8) J K^{-1} mol^{-1}. This fact provides definite evidence that the intramolecular electron transfer does proceed in cooperation with orientational disordering of the solvate molecule.

As evidenced by many instances (see Table 8), the intramolecular electron transfer occurs in these trinuclear mixed-valence complexes by coupling with the onset of orientational disordering of the solvate molecules. The intermolecular interactions responsible for such a coupling may be electric dipole−dipole interactions between the complex and the solvate molecules. Actually, when the solvate molecule is benzene having no electric dipole moment, the mixed-valence complex does not bring about a phase transition arising from the electron transfer.

A simple but fundamental question arises here as to why only the $[Fe_3O(O_2CCH_3)_6(py)_3]\cdot$(py) complex exhibits two phase transitions (a first-order phase transition at low temperature and a higher-order transition at high temperature) in contrast to a single first-order phase transitions in other complexes. The first statistical theoretical model to describe the phase transitions observed for mixed-valence Fe_3O complexes was proposed by Kambara et al.[404] Stratt and Adachi[415] took an imaginative and insightful approach. Although their theory ignores the effects of the solvate molecules, qualitative aspects inherent in the phase transitions occurring in the trinuclear mixed-valence complexes are well-interpreted.

It should be remarked here that the onset of conformational change of solvate molecule is not necessarily a condition for intramolecular electron transfer. For example, although a crystal of mixed-valence complex $[Fe_3O(O_2CCH_2CN)_6(H_2O)_3]$ does not contain any solvate molecules, a phase transition due to valence-detrapping really occurs at 128 K.[416] Nakamoto et al.[417] reported that the mixed-valence trinuclear iron monoiodoacetate complex previously reported as $[Fe_3O(O_2CCH_2I)_6(H_2O)_3]$[418] is an unusual compound. On the basis of XRD analysis, they found that its correct formula should be $[Fe^{III}_2Fe^{II}O(O_2CCH_2I)_6(H_2O)_3][Fe^{III}_3O(O_2CCH_2I)_6(H_2O)_3]I$. The two kinds of Fe_3O molecules ($Fe^{III}_2Fe^{II}O$ and Fe^{III}_3O) are crystallographically indistinguishable. All of the iron atoms are crystallographically equivalent because of a crystallographic 3-fold symmetry. The heat capacity of this complex seems to exhibit no thermal anomaly in the temperature range of 5.5−309 K, although the valence detrapping phenomenon has been observed in this temperature range. This fact indicates that the valence-detrapping phenomenon in this complex occurs without any phase transition, leading this complex to a glassy state, probably because the crystal of this complex is just like a solid solution

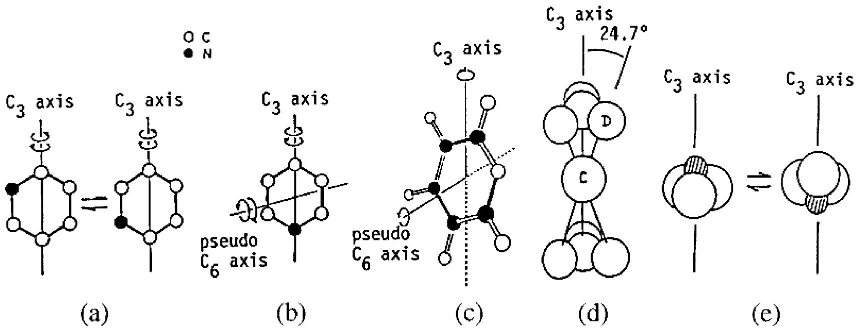

Figure 82. Orientational disordering of the solvate molecules in the crystal lattice of the trinuclear complexes $[M_3O(O_2CCH_3)_6(L1)_3]\cdot$(solvate), designating [M, L1, solvate] for short. (a) Pyridine in [Fe, py, py],[398] (b) pyridine in $[Fe_2CoO(O_2CCH_3)_6(py)_3]$(py),[414] (c) pyridine in [Mn, py, py],[408] (d) deuterated chloroform in [Fe, py, $CDCl_3$],[409] and (e) chloroform in [Fe, 4-Me-py, $CDCl_3$].[411]

of distorted mixed-valence $Fe^{III}_2Fe^{II}O$ molecules and permanently undistorted Fe^{III}_3O molecules, which may act as an inhibitor for a cooperative valence-trapping.

Stadler et al.[419] reported electron transfer in a trinuclear oxo-centered mixed-valence iron complex $[Fe^{III}_2Fe^{II}OL_3]$, in which L^{2-} is a pentadentate ligand designed to coordinate all three metal atoms in the central cluster. The crystal structure of this complex shows 3-fold symmetry, attributed to rotational disorder. The magnetization data indicate strong superexchange between basis oxidation states Fe(3+, 3+, 2+). The Mössbauer spectra indicate significant valence delocalization even at a low temperature (4.2 K) with estimated valences Fe(2.9+, 2.9+, 2.2+) in the solid state. At higher temperatures, no lifetime broadening is observed but additional Mössbauer absorptions are consistent with increasing proportions of trinuclear complexes with greater delocalization, Fe(2.75+, 2.75+, 2.5+).

8.2. Binuclear Mixed-Valence Compounds

Electron transfer in binuclear mixed-valence complexes consisting of 1′,1‴-disubstituted biferrocenium cations (see Figure 83) is also of interest. Electron transfer in mixed-valence molecular systems is generally described by the PKS model[232] based on a vibronic approach. As mixed-valence complexes are electronically labile, the lowest energy electronic states are vibronic, and as a result, the complexes are very sensitive to their environments.[420] In the absence of environmental effects, a binuclear $Fe^{II}Fe^{III}$ mixed-valence complex has two electronic states, which would be electronically degenerate. The two potential energy curves would be superimposed and strong vibronic coupling would result. Certain vibrational coordinates, such as the out-of-phase combination of the totally symmetric ring−metal−ring breathing modes on each metallocene moiety in Figure 83 would couple to the two electronic states. Two energetically degenerate vibronic states result, for which the two parabolic potential-energy curves are displaced relative to each other in the nuclear coordinate space Q_0 of the coupled vibrational mode.[397,421] If these two vibronic states interact, one can expect an adiabatic potential shown in Figure 84a.[421] The ground-state surface has two minima, both at the same energy. In general, there will be several vibrational energy levels below the barrier height ΔE_B. In Figure 84a, only the zeroth vibrational level and one fundamental at $h\nu$ are shown, where h is the Planck constant and ν is the vibrational frequency.

For a binuclear $Fe^{II}Fe^{III}$ complex in an asymmetric environment, just as in the solid state, the potential energy diagram is as shown in Figure 84b. The two vibronic states are not at the same energy. There is an energy difference ΔE between the two states. This difference reflects the different environments near the two iron ions in the binuclear complex. The $Fe_a^{II}Fe_b^{III}$ vibronic state is stabilized relative to the $Fe_a^{III}Fe_b^{II}$ vibronic state. When the thermal energy kT is less than ΔE, the complex is found in the $Fe_a^{II}Fe_b^{III}$ state. If the complex is to convert from $Fe_a^{II}Fe_b^{III}$ to $Fe_a^{III}Fe_b^{II}$, it needs to be thermally excited by ΔE or more. Because there will be many vibrational levels on both sides of the asymmetric double well, it can then tunnel from a “left” vibrational level to a vibrational level on the “right” side.

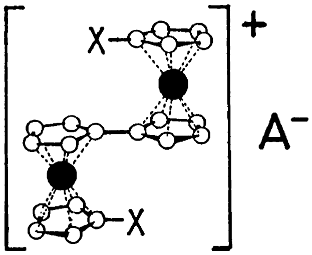

Figure 83. Schematic drawing of molecular structure of mixed-valence 1′,1‴-disubstituted biferrocenium cation (X, substituent, A^-, anion such as I_3^-, PF_6^-, or SbF_6^-).

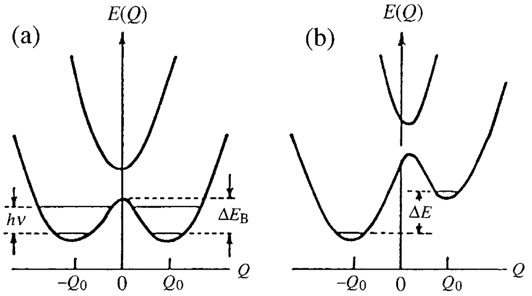

Figure 84. Potential energy surface $E(q)$ drawn as a function of the out-of-phase combination ($Q = Q_A - Q_B$) of the two symmetric metal−ligand breathing vibrational modes (Q_A and Q_B) of the two halves of a binuclear mixed-valence species (a) for a symmetric mixed-valence complex in the absence of environmental effects and (b) for results if the environment about the binuclear mixed-valence complex is asymmetric. Reprinted with permission from ref 421. Copyright 1987 American Institute of Physics.

Vibronic coupling works efficiently to make a small polaron migrate over the metal centers within a complex molecule. Those compounds possess a potential of charge ordering in their crystalline phases at low temperatures.[422,423] Transitions between such a valence-trapped and a valence-detrapped state have been observed by Mössbauer spectroscopy in some binuclear complexes. Nonsubstituted biferrocenium triiodide[424] and many dialkylbiferrocenium triiodides[425,426] are known to bring about a transition from a valence-trapped to a valence-detrapped state above 200 K.

1′,1‴-Diiodobiferrocenium hexafluoroantimonate[427] really gave rise to a phase transition arising from the valence-detrapping at 134 K. The entropy gain (6.0 ± 0.5) J K^{-1} mol^{-1} is very close to $R \ln 2$ (= 5.76 J K^{-1} mol^{-1}), the value expected for two energetically equal vibronic states as shown in Figure 84a. In contrast to this, biferrocenium triiodide[428] and 1′,1‴-diethylbiferrocenium triiodide[429] bring about very small heat-capacity anomalies at 328 and 250 K with the entropy gains of only (1.77 ± 0.06) and 1.0 J K^{-1} mol^{-1}, respectively.

Interestingly, when the substituent X in Figure 83 is Br or I and A^- is I_3^-, the 1′,1‴disubstituted-biferrocenium triiodides remain in a valence-detrapped state even at 4.2 K.[430,431] Structural analysis for 1′,1‴-diiodobiferrocenium triiodide (hereafter, $I_2Fe_2^+I_3^-$ for short)[432] revealed that two iron atoms in a cation are related to each other by a symmetry center and thus are equivalent at room temperature. This fact means that $I_2Fe_2^+I_3^-$ is in the valence-detrapped state at room temperature. Even at 4.2 K, the two iron atoms in the cation remain equivalent, because only one quadrupole-split doublet was observed by ^{57}Fe Mössbauer spectroscopy and EPR measurements at 4.2 K gave a relatively isotropic g tensor characteristic of a valence-detrapped state.[430] It is noted,

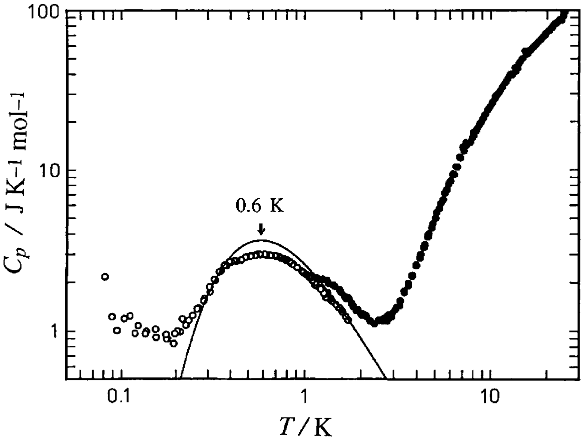

Figure 85. Molar heat capacity of the mixed-valence complex 1′,1‴-diiodobiferrocenium triiodide. The solid curve shows the two-energy level Schottky anomaly with $\delta/hc = 1$ cm^{-1}. Reprinted with permission from ref 433. Copyright 1992 Elsevier Ltd.

however, that the valence-detrapped phase should be interpreted not as a statically electron-delocalized state (i.e., single-minimum potential) but as a dynamically disordered state, because IR spectroscopy shows the existence of a potential barrier separating two valence-trapped configurations of the cation.[432] These two configurations are, therefore, degenerate at high temperatures and contribute R ln 2 to the entropy.

To elucidate how this entropy is removed at low temperatures, say below 4.2 K, following the requirement of the third law of thermodynamics, Nakano et al.[433] measured the heat capacity of $I_2Fe_2^+I_3^-$ complex by adiabatic calorimetry between 80 mK and 25 K. One of two ways might be anticipated as follows: either a phase transition or none. If a phase transition occurs, this complex would have a charge-ordered ground state similar to those in other biferrocenium salts.[427−429] On the other hand, if no phase transitions take place, a quantum-mechanical tunneling would be incorporated into the double-minimum adiabatic potential so as to lift the degeneracy without long-range order. The observed heat capacity of the $I_2Fe_2^+I_3^-$ complex is shown in Figure 85 on a logarithmic scale. Open circles plotted below 2 K correspond to a pellet sample, while solid circles between 1 and 25 K are for a powder sample. A discrepancy detected between the two sets of data is based on a result in the pellet sample.[433] Two heat-capacity anomalies were found as follows: One takes place below ca. 0.2 K, and the other is a broad peak centered around 0.6 K. The former arises from a magnetic interaction between the paramagnetic cations. The anomaly occurring around 0.6 K is obviously a Schottky type heat capacity corresponding to a thermal excitation between two energy levels. The solid curve in Figure 85 corresponds to a two-level Schottky heat capacity with an energy difference of $\delta/hc = 1$ cm^{-1}, where c is the velocity of light. The presence of the Schottky heat-capacity anomaly demonstrates the existence of a double-well potential: There is a tunnel splitting between the vibronic ground states and hence a charge-ordering phase transition in $I_2Fe_2^+I_3^-$ is absent. This type of nuclear tunneling has been expected to exist in the mixed-valence systems both from experiment[428] and from a theoretical treatment by Kambara et al.[421,434] However, it is indeed in this complex that the nuclear tunneling was actually and directly observed for the first time. In the sense that the quantum effect prevents the charge ordering with ferroelectric long-range order, the $I_2Fe_2^+I_3^-$ complex is regarded as a molecular quantum paraelectric. In fact, a Curie-like behavior characteristic of a paraelectric was observed in a preliminary dielectric measurement with the 0.4−20 kHz frequency range between 4 and 300 K.[433]

9. Thermochromic Complexes

Many transition metal complexes change color in the solid state depending on the temperature. This phenomenon, the so-called thermochromism,[435,436] involves a change in electronic state of a molecule and thus a change in the magnetic properties. Because a review for calorimetric studies on thermochromic complexes has already been given elsewhere,[11,12,14] a brief summary will be presented here.

The electronic energy of transition-metal complexes may be perturbed by changes in (i) electron configuration, (ii) coordination geometry, (iii) coordination number, (iv) molecular motion of ligands, and so on. A typical example due to cause (i) is encountered in the spin crossover complexes described in chapter 7. Thermochromism due to (ii) is observed in structural isomers of coordination compounds. Some nickel complexes are known to exhibit two structural isomers: One is a diamagnetic green form with square-planar coordination geometry, and the other is a tetrahedral paramagnetic brown form. A calorimetric study has been done for bis[*N*-(3-methoxysalicylidene)isopropylaminato]nickel(II).[437]

9.1. Thermochromism Due to a Change in the Coordination Number

Thermochromism due to (iii) is seen in (i-PrNH$_3$)[CuCl$_3$], where the color of the solid abruptly changes from brown to orange when the crystal is heated above room temperature. On the basis of XRD, NMR, EPR, DSC, and magnetic susceptibility measurements, Roberts et al.[438] revealed that the LT phase of (i-PrNH$_3$)[CuCl$_3$] belongs to a triclinic crystal system, while the HT phase is orthorhombic and that the coordination geometry around the central copper atom changes grossly through the thermochromic transition at 324 K: The coordination number of a copper atom changes from five in the LT phase to six in the HT phase. The isopropylammoniumu cations are ordered and hydrogen-bonded to one of the terminal chloride ions in the LT phase. In contrast, in the HT phase, the isopropylammoniumu cations are disordered and thereby the hydrogen bonds are weakened. As a result, the terminal chloride ion that is otherwise hydrogen-bonded to isopropylammonium cation bridges two adjacent copper ions. The HT phase contains tribridged linear chains of $[(CuCl_3)^-]_\infty$, while the LT phase contains bibridged linear chains of $[(Cu_2Cl_6)^{2-}]_\infty$. The heat capacity determined by Nishimori and Sorai[439] revealed a phase transition at 335.6 K. The enthalpy and entropy gains at the thermochromic phase transition were $\Delta H = 5.54$ kJ mol^{-1} and $\Delta S = 16.5$ J K^{-1} mol^{-1}, respectively. Of the observed entropy gain, $\Delta S = 16.5$ J K^{-1} mol^{-1}, the 2-fold disordering of the cations contributes R ln 2 (= 5.8 J K^{-1} mol^{-1}) to the entropy, while there is substantially no contribution from the acoustic lattice vibrations because of no volume change at the transition. The remaining entropy, 10.7 J K^{-1} mol^{-1} may be attributed to the excess contribution from the optical metal−ligand skeletal vibrations due to the change in the coordination number.

9.2. Thermochromism Due to Molecular Motion of the Ligands

A typical example of the thermochromism due to (iv) is that occurring in square-planar copper(II) complex $[Cu(daco)_2](NO_3)_2$ (daco, 1,5-diazacyclooctane, an eight-membered ring molecule shown in Figure 86).[440] The color of the crystal is brilliant orange but changes to violet discontinuously when heated above 360 K and reverts to orange on cooling. On the basis of X-ray study for a single crystal, Hoshino et al.[441] concluded that the thermochromic mechanism for $[Cu(daco)_2](NO_3)_2$ might involve a ligand−anion interaction rather than metal−anion bonding. Figure 87 illustrates the molar heat capacity of $[Cu(daco)_2](NO_3)_2$ determined by adiabatic calorimetry by Hara and Sorai.[442] A large heat-capacity anomaly associated with the thermochromic phenomenon was found at 359 K. This phase transition exhibits both superheating and supercooling effects, indicating a first-order phase transition. The thermodynamic quantities due to the phase transition were $\Delta H = (8.40 \pm 0.22)$ kJ mol^{-1} and $\Delta S = (23.4 \pm 0.8)$ J K^{-1} mol^{-1}. The large entropy gain implies that softening of molecular or lattice vibrations and/or onset of orientational disordering of the daco ligand or the nitrate anion would be involved in the phase transition. For the present thermochromic compound, however, the possibility of softening of optical vibrational modes is precluded, because the IR spectra showed no detectable shift of absorption bands on going from one phase to the other. The authors[442] speculated that dynamic interconversion of a daco-ligand between a chair and a boat form might take place in the HT phase. If this is the case, each daco-ring will gain four conformations as shown in Figure 88 (i.e., chair−chair, chair−boat, boat−chair, and boat−boat), and the total number of conformations per $[Cu(daco)_2]^{2+}$ cation amounts to 16 (= 4 × 4), because a cation contains two daco ligands. According to the Boltzmann principle, the conformational entropy is estimated to be $R \ln 16$ (= 23.05 J K^{-1} mol^{-1}). This entropy gain accounts surprisingly well for the observed transition entropy of $\Delta S = (23.4 \pm 0.8)$ J K^{-1} mol^{-1}.

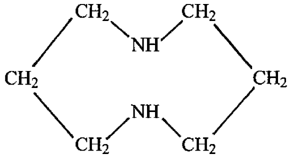

Figure 86. Molecular structure of eight-membered ring molecule 1,5-diazacyclooctane (daco for short).

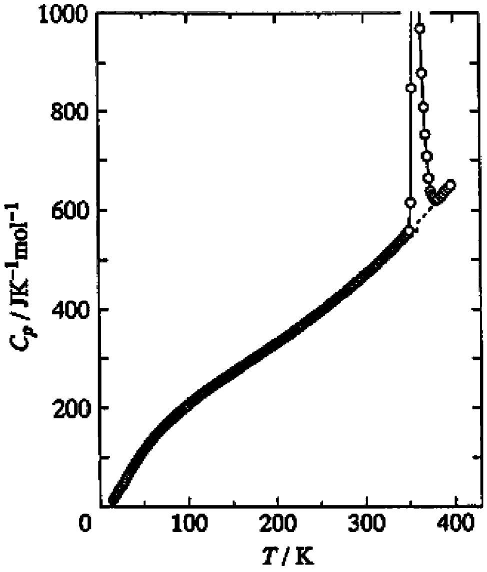

Figure 87. Molar heat capacity of the thermochromic compound $[Cu(daco)_2](NO_3)_2$. The broken curve shows the normal heat capacity. Reprinted with permission from ref 442. Copyright 1995 Elsevier Ltd.

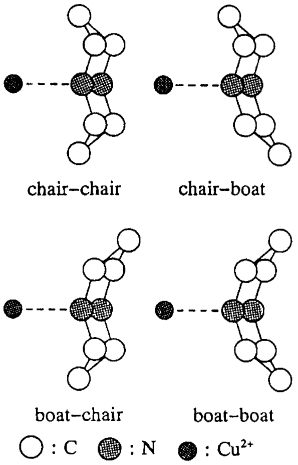

Figure 88. Schematic drawing of four conformations of the eight-membered daco ring having almost equal energy. Reprinted with permission from ref 442. Copyright 1995 Elsevier Ltd.

The relationship between the color change and the change in the electronic state of the $[Cu(daco)_2]^{2+}$ ion is interpreted as follows. A single-crystal X-ray study[441] revealed that the structure is centrosymmetric with the center of symmetry on the site of Cu and the CuN_4 chelate plane is planar, but it is not precisely square since the two Cu−N coordination bonds of a daco ligand differ in length significantly. On the other hand, in the HT phase, eight-membered daco ligands undergo dynamic conformational changes between the boat and the chair forms, and thereby, the CuN_4 chelate plane is dynamically distorted from a planar form probably to a distorted tetrahedral coordination geometry. When such a planar-to-tetrahedral geometrical change occurs, a red shift in the *d*−*d* transition is expected, as indicated by a theoretical angular overlap method.[443] The visible spectrum of $[Cu(daco)_2](NO_3)_2$ indeed exhibits such a red shift.[440,441]

9.3. Enthalpy Change Due to Thermochromism

A quite similar situation has been encountered in a homologous series of thermochromic complexes with formula $[M(dieten)_2]X_2$, where M is Cu(II) or Ni(II), dieten is *N*,*N*-diethyl-ethylenediamine, and X is BF_4^- or ClO_4^-. The copper complexes show a color change from red to blue-violet and the color of the nickel complexes changes from orange to red when they undergo phase transition in the solid state. It was initially thought that the thermochromism was caused by axial approach of the anions to the copper or nickel ion. However, when the crystal structures of both the LT and the HT phases were determined, that idea turned out to be wrong.[444,445] There exists no axial coordination of the counteranions in either of the phases because the bulky alkyl groups bonded to the nitrogen atoms prevent the counter-anions from approaching the central metal atom. A new mechanism of thermochromism was proposed as follows: In the HT phase, the chelate rings pucker up and down while they remain static in the LT phase. Such ring motion affects the ligand field strength, leading to the color change. This mechanism seems to be consistent with various experimental

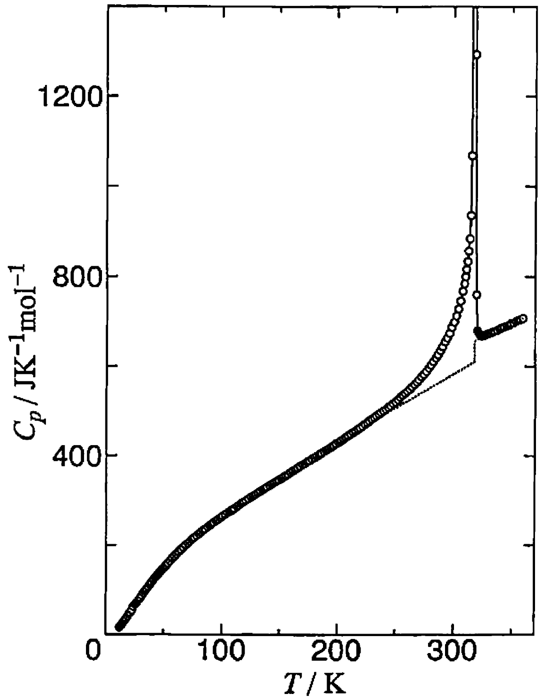

Figure 89. Molar heat capacity of the thermochromic compound [Cu(dieten)$_2$](ClO$_4$)$_2$. Dotted curves show the normal heat capacities of the LT and HT phases, resulting in a heat capacity jump at the transition temperature. Reprinted with permission from ref 450. Copyright 1996 Taylor & Francis Group.

results so far available. However, the relationship between the microscopic aspects[444−448] hitherto reported and the macroscopic energetic and entropic aspects was still unclear.

Nishimori et al. measured heat capacities of [Cu(dieten)$_2$]X$_2$ by adiabatic calorimetry.[449,450] Figure 89 represents the molar heat capacity of [Cu(dieten)$_2$](ClO$_4$)$_2$.[450] A large single peak due to the thermochromic phase transition was found at 317.64 K. This phase transition is characterized by a long heat-capacity tail extending down to about 200 K. Moreover, the normal heat-capacity curve has a jump of 46 J K^{-1} mol^{-1} at the transition temperature between the LT and the HT phases. Thermodynamic gains were $\Delta H = 17.4$ kJ mol^{-1} and $\Delta S = 55.2$ J K^{-1} mol^{-1}.

XRD analysis[444,445] provides a useful clue to the molecular freedom responsible for the entropy gain. The most remarkable change in the structure occurring through the phase transition is the motion of the chelate rings, which is easily seen from anisotropic thermal ellipsoids of the constituent atoms. The chelate rings are puckering up and down from the CuN$_4$ plane in the HT phase. Provided that this chelate ring puckering is responsible for an essential part of the transition mechanism, the enthalpy gain at the phase transition is estimated as follows. One assumes that the chelate rings are static at very low temperatures, whereas they pucker in the HT phase. There are two chelate rings in a cation, consisting of a five-membered CuN$_2$C$_2$ ring. When the plane formed by the CuN$_2$ is fixed, the five-membered ring has four different conformations: two conformations in which two carbon atoms are tipped off to the same side of the plane and two conformations in which two carbon atoms are tipped off to the opposite sides of the plane. It should be remarked that the number of degrees of freedom for the puckering motion of a five-membered ring is two. Moreover, because there exist two chelate rings in a cation, so the total number of the puckering modes amounts to four. These four modes are roughly assumed to be degenerate and can be simply approximated by the Einstein harmonic oscillator. If one assumes that this puckering motion is responsible for the total entropy of transition, the Einstein characteristic frequency is estimated to be 115 cm^{-1} for [Cu(dieten)$_2$](ClO$_4$)$_2$. On the basis of this frequency, the heat-capacity jump at the transition temperature is estimated as ΔC(ligand) = 33 J K^{-1} mol^{-1} and ΔH(ligand) = 8.0 kJ mol^{-1}. The heat-capacity jump is comparable with the observed value of 46 J K^{-1} mol^{-1}. The contribution of the chelate-ring puckering ΔH(ligand) to the observed ΔH(obsd) is about 46%.

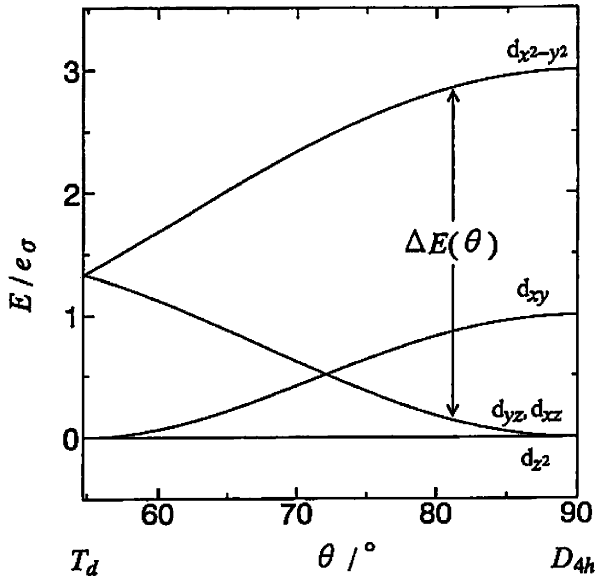

Figure 90. Energy level diagram correlating tetrahedral and planar coordination geometries calculated on the basis of the angular overlap model. Reprinted with permission from ref 450. Copyright 1996 Taylor & Francis Group.

According to the X-ray structural analysis of [Cu(dieten)$_2$](ClO$_4$)$_2$,[444,445] there is no significant change in the Cu−N distances, whereas the trans bond angles of N−Cu−N change slightly through the phase transition. In the LT phase, the angles are 180.0° while in the HT phase they are 178.0 and 174.7°. The [Cu(dieten)$_2$]$^{2+}$ cation is characterized by a square-planar coordination geometry in the LT phase. This geometry is slightly distorted toward a tetrahedral coordination in the HT phase. Despite such a small geometrical change, the color of complexes changes dramatically when the phase transition occurs. The color of the complexes depends obviously on the absorption of visible light by a molecule. The absorption spectra in the visible region depend on the energy-level splitting of the d-orbitals. Variable-temperature d−d transition of [M(dieten)$_2$]X$_2$ has already been studied.[446,447] These complexes show a red shift in the d−d transition when they are heated. To investigate the relationship between the absorption spectra and the d-orbital energy levels, the angular overlap model (AOM)[443] was adopted. The relative energies of the five d-orbitals can be calculated as a function of the polar angles (θ, ϕ) of the ligand position vectors. The calculated energy levels are illustrated in Figure 90 as a function of θ.[450] The visible light absorption maximum (ν_{max}) is shifted from 20700 cm^{-1} in the LT phase to 19305 cm^{-1} in the HT phase for [Cu(dieten)$_2$](ClO$_4$)$_2$.[446,447] The absorption maximum in the electronic spectrum corresponds to the d_{yz}, d_{xz} → $d_{x^2-y^2}$ transition. Namely, the transition energy is the energy difference between these two orbitals, $\Delta E(\theta)$ in Figure 90. In the LT phase, because the coordination geometry is D_{4h}, $\Delta E(90°)$ is equal to the absorption maximum observed at lower temperature, while in the HT phase $\Delta E(\theta)$ is equal to the absorption maximum recorded at higher temperature. Therefore, the following relation is obtained

$$\frac{\Delta E(90°)}{\Delta E(\theta)} = \frac{h\nu_{\max} \text{ at low temperature}}{h\nu_{\max} \text{ at high temperature}} \qquad (10)$$

The enthalpy (actually the internal energy) of the *d*-orbitals is the sum of each electron's energy. The d-electrons are accommodated in the energy level diagram shown in Figure 90, one by one from bottom to top. There are nine d-electrons in the copper complexes. The energy of the *d*-orbitals in the LT phase is calculated from the energy scheme at $\theta = 90°$ whereas that in the HT phase is calculated from the scheme at the θ estimated from the equation given above. Consequently, the enthalpy change of the *d*-orbitals arising from the change in the coordination geometry is straightforwardly determined as the difference between the electron energies of the LT and the HT phases. The contribution of the *d*-orbital energy to the transition enthalpy amounted to 8.4 kJ mol^{-1} for [Cu(dieten)$_2$](ClO$_4$)$_2$.

The observed transition enthalpy may be regarded as consisting of two contributions: One is the enthalpy gain due to the onset of the puckering motion of the metal−ligand chelate rings and the other is the electronic energy gained by a change in the coordination geometry across the phase transition. These two contributions were analyzed in terms of the harmonic oscillator model and the angular overlap model, respectively. As estimated above, the former is ΔH(ligand) = 8.0 kJ mol^{-1} and the latter amounts to ΔH(AOM) = 8.4 kJ mol^{-1}. The sum of these contributions corresponds to ΔH(total) = 16.4 kJ mol^{-1}. Surprisingly, this theoretical value well accounts for the observed value, ΔH (obsd) = 17.4 kJ mol^{-1}. Even better agreement has been attained for [Cu(dieten)$_2$](BF$_4$)$_2$, in which ΔH(obsd) and ΔH(total) are 16.6 and 16.8 kJ mol^{-1}, respectively.

10. Concluding Remarks

Important and unique roles played by heat-capacity calorimetry in the fields of molecule-based magnetism have been reviewed by focusing on phase transitions occurring not only under ambient pressure but also under applied pressure and magnetic field. The subjects cover genuine organic free radicals, hybrid compounds between organic and inorganic moieties, assembled-metal complexes, single-molecule magnets, spin crossover complexes, mixed-valence complexes, and thermochromic complexes. The molecule-based magnets exhibit low-dimensionality concerning the magnetic lattices formed by magnetic interactions, owing to structural anisotropy inherent in the constituent molecule moieties. This aspect is clearly reflected in the heat-capacity calorimetry. By revealing the mechanisms of magnetic interactions inherent in such low-dimensional systems, one can gain fundamental insights into fascinating molecule-based magnets.

The most precise and accurate heat-capacity calorimetry has so far been accomplished by traditional adiabatic calorimetry. This will also be the case in the future. However, because this calorimetry requires special skills of researchers to construct calorimeters and to operate them, the number of papers, in which the adiabatic calorimetry is used, has been not so many. Thanks to recent development of relaxation calorimetry, in particular commercially available apparatuses, calorimetric studies based on this calorimetry have become popular. It is a great merit that the amount of sample required for this method is only ∼10 to ∼100 mg. Easy measurement under applied magnetic field is also a big merit for the studies of molecule-based magnets.

Complementary roles played by macroscopic thermodynamic studies and microscopic spectroscopic studies are crucially important for deep understanding of materials and phenomena. In that sense, thermodynamic studies, in particular molecular thermodynamics related to statistical mechanics and quantum chemistry, will continue to provide us with important information concerning energetic and entropic aspects.

11. Acknowledgments

M.S. expresses his sincere thanks to Prof. Emer. Syûzô Seki (Osaka University), who was the supervisor when he started chemical thermodynamic study, and Prof. Emer. Hiizu Iwamura (The University of Tokyo) for recommending him as a contributor to this journal. Although this is a review article covering papers of various research groups, many papers of the present authors and their co-workers are involved. On this occasion, we express our sincere thanks to all of the colleagues, students, and collaborators over the world. It is a great pleasure to acknowledge Prof. Emer. Philipp Gütlich (University of Mainz), Prof. David N. Hendrickson (University of California at San Diego), the late Prof. Olivier Kahn (ICMC Bordeaux), and Prof. Emer. Wolfgang Haase (Technical University of Darmstadt) with whom the Cooperative Research Projects were concerned.

12. References

(1) Ihoh, K., Kinoshita, M., Eds. *Molecular Magnetism: New Magnetic Materials*; Kodansha, Gordon and Breach Science Publishers: Tokyo, 2000.
(2) Gatteschi, D., Kahn, O., Miller, J. S., Palacio, F., Eds. *Magnetic Molecular Materials*; NATO ASI Series 198; Kluwer Academic Publishers: Dordrecht, 1991.
(3) Kahn, O. *Molecular Magnetism*; Wiley-VCH Inc.: New York, 1993.
(4) Turnbull, M. M., Sugimoto, T., Tompson, L. K., Eds. *Molecule-Based Magnetic Materials: Theory, Techniques, and Applications*; ACS Symposium Series 644; American Chemical Society: Washington, DC, 1996.
(5) Kahn, O., Ed. *Magnetism: A Supramolcular Function*; NATO ASI Series C; Kluwer Academic Publishers: Dordrecht, 1996; Vol. 484.
(6) Lahti, P. M., Ed. *Magnetic Properties of Organic Materials*; Marcel Dekker: New York, 1999.
(7) (a) Miller, J. S., Drillon, M., Eds. *Magnetism: Molecules to Materials*; Wiley-VCH Verlag: Weinheim, 2001; Vol. I, Models and Experiments; (b) 2001; Vol. II, Molecule-Based Materials; (c) 2002; Vol. III, Nanosized Magnetic Materials; (d) 2003; Vol. IV; (e) 2005; Vol. V.
(8) Sorai, M. In *Molecule-Based Magnetic Materials: Theory, Techniques, and Applications*; Turnbull, M. M., Sugimoto, T., Tompson, L. K., Eds.; ACS Symposium Series 644; American Chemical Society: Washington, DC, 1996; p 99.
(9) Sorai, M.; Miyazaki, Y.; Hashiguchi, T. In *Magnetic Properties of Organic Materials*; Lahti, P. M., Ed.; Marcel Dekker: New York, 1999; p 475.
(10) Sorai, M.; Miyazaki, Y. In *Molecular Magnetism: New Magnetic Materials*; Itoh, K., Kinoshita, M., Eds.; Kodansha Ltd., & Gordon and Breach Science Publishers: Tokyo, 2000; p 112.
(11) Sorai, M. *Bull. Chem. Soc. Jpn.* **2001**, *74*, 2223.
(12) Sorai, M. *J. Chem. Thermodyn.* **2002**, *34*, 1207.
(13) Sorai, M. In *Spin Crossover in Transition Metal Compounds III*; Gütlich, P., Goodwin, H. A., Eds.; Series: Topics in Current Chemistry; Springer: Berlin, 2004; Vol. 235, p 153.
(14) Sorai, M. *Pure Appl. Chem.* **2005**, *77*, 1331.
(15) (a) de Jongh, L. J.; Miedema, A. R. *Experiments on Simple Magnetic Model Systems*; Taylor & Francis Ltd.: London, 1974. (b) de Jongh, L. J.; Miedema, A. R. *Adv. Phys.* **1974**, *23*, 1.

(16) Carlin, R. L. *Magnetochemistry*; Springer-Verlag: Berlin, 1986.
(17) de Jongh, L. J., Ed. *Magnetic Properties of Layered Transition Metal Compounds*; Kluwer Academic Publishers: Dordrecht, 1990.
(18) Domb, C. *Adv. Phys*. **1960**, *9*, 149.
(19) Onsager, L. *Phys. Rev*. **1944**, *65*, 117.
(20) Sorai, M.; Seki, S. *J. Phys. Soc. Jpn*. **1972**, *32*, 382.
(21) The Japan Society of Calorimetry and Thermal Analysis, Ed.; Sorai, M., Ed. *Comprehensive Handbook of Calorimetry and Thermal Analysis*; John Wiley & Sons, Ltd.: Chichester, 2004.
(22) Tamura, M.; Nakazawa, Y.; Shiomi, D.; Nozawa, K.; Hosokoshi Y.; Ishikawa, M.; Takahashi, M.; Kinoshita, M. *Chem. Phys. Lett*. **1991**, *186*, 401.
(23) Nakatsuji, S.; Saiga, M.; Haga, N.; Naito, A.; Hirayama, T.; Nakagawa, M.; Oda, Y.; Anzai, H.; Suzuki, K.; Enoki, T.; Mito, M.; Takeda, K. *New J. Chem.* **1998**, *22*, 275.
(24) Sugawara, T.; Matsushita, M. M.; Izuoka, A.; Wada, N.; Takeda, N.; Ishikawa, M. *J. Chem. Soc., Chem. Commun.* **1994**, 1723.
(25) Cirujeda, J.; Mas, M.; Molins, E.; de Panthou, F. L.; Laugier, J.; Park, J. G.; Paulsen, C.; Rey, P.; Rovira, C.; Veciana, J. *J. Chem. Soc., Chem. Commun*. **1995**, 709.
(26) Nakatsuji, S.; Morimoto, H.; Anzai, H.; Kawashima, J.; Maeda, K.; Mito, M.; Takeda, K. *Chem. Phys. Lett.* **1998**, *296*, 159.
(27) Nogami, T.; Tomioka, K.; Ishida, T.; Yoshikawa, H.; Yasui, M.; Iwasaki, F.; Iwamura, H.; Takeda, N.; Ishikawa, M. *Chem. Lett.* **1994**, 29.
(28) Ishida, T.; Tsuboi, H.; Nogami, T.; Yoshikawa, H.; Yasui, M.; Iwasaki, F.; Iwamura, H.; Takeda, N.; Ishikawa, M. *Chem. Lett.* **1994**, 919.
(29) Nogami, T.; Ishida, T.; Yoshikawa, H.; Yasui, M.; Iwasaki, F.; Iwamura, H.; Takeda, N.; Ishikawa, M. *Synth. Met*. **1995**, *71*, 1813.
(30) Nogami, T.; Ishida, T.; Tsuboi, H.; Yoshikawa, H.; Yamamoto, H.; Yasui, M.; Iwasaki, F.; Iwamura, H.; Takeda, N.; Ishikawa, M. *Chem. Lett.* **1995**, 635.
(31) Nogami, T.; Ishida, T.; Yasui, M.; Iwasaki, F.; Iwamura, H.; Takeda, N.; Ishikawa, M. *Mol. Cryst. Liq. Cryst*. **1996**, *279*, 97.
(32) Togashi, K.; Imachi, R.; Tomioka, K.; Tsuboi, H.; Ishida, T.; Nogami, T.; Takeda, N.; Ishikawa, M. *Bull. Chem. Soc. Jpn*. **1996**, *69*, 2821.
(33) Takeda, K.; Hamano, T.; Kawae, T.; Hidaka, M.; Takahashi, M.; Kawasaki, S.; Mukai, K. *J. Phys. Soc. Jpn.* **1995**, *64*, 2343.
(34) Chiarelli, R.; Novak, M. A.; Rassat, A.; Tholence, J. L. *Nature* **1993**, *363*, 147.
(35) Allemand, P.-M.; Khemani, K. C.; Koch, A.; Wudl, F.; Holczer, K.; Donovan, S.; Grüner, G.; Thompson, J. D. *Science* **1991**, *253*, 301.
(36) Allemand, P.-M.; Fite, C.; Srdanov, G.; Keder, N.; Wudl, F.; Canfield, P. *Synth. Met*. **1991**, *41*−*43*, 3291.
(37) Awaga, K.; Maruyama, Y. *Chem. Phys. Lett*. **1989**, *158*, 556.
(38) Awaga, K.; Maruyama, Y. *J. Chem. Phys*. **1989**, *91*, 2743.
(39) Nakazawa, Y.; Tamura, M.; Shirakawa, N.; Shiomi, D.; Takahashi, M.; Kinoshita, M.; Ishikawa, M. *Phys. Rev. B* **1992**, *46*, 8906.
(40) Turek, P.; Nozawa, K.; Shiomi, D.; Awaga, K.; Inabe, T.; Maruyama, Y.; Konishita, M. *Chem. Phys. Lett*. **1991**, *180*, 327.
(41) Kinoshita, M.; Turek, P.; Tamura, M.; Nozawa, K.; Shiomi, D.; Nakazawa, Y.; Ishikawa, M.; Takahashi, M.; Awaga, K.; Inabe, T.; Maruyama, Y. *Chem. Lett*. **1991**, 1225.
(42) Takahashi, M.; Turek, P.; Nakazawa, Y.; Tamura, M.; Nozawa, K.; Shiomi, D.; Ishikawa, M.; Kinoshita, M. *Phys. Rev. Lett.* **1991**, *67*, 746.
(43) Takahashi, M.; Kinoshita, M.; Ishikawa, M. *J. Phys. Soc. Jpn*. **1992**, *61*, 3745.
(44) Takeda, K.; Konishi, K.; Tamura, M.; Kinoshita, M. *Phys. Rev. B* **1996**, *53*, 3374.
(45) Mito, M.; Kawae, T.; Takumi, M.; Nagata, K.; Tamura, M.; Kinoshita, M.; Takeda, K. *Phys. Rev. B* **1997**, *56*, R14255.
(46) Takeda, K.; Mito, M.; Kawae, T.; Takumi, M.; Nagata, K.; Tamura, M.; Kinoshita, M. *J. Phys. Chem. B* **1998**, *102*, 671.
(47) Matsushita, M. M.; Izuoka, A.; Sugawara, T.; Kobayashi, T.; Wada, N.; Takeda, N.; Ishikawa, M. *J. Am. Chem. Soc.* **1997**, *119*, 4369.
(48) Mito, M.; Deguchi, H.; Tanimoto, T.; Kawae, T.; Nakatsuji, S.; Morimoto, H.; Anzai, H.; Nakao, H.; Murakami, Y.; Takeda, K. *Phys. Rev. B* **2003**, *67*, 024427.
(49) Mito, M.; Kawae, T.; Ikegami, A.; Hikata, M.; Takeda, K.; Nakatsuji, S.; Morimoto, H.; Anzai, H. *Physica B* **2000**, *284*−*288*, 1493.
(50) Hosokoshi, Y.; Tamura, M.; Shiomi, D.; Iwasawa, N.; Nozawa, K.; Kinoshita, M.; Aruga Katori, H.; Goto, T. *Physica B* **1994**, *201*, 497.
(51) Takahashi, M.; Hosokoshi, Y.; Nakano, H.; Goto, T.; Takahashi, M.; Kinoshita, M. *Mol. Cryst. Liq. Cryst*. **1997**, *306*, 111.
(52) Hosokoshi, Y.; Tamura, M.; Kinoshita, M. *Mol. Cryst. Liq. Cryst*. **1997**, *306*, 423.
(53) Mito, M.; Kawae, T.; Hosokoshi, Y.; Inoue, K.; Kinoshita, M.; Takeda, K. *Solid State Commun*. **1999**, *111*, 607.
(54) Yoshida, Y.; Yurue, K.; Mitoh, M.; Kawae, T.; Hosokoshi, Y.; Inoue, K.; Kinoshita, M.; Takeda, K. *Physica B* **2003**, *329*−*333*, 979.
(55) Yoshida, Y.; Tateiwa, N.; Mitoh, M.; Hidaka, M.; Kawae, T.; Hosokoshi, Y.; Inoue, K.; Kinoshita, M.; Takeda, K. *J. Magn. Magn. Mater.* **2004**, *272*−*276*, 872.
(56) Yoshida, Y.; Tateiwa, N.; Mito, M.; Kawae, T.; Takeda, K.; Hosokoshi, Y.; Inoue, K. *Phys. Rev. Lett*. **2005**, *94*, 037203.
(57) Wang, X.; Yu, L. *Phys. Rev. Lett*. **2000**, *84*, 5399.
(58) Lemaire, H.; Rey, P.; Rassat, A.; de Combarieu, A.; Michel, J.-C. *Mol. Phys*. **1968**, *14*, 201.
(59) Sugimoto, H.; Aota, H.; Harada, A.; Morishima, Y.; Kamachi, M.; Mori, W.; Kishita, M.; Ohmae, N.; Nakano, M.; Sorai, M. *Chem. Lett.* **1991**, 2095.
(60) Kajiwara, A.; Mori, W.; Sorai, M.; Yamaguchi, K.; Kamachi, M. *Mol. Cryst. Liq. Cryst*. **1995**, *272*, 289.
(61) Kamachi, M.; Sugimoto, H.; Kajiwara, A.; Harada, A.; Morishima, Y.; Mori, W.; Ohmae, N.; Nakano, M.; Sorai, M.; Kobayashi, T.; Amaya, K. *Mol. Cryst. Liq. Cryst*. **1993**, *232*, 53.
(62) Kobayashi, T.; Takiguchi, M.; Amaya, K.; Sugimoto, H.; Kajiwara, A.; Harada, A.; Kamachi, M. *J. Phys. Soc. Jpn*. **1993**, *62*, 3239.
(63) Ohmae, N.; Kajiwara, A.; Miyazaki, Y.; Kamachi, M.; Sorai, M. *Thermochim. Acta* **1995**, *267*, 435.
(64) Kobayashi, T. C.; Takiguchi, M.; Hong, C. U.; Amaya, K.; Kajiwara, A.; Harada, A.; Kamachi, M. *J. Magn. Magn. Mater*. **1995**, *140*−*144*, 1447.
(65) Kobayashi, T. C.; Takiguchi, M.; Hong, C.; Okada, A.; Amaya, K.; Kajiwara, A.; Harada, A.; Kamachi. *J. Phys. Soc. Jpn.* **1996**, *65*, 1427.
(66) Miyazaki, Y.; Matsumoto, T.; Ishida, T.; Nogami, T.; Sorai, M. *Bull. Chem. Soc. Jpn.* **2000**, *73*, 67.
(67) Sakakibara, T.; Miyazaki, Y.; Ishida, T.; Nogami, T.; Sorai, M. *J. Phys. Chem. B* **2002**, *106*, 6390.
(68) Mito, M.; Kawae, T.; Hitaka, M.; Takeda, K.; Ishida, T.; Nogami, T. *Chem. Phys. Lett*. **2001**, *333*, 69.
(69) Allemand, P.-M.; Srdanov, G.; Wudl, F. *J. Am. Chem. Soc*. **1990**, *112*, 9391.
(70) Mukai, K.; Konishi, K.; Nedachi, K.; Takeda, K. *J. Magn. Magn. Mater.* **1995**, *140*, 1449.
(71) Ballüder, K.; Kelemen, M.; Pérez, F.; Pilawa, B.; Wachter, Ch.; Dormann, E. *Ber. Bunsen-Ges. Phys. Chem.* **1997**, *101*, 1882.
(72) Mito, M.; Takeda, K.; Mukai, K.; Azuma, N.; Gleiter, M. R.; Krieger, C.; Neugebauer, F. A. *J. Phys. Chem. B* **1997**, *101*, 9517.
(73) Mukai, K.; Wada, N.; Jamali, J. B.; Achiwa, N.; Narumi, Y.; Kindo, K.; Kobayashi, T.; Amaya, K. *Chem. Phys. Lett.* **1996**, *257*, 538.
(74) Mukai, K.; Nedachi, K.; Jamali, J. B.; Achiwa, N. *Chem. Phys. Lett*. **1993**, *214*, 559.
(75) Takeda, K.; Konishi, K.; Hitaka, M.; Nedachi, K.; Mukai, K. *J. Magn. Magn Mater*. **1995**, *140*, 1635.
(76) Takeda, K.; Konishi, K.; Nedachi, K.; Mukai, K. *Phys. Rev. Lett*. **1995**, *74*, 1673.
(77) Mukai, K.; Konishi, K.; Nedachi, K.; Takeda, K. *Mol. Cryst. Liq. Cryst.* **1996**, *278*, A195.
(78) Mukai, K.; Konishi, K.; Nedachi, K.; Takeda, K. *J. Phys. Chem.* **1996**, *100*, 9658.
(79) Takeda, K.; Hamano, T.; Kawae, T.; Hitaka, M.; Kawasaki, S.; Takahashi, M.; Mukai, K. *Mol. Cryst. Liq. Cryst.* **1996**, *278*, A107.
(80) Mito, M.; Nakano, H.; Kawae, T.; Hitaka, M.; Takagi, S.; Deguchi, H.; Suzuki, K.; Mukai, K.; Takeda, K. *J. Phys. Soc. Jpn.* **1997**, *66*, 2147.
(81) Takeda, K.; Mito, M.; Kawae, T.; Nakano, H.; Hitaka, M.; Suzuki, K.; Mukai, K. *J. Magn. Magn. Mater* **1998**, *177*, 817.
(82) Mukai, K.; Wada, N.; Jamali, J. B.; Achiwa, N.; Narumi, Y.; Kindo, K.; Kobayashi, T.; Amaya, K. *Chem. Phys. Lett.* **1996**, *257*, 538.
(83) Hamamoto, T.; Narumi, Y.; Kindo, K.; Mukai, K.; Shimobe, Y.; Kobayashi, T. C.; Muramatsu, T.; Amaya, K. *Physica B* **1998**, *246*−*247*, 36.
(84) Mito, M.; Tanaka, S.; Kawae, T.; Takeda, K.; Yanagimoto, M.; Mukai, K. *Physica B (Amsterdam)* **2003**, *329*, 1150.
(85) Mukai, K.; Yanagimoyo, M.; Tanaka, S.; Mito, M.; Kawae, T.; Takeda, K. *J. Phys. Soc. Jpn.* **2003**, *72*, 2312.
(86) Mukai, K.; Yanagimoto, M.; Tanaka, S.; Mito, M.; Kawae, T.; Takeda, K. *Polyhedron* **2003**, *22*, 2091.
(87) Rawson, J.; Palacio, F. *Struct. Bonding (Berlin)* **2001**, *100*, 94.
(88) Bryan, C. D.; Cordes, A. W.; Fleming, R. M.; George, N. A.; Glarum, S. H.; Haddon, R. C.; Oakley, R. T.; Palstra, T. T. M.; Perel, A. S.; Schneemeyer, L. F.; Waszczak, J. V. *Nature* **1993**, *365*, 821.
(89) Enright, G. D.; Morton, J. R.; Passmore, J.; Preston, K. F.; Thompson, R. C.; Wood, D. J. *J. Chem. Soc., Chem. Commun*. **1996**, 967.
(90) Palacio, F.; Antorrena, G.; Castro, M.; Burriel, R.; Rawson, J.; Smith, J. N. B.; Bricklebank, N.; Novoa, J.; Ritter, C. *Phys. Rev. Lett*. **1997**, *79*, 2336.
(91) Barclay, T. M.; Cordes, A. W.; George, N. A.; Haddon, R. C.; Itkis, M. E.; Mashuta, M. S.; Oakley, R. T.; Patenaude, G. W.; Reed, R. W.; Richaedson, J. F.; Zhang, H. *J. Am. Chem. Soc*. **1998**, *120*, 352.
(92) Fujita, W.; Awaga, K. *Science* **1999**, *286*, 261.

(93) Banister, A. J.; Bricklebank, N.; Clegg, W.; Elsegood, M. R. J.; Gregory C. I.; Lavender, I.; Rawson, J. M.; Tanner, B. K. *J. Chem. Soc., Chem. Commun*. **1995**, 679.
(94) Banister, A. J.; Bricklebank, N.; Lavender, I.; Rawson, J. M.; Gregory, C. I.; Tanner, B. K.; Clegg, W.; Elsegood, M. R. J.; Palacio, F. *Angew. Chem., Int. Ed. Engl*. **1996**, *35*, 2533.
(95) Palacio, F.; Castro, M.; Antorrena, G.; Burriel, R.; Ritter, C.; Bricklebank, N.; Rawson, J.; Smith, J. N. B. *Mol. Cryst. Liq. Cryst.* **1997**, *306*, 293.
(96) Fujita, W.; Awaga, K.; Nakazawa, Y.; Saito, K.; Sorai, M. *Chem. Phys. Lett*. **2002**, *352*, 348.
(97) Takagi, S.; Deguchi, H.; Takeda, K.; Mito, M.; Takahashi, M. *J. Phys. Soc. Jpn*. **1996**, *65*, 1934.
(98) Wada, N.; Kobayashi, T.; Yano, H.; Okuno, T.; Yamaguchi, A.; Awaga, K. *J. Phys. Soc. Jpn*. **1997**, *66*, 961.
(99) Awaga, K.; Okuno, T.; Yamaguchi, A.; Hasegawa, M.; Inabe, T.; Maruyama, Y.; Wada, N. *Phys. Rev. B* **1994**, *49*, 3975.
(100) Uekusa, Y.; Oguchi, A. *J. Phys. Soc. Jpn*. **2001**, *70*, 3464.
(101) Teki, Y.; Itoh, K.; Miura, Y.; Kurokawa, S.; Ueno, S.; Okada, A.; Yamakage, H.; Kobayashi, T.; Amaya, K. *Mol. Cryst. Liq. Cryst*. **1997**, *306*, 95.
(102) Hosokoshi, Y.; Nakazawa, Y.; Inoue, K.; Takizawa, K.; Nakano, H. Y.; Takahashi, M.; Goto, T. *Phys. Rev. B* **1999**, *60*, 12924.
(103) Hosokoshi, Y.; Katoh, K.; Nakazawa, Y.; Nakano, H.; Inoue, K. *J. Am. Chem. Soc*. **2001**, *123*, 7921.
(104) Ferrer, J. R.; Lahti, P. M.; George, C.; Antorrena, G.; Palacio, F. *Chem. Mater*. **1999**, *11*, 2205.
(105) Lahti, P. M.; Ferrer, J. R.; George, C.; Oliete, P.; Julier, M.; Palacio, F. *Polyhedron* **2001**, *20*, 1465.
(106) Miyazaki, Y.; Sakakibara, T.; Ferrer, J. R.; Lahti, P. M.; Antorrena, G.; Palacio, F.; Sorai, M. *J. Phys. Chem. B* **2002**, *106*, 8615.
(107) Miller, J. S.; Calabrese, J. C.; Epstein, A. J.; Bigelow, R. W.; Zhang, J. H.; Reiff, W. M. *J. Chem. Soc., Chem. Commun.* **1986**, 1026.
(108) Miller, J. S.; Calabrese, J. C.; Rommelmann, H.; Chittipeddi, S. R.; Zhang, J. H.; Reiff, W. M.; Epstein, A. J. *J. Am. Chem. Soc.* **1987**, *109*, 769.
(109) Epstein, A. J.; Chittipeddi, S.; Chakraborty, A.; Miller, J. S. *J. Appl. Phys.* **1988**, *63*, 2952.
(110) Chakraborty, A.; Epstein, A. J.; Lawless, W. N.; Miller, J. S. *Phys. Rev. B* **1989**, *40*, 11422.
(111) Nakano, M.; Sorai, M. *Chem. Phys. Lett.* **1990**, *169*, 27.
(112) Chittipeddi, S.; Selover, M. A.; Epstein, A. J.; O’Hare, D. M.; Manriquez, J.; Miller, J. S. *Synth. Met.* **1988**, *27*, 417.
(113) Miller, J. S.; Zhang, J. H.; Reiff, W. M.; Dixon, D. A.; Preston, L. D.; Reis, A. H.; Gebert, E.; Extine, M.; Troup, J.; Epstein, A. J.; Ward, M. D. *J. Phys. Chem. Soc.* **1987**, *91*, 4344.
(114) Nakano, M.; Sorai, M. *Mol. Cryst. Liq. Cryst.* **1993**, *232*, 521.
(115) Nakatani, K.; Carriat, J. Y.; Journaux, Y.; Kahn, O.; Lloret, F.; Renard, J. P.; Pei, Y.; Sletten, J.; Verdaguer, M. *J. Am. Chem. Soc.* **1989**, *111*, 5739.
(116) (a) Asano, K.; Inoue, K.; Nakano, M.; Miyazaki, Y.; Sorai, M.; Nakatani, K.; Kahn, O. *Bull. Chem. Soc. Jpn.* **1999**, *72*, 1749. (b) Asano, K.; Miyazaki, Y.; Mori, W.; Nakatani, K.; Kahn, O.; Sorai, M. *Bull. Chem. Soc. Jpn.* **2000**, *73*, 885.
(117) Sands, R. H.; Dunham, W. R. *Q. Rev. Biophys.* **1975**, *7*, 443.
(118) Coronado, E.; Drillon, M.; Nugteren, P. R.; de Jongh, L. J.; Beltran, D.; Georges, R. *J. Am. Chem. Soc.* **1989**, *111*, 3874.
(119) Drillon, M.; Coronado, E.; Georges, R.; Gianduzzo, J. C.; Curely, J. *Phys. Rev. B* **1989**, *40*, 10992.
(120) Evangelisti, M.; Bartolomé, F.; Bartolomé, J.; Kahn, M. L.; Kahn, O. *J. Magn. Magn. Mater*. **1999**, *197*, 584.
(121) (a) Evangelisti, M.; Bartolomé, J.; Mettes, F.; de Jongh, L. J.; Kahn, M. L.; Mathonière, C.; Kahn, O. *Polyhedron* **2001**, *20*, 1447. (b) Evangelisti, M.; Kahn, M. L.; Bartolomé, J.; de Jongh, L. J.; Meyers, C.; Leandri, J.; Leroyer, Y.; Mathonière, C. *Phys. Rev. B* **2003**, *68*, 184405.
(122) Harada, I. *J. Phys. Soc. Jpn.* **1984**, *53*, 1643.
(123) Affronte, M.; Caneschi, A.; Cucci, C.; Gatteschi, D.; Lasjaunias, J. C.; Paulsen, C.; Pini, M. G.; Rettori, A.; Sessoli, R. *Phys. Rev. B* **1999**, *59*, 6282.
(124) Benelli, C.; Gatteschi, D.; Sessoli, R.; Rettori, A.; Pini, M. G.; Bartolome, F.; Bartolome, J. *J. Magn. Magn. Mater.* **1995**, *140*, 1649.
(125) Bartolome, F.; Bartolome, J.; Benelli, C.; Caneschi, A.; Gatteschi, D.; Paulsen, C.; Pini, M. G.; Rettori, A.; Sessoli, R.; Volokitin, Y. *Phys. Rev. Lett.* **1996**, *77*, 382.
(126) Lascialfari, A.; Ullu, R.; Affronte, M.; Cinti, F.; Caneschi, A.; Gatteschi, D.; Rovai, D.; Pini, M. G.; Rettori, A. *Phys. Rev. B* **2003**, *67*, 224408.
(127) Dumm, M.; Dressel, M.; Nicklas, M.; Lunkenheimer, P.; Loidl, A.; Weiden, M.; Steglich, F.; Assmann, B.; Homborg, H.; Fulde, P. *Eur. Phys. J. B* **1998**, *6*, 317.
(128) Dumm, M.; Nicklas, M.; Loidl, A. *Synth. Met.* **1999**, *103*, 2070.
(129) Hammar, P. R.; Stone, M. B.; Reich, D. H.; Broholm, C.; Gibson, P. J.; Turnbull, M. M.; Landee, C. P.; Oshikawa, M. *Phys. Rev. B* **1999**, *59*, 1008.
(130) Kitagawa, H.; Onodera, N.; Ahn, J.-S.; Mitani, T.; Kim, M.; Ozawa, Y.; Toriumi, K.; Yasui, K.; Manabe, T.; Yamashita, M. *Mol. Cryst. Liq. Cryst.* **1996**, *285*, 311.
(131) Kitagawa, H.; Onodera, N.; Ahn, J.-S.; Mitani, T.; Toriumi, K.; Yamashita, M. *Synth. Met.* **1997**, *86*, 1931.
(132) Kitagawa, H.; Onodera, N.; Sonoyama, T.; Yamamoto, M.; Fukawa, T.; Mitani, T.; Seto, M.; Maeda, Y. *J. Am. Chem. Soc.* **1999**, *121*, 10068.
(133) Kitagawa, H.; Mitani, T. *Coord. Chem. Rev.* **1999**, *190*−*192*, 1169.
(134) Ozawa, Y.; Kim, M.; Ozawa, Y.; Takata, K.; Toriumi, K. Manuscript in preparation.
(135) Miyazaki, Y.; Wang, Q.; Sato, A.; Saito, K.; Yamamoto, M.; Kitagawa, H.; Mitani, T.; Sorai, M. *J. Phys. Chem. B* **2002**, *106*, 197.
(136) Ikeuchi, S.; Saito, K.; Nakazawa, Y.; Mitsumi, M.; Toriumi, K.; Sorai, M. *J. Phys. Chem. B* **2004**, *108*, 387.
(137) Ikeuchi, S.; Saito, K.; Nakazawa, Y.; Sato, A.; Mitsumi, M.; Toriumi, K.; Sorai, M. *Phys. Rev. B* **2002**, *66*, 115110.
(138) Saito, K.; Ikeuchi, S.; Nakazawa, Y.; Sato, A.; Mitsumi, M.; Yamashita, T.; Toriumi, K.; Sorai, M. *J. Phys. Chem. B* **2005**, *109*, 2956.
(139) Mitsumi, M.; Murase, T.; Kishida, H.; Yoshinari, T.; Ozawa, Y.; Toriumi, K.; Sonoyama, K.; Kitagawa, H.; Mitani, T. *J. Am. Chem. Soc.* **2001**, *123*, 11179.
(140) Mitsumi, M.; Umebayashi, S.; Ozawa, Y.; Toriumi, K.; Hiroshi Kitagawa, H.; Mitani, T. *Chem. Lett.* **2002**, 258.
(141) Ito, H.; Hasegawa, Y.; Tanaka, H.; Kuroda, S.; Mitsumi, M.; Toriumi, K. *J. Phys. Soc. Jpn.* **2003**, *72*, 2149.
(142) Mitsumi, M.; Kitamura, K.; Morinaga, A.; Ozawa, Y.; Kobayashi, M.; Toriumi, K.; Iso, Y.; Kitagawa, H.; Mitani, T. *Angew. Chem., Intl. Ed.* **2002**, *41*, 2767.
(143) Tanaka, H.; Kuroda, S.; Yamashita, T.; Mitsumi, M.; Toriumi, K. *J. Phys. Soc. Jpn.* **2003**, *72*, 2169.
(144) Sorai, M.; Saito, K. *Chem. Rec.* **2003**, *3*, 29.
(145) Sorai, M.; Tsuji, K.; Suga, H.; Seki, S. *Mol. Cryst. Liq. Cryst.* **1980**, *59*, 33.
(146) Sato, A.; Yamamura, Y.; Saito, K.; Sorai, M. *Liq. Cryst.* **1999**, *26*, 1185.
(147) Saito, K.; Shinhara, T.; Nakamoto, T.; Kutsumizu, S.; Yano, S.; Sorai, M. *Phys. Rev. E* **2002**, *65*, 031719.
(148) Ikeuchi, S.; Sato, A.; Saito, K.; Nakazawa, Y.; Mitsumi, M.; Toriumi, K.; Sorai, M. Manuscript in preparation.
(149) Miller, J. S.; Calabrese, J. C.; McLean, R. S.; Epstein, A. J. *Adv. Mater.* **1992**, *4*, 498.
(150) Brinckerhoff, W. B.; Morin, B. G.; Brandon, E. J.; Miller, J. S.; Epstein, A. J. *J. Appl. Phys.* **1996**, *79*, 6147.
(151) Bałanda, M.; Falk, K.; Griesar, K.; Tomkowicz, Z.; Haase, W. *J. Magn. Magn. Mater.* **1999**, *205*, 14.
(152) Falk, K.; Balanda, M.; Tomkowicz, Z.; Mascarenhas, F.; Schilling, J.; Klavins, P.; Haase, W. *Polyhedron* **2001**, *20*, 1521.
(153) Bhattacharjee, A.; Falk, K.; Haase, W.; Sorai, M. *J. Phys. Chem. Solids* **2005**, *66*, 147.
(154) Nakazawa, Y.; Hoffman, W.; Miller, J. S.; Sorai, M. *Solid State Commun.* **2005**, *135*, 71.
(155) Cowen, J.; Clérac, R.; Heintz, R. A.; O’Kane, S.; Xiang, O.-Y.; Zhao, H.-H.; Dunbar, K. R. *Mol. Cryst. Liq. Crys.* **1999**, *334*, 825.
(156) Clérac, R.; O’Kane, S.; Cowen, J.; Ouyang, X.; Heintz, R.; Zhao, H. H.; Bazile, M. J.; Dunbar, K. R. *Chem. Mater*. **2003**, *15*, 1840.
(157) (a) Haldane, F. D. M. *Phys. Lett.* **1983**, *A93*, 464. (b) Haldane, F. D. M. *Phys. Rev. Lett.* **1983**, *50*, 1153.
(158) Schollwöck, U., Richter, J., Farnell, D. J. J., Bishop, R. F., Eds. *Quantum Magnetism*; Springer-Verlag: Berlin, 2004.
(159) Miller, J. S., Drillon, M., Eds. *Magnetism: Molecules to Materials I, Models and Experiments*; Wiley-VCH Verlag: Weinheim, 2001; Chapter 2.
(160) Yamashita, M.; Ishii, T.; Matsuzaka, H. *Coord. Chem. Rev.* **2000**, *198*, 347.
(161) Daggoto, E.; Rice, T. M. *Science* **1996**, *271*, 618.
(162) Kobayashi, T.; Tabuchi, Y.; Amaya, K.; Ajiro, Y.; Yoshida, T.; Date, M. *J. Phys. Soc. Jpn.* **1992**, *61*, 1772.
(163) Deguchi, H.; Ito, M.; Takeda, K. *J. Phys. Soc. Jpn.* **1992**, *61*, 3470.
(164) Kobayashi, T.; Kohda, A.; Amaya, K.; Ito, M.; Deguchi, H.; Takeda, K.; Asano, T.; Ajiro, Y.; Mekata, M. *J. Phys. Soc. Jpn.* **1994**, *63*, 1961.
(165) (a) Honda, Z.; Katsumata, K.; Aruga Katori, H.; Yamada, K.; Ohishi, T.; Manabe, T.; Yamashita, M. *J. Phys.: Condens. Matter* **1997**, *9*, L83. (b) Honda, Z.; Katsumata, K.; Aruga Katori, H.; Yamada, K.; Ohishi, T.; Manabe, T.; Yamashita, M. *J. Phys.: Condens. Matter* **1997**, *9*, 3487.

(166) Honda, Z.; Asakawa, H.; Katsumata, K. *Phys. Rev. Lett.* **1998**, *81*, 2566.

(167) Honda, Z.; Katsumata, K.; Nishiyama, Y.; Harada, I. *Phys. Rev. B* **2001**, *63*, 064420.

(168) Tsujii, H.; Honda, Z.; Andraka, B.; Katsumata, K.; Takano, Y. *Physica B* **2003**, *329*−*333*, 975.

(169) Katsumata, K.; Honda, Z. *J. Phys. Chem. Solids* **2004**, *65*, 51.

(170) Ferré, J.; Jamet, J. P.; Landee, C. P.; Reza, K. A.; Renard, J. P. *J. Phys. (Paris) Colloq.* **1988**, *C8*, 1441.

(171) Hammar, P. R.; Reich, D. H.; Broholm, C.; Trouw, F. *Phys. Rev. B* **1998**, *57*, 7846.

(172) Calemczuk, R.; Riera, J.; Poilblanc, D.; Boucher, J.-P.; Chaboussant, G.; Lévy, L.; Piovesana, O. *Eur. Phys. J. B* **1999**, *7*, 171.

(173) Hagiwara, M.; Aruga Katori, H.; Schollwöck, U.; Mikeska, H.-J. *Phys. Rev. B* **2000**, *62*, 1051.

(174) Hagiwara, M.; Aruga Katori, H.; Schollwöck, U.; Mikeska, H.-J. *Physica B* **2000**, *284*−*288*, 1601.

(175) Stone, M. B.; Chen, Y.; Rittner, J.; Yardimci, H.; Reich, D. H.; Broholm, C.; Ferraris, D. V.; Lectka, T. *Phys. Rev. B* **2002**, *65*, 064423.

(176) Elstner, N.; Singh, R. R. P. *Phys. Rev. B* **1998**, *58*, 11484.

(177) Manaka, H.; Yamada, I.; Honda, Z.; Aruga Katori, H.; Katsumata, K. *J. Phys. Soc. Jpn.* **1998**, *67*, 3913.

(178) Pei, Y.; Verdaguer, M.; Kahn, O.; Sletten, J.; Renard, J. P. *J. Am. Chem. Soc.* **1986**, *108*, 7428.

(179) Pei, Y.; Verdaguer, M.; Kahn, O.; Sletten, J.; Renard, J. P. *Inorg. Chem*. **1987**, *26*, 138.

(180) Kahn, O.; Pei, Y.; Verdaguer, M.; Renard, J. P.; Sletten, J. *J. Am. Chem. Soc*. **1988**, *110*, 782.

(181) Zhong, Z.-J.; Matsumoto, N.; Ōkawa, H.; Kida, S. *Chem. Lett.* **1990**, 87.

(182) Tamaki, H.; Zhong, Z.-J.; Matsumoto, N.; Kida, S.; Koikawa, M.; Achiwa, N.; Hashimoto, Y.; Ōkawa, H. *J. Am. Chem. Soc*. **1992**, *114*, 6974.

(183) Tamaki, H.; Mitsumi, M.; Nakamura, K.; Matsumoto, N.; Kida, S.; Ōkawa, H.; Iijima, S. *Chem. Lett.* **1992**, 1975.

(184) Hashiguchi, T.; Miyazaki, Y.; Asano, K.; Tamaki, H.; Matsumoto, N.; Okawa, H.; Sorai, M. *Mol. Cryst. Liq. Cryst.* **2000**, *342*, 185.

(185) Hashiguchi, T.; Miyazaki, Y.; Asano, K.; Nakano, M.; Sorai, M.; Tamaki, H.; Matsumoto, N.; Ōkawa, H. *J. Chem. Phys.* **2003**, *119*, 6856.

(186) Hashiguchi, T. Doctoral Thesis, Osaka University, 2003.

(187) Decurtins, S.; Schmalle, H. W.; Oswald, H. R.; Linden, A.; Ensling, J.; Gütlich, P.; Hauser, A. *Inorg. Chim. Acta* **1994**, *216*, 65.

(188) Ovanesyan, N. S.; Shilov, G. V.; Atovmyan, L. O.; Lyubovskaya, R. N.; Pyalling, A. A.; Morozov, Yu. G. *Mol. Cryst. Liq. Cryst.* **1995**, *273*, 175.

(189) Bhattacharjee, A.; Miyazaki, Y.; Sorai, M. *J. Phys. Soc. Jpn.* **2000**, *69*, 479.

(190) Bhattacharjee, A.; Miyazaki, Y.; Feyerherm, R.; Steiner, M.; Sorai, M. *Indian J. Phys.* **2001**, *75A*, 399.

(191) Bhattacharjee, A.; Saito, K.; Sorai, M. *Solid State Commun.* **2000**, *113*, 543.

(192) Bhattacharjee, A.; Miyazaki, Y.; Sorai, M. *Solid State Commun.* **2000**, *115*, 639.

(193) Bhattacharjee, A.; Sorai, M. *J. Alloys Compd.* **2001**, *326*, 251.

(194) Bhattacharjee, A.; Miyazaki, Y.; Sorai, M. *J. Magn. Magn. Mater.* **2004**, *280*, 1.

(195) Antorrena, G.; Palacio, F.; Castro, M.; Pellaux, R.; Decurtins, S. *J. Magn. Magn. Mater.* **1999**, *196*−*197*, 581.

(196) Mathonière, C.; Nuttall, C. J.; Carling, S. G.; Day, P. *Inorg. Chem.* **1996**, *35*, 1201.

(197) Miyasaka, H.; Matsumoto, N.; Ōkawa, H.; Re, N.; Gallo, E.; Floriani, C. *Angew. Chem., Int. Ed. Engl.* **1995**, *34*, 1446.

(198) Miyasaka, H.; Matsumoto, N.; Ōkawa, H.; Re, N.; Gallo, E.; Floriani, C. *J. Am. Chem. Soc*. **1996**, *118*, 981.

(199) Miyasaka, H.; Matsumoto, N.; Re, N.; Gallo, E.; Floriani, C. *Inorg. Chem.* **1997**, *36*, 670.

(200) Ohba, M.; Ōkawa, H. *Coord. Chem. Rev.* **2000**, *198*, 313.

(201) Miyazaki, Y.; Wang, Q.; Yu, Q.-S.; Matsumoto, T.; Miyasaka, H.; Matsumoto, N.; Sorai, M. *Thermochim. Acta* **2005**, *431*, 144.

(202) Miyazaki, Y.; Sakakibara, T.; Miyasaka, H.; Matsumoto, N.; Sorai, M. *J. Therm. Anal. Calorim.* **2005**, *81*, 603.

(203) Haddad, M. S.; Federer, W. D.; Lynch, M. W.; Hendrickson, D. N. *J. Am. Chem. Soc*. **1980**, *102*, 1468.

(204) Haddad, M. S.; Lynch, M. W.; Federer, W. D.; Hendrickson, D. N. *Inorg. Chem*. **1981**, *20*, 123.

(205) Haddad, M. S.; Federer, W. D.; Lynch, M. W.; Hendrickson, D. N. *Inorg. Chem*. **1981**, *20*, 131.

(206) Sorai, M.; Hendrickson, D. N. The 37th Annual Meeting on Coordination Chemistry, Tokyo, 1987; 2B14.

(207) Bhattacharjee, A.; Miyazaki, Y.; Nakazawa, Y.; Koner, S.; Iijima, S.; Sorai, M. *Physica B* **2001**, *305*, 56.

(208) Kahn, O.; Joulia Larionova, J.; Ouahab, L. *J. Chem. Doc., Chem. Commun.* **1999**, 945.

(209) Podgajny, R.; Korzeniak, T.; Bałanda, M.; Wasiutyński, T.; Errington, W.; Kemp, T. J.; Alcock, N. W.; Sieklucka, B. *J. Chem. Soc., Chem. Commun.* **2002**, 1138.

(210) Korzeniak, T.; Podgajny, R.; Alcock, N. W.; Lewiński, K.; Bałanda, M.; Wasiutyński, T.; Sieklucka, B. *Polyhedron* **2003**, *22*, 2183.

(211) Sieklucka, B.; Korzeniak, T.; Podgajny, R.; Bałanda, M.; Nakazawa, Y.; Miyazaki, Y.; Sorai, M.; Wasiutyński, T. *J. Magn. Magn. Mater*. **2004**, *272*−*276*, 1058.

(212) Pełka, R.; Bałanda, M.; Wasiutyński, T.; Nakazawa, Y.; Sorai, M.; Podgajny, R.; Sieklucka, B. *Czech. J. Phys*. **2004**, *54*, D595.

(213) Kojima, N.; Aoki, W.; Seto, M.; Kobayashi, Y.; Maeda, Yu. *Synth. Met.* **2001**, *121*, 1796.

(214) Kojima, N.; Aoki, W.; Itoi, M.; Ono, Y.; Seto, M.; Kobayashi, Y.; Maeda, Yu. *Solid State Commun.* **2001**, *120*, 165.

(215) Itoi, M.; Taira, A.; Enomoto, M.; Matsushita, N.; Kojima, N.; Kobayashi, Y.; Asai, K.; Koyama, K.; Nakano, T.; Uwatoko, Y.; Yamaura, J. *Solid State Commun.* **2004**, *130*, 415.

(216) Nakamoto, T.; Miyazaki, Y.; Itoi, M.; Ono, Y.; Kojima, N.; Sorai, M. *Angew. Chem., Intl. Ed*. **2001**, *40*, 4716.

(217) Shannon, R. D. *Acta Crystallogr., Sect. A: Found. Crystallogr.* **1976**, *32*, 751.

(218) Mermin, N. D.; Wagner, H. *Phys. Rev. Lett.* **1966**, *17*, 1133.

(219) Woodward, F. M.; Albrecht, A. S.; Wynn, C. M.; Landee, C. P.; Turnbull, M. M. *Phys. Rev. B* **2002**, *65*, 144412.

(220) Matsumoto, T.; Miyazaki, Y.; Albrecht, A. S.; Landee, C. P.; Turnbull, M. M.; Sorai, M. *J. Phys. Chem. B* **2000**, *104*, 9993.

(221) de Jongh, L. J. In *Magneto-Structural Correlations in Exchange-Coupled Systems*; Willett, R. D., Gatteschi, D., Kahn, O., Eds.; NATO-ASI Series; Reidel: Dordrecht, 1983; Vol. C-140, p 1.

(222) Coronado, E.; Clemente-León, M.; Galán-Mascarós, J. R.; Giménez-Saiz, C.; Gómez-Garcia, C. J.; Martínez-Ferrero, E. *J. Chem. Soc., Dalton Trans.* **2000**, 3955.

(223) Clemente-León, M.; Coronado, E.; Galán-Mascarós, J. R.; Gómez-Garcia, C. J. *J. Chem. Soc., Chem. Commun.* **1997**, 1727.

(224) Coronado, E.; Galán-Mascarós, J. R.; Gómez-Garcia, C. J.; Burriel, R. *J. Magn. Magn. Mater*. **1999**, *196*−*197*, 558.

(225) Coronado, E.; Galán-Mascarós, J. R.; Gómez-Garcia, C. J.; Laukhin, V. *Nature* **2000**, *408*, 447.

(226) Gadet, V.; Bujoli-Doeuff, M.; Force, L.; Verdaguer, M.; El Malkhi, K.; Deroy, A.; Besse, J. P.; Chappert, C.; Veillet, P.; Renard, J. P.; Beauvillain, P. In *Magnetic Molecular Materials*; Gatteschi, D., Kahn, O., Miller, J. S., Palacio, F., Eds.; NATO ASI Series 198; Kluwer Academic Publishers: Dordrecht, 1991; p 281.

(227) Mallah, T.; Thiebaut, S.; Verdaguer, M.; Veillet, P. *Science* **1993**, *262*, 1554.

(228) Ferlay, S.; Mallah, T.; Ouahés, R.; Veillet, P.; Verdaguer, M. *Nature* **1995**, *378*, 701.

(229) Ohkoshi, S.; Tokoro, H.; Utsunomiya, M.; Mizuno, M.; Abe, M.; Hashimoto, K. *J. Phys. Chem. B* **2002**, *106*, 2423.

(230) Tokoro, H.; Ohkoshi, S.; Matsuda, T.; Hashimoto, K. *Inorg. Chem.* **2004**, *43*, 5231.

(231) Robin, M. B.; Day, P. *Adv. Inorg. Chem. Radiochem*. **1967**, *10*, 247.

(232) Piepho, S. B.; Krausz, E. R.; Schatz, P. N. *J. Am. Chem. Soc*. **1978**, *100*, 2996.

(233) Tokoro, H.; Ohkoshi, S.; Matsuda, T.; Hozumi, T.; Hashimoto, K. *Chem. Phys. Lett.* **2004**, *388*, 379.

(234) Mayoh, B.; Day, P. *J. Chem. Soc., Dalton* **1976**, *15*, 1483.

(235) Ohkoshi, S.; Matsuda, T.; Tokoro, H.; Hashimoto, K. *Chem. Mater.* **2005**, *17*, 81.

(236) Larionova, J.; Kahn, O.; Bartolome, J.; Burriel, R.; Castro, M.; Ksenofontov, V.; Gütlich, P. *Chem. Mater.* **1999**, *11*, 3400.

(237) Manson, J. L.; Kmety, C. R.; Huang, Q. Z.; Lynn, J. W.; Bendele, G. M.; Pagola, S.; Stephens, P. W.; Liable-Sands, L. M.; Rheingold, A. L.; Epstein, A. J.; Miller, J. S. *Chem. Mater.* **1998**, *10*, 2552.

(238) Kurmoo, M.; Kepert, C. J. *New J. Chem.* **1998**, *22*, 1515.

(239) Batten, S. R.; Jensen, P.; Kepert, C. J.; Kurmoo, M.; Moubaraki, B.; Murray, K. S.; Price, D. J. *J. Chem. Soc., Dalton Trans.* **1999**, 2987.

(240) Kmety, C. R.; Huang, Q. Z.; Lynn, J. W.; Erwin, R. W.; Manson, J. L.; McCall, S.; Crow, J. E.; Stevenson, K. L.; Miller, J. S.; Epstein, A. J. *Phys. Rev. B* **2000**, *62*, 5576.

(241) Kmety, C. R.; Manson, J. L.; McCall, S.; Crow, J. E.; Stevenson, K. L.; Epstein, A. J. *J. Magn. Magn. Mater.* **2002**, *248*, 52.

(242) (a) Manson, J. L.; Huang, Q.-Z.; Lynn, J. W.; Koo, H.-J.; Whangbo, M.-H.; Bateman, R.; Otsuka, T.; Wada, N.; Argyriou, D. N.; Miller, J. S. *J. Am. Chem. Soc.* **2001**, *123*, 162. (b) Manson, J. L.; Chapn, L. C.; Bordallo, H. N.; Feyerherm, R.; Argyriou, D. N.; Loose, A. *J. Magn. Magn. Mater.* **2003**, *260*, 462.

(243) Černák, J.; Chomič, J.; Gravereau, P.; Orendáčová, A.; Orendáč, M.; Kovác, J.; Feher, A.; Kappenstein, C. *Inorg. Chim. Acta* **1998**, *281*, 134.

(244) Orendáčová, A.; Orendáč, M.; Černák, J.; Feher, A. *J. Magn. Magn. Mater.* **1995**, *157–158*, 583.
(245) Orendáč, M.; Orendáčová, A.; Černák, J.; Feher, A. *Solid State Commun.* **1995**, *94*, 833.
(246) Orendáč, M.; Orendáčová, A.; Feher, A.; Chomič, J.; Zvyagin, S. A.; Eremenko, V. V.; Pishko, V. V. *J. Magn. Magn. Mater.* **1995**, *140–144*, 1645.
(247) Christou, G.; Gatteschi, D.; Hendrickson, D. N.; Sessoli, R. *MRS Bull.* **2000**, *25*, 66.
(248) Gatteschi, D.; Sessoli, R. *Angew. Chem., Int. Ed.* **2003**, *42*, 268.
(249) Barra, A. L.; Gatteschi, D.; Sessoli, R. *Phys. Rev. B* **1997**, *56*, 8192.
(250) Sun, Z.; Ruiz, D.; Dilley, N. R.; Soler, M.; Ribas, J.; Folting, K.; Maple, M. B.; Christou, G.; Hendrickson, D. N. *J. Chem. Soc., Chem. Commun.* **1999**, 1973.
(251) Gomes, A. M.; Novak, M. A.; Sessoli, R.; Caneschi, A.; Gatteschi, D. *Phys. Rev. B* **1998**, *57*, 5021.
(252) Novak, M. A.; Gomes, A. M.; Rapp, R. E. *J. Appl. Phys.* **1998**, *83*, 6943.
(253) Novak, M. A.; Gomes, A. M.; Folly, W. S. D.; Rapp, R. E. *Magn. Magn. Mater. Appl., Mater. Sci. Forum* **1999**, *302–303*, 334.
(254) Gomes, A. M.; Novak, M. A.; Nunes, W. C.; Rapp, R. E. *J. Magn. Magn. Mater*. **2001**, *226*, 2015.
(255) Miyazaki, Y.; Bhattacharjee, A.; Nakano, M.; Saito, K.; Aubin, S. M. J. Eppley, H. J.; Christou, G.; Hendrickson, D. N.; Sorai, M. *Inorg. Chem.* **2001**, *40*, 6632.
(256) Fominaya, F.; Fournier, T.; Gandit, P.; Chaussy, J. *Rev. Sci. Instrum.* **1997**, *68*, 4191.
(257) Fominaya, F.; Villain, J.; Fournier, T.; Gandit, P.; Chaussy, J.; Fort, A.; Caneschi, A. *Phys. Rev. B* **1999**, *59*, 519.
(258) Luis, F.; Mettes, F. L.; Tejada, J.; Gatteschi, D.; de Jongh, L. J. *Phys. Rev. Lett*. **2000**, *85*, 4377.
(259) Luis, F.; Mettes, F. L.; Tejada, J.; Gatteschi, D.; de Jongh, L. J. *Polyhedron* **2001**, *20*, 1451.
(260) Mettes, F. L.; Luis, F.; de Jongh, L J. *Phys. Rev. B* **2001**, *64*, 174411.
(261) Fominaya, F.; Villain, J.; Gandit, P.; Chaussy, J.; Caneschi, A. *Phys. Rev. Lett.* **1997**, *79*, 1126.
(262) Fernandez, J. F.; Luis, F.; Bartolome, J. *Phys. Rev. Lett*. **1998**, *80*, 5659.
(263) Sales, M.; Hernandez, J. M.; Tejada, J.; Martinez, J. L. *Phys. Rev. B* **1999**, *60*, 14557.
(264) Luis, F.; Mettes, F.; Evangelisti, M.; Morello, A.; de Jongh, L. J. *J. Phys. Chem. Solids* **2004**, *65*, 763.
(265) Gaudin, G.; Gandit, P.; Chaussy, J.; Sessoli, R. *J. Magn. Magn. Mater*. **2002**, *242*, 915.
(266) Fominaya, F.; Gandit, P.; Gaudin, G.; Chaussy, J.; Sessoli, R.; Sangregorio, C. *J. Magn. Magn. Mater*. **1999**, *195*, L253.
(267) Yamaguchi, A.; Kusumi, N.; Ishimoto, H.; Mitamura, H.; Goto, T.; Mori, N.; Nakano, M.; Awaga, K.; Yoo, J.; Hendrickson, D. N.; Christou, G. *J. Phys. Soc. Jpn*. **2002**, *71*, 414.
(268) Affronte, M.; Lasjaunias, J. C.; Wernsdorfer, W.; Sessoli, R.; Gatteschi, D.; Heath, S. L.; Fort, A.; Rettori, A. *Phys. Rev. B* **2002**, *66*, 064408.
(269) Affronte, A.; Sessoli, R.; Gatteschi, D.; Wernsdorfer, W.; Lasjaunias, J. C.; Heath, S. L.; Powell, A. K.; Fort, A.; Rettori, A. *J. Phys. Chem. Solids* **2004**, *65*, 745.
(270) Morello, A.; Mettes, F. L.; Luis, F.; Fernández, J. F.; Krzystek, J.; Aromí, G.; Christou, G.; de Jongh, L. J. *Phys. Rev. Lett.* **2003**, *90*, 017206.
(271) Barra, A. L.; Caneschi, A.; Cornia, A.; de Biani, F. F.; Gatteschi, D.; Sangregorio, C.; Sessoli, R.; Sorace, L. *J. Am. Chem. Soc*. **1999**, *121*, 5302.
(272) Amoretti, G.; Carretta, S.; Caciuffo, R.; Casalta, H.; Cornia, A.; Affronte, M.; Gatteschi, D. *Phys. Rev. B* **2001**, *64*, 104403.
(273) Mettes, F. L.; Aromi, G.; Luis, F.; Evangelisti, M.; Christou, G.; Hendrickson, D. N.; de Jongh, L. J. *Polyhedron* **2001**, *20*, 1459.
(274) Evangelisti, M.; Luis, F.; Mettes, F. L.; Aliaga, N.; Aromi, G.; Christou, G.; de Jongh, L. J. *Polyhedron* **2003**, *22*, 2169.
(275) Evangelisti, M.; Luis, F.; Mettes, F. L.; Aliaga, N.; Aromí, G.; Alonso, J. J.; Christou, G.; de Jongh, L. J. *Phys. Rev. Lett.* **2004**, *93*, 117202.
(276) Glauber, R. J. *J. Math. Phys.* **1963**, *4*, 294.
(277) Caneschi, A.; Gatteschi, D.; Lalioti, N.; Sangregorio, C.; Sessoli, R.; Venturi, G.; Vindigni, A.; Rettori, A.; Pini, M. G.; Novak, M. A. *Angew. Chem., Int. Ed.* **2001**, *40*, 1760.
(278) Clérac, R.; Miyasaka, H.; Yamashita, M.; Coulon, C. *J. Am. Chem. Soc.* **2002**, *124*, 12837.
(279) Bhattacharjee, A.; Miyazaki, Y.; Nakano, M.; Yoo, J.; Christou, G.; Hendrickson, D. N.; Sorai, M. *Polyhedron* **2001**, *20*, 1607.
(280) Gao, S.; Su, G.; Yi, T.; Ma, B.-Q. *Phys. Rev. B* **2001**, *63*, 054431.
(281) Yoo, J.; Wernsdorfer, W.; Yang, E.-C.; Nakano, M.; Rheingold, A. L.; Hendrickson, D. N. *Inorg. Chem.* **2005**, *44*, 3377.
(282) Chiolero, A.; Loss, D. *Physica E* **1997**, *1*, 292.
(283) Affronte, M.; Lasjaunias, J. C.; Cornia, A. *Eur. Phys. J. B* **2000**, *15*, 633.
(284) Affronte, M.; Lasjaunias, J. C.; Cornia, A. *Physica B* **2000**, *284*, 1233.
(285) Affronte, M.; Lasjaunias, J. C.; Cornia, A.; Caneschi, A. *Phys. Rev. B* **1999**, *60*, 1161.
(286) Affronte, M.; Cornia, A.; Lascialfari, A.; Borsa, F.; Gatteschi, D.; Hinderer, J.; Horvatić, M.; Jansen, A. G. M.; Julien, M.-H. *Phys. Rev. Lett.* **2002**, *88*, 167201.
(287) Affronte, M.; Lasjaunias, J. C.; Abbati, L. *Phys. Rev. B* **2002**, *66*, 180405.
(288) Carretta, S.; van Slageren, J.; Guidi, T.; Liviotti, E.; Mondelli, C.; Rovai, D.; Cornia, A.; Dearden, A. L.; Carsughi, F.; Affronte, M.; Frost, C. D.; Winpenny, R. E. P.; Gatteschi, D.; Amoretti, G.; Caciuffo, R. *Phys. Rev. B* **2003**, *67*, 094405.
(289) Affronte, M.; Guidi, T.; Caciuffo, R.; Carretta, S.; Amoretti, G.; Hinderer, J.; Sheikin, I.; Jansen, A. G. M.; Smith, A. A.; Winpenny, R. E. P.; van Slageren, J.; Gatteschi, D. *Phys. Rev. B* **2003**, *68*, 104403.
(290) Carretta, S.; Santini, P.; Liviotti, E.; Magnani, N.; Guidi, T.; Caciuffo, R.; Amoretti, G. *J. Appl. Phys.* **2004**, *95*, 7348.
(291) König, E.; Ritter, G.; Kulshreshtha, S. K. *Chem. Rev.* **1985**, *85*, 219.
(292) Gütlich, P.; Hauser, A.; Spiering, H. *Angw. Chem. Int. Ed. Engl.* **1994**, *33*, 2024.
(293) Gütlich, P., Goodwin, H. A., Eds. *Spin Crossover in Transition Metal Compounds I, II, III*; Series: Topics in Current Chemistry; Springer: Berlin, 2004; Vol. 233, 234, 235.
(294) Tanabe, Y.; Sugano, S. *J. Phys. Soc. Jpn.* **1954**, *9*, 753.
(295) König, E.; Madeja, K. *Inorg. Chem*. **1967**, *6*, 48.
(296) Baker, W. A., Jr.; Bobonich, H. M. *Inorg. Chem.* **1964**, *3*, 1184.
(297) Sorai, M.; Seki, S. *J. Phys. Soc. Jpn*. **1972**, *33*, 575.
(298) Sorai, M.; Seki, S. *J. Phys. Chem. Solids* **1974**, *35*, 555.
(299) Takemoto, J. H.; Hutchinson, B. *Inorg. Chem.* **1973**, *12*, 705.
(300) Bousseksou, A.; McGarvey, J. J.; Varret, F.; Real, J. A.; Tuchagues, J.-J.; Dennis, A. C.; Boillot, M. L. *Chem. Phys. Lett.* **2000**, *318*, 409.
(301) Tuchagues, J.-J.; Bousseksou, A.; Molnár, G.; McGarvey, J. J.; Varret, F. In *Spin Crossover in Transition Metal Compounds*; Gütlich, P., Goodwin, H. A., Eds.; Series: Topics in Current Chemistry 235; Springer: Berlin, 2004; Vol. III, p 85.
(302) Brehm, G.; Reiher, M.; Schneider, S. *J. Phys. Chem. A* **2002**, *106*, 12024.
(303) Kaji, K.; Sorai, M. *Thermochim. Acta* **1985**, *88*, 185.
(304) Sorai, M.; Maeda, Y.; Oshio, H. *J. Phys. Chem. Solids* **1990**, *51*, 941.
(305) Jakobi, R.; Romstedt, H.; Spiering, H.; Gütlich, P. *Angew. Chem., Int. Ed. Engl.* **1992**, *31*, 178.
(306) Real, J. A.; Bolvin, H.; Bousseksou, A.; Dworkin, A.; Kahn, O.; Varret, F.; Zarembowitch, J. *J. Am. Chem. Soc.* **1992**, *114*, 4650.
(307) Sorai, M.; Yumoto, Y.; Halepoto, D. M.; Larkworthy, L. F. *J. Phys. Chem. Solids* **1993**, *54*, 421.
(308) Conti, A. J.; Kaji, K.; Nagano, Y.; Sena, K. M.; Yumoto, Y.; Chadha, R. K.; Rheingold, A. L.; Sorai, M.; Hendrickson, D. N. *Inorg. Chem*. **1993**, *32*, 2681.
(309) Kaji, K.; Sorai, M.; Conti, A. J.; Hendrickson, D. N. *J. Phys. Chem. Solids* **1993**, *54*, 1621.
(310) Sorai, M.; Nagano, Y.; Conti, A. J.; Hendrickson, D. N. *J. Phys. Chem. Solids* **1994**, *55*, 317.
(311) Kröber, J.; Audière, J.-P.; Claude, R.; Codjovi, E.; Kahn, O.; Haasnoot, J. G.; Grolière, F.; Jay, C.; Bousseksou, A.; Linarès, J.; Varret, F.; Gonthier-Vassal, A. *Chem. Mater.* **1994**, *6*, 1404.
(312) Boinnard, D.; Bousseksou, A.; Dworkin, A.; Savariault, J.-M.; Varret, F.; Tuchagues, J.-P. *Inorg. Chem.* **1994**, *33*, 271.
(313) Garcia, Y.; Kahn, O.; Rabardel, L.; Chansou, B.; Salmon, L.; Tuchagues, J. P. *Inorg. Chem.* **1999**, *38*, 4663.
(314) Boča, R.; Boča, M.; Dlháň, L.; Falk, K.; Fuess, H.; Haase, W.; Jaroščiak, R.; Papánková, B.; Renz, F.; Vrbová, M.; Werner, R. *Inorg. Chem.* **2001**, *40*, 3025.
(315) Nakamoto, T.; Tan, Z.-C.; Sorai, M. *Inorg. Chem*. **2001**, *40*, 3805.
(316) Papánková, B.; Vrbová, M.; Boča, R.; Šimon, P.; Falk, K.; Miehem, G.; Fuess, H. *J. Therm. Anal. Calorim.* **2002**, *67*, 721.
(317) Moliner, N.; Salmon, L.; Capes, L.; Munoz, M. C.; Létard, J. F.; Bousseksou, A.; Tuchagues, J. P.; McGarvey, J. J.; Dennis, A. C.; Castro, M.; Burriel, R.; Real, J. A. *J. Phys. Chem. B* **2002**, *106*, 4276.
(318) Roubeau, O.; de Vos, M.; Stassen, A. F.; Burriel, R.; Haasnoot, J. G.; Reedijk, J. *J. Phys. Chem. Solids* **2003**, *64*, 1003.
(319) Nakamoto, T.; Bhattacharjee, A.; Sorai, M. *Bull. Chem. Soc. Jpn.* **2004**, *77*, 921.
(320) König, E. *Prog. Inorg. Chem.* **1987**, *35*, 527.
(321) Guionneau, P.; Marchivie, M.; Bravic, G.; Létard, J.-F.; Chasseau, D. In *Spin Crossover in Transition Metal Compounds*; Gütlich, P., Goodwin, H. A., Eds.; Series: Topics in Current Chemistry 234; Springer: Berlin, 2004; Vol. II, p 97.
(322) Kusz, J.; Gütlich, P.; Spiering, H. In *Spin Crossover in Transition Metal Compounds*; Gütlich, P., Goodwin, H. A., Eds.; Series: Topics in Current Chemistry 234; Springer: Berlin, 2004; Vol. II, p 129.

(323) Gallois, B.; Real, J.-A.; Hauw, C.; Zarembowitch, J. *Inorg. Chem.* **1990**, *29*, 1152.

(324) Greenaway, A. M.; Sinn, E. *J. Am. Chem. Soc.* **1978**, *100*, 8080.

(325) Katz, B. A.; Strouse, C. E. *J. Am. Chem. Soc.* **1979**, *101*, 6214.

(326) Greenaway, A. M.; O'Connor, C. J.; Schrock, A.; Sinn, E. *Inorg. Chem.* **1979**, *18*, 2692.

(327) Mikami, M.; Konno, M.; Saito, Y. *Chem. Phys. Lett.* **1979**, *63*, 566.

(328) Mikami, M.; Konno, M.; Saito, Y. *Acta Crystallogr.* **1980**, *B36*, 275.

(329) Chernyshov, D.; Hostettler, M.; Törnroos, K. W.; Bürgi, H.-B. *Angew. Chem., Int. Ed.* **2003**, *42*, 3825.

(330) Vos, G.; de Graaff, R. A. G.; Haasnoot, J. G.; van der Kraan, A. M.; de Vaal, P.; Reedijk, J. *Inorg. Chem.* **1984**, *23*, 2905.

(331) Wiehl, L.; Kiel, G.; Köhler, C. P.; Spiering, H.; Gütlich, P. *Inorg. Chem.* **1986**, *25*, 1565.

(332) Claude, R.; Real, J.-A.; Zarembowitch, J.; Kahn, O.; Ouahab, L.; Grandjean, D.; Boukheddaden, K.; Varret, F.; Dworkin, A. *Inorg. Chem.* **1990**, *29*, 4442.

(333) Oshio, H.; Toriumi, K.; Maeda, Y.; Takashima, Y. *Inorg. Chem.* **1991**, *30*, 4252.

(334) Real, J.-A.; Gallois, B.; Granier, T.; Suez-Panamá, F.; Zarembowitch, J. *Inorg. Chem.* **1992**, *31*, 4972.

(335) Real, J.-A.; Muñoz, M. C.; Andrés, E.; Granier, T.; Gallois, B. *Inorg. Chem.* **1994**, *33*, 3587.

(336) Létard, J.-F.; Guionneau, P.; Rebardel, L.; Howard, J. A. K.; Goeta, A. E.; Chasseau, D.; Kahn, O. *Inorg. Chem.* **1998**, *37*, 4432.

(337) Guionneau, P.; Létard, J.-F.; Yufit, D. S.; Chasseau, D.; Bravic, G.; Goeta, A. E.; Howard, J. A. K.; Kahn, O. *J. Mater. Chem.* **1999**, *9*, 985.

(338) Reger, D. L.; Little, C. A.; Young, V. G., Jr.; Pink, M. *Inorg. Chem.* **2001**, *40*, 2870.

(339) Matouzenko, G. S.; Létard, J.-F.; Lecocq, S.; Bousseksou, A.; Capes, L.; Salmon, L.; Perrin, M.; Kahn, O.; Collet, A. *Eur. J. Inorg. Chem.* **2001**, 2935.

(340) Chun, H.; Bill, E.; Weyhermüller, T.; Wieghardt, K. *Inorg. Chem.* **2003**, *42*, 5612.

(341) Hibbs, W.; van Koningsbruggen, P. J.; Arif, A. M.; Shum, W. W.; Miller, J. S. *Inorg. Chem.* **2003**, *42*, 5645.

(342) Matouzenko, G. S.; Bousseksou, A.; Borshch, S. A.; Perrin, M.; Zein, S.; Salmon, L.; Molnar, G.; Lecocq, S. *Inorg. Chem.* **2004**, *43*, 227.

(343) Matouzenko, G. S.; Luneau, D.; Gábor Molnár, G.; Bousseksou, A.; Zein, S.; Borshch, S. A.; Ould-Moussa, N.; Averseng, F. *Eur. J. Inorg. Chem.*, submitted.

(344) Rao, P. S.; Reuveni, A.; McGarvey, B. R.; Gangli, P.; Gütlich, P. *Inorg. Chem.* **1981**, *20*, 204.

(345) Frenkel, J. *Kinetic Theory of Liquids*; Oxford University Press: London, 1947.

(346) Privalov, P. L. *Adv. Protein Chem.* **1979**, *33*, 167.

(347) Privalov, P. L.; Gill, S. J. *Adv. Protein Chem.* **1988**, *39*, 191.

(348) Gütlich, P.; Link, R.; Steinhäuser, H. G. *Inorg. Chem.* **1978**, *17*, 2509.

(349) Dose, E. V.; Murphy, K. M. M.; Wilson, L. J. *Inorg. Chem.* **1976**, *15*, 2622.

(350) König, E.; Ritter, G.; Goodwin, H. A. *J. Inorg. Nucl. Chem.* **1977**, *39*, 1131 and 1773.

(351) Reeder, K. A.; Dose, E. V.; Wilson, L. J. *Inorg. Chem.* **1978**, *17*, 1071.

(352) Dose, E. V.; Hoselton, M. A.; Sutin, N.; Tweedle, M. F.; Wilson, L. J. *J. Am. Chem. Soc.* **1978**, *100*, 1141.

(353) Evans, D. F.; James, T. A. *J. Chem. Soc., Dalton Trans.* **1979**, 723.

(354) Wajnflasz, J.; Pick, R. *Phys. Status Solidi* **1970**, *40*, 537.

(355) Slichter, C. P.; Drickamer, H. G. *J. Chem. Phys.* **1972**, *56*, 2142.

(356) Bolvin, H.; Kahn, O. *Chem. Phys.* **1995**, *192*, 295.

(357) Doan, P. E.; McGarvey, B. R. *Inorg. Chem.* **1990**, *29*, 874.

(358) Nishino, M.; Miyashita, S.; Boukheddaden, K. *J. Chem. Phys*. **2003**, *118*, 4594.

(359) Renovitch, G. A.; Baker, W. A., Jr. *J. Am. Chem. Soc.* **1967**, *89*, 6377.

(360) Sorai, M.; Ensling, J.; Gütlich, P. *Chem. Phys*. **1976**, *18*, 199.

(361) Sorai, M.; Ensling, J.; Hasselbach, K. M.; Gütlich, P. *Chem. Phys*. **1977**, *20*, 197.

(362) Köppen, H.; Müller, E. W.; Köhler, C. P.; Spiering, H.; Meissner, E.; Gütlich, P. *Chem. Phys. Lett*. **1982**, *91*, 348.

(363) Petrouleas, V.; Tuchagues, J.-P. *Chem. Phys. Lett.* **1987**, *137*, 21.

(364) Sasaki, N.; Kambara, T. *Phys. Rev. B* **1989**, *40*, 2442.

(365) Bousseksou, A.; Nasser, J.; Linares, J.; Boukheddaden, K.; Varret, F. *Mol. Cryst. Liq. Cryst.* **1993**, *234*, 269.

(366) Kohlhaas, Th.; Spiering, H.; Gütlich, P. *Z. Phys. B* **1997**, *102*, 455.

(367) Romstedt, H.; Hauser, A.; Spiering, H. *J. Phys. Chem. Solids* **1998**, *59*, 265.

(368) Romstedt, H.; Spiering, H.; Gütlich, P. *J. Phys. Chem. Solids* **1998**, *59*, 1353.

(369) Koudriavtsev, A. B. *Chem. Phys.* **1999**, *241*, 109.

(370) Nishino, M.; Boukheddaden, K.; Miyashita, S.; Varret, F. *Phys. Rev. B* **2003**, *68*, 224402.

(371) Personage, N. G.; Staveley, L. A. K. *Disorder in Crystals*; Oxford University Press: London, 1978; p 36.

(372) König, E.; Ritter, G. *Solid State Commun.* **1976**, *18*, 279.

(373) König, E.; Ritter, G.; Irler, W.; Nelson, S. M. *Inorg. Chim. Acta* **1979**, *37*, 169.

(374) König, E.; Ritter, G.; Grünsteudel, H.; Dengler, J.; Nelson, J. *Inorg. Chem.* **1994**, *33*, 837.

(375) Constant-Machado, H.; Stancu, A.; Linares, J.; Varret, F. *IEEE Trans. Magn.* **1998**, *34*, 2213.

(376) König, E.; Ritter, G.; Irler, W.; Goodwin, H. A. *J. Am. Chem. Soc.* **1980**, *102*, 4681.

(377) König, E.; Kanellakopulos, B.; Powietzka, B.; Goodwin, H. A. *Inorg. Chem*. **1990**, *29*, 4944.

(378) König, E.; Ritter, G.; Kulshreshtha, S. K.; Nelson, S. M. *Inorg. Chem.* **1982**, *21*, 3022.

(379) König, E.; Ritter, G.; Kulshreshtha, S. K.; Waigel, J.; Goodwin, H. A. *Inorg. Chem.* **1984**, *23*, 1896.

(380) König, E.; Ritter, G.; Kulshreshtha, S. K.; Goodwin, H. A. *Inorg. Chem.* **1984**, *23*, 1903.

(381) Kröber, J.; Codjovi, E.; Kahn, O.; Grolière, F.; Jay, C. *J. Am. Chem. Soc.* **1993**, *115*, 9810.

(382) Kahn, O.; Codjovi, E. *Philos. Trans. R. Soc. London A* **1996**, *354*, 359.

(383) Codjovi, E.; Sommier, L.; Kahn, O.; Jay, C. *New J. Chem.* **1996**, *20*, 503.

(384) Garcia, Y.; van Koningsbruggen, P. J.; Codjovi, E.; Lapouyade, R.; Kahn, O.; Rabardel, L. *J. Mater. Chem.* **1997**, *7*, 857.

(385) Garcia, Y.; van Koningsbruggen, P. J.; Lapouyade, R.; Fournès, L.; Rabardel, L.; Kahn, O.; Ksenofontov, V.; Levchenko, G.; Gütlich, P. *Chem. Mater.* **1998**, *10*, 2426.

(386) Létard, J.-F.; Guionneau, P.; Codjovi, E.; Lavastre, O.; Bravic, G.; Chasseau, D.; Kahn, O. *J. Am. Chem. Soc.* **1997**, *119*, 10861.

(387) Garcia, Y.; van Koningsbruggen, P. J.; Lapouyade, R.; Rabardel, L.; Kahn, O.; Wieczorek, M.; Bronisz, R.; Ciunik, Z.; Rudolf, M. F. *C. R. Acad. Sci. Paris* **1998**, *Ser. II*, 523.

(388) Slichter, C. P.; Drickamer, M. G. *J. Chem. Phys.* **1972**, *56*, 2142.

(389) Kah, O. *Chem. Br.* **1999**, *Feb*, 24.

(390) Ogasahara, K.; Sorai, M.; Suga, H. *Chem. Phys. Lett*. **1979**, *68*, 457.

(391) Ogasahara, K.; Sorai, M.; Suga, H. *Mol. Cryst. Liq. Cryst*. **1981**, *71*, 189.

(392) Allen, G. C.; Hush, N. S. *Prog. Inorg. Chem.* **1967**, *8*, 357.

(393) Brown, D. B., Ed. *Mixed-Valence Compounds, Theory and Applications in Chemistry, Physics, Geology, and Biology*; Reidel: Dordrecht, 1980.

(394) Day, P. *Int. Rev. Phys. Chem*. **1981**, *1*, 149.

(395) Prassides, K., Ed. *Mixed Valency Systems: Applications in Chemistry, Physics and Biology*; Kluwer Academic Publishers: Dordrecht, 1991.

(396) Sorai, M.; Hendrickson, D. N. *Pure Appl. Chem.* **1991**, *63*, 1503.

(397) Hendrickson, D. N. In *Mixed Valency Systems: Applicaions in Chemistry, Physics and Biology*; Prassides, K., Ed.; Kluwer Academic Publishers: Dordrecht, 1991; p 67.

(398) Woehler, S. E.; Wittebort, R. J.; Oh, S. M.; Kambara, T.; Hendrickson, D. N.; Inniss, D.; Strouse, C. E. *J. Am. Chem. Soc*. **1987**, *109*, 1063.

(399) Oh, S. M.; Hendrickson, D. N.; Hassett, K. L.; Davis, R. E. *J. Am. Chem. Soc*. **1984**, *106*, 7984.

(400) Oh, S. M.; Hendrickson, D. N.; Hassett, K. L.; Davis, R. E. *J. Am. Chem. Soc.* **1985**, *107*, 8009.

(401) Launay, J. P.; Babonneau, F. *Chem. Phys*. **1982**, *67*, 295.

(402) Borshch, S. A.; Kotov, I. N.; Bersuker, I. B. *Chem. Phys. Lett*. **1982**, *89*, 381.

(403) Cannon, R. D.; Montri, L.; Brown, D. B.; Marshall, K. M.; Elliot, C. M. *J. Am. Chem. Soc*. **1984**, *106*, 2591.

(404) Kambara, T.; Hendrickson, D. N.; Sorai, M.; Oh, S. M. *J. Chem. Phys*. **1986**, *85*, 2895.

(405) Oh, S. M.; Kambara, T.; Hendrickson, D. N.; Sorai, M.; Kaji, K.; Woehler, S. E.; Wittebort, R. J. *J. Am. Chem. Soc*. **1985**, *107*, 5540.

(406) Sorai, M.; Kaji, K.; Hendrickson, D. N.; Oh, S. M. *J. Am. Chem. Soc*. **1986**, *108*, 702.

(407) Nakano, M.; Sorai, M.; Vincent, J. B.; Christou, G.; Jang, H. G.; Hendrickson, D. N. *Inorg. Chem*. **1989**, *28*, 4608.

(408) Jang, H. G.; Vincent, J. B.; Nakano, M.; Huffman, J. C.; Christou, G.; Sorai, M.; Wittebort, R. J.; Hendrickson, D. N. *J. Am. Chem. Soc*. **1989**, *111*, 7778.

(409) Jang, H. G.; Geib, S. J.; Kaneko, Y.; Nakano, M.; Sorai, M.; Rheingold, A. L.; Montez, B.; Hendrickson, D. N. *J. Am. Chem. Soc*. **1989**, *111*, 173.

(410) Kaneko, Y.; Nakano, M.; Sorai, M.; Jang, H. G.; Hendrickson, D. N. *Inorg. Chem*. **1989**, *28*, 1067.

(411) Jang, H. G.; Wittebort, R. J.; Sorai, M.; Kaneko, Y.; Nakano, M.; Hendrickson, D. N. *Inorg. Chem*. **1992**, *31*, 2265.

(412) Sorai, M.; Shiomi, Y.; Hendrickson, D. N.; Oh, S. M.; Kambara, T. *Inorg. Chem*. **1987**, *26*, 223.

(413) Nishimori, A.; Nagano, Y.; Sorai, M.; Hendrickson, D. N. The 22nd Annual Meeting of the Japan Society of Calorimetry and Thermal Analysis, Tsukuba, 1986; D310.
(414) Jang, H. G.; Kaji, K.; Sorai, M.; Wittebort, R. J.; Geib, S. J.; Rheingold, A. L.; Hendrickson, D. N. *Inorg. Chem*. **1990**, *29*, 3547.
(415) Stratt, R. M.; Adachi, S. H. *J. Chem. Phys*. **1987**, *86*, 7156.
(416) Nakamoto, T.; Hanaya, M.; Katada, M.; Endo, K.; Kitagawa, S.; Sano, H. *Inorg. Chem*. **1997**, *36*, 4347.
(417) Nakamoto, T.; Wang, Q.; Miyazaki, Y.; Sorai, M. *Polyhedron* **2002**, *21*, 1299.
(418) Sato, T.; Katada, M.; Endo, K.; Nakada, M.; Sano, H. *J. Radioanal. Nucl. Chem*. **1993**, *173*, 107.
(419) Stadler, C.; Daub, J.; Kohler, J.; Saalfrank, R. W.; Coropceanu, V.; Schunemann, V.; Ober, C.; Trautwein, A. X.; Parker, S. F.; Poyraz, M.; Inomata, T.; Cannon, R. D. *J. Chem. Soc., Dalton Trans.* **2001**, 3373.
(420) Hendrickson, D. N.; Oh, S. M.; Dong, T.-Y.; Kambara, T.; Cohn, M. J.; Moore, M. F. *Comments Inorg. Chem*. **1985**, *4*, 329.
(421) Kambara, T.; Hendrickson, D. N.; Dong, T.-Y.; Cohn, M. J. *J. Chem. Phys*. **1987**, *86*, 2362.
(422) Klokishner, S. I.; Tsukerblat, B. S. *Chem. Phys*. **1988**, *125*, 11.
(423) Koryachenko, A. V.; Klokishner, S. I.; Tsukerblat, B. S. *Chem. Phys.* **1991**, *150*, 295.
(424) Cohn, M. J.; Dong, T.-Y.; Hendrickson, D. N.; Geib, S. J.; Rheingold, A. L. *J. Chem. Soc., Chem. Commun*. **1985**, 1095.
(425) Iijima, S.; Saida, R.; Motoyama, I.; Sano, H. *Bull. Chem. Soc. Jpn.* **1981**, *54*, 1375.
(426) Dong, T.-Y.; Hendrickson, D. N.; Iwai, K.; Cohn, M. J.; Geib, S. J.; Rheingold, A. L.; Sano, H.; Motoyama, I.; Nakashima, S. *J. Am. Chem. Soc*. **1985**, *107*, 7996.
(427) Webb, R. J.; Hagen, P. M.; Wittebort, R. J.; Sorai, M.; Hendrickson, D. N. *Inorg. Chem*. **1992**, *31*, 1791.
(428) Sorai, M.; Nishimori, A.; Hendrickson, D. N.; Dong, T.-Y.; Cohn, M. J. *J. Am. Chem. Soc*. **1987**, *109*, 4266.
(429) Nakashima, S.; Nishimori, A.; Masuda, Y.; Sano, H.; Sorai, M. *J. Phys. Chem. Solids* **1991**, *52*, 1169.
(430) Morrison, W. H., Jr.; Hendrickson, D. N. *Inorg. Chem*. **1975**, *14*, 2331.
(431) Motoyama, I.; Suto, K.; Katada, M.; Sano, H. *Chem. Lett*. **1983**, 1215.
(432) Dong, T.-Y.; Hendrickson, D. N.; Pierpont, C. G.; Moore, M. F. *J. Am. Chem. Soc*. **1986**, *108*, 963.
(433) Nakano, M.; Sorai, M.; Hagen, P. M.; Hendrickson, D. N. *Chem. Phys. Lett*. **1992**, *196*, 486.
(434) Kambara, T.; Sasaki, N. *J. Coord. Chem*. **1988**, *18*, 129.
(435) Bloomquist, D. R.; Willett, R. D. *Coord. Chem. Rev.* **1982**, *47*, 125.
(436) Sone, K.; Fukuda, Y. *Inorganic Thermochromism*; Springer-Verlag: Berlin, 1987.
(437) Arai, N.; Sorai, M.; Seki, S. *Bull. Chem. Soc. Jpn*. **1972**, *45*, 2398.
(438) Roberts, S. A.; Bloomquist, D. R.; Willett, R. D.; Dodgen, H. W. *J. Am. Chem. Soc*. **1981**, *103*, 2603.
(439) Nishimori, A.; Sorai, M. *J. Phys. Chem. Solids* **1999**, *60*, 895.
(440) Yamaki, S.; Fukuda, Y.; Sone, K. *Chem. Lett*. **1982**, 269.
(441) Hoshino, N.; Fukuda, Y.; Sone, K.; Tanaka, K.; Marumo, F. *Bull. Chem. Soc. Jpn*. **1989**, *62*, 1822.
(442) Hara, H.; Sorai, M. *J. Phys. Chem. Solids* **1995**, *56*, 223.
(443) Burdett, J. K. *Adv. Inorg. Chem. Radiochem*. **1978**, *21*, 113.
(444) Andino, M. M.; Curet, J. D.; Muir, M. M. *Acta Crystallogr. Ser. B* **1976**, *32*, 3185.
(445) Grenthe, L.; Paoletti, P.; Sandström, M.; Glikberg, S. *Inorg. Chem*. **1979**, *18*, 2687.
(446) Lever, A. B. P.; Montovani, E.; Donini, J. C. *Inorg. Chem*. **1971**, *10*, 2424.
(447) Ferraro, J. R.; Basile, L. J.; Garcia-Ineguez, L. R.; Paoletti, P.; Fabbrizzi, L. *Inorg. Chem*. **1976**, *15*, 2342.
(448) Pylkki, R. J.; Willett, R. D.; Dodgen, H. W. *Inorg. Chem*. **1984**, *23*, 594.
(449) Nishimori, A.; Schmitt, E. A.; Hendrickson, D. N.; Sorai, M. *J. Phys. Chem. Solids* **1994**, *55*, 99.
(450) Nishimori, A.; Schmitt, E. A.; Hendrickson, D. N.; Sorai, M. *J. Coord. Chem*. **1996**, *37*, 327.

CR960049G